Contribution to the study of the ITER Vacuum Vessel constituent material (SS316L(N)-IG) : thermomechanical modelling and numerical simulations

Flavien Sabourin

École Doctorale 353 SCIENCES POUR L'INGÉNIEUR :

Mécanique, Physique, Micro et Nanoélectronique

Spécialité : Mécanique des solides

Thèse

Pour obtenir le grade de

DOCTEUR DE L'ÉCOLE CENTRALE DE MARSEILLE

Par

Flavien SABOURIN

Contribution to the study of the ITER Vacuum Vessel constituent material (SS316L(N)-IG)

– thermomechanical modelling and numerical simulations –

Soutenance prévue le 16 Décembre 2021 devant le jury suivant :

Carole NADOT-MARTIN	Professeure des universités, École nationale supérieure de mécanique et d'aérotechnique, Poitiers	Rapporteur
Yves CHEMISKY	Professeur des universités, Université de Bordeaux	Rapporteur
Farid ABED-MERAIM	Professeur des universités, École nationale supérieure des arts et métiers, Metz	Président du jury
Noël LAHELLEC	Professeur des universités, Aix-Marseille Université	Examinateur
Jean-Marc MARTINEZ	Ingénieur, ITER Organisation, Cadarache	Invité
Thierry DÉSOYER	Professeur des universités, Ecole Centrale de Marseille	Directeur
Stéphane LEJEUNES	Ingénieur de recherche, Laboratoire de Mécanique et d'Acoustique, Marseille	Co-directeur

Affidavit

I, undersigned, Flavien Sabourin, hereby declare that the work presented in this manuscript is my own work, carried out under the scientific direction of Thierry Désoyer and Stéphane Lejeunes, in accordance with the principles of honesty, integrity and responsibility inherent to the research mission. The research work and the writing of this manuscript have been carried out in compliance with both the French national charter for Research Integrity and the Aix-Marseille University charter on the fight against plagiarism.

This work has not been submitted previously either in this country or in another country in the same or in a similar version to any other examination body.

Eyguières, Octobre 9th, 2021.

ITER Disclaimer

The views and opinions expressed herein do not necessarily reflect those of the ITER Organization.

List of publications and participation in conferences

Publication produced as part of the PhD thesis:

F. Sabourin and al., "Development of a thermo-mechanical behaviour model adapted to the ITER vacuum vessel material", *Fusion Engineering and Design*, Volume 173, December 2021.

Participation in conference during the PhD thesis period:

The 13th International Symposium on Fusion Nuclear Technology (ISFNT), September 25th-29th, 2017, Kyoto Japan.

Glossary

notations	
x	scalar
$\mathbf{X}$	tensor
[X]	matrix
$\mathbf{x}$	deviatoric tensor, $\mathbf{x} = \boldsymbol{Dev}(\boldsymbol{X})$
J($\mathbf{X}$)	Von Mises equivalent stress, $J(\mathbf{X}) = \sqrt{\frac{3}{2}\boldsymbol{Dev}(\boldsymbol{X}):\boldsymbol{Dev}(\boldsymbol{X})}$
f($\mathbf{X}$)	function
< >	Mc Cauley parenthesis, <f($\mathbf{X}$)>= f($\mathbf{X}$) if f($\mathbf{X}$)≥0 and <f($\mathbf{X}$)>= 0 if f($\mathbf{X}$)<0

Symbols	
C_ε	calorific capacity at constant volume (J/kg.K)
E	Young modulus (Pa)
e	internal energy (J/kg)
f^v	volumic forces (N/m^3)
k	Isotropic coefficient of thermal conductivity (W/m.°C)
$\mathbf{G}$	identity tensor
p	isotropic parameter
r^v	volumic heating (W/m^3)
R	isotropic variable
s	mass entropy (J/ kg.K)
T_0	initial temperature (K)
T	temperature (K)

Greek symbols	
γ	coefficient of thermal expansion (K^{-1})
$\boldsymbol{\varepsilon}$	total strain tensor (m/m)
$\boldsymbol{\varepsilon^p}$	plastic strain tensor (m/m)
η	viscosity characteristic coefficients of the material (s-1)
$\boldsymbol{\sigma}$	Stress tensor (Pa)
σ_0	initial stress threshold criterion (Pa)
λ	First Lamé coefficient (Pa)
Λ	plastic multiplier (s^{-1})
μ	Second Lamé coefficient (Pa)
υ	Poisson coefficient (Unit less)
ρ_0	Initial density (kg/m^3)
ρ	density (kg/m^3)
Ψ	free energy (J/kg)
Γ	material parameters (Unit less)

Abstract

The ITER machine has been classified as a Basic Nuclear Installation (INB n°174) by the French nuclear regulator, which implies that it will be the first fusion reactor to go through the complete French nuclear licencing process. The combination of mechanic and electromagnetic phenomena with the heat loads caused by neutron streaming requires a multi-physics approach to the damage assessment; this has not yet been implemented in the common nuclear codes and standards.

In most cases, structural integrity is justified within a linear elastic behaviour. When this route is not enough to respect the design criteria, several non-linear approaches to the material's mechanical behaviour can be considered, requiring a more elaborated demonstration of the design compliance. Nevertheless, the models proposed in the nuclear model database are sometimes not sufficient to properly describe the experimentally observed cyclic plasticity behaviour and, in particular, the ratcheting and shakedown phenomena.

The ratcheting phenomenon is an old topic as many papers discuss this subject from the material characterisation up to the model development; most of the studies were performed by J. L. Chaboche and his collaborators. However, the application of a thermomechanical approach to assess this phenomenon remains rare: that is why we proposed to develop a fully coupled thermomechanical model.

In the first step of our work, we carried out a mechanical test campaign, executed on the SS316L(N)-IG which is the ITER Vacuum Vessel (VV) structural material. This campaign was composed of several cyclic tension/compression tests performed with an imposed stress (almost non-existent in the literature) and cyclic torsion tests conducted with an imposed moment. The objective was to observe the material response under low cyclic fatigue, to better understand the shakedown (elastic and/or plastic) and ratcheting.

In the second step of our work, we developed the material behaviour model, starting from a Chaboche's model available in the literature (elasto-(visco)-plastic model, with various types of hardening). We then enriched it to explicitly take into account the influence of the temperature on the mechanical behaviour and, reciprocally, the influence of the mechanical behaviour on the temperature, i.e. the thermomechanical coupling. In addition, based on the observations made on the cyclic tests, we proposed to implement a damage variable on both kinematic and isotropic hardening behaviours.

In the final step of our work, we implemented the model in the Abaqus® finite element software and simulated different scenarios including a simplified VV geometry, called the VV "rails", which was tested under thermomechanical cyclic loading.

Keywords: *Thermo-mechanical coupling, material behaviour model, non-linear hardening, damage, return radial, ratcheting, SS316L(N)-IG.*

Acknowledgement

After four years of work on PhD Thesis in parallel with my ITER activities, I acknowledge that this task required much motivation, willingness and personal involvement. On top of that, its achievement will not have been possible without the unfailing support of all persons that have trusted me and have contributed in their own way and at different levels to ensure the success of this rewarding experience.

My sincere thanks go first to Jean-Marc MARTINEZ, who was the first one to trust me, offering this adventure sharing a beer together in Barcelona in 2016.

One day, a PhD student told me that "*80% of the thesis success and interest is linked to your Director and co-directors*". Today, I can confirm that this work has been possible only due the continuous support and the excellent knowledge they provided me with during these 4 years. For this reason, I want to extend special thanks to Thierry DÉSOYER and Stéphane LEJEUNES.

One of the singularities of this thesis was the mechanical tensile compression tests, performed in imposed stress, and torsional tests performed in imposed torque. This has been possible only due to the investigation of Frederic MAZEROLLE, for whom I make a dedicated thank.

Then, I wish to thank my hierarchy, namely Chang Ho CHOI, Alexander ALEKSEEV and Xavier BRAVO, who allowed me to perform this work in addition to my ITER duties. Many thanks also to Alex MARTIN, who provided me with the ITER VV material sample that was used for the mechanical tests campaign.

A great thank to Mikhail PRIVALOV who helped me in the use of ABQUS and MathCad. He also helped taking some part of my ITER work under his responsibility in order to free up my time for the Thesis.

Thanks to Vladimir BARABASH who provided me with the first bibliographic papers on the subject (one written in Russian).

The most complex exercise of the Thesis, above the equation setting and resolution, is writing the final dissertation. It will not have been possible without the help of my wife Ann-Sophie GABELLINI, Olivia SCHETRIT-BELMAR, James DAVIS and Esmeralda MOSCATELLI.

Finally, I want to thank the members of IO-CT who have worked conjointly as the Vacuum Vessel Project Team, and the LMA members for the various activities reported in this manuscript.

Table of contents

Introduction

The first nuclear fusion reactor was created in the sixties in Russia and since that time, a lot of machines have been built all over the world for testing and understanding the complexities linked to the production of power via fusion; see Figure 1. In the eighties, many programs were launched to prove that fusion can be used as a large-scale energy source and as an alternative to nuclear fission power plants and fossil fuel power stations.

The ITER Organization was born of the idea of a collaborative international project that gathers different technologies to produce fusion power energy for commercial use. ITER will be used as an experimental reactor for testing plasma operations and accident scenarios, and to obtain information on design, technologies, materials and processes in fusion reactor environment that are relevant for the development of DEMO campaign (Salavy, 2009).

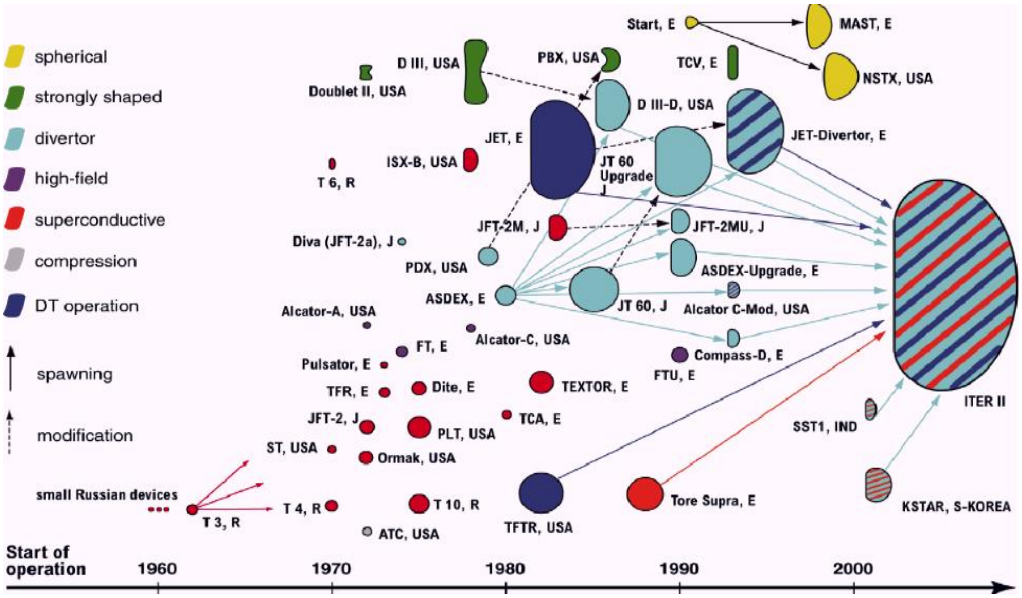

Figure 1 – Overview of the development of tokamaks during the past 50 years in terms of their size, poloidal shape, power and particle exhaust concept, magnet technology and mode of plasma operation (Ikeda, 2009).

The ITER Vacuum Vessel, which is the first confinement barrier made in SS316L(N)-IG, must withstand 30 000 plasma pulses generating heat loads caused by neutron streaming, combined with water pressure, electromagnetic loads and inertial loads. Although fusion reactors are completely different in their design and operation in comparison to fission reactors, they have to follow the nuclear design codes and standards based on the fission nuclear plant service experience feedback. Their structural integrity is generally justified by analytical or Finite Element Method (FEM), according to the nuclear design codes rules. However, some cases, like the oligocyclic fatigue, can lead to a ratcheting failure mode. Here, the rules proposed by the codes are too stringent and not adapted to a tokamak device environment like ITER.

That is why we propose to develop a specific material model, adapted to ITER's specific properties, for the prevention of damage under thermo-mechanical constraint for low cyclic fatigue.

The present work has been achieved in collaboration between the ITER Organisation (IO) and the Laboratory of Mechanics and Acoustic (LMA) to assess a non-linear behaviour model with a strong thermo-mechanical coupling, including a damage parameter. The initial objective was to enrich existing models available in the literature (elasto-visco-plasticity models, with various types of hardening), in order to explicitly take into account the influence of the temperature on the mechanical behaviour and, reciprocally, the influence of the mechanical behaviour on the temperature. However, this work goes further; the developed model representing shakedown and/or ratcheting responses under cyclic loadings are central in the design justification of pressurised structures under thermal cyclic loadings, like the ITER Vacuum Vessel (VV).

More precisely, the following points are developed in this report:

- **Chapter 1 specifies the context of the study**.
  Technical elements are described regarding the design rules provided by the nuclear codes and standards. Details are given to defined what loads are defined as "primary" and "secondary" loads. Basic notions related to metal deformation mechanisms, from the crystallography to the macroscopic scale, are described with a dedicated attention on the ratcheting phenomenon. Some examples of the main (thermo)-mechanical tests for the material parameter identification are provided. Since our model development includes a damage variable, combined with the nuclear environment of the structure, a short introduction to the neutron damage on steel structures is presented. Finally, an overview of the phenomenological approach for the modelling of metal plasticity in the standard thermodynamic framework is developed.

- **Chapter 2 presents the results of the oligocyclic fatigue tests made on the ITER VV material**.
  As the model development is dedicated to the ratcheting response under imposed stress, the extensometer was adapted for measuring the evolution of the test sample diameter. This configuration made it possible to measure the true stress during imposed force test and to conduct the test with an imposed stress. Finally, some cyclic torsion tests were conducted with an imposed angle and force to observe the non-stabilised response of the material under inhomogeneous stress distribution.

- **Chapter 3 describes the model development including strong thermo-mechanical coupling and damage variable.**
  The proposed model is based on the superposition of several hardening functions to represent the following hardening behaviours: Bauschinger effect, cyclic softening and hardening, shakedown (elastic and/or plastic), and ratcheting. The damage variable takes into account the general framework of continuum damage mechanics for which the ductile fracture results from the competition between hardening and damage. The proposed model was tested on a homogeneous problem and the results were compared with uniaxial test results (0D analysis).

- **Chapter 4 recalls the basic Finite Element (FE) resolution for a thermomechanical problem and details the FE implementation done in Abaqus®.**
  Even if the return radial method was retained for local integration, it had to be adapted to our model due to the thermo-mechanical coupling and the damage variable. Technical details are provided on how to calculate consistent tangent operators that are required for an integration in Abaqus'® users subroutines (UMAT and UMATHT in our case). A tentative of model validation was made using a tensile-compression and cyclic torsion test simulation. Finally, a simplified VV geometry called the VV "rails" was tested under thermo-mechanical cyclic loading.

Chapter 1. Scientific context

1.1. Introduction

The ITER Vacuum Vessel, which is the first confinement barrier made in SS316L(N)-IG, have to withstand 30 000 plasma pulses generating cyclic heat loads. Although fusion reactors are completely different in their design and operation in comparison to fission ones, they have to follow the nuclear design codes and standards based on the fission nuclear plant service experience feedback. However, in some cases like the oligocyclic fatigue, the rules proposed are too stringent and not adapted to a tokamak device environment like ITER.

More particularly, the ratcheting, which is one of the predominant failure mode for oligocyclic fatigue, is only generally treated by a pure mechanical approach according to a preliminary literature survey.

This Chapter describes the specific environment of the ITER tokamak and associated thermo-mechanical constrains, so as to understand how the ITER Vacuum vessel structural material types have been selected. Moreover, a brief introduction of the nuclears codes and standards is presented, for a better understanding of the main failure modes and associated classification. Coming back to the fundamentals, a description of the structure and mechanisms of deformation of the metals, from the atomic to the macroscopic levels, is done. These parts are completed with a description of the main used mechanical tests that are performed for undertansing the material behaviour and for mesuring material parameters. In a second step, the basics of continuum solid mechanics and thermodynamics that are used in the finite element method are recalled, following a so-called phenomenological approach.

1.2. The ITER vacuum vessel: constrains and requirements

The ITER vacuum vessel is one of the main components of ITER machine and it has been denominated as the first confinement barrier.

The Vacuum Vessel (VV) is a torus, with several openings on three levels: 18 upper ports, 17 equatorial ports, and 9 lower ports, allowing access for plasma heating, fuelling, diagnostics, and in-vessel component services, see Figure 2. This doughnut shape is structurally made up of a double wall structure filled with cooling water, to remove the heat deposited during plasma operation and to maintain a homogeneous temperature.

A maximal cooling water pressure of 1.1 MPa at normal operation (up to 2.4 MPa during baking) classifies it as Nuclear Pressure Equipment (NPE), which requires a third party organisation, i.e., an agreed notified body (ANB), authorized by the nuclear regulator to assure design, fabrication and conformance testing.

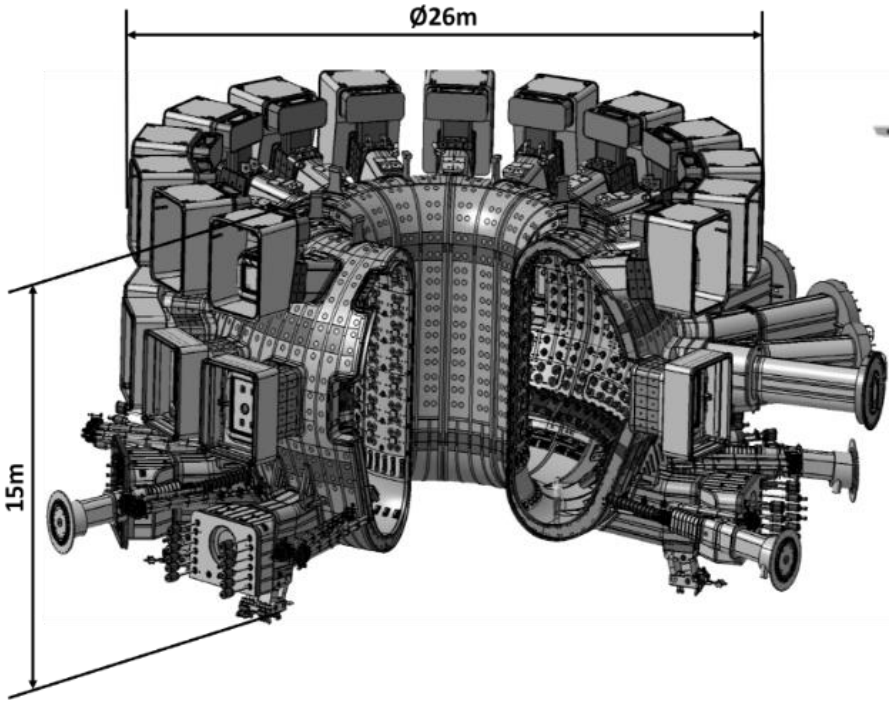

Figure 2 – ITER Vacuum vessel.

1.2.1. The multiphysics constrains of ITER tokamak

In addition to assembly and manufacturing tolerances constrains relative to any structure, the ITER tokamak components are subjected to physical phenomena specific to a fusion device.

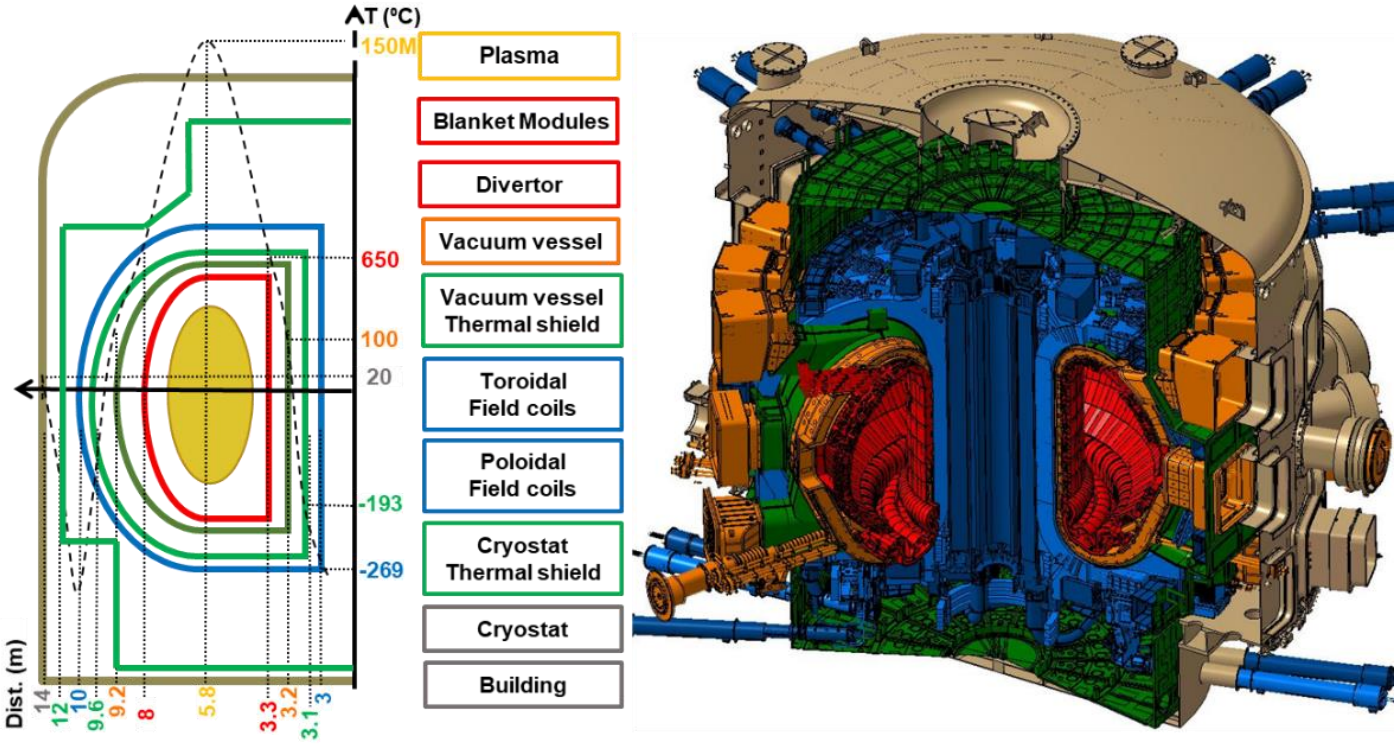

Figure 3 –ITER tokamak components and associated normal operation temperatures (Sabourin, 2018)

In normal operation, the thermo-mechanical constrains drive the design of the reactor, made of superposition of components whose temperatures vary from 150x10^{6}K at plasma core to 4K at the superconductive components at a distance of less than 5m, see Figure 3. The main thermal loadings are produced by the nuclear fusion reaction, which heats up the surrounding components via two phenomena; the surface heat fluxes due to the interaction of ionised particles with Plasma Facing Components (PFC) (Mitteau, 2010) and the nuclear heating which results from highly energetic neutron fluxes interacting with the constitutive material of the components (Fabbri, 2018).

For maintaining components to an operational temperature, in general below thermal creep limit, those are actively cooled with pressurised fluid (water in most of the case). Design choices are made of compromise between low thickness, to minimize thermal gradient, and sufficient strength to withstand water pressure (Perez, 2014) (Colomer, 2017).

Among the different plasma scenarios that ITER might have to undergo, the plasma disruption and associated electromagnetic forces would be the most severe for the reactor structures. Effectively, when the magneto-hydrodynamic of the plasma becomes instable, it results in rapid heat loss and current discharge (halo current) through PFC, so-called the major disruption (MD). During this event, current/magnetic field's interaction generates Laplace forces into the PFC, which are transmitted to the VV on dedicated reacting features.

The second major electromagnetic event, which could occur in the same time that the MD, is the vertical displacement event (VDE). During this event, the plasma control is lost, triggering a vertical motion which generates eddy current in addition to halo current, see Figure 4. The magnetic field of these currents can interact with the poloidal magnetic field of the central solenoid, resulting in an upward force on the vacuum vessel – these can amount to many Giga-Newtons, and make the entire vessel moving significantly. The shock induced during this motion could generate inertial loads on the machine, in turn inducing mutual dynamic interactions between tokamak components.

ITER is made of two vacuum chambers: one required for the plasma condition, i.e. the vacuum vessel, and a second one required for thermally insulating superconductors from surrounding structures, i.e. the cryostat. When the cryostat volume is filled with gas due to three types of accidental fluid leaks (water, air and/or helium), a rapid heat transfer through convection between all components occurs, causing a temperature drop (Lo_Frano, 2016), see Figure 5.

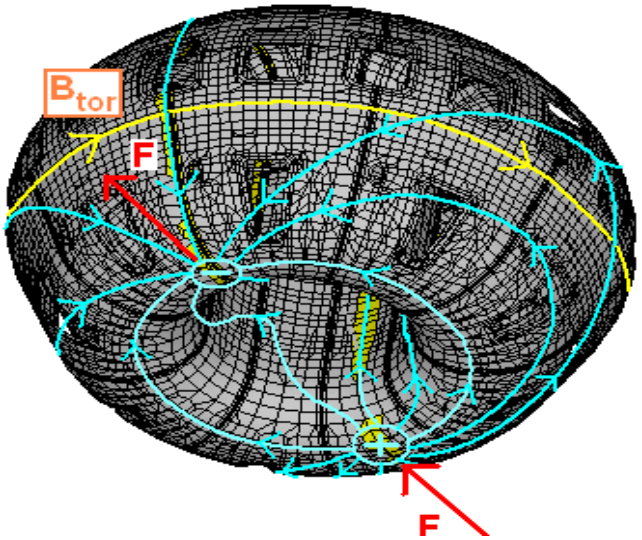

Figure 4 – Current distribution in VV during VDE-DW

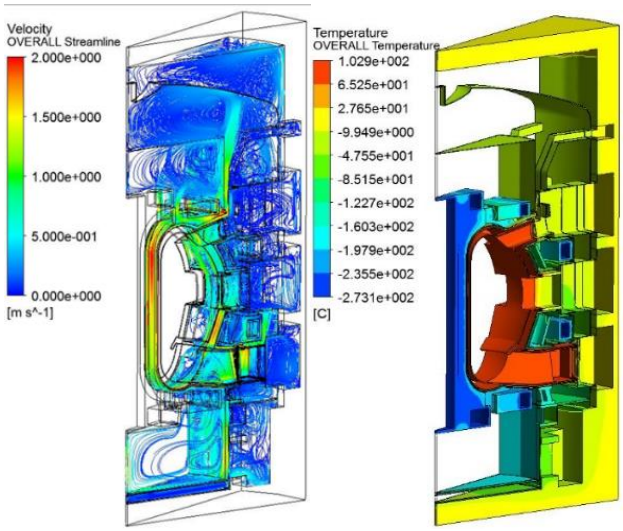

Figure 5 – In cryostat helium flow streamlines during leak of magnet cooling system

1.2.2. Structural material: annealed austenistic stainless steel 316L(N)-IG

In nuclear industry, most of the structures are made of austenistic stainless steel, the most currently used being those of types 304, 309, 321, 347, 348 and 316. In the nineties, when the ITER materials have been selected, the nuclear plant service experience feedback, and the results of R&D on fusion and fast breeder reactor programs, had led to select the annealed SS316LN as the structural material. This type of steel is low carbon grade (letter "L" in the denomination) with added nitrogen (letter "N" in the denomination) to compensate the loss of strength due to a reduction in carbon content. Its advantages are a good strength, a high fatigue resistance and an adequate ductility for absorbing unexpected chocks, a good weldability, resistance to corrosion and a vacuum environment compatibility.

Among 316LN stainless steel materials, with differences in standards and grades and slight variations in specifications, ITER materials experts have designated a specific ITER material based on SS316L-SPH selected, from the service experience feedback of the three generations of fast breeder reactors in France (Rapsodie, Phénix, Super-phénix) (Tavassoli, 1995). The 316L(N)-IG steel (i.e. "IG" are for "ITER Grade"), presents a similar chemical composition than the SS316LN-SPH where only the cobalt (Co.) content has been decreased from 0.25 to 0.05 wt%, see Table 8 (Kalinin, 2000). This modification does not affect the material properties but make the induced radioactivity level decreasing and significantly improves several safety related issues (Kalinin, 1996).

The VV will operate at a temperature range from 20°C (manufacturing and assembly stage) up to 100-200°C (operation) with expected neutron damage dose below 0.5 dpa (Barabash, 2007). Many mechanical tests campaigns on the SS316L(N)-IG have been performed for characterising the material properties (e.g. (Kalinin, 2000), (Kalinin, 1996) and (Barabash, 2007)).

Table 1 – Chemical composition (in wt. %) of type 316L(N)-IG steel (X2CrNiMo17-12-2 controlled nitrogen)

Element	Wt. %	
	min	max
C		0.030
Mn	1.60	2.00
Si		0.50
P		0.025
S		0.010
Cr	17.00	18.00
Ni	12.00	12.50
Mo	2.30	2.70
N	0.060	0.080
B		0.0010** 0.0020
Cu		0.30
Co		0.05
Nb*		0.01
Ta*		0.01
Ti*		0.1

1.2.3. Nuclear Codes and Standard (C&S)

The nuclear code provides detailed and basic rules for design, manufacturing, installation, commissioning and in-service inspection of nuclear plant devices.

The singularity of ITER – in terms of fusion device under nuclear licencing with international collaboration – requires having a multi-code approach for the various components (Sannazzaro, 2013). This strategy induces the use of a single code for each specific component to ensure a consistency between design, manufacturing, inspections and testing. In addition, a significant attention has to be paid to the definition of the interface between components and systems, which is needed for the overall integration and operation of the ITER facility.

For most of the plant components, the ASME (ASM) codes have been selected due to the fact that many ITER members are familiar with this US C&S and also due to the similitudes with others national standards.

The in-vessel components are not subjected to any licencing since they are not "Safety Important Class". Nevertheless it is important to justify their structural integrity during ITER operation. That is why an internal code has been developed for the assessment of irradiated components in ITER (Sannazzaro, 2013), i.e. the SDC-IC (ITER, 2012) which is based on the RCC-MR code.

Other components, which are not subjected to nuclear safety and specific loading due to the nuclear fusion reaction, are based on EU harmonized standards.

The VV is classified as safety class-1 component according to the ITER classification: this is the primary confinement barrier of ITER nuclear installation. In order to obtain the commissioning license for this pressure equipment from the French regulator (ASN), it has been decided to implement the RCC-MR (AFCEN, 2007) as the reference design and construction code with the so-called ITER Addendum, which includes some new features, not covered by the existing code.

1.2.4. Structural integrity verification

From the preliminary design phase up to the operational one, it is mandatory to justify the behaviour of a structure under the scheduled loads (Martinez, 2016). One part of the nuclear C&S is dedicated to the design justification through analytical methods, Finite Element Method (FEM) and/or experiment methods. The objective is to ensure that required safety margins are maintained in case of critical thermo-mechanical loadings, which are likely to damage all or part of the structure.

The development of the RCC-MR design rules for damage prevention, guaranteeing the components' structural integrity, has mainly a double origin:

- The P-type damage, resulting from the application to a structure of a steadily and regularly increasing load or a constant load up to:
  - Ductile damage modes; immediate plastic collapse, immediate plastic instability,
  - Non ductile damage modes; immediate plastic flow localization, immediate local fracture due to ductility exhaustion, fast fracture.

- The S-type damage, resulting from repeated applications of load, associated with:

- Progressive deformations; the permanent overall deformation increases at every loading cycle, inducing additional deformations (i.e., ratcheting) and the structure undergoes gradual changes in its original shape,
- Fatigue (by progressive cracking); time independent fatigue and time dependent fatigue.

Following the RCC-MR rules, the S-type damage prevention has to be started only when the structural integrity is guaranteed against, the P-type damage. Note also that the buckling, which is a form of instability that depends on the geometry, may result in immediate collapse and is not, strictly speaking, a type of damage but have also to be considered.

In most of the cases, the structural integrity verification is performed by FEM computations, under the assumption of a linear, elastic behaviour (Hooke's law). In that case, the code provides design criteria, which are based on decomposition of total stress in a cross-section or a line path, generally representative of a possible crack propagation area or path. This principle is applicable to single-layer homogeneous structures along a supporting line integration segment through the thickness of the structure (line path) (AFCEN, 2007).

When the design criteria are not satisfied after an elastic computation, several non-linear approaches of the mechanical behaviour of the materials can be considered, for a more elaborated demonstration of the design compliance (Martinez, 2015).

The P-type damage justification via non-linear approach requires basic mechanical model and provides confident results. While for the cyclic loadings, which can lead to complex rupture modes, the methodology used requires more margins due to the uncertainty of results.

That is why for S-type damage justification, all the complexity remains in identifying if the structure behaviour under the cyclic loading is able to reach a stabilised mode, i.e. that ratcheting cannot occur. It is only at this stage, when stabilised mode is guaranteed, that the number of cycle is calculated (fatigue), based on the amplitude strain $\Delta\varepsilon$ fully dependent of the material model.

The ITER fusion reactor has been designed for operating under 30 000 plasma pulses with a maximum power fusion of 500MW. Even though the ITER machine is designed under a full nuclear licencing, it remains an experimental reactor for which non expected case could occur after a "small numbers of cycles". For this reason, according to ITER community experts of materials and analyses, the phenomenon of ratcheting and shake-down are central in the design of components subjected to cyclic plastic deformation.

Figure 6, which is extracted from the RCC-MR code, shows that there are no suitable material models able to represent precisely the different material response observed under low cycle fatigue, for guarantying the best prediction of the S-type damage under ratcheting failure mode.

Collapse mode → / Constitutive models ↓		Excessive deformation, Plastic instability	Buckling	Progressive deformation	Fatigue
Perfect plastic		*Suitable (1)*	*Suitable* (4)	*Avoid*	*Avoid*
Isotropic strain hardening	Bilinear hardening	*Avoid*	*Avoid*	*Avoid*	*Avoid*
	Multilinear hardening	*Suitable (2)*	*Suitable*	*Avoid*	*Avoid*
	Non-linear hardening	*Suitable (2)*	*Suitable*	*Avoid*	*Avoid*
Kinematic hardening	Bilinear hardening	*Avoid*	*Avoid*	*Avoid*	*Use with care (5)*
	Multilinear hardening	*Avoid*	*Avoid*	*Use with care (3)*	*Use with care (5)*
	Non-linear hardening	*Avoid*	*Avoid*	*Use with care (7)*	*Use with care (5)*
Combined hardening (Chaboche elastoplastic, etc.)		*Suitable*	*Suitable* (8)	*Use with care*	*Suitable*

Figure 6 – Model behaviour to be used depending of the failure mode (AFCEN, 2007).

1.3. Metallic structure and mechanical behaviours

All the (thermo)mechanical models detailed and used in the rest of the study are formulated at the macroscopic scale. All the physical quantities they involve are thus macro-quantities, first and foremost the stresses and the strains. Nevertheless, it is mandatory to have a basic understanding of these mechanisms at the microscopic scale as described in (Chaboche, et al., 1988).

1.3.1. Elements of crystallography

Metals and alloys are made of arrangement of atoms held together by electromagnetic forces, i.e. they are crystalline. The crystalline state is an elementary parallelpipedic pattern or lattice of crystals which repeats itself periodically in all directions. Most of the metallic lattices belong to one of the three following systems:

- Body Centred Cubic (BCC) crystals: Feα, Cr, Mo,
- Face Centered Cubic (FCC) crystals: Cu, Ag, Al, Ni,
- Hexagonal Close Packed (HCP) crystals: Mg, Zn, Tiα, Coα.

The fundamental difference between single crystal, polycrystalline and amorphous solids is the length scale over which the atoms are related to one another by translational symmetry. Single crystals have infinite periodicity, polycristals have local periodicity, and amorphous solids (and liquids) have no long-range order, see Figure 7.

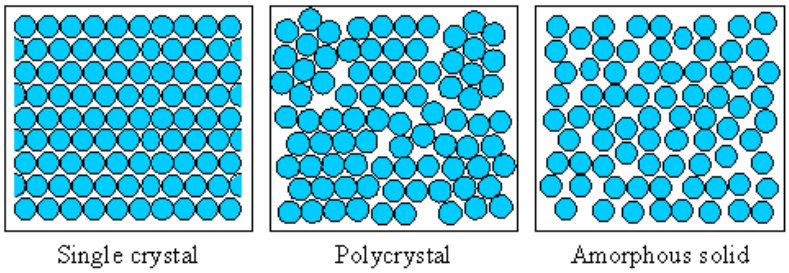

Figure 7 –Main crystallographic structure arrangement

For a polycrystalline structure, the monocristal size varies from a few microns (10^{-3}mm) to a few millimeters depending on the nature of the constituve elements, as well as the thermal and mechanical treatments applied to the material.

Figure 8 shows a microscopic view of the polycristalline configuration of an austenitic stainless steel type 316L, i.e. this of the structural material of the VV.

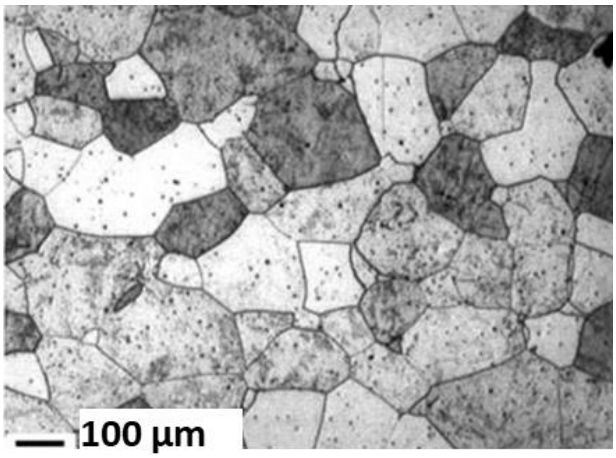

Figure 8 – SS316L polycristal configurations

1.3.2. Monotonic tensile test: mechanisms of deformation

The tensile test is one of the easiest mechanical tests to perform, and it allows to obtain a uniform stress state, which facilitate the parameter identification.

1.3.2.1. Rigorous description of the test

In a fixed environment temperature, the monotonic test consists in applying on a specimen, see Figure 9, an axial load (force or displacement) at a constant rate. This load produces a uniform state of stress in the specimen, which is positive under tensile load ($\sigma > 0$) and negative under compression load ($\sigma < 0$). The results in terms of forces and displacement, are converted into a stress - strain curve (σ as a function of ε), see Figure 10.

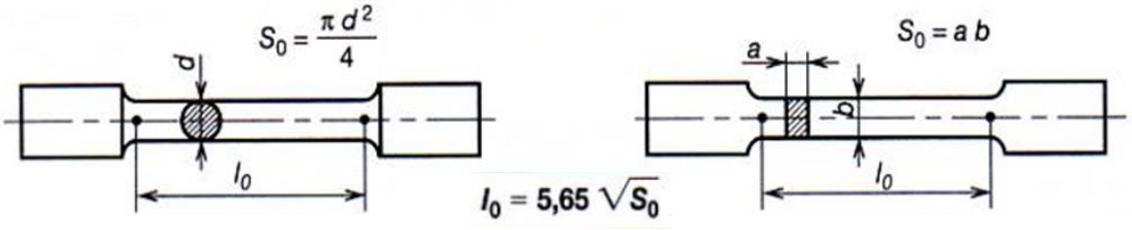

Figure 9 – Cylindrical specimen (left) and flat specimen (right) (Hazard, et al., 1997).

In a given orthonormal basis ($\mathbf{e}_1$, $\mathbf{e}_2$, $\mathbf{e}_3$), an imposed force F (in N) along the direction $\mathbf{e_1}$ can be traduced as an imposed stress $\sigma(t)$ homogeneously distributed on the cross section S_0 in (m^2), where the stress tensor is defined as:

$$\sigma_{11}(t) = \frac{F}{S_0} \tag{1}$$

The resulting measured strain tensor is defined as:

$$\varepsilon_{11}(t) = \frac{l(t) - l_0}{l_0} \tag{2}$$

where l_0 is the initial gauge length (in m), as described in Figure 9, l (in m) is the measured specimen elongation along the direction $\mathbf{e_1}$.

From this test, λ (in Pa) and μ (in Pa) can be identified, first and second Lamé coefficients linked to the Young's modulus E (in Pa) and the Poisson's ratio υ (unitless), see eq.(13). Additionally, the yield stress σ_0 (in Pa), which is difficult to be identify, is represented as a fixed amount of permanent strain, 0.02% in general, see eq.(11).

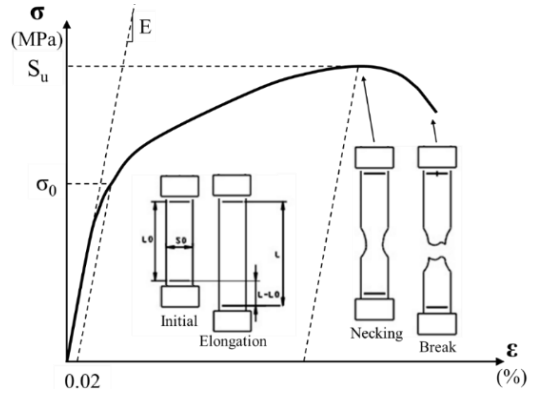

Figure 10 – Typical tensile stress-strain curve

1.3.2.2. Microstructural origin of the different behavioural phases

For highlighting the main features of the mechanical behaviour that can be observed at the microscopic level, it is proposed here to describe, in a schematic way, the sequence of mechanisms which occur in the deformation of a polycristal during a monotonic tensile test.

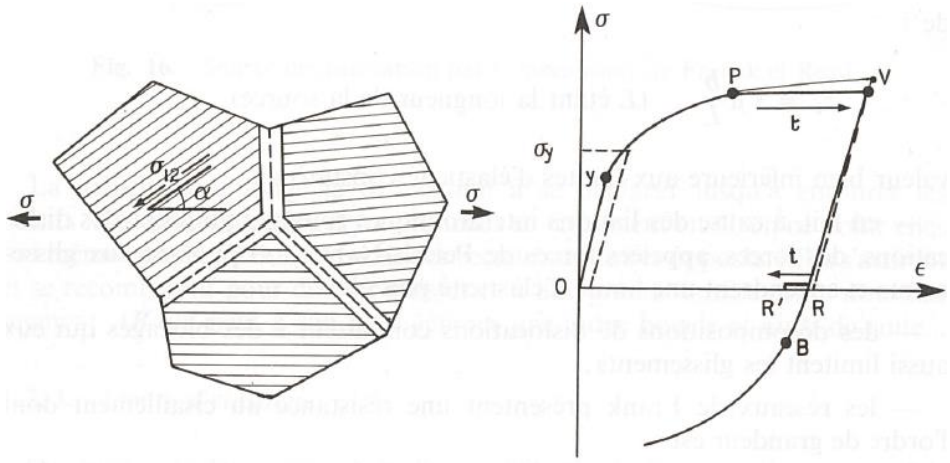

Figure 11 – Deformation of polycristal (Chaboche, et al., 1988)

The first step (OY in Figure 11), represents the elastic deformations, which corresponds to a grain deformation. In a purely elastic deformation, as soon as the load is removed, the initial configuration of atoms is restored.

Over the elastic limit (point Y in Figure 11), the first irreversible motions of dislocations occur, which corresponds to the incipience of permanent deformations. Due to the complexity of detecting the elastic limit, it is represented as a fixed amount of permanent strain (0.02% in general) so called the yield stress σ_0.

Plastic or permanent deformations occur at the crystal level and are mainly intragranular (inside the grains). They correspond to an irreversible, relative displacement of atoms. When the stress continues to rise, the dislocation density and the number of barriers increase. The macroscopic consequence of the increasing resistance to the slip deformation is the hardening phenomenon, which can also result from the presence of intercrystalline microstresses induced by the incompatibility of grain to grain deformation (YP in Figure 11).

Viscoplastic deformations occur when the slips inside the grain grow up to the grain boundary and follow up to it. This phenomenon of intergranular slip is favoured by thermal activation and is especially significant at temperatures higher than one third of the absolute melting temperature, so called thermal creep. When the deformation can progress under constant stress with no possibility of equilibrium, creep flow linked to the applied stress can appear: this is the domain of viscoplasticity (see PV in Figure 11).

When the load is removed or reversed (compressive load); the amount of atoms interstice decreases and dislocations of opposite signs are neutralized. This stage corresponds to the recovery, which is function of time and favoured by thermal activation (see RR' in Figure 11).

Under compressive load, only elastic deformations produce a noticeable volume change. The change due to the increase of dislocations density always remain very small, this phenomenon

corresponds to the plastic or viscoplastic incompressibility ($Tr(\boldsymbol{\varepsilon}^p)=0$): the Baushinger effect is the simplest manifestation of it (B in Figure 11).

1.3.2.3. Velocity influence

The SS316L(N)-IG, which is a ductile material, has some viscosity that can be identified by performing tensile test at different velocity. Figure 12 describes the effect of the strain rate on a viscoplastic material where the top curve corresponds to a fast strain rate (infinite) and the bottom one to a low strain rate. This method allows to identify the viscoplastic parameters η (in s^{-1}) used for the expression of the plastic multiplier for viscoplastic models.

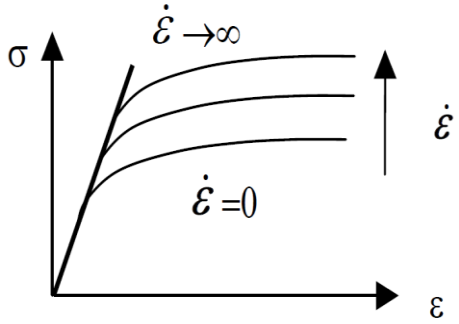

Figure 12 – Effect of test velocity on material response (viscosity identification)

1.3.3. Effect of cyclic loadings

1.3.3.1. Tension-compression cyclic test

Based on the same methodology than the tensile test, the fatigue test consists in applying periodic load (stress or strain) on the specimen. The cyclic response is studied through a graph where **σ** is a function of **ε** as described in Figure 13 and Figure 14.

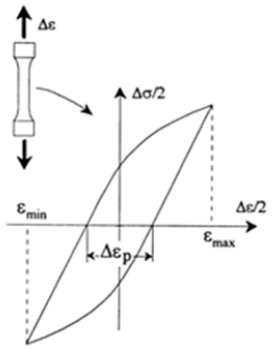

Figure 13 – Cyclic test under imposed strain

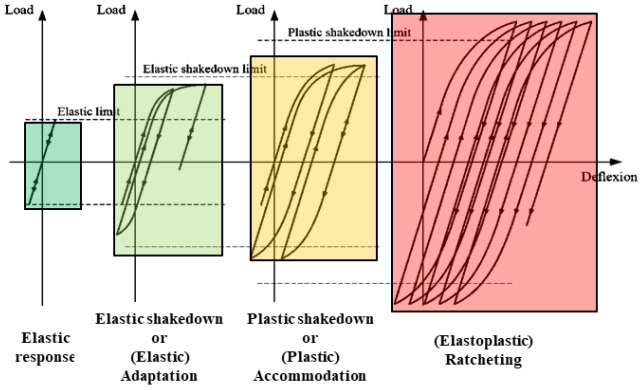

Figure 14 – Main material responses under uniaxial cyclic test

The Wöhler Curve (or S-N curve), see Figure 16, is obtained by gathering the peaks of the stabilized loops at different stress ranges and associated number of cycles up to failure mode, see Figure 15. In this curve, three main domains can be observed:

- Polycyclic domain; the material can support an infinity of cycles, i.e. its endurance is unlimited. The main stabilised mode in this domain is the elastic response of the material, which corresponds to the asymptotic part of the curve, see Figure 16. At this stage, the yield

limit of the material has not yet been reached. Above this elastic limit, some plastic deformations can occur and stabilize to an elastic response (Elastic adaptation or elastic shakedown, see Figure 14).

- Fatigue domain; for austenitic stainless steel, the number of cycles are in the range [10^5, 10^7], i.e. a limited endurance. In this domain, the stress intensity is higher and lead to an elastoplastic hysteresis cycle (plastic accommodation or plastic shakedown).
- Oligocyclic domain; stress amplitude is so high that the sample never reaches a periodic state, meaning that the plastic deformation is constantly growing up to the failure mode (ratcheting response).

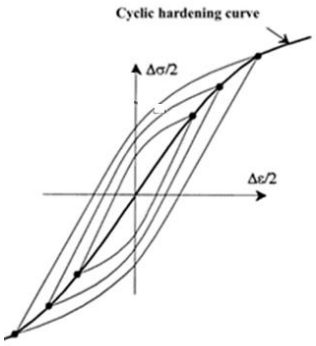

Figure 15 – Wöhler Curve construction principle

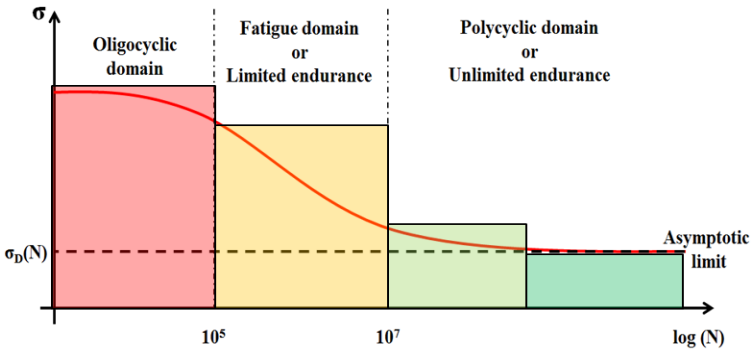

Figure 16 – Wöhler Curve (or S-N curve)

1.3.3.2. Shakedown and Ratcheting

Under cyclic tensile/compression test, the mechanisms of deformation presented in §1.3.2.2 are repeated after each cycle and, depending on the loading conditions and hardening properties, different responses can be observed along the cycles. At this stage, we start to study the material behavior at the macroscopic level.

Baushinger effect appears in tension/compression test during the first compression load. The material has hardened in tension (increase of yield stress) but has softened in compression. Figure 17 shows that the yield in compression is lower than that if the test were carried out in compression first.

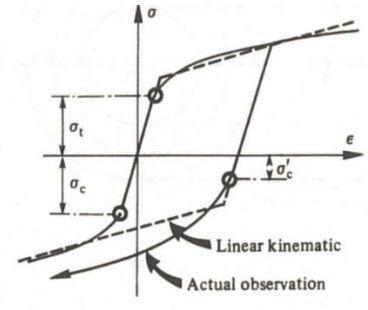

Figure 17 – Baushinger effect

In tension-compression cyclic loading, many experiments show that metals and alloys undergo variations in their hardening properties during cycles. They may soften (Figure 18 and Figure 19) or harden (Figure 20and Figure 21); depending on the material itself, its temperature, and its initial state.

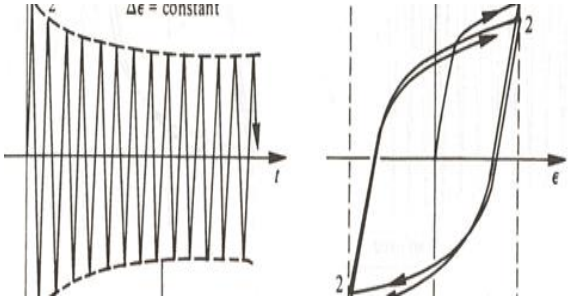

Figure 18 – Softening phenomenon with imposed strain (Chaboche, et al., 1988)

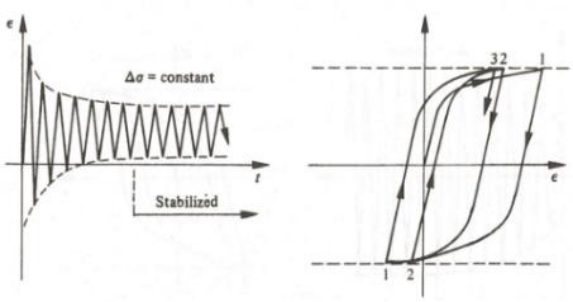

Figure 19 – Hardening phenomenon with imposed stress (Chaboche, et al., 1988)

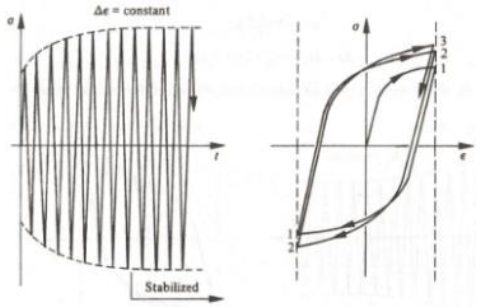

Figure 20 –Hardening phenomenon with imposed strain (Chaboche, et al., 1988)

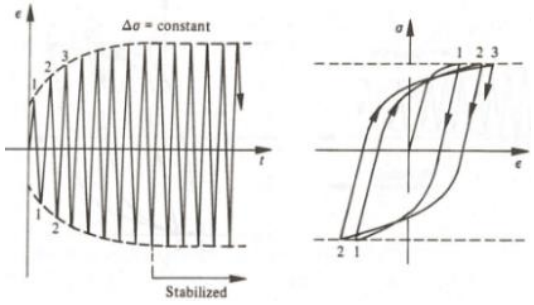

Figure 21 – Softening phenomenon with imposed stress (Chaboche, et al., 1988)

Beyond these hardening or softening phenomena, another phenomenon may appear: the shakedown, either elastic (also called elastic adaptation) or plastic (also called plastic accommodation, see Figure 23 & Figure 22). In the worst case, under non-symmetric loading with imposed stress, the sample undergoes plastic deformations which could constantly increase up to fracture (ratcheting, see Figure 25). Correspondingly, in case of non-symmetric loading with imposed strain condition, the ratcheting is materialised by a relaxation of the mean stress, see Figure 24.

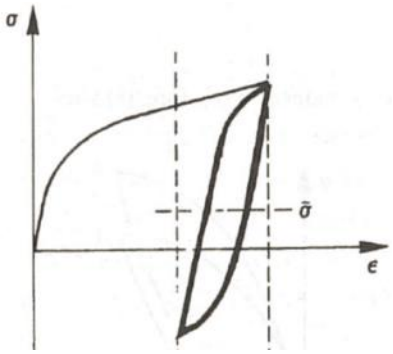

Figure 22 – non-relaxation of the mean stress with imposed strain (Chaboche, et al., 1988)

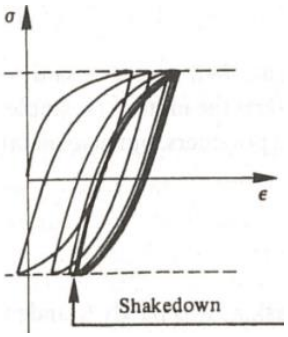

Figure 23 – Plastic shakedown (or plastic accommodation) with imposed stress (Chaboche, et al., 1988)

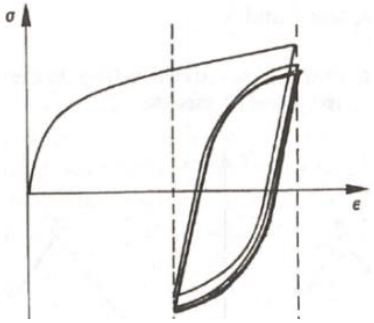

Figure 24 –relaxation of the mean stress with imposed strain (Chaboche, et al., 1988)

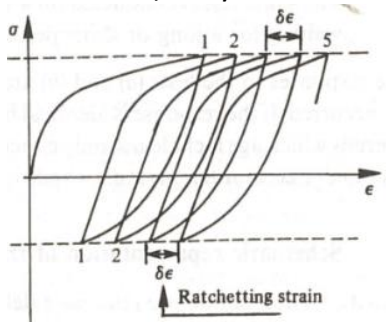

Figure 25 – Ratcheting with imposed stress (Chaboche, et al., 1988)

1.3.4. Effect of temperature

When the material is subjected to different environment temperature, tensile test are performed at different temperature to check the parameters evolution.

1.3.4.1. Thermomechanical tensile test and influence of temperature on cyclic and monotonic strain hardening

Using the same configuration than in the tensile test, a thermal load is applied on the specimen. In Figure 26, the thermal load is made by a radio frequency induction heating and forced air cooling through the centre of the specimen in order to achieve rapid heating and cooling.

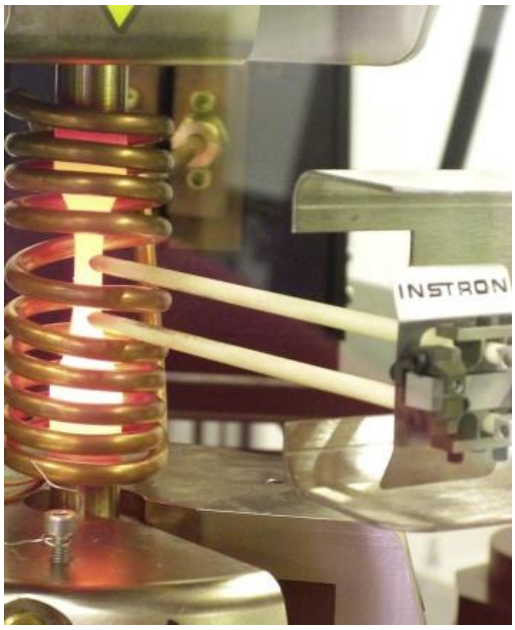

Figure 26 – Thermomechanical test configuration (Hyde, et al., 2010)

In case of homogeneous imposed thermal load, with boundary conditions allowing the thermal expansion of the structure (meaning that the specimen is stress free), in a given orthonormal basis ($\mathbf{e}_1$, $\mathbf{e}_2$, $\mathbf{e}_3$), starting from expression of the thermoelasticity, it appears:

$$0 = \lambda Tr(\boldsymbol{\varepsilon})\boldsymbol{G} + 2\mu(\boldsymbol{\varepsilon}) - (3\lambda + 2\mu)\gamma(T - T_0)\,\boldsymbol{G} \quad (3)$$

The thermal expansion being isotropic, for the studied case where thermal is the unique load, it appears that $Tr(\boldsymbol{\varepsilon})\mathbf{G}=3\boldsymbol{\varepsilon}$ from which it can be deduced:

$$\boldsymbol{\varepsilon} = \gamma(T - T_0)\,\boldsymbol{G} \quad (4)$$

From this method, the thermal expansion parameter γ (in K^{-1}) can be identified.

Figure 27 shows the results of the tests carried out onZ2CND18 stainless steel (similar to SS316L(N)-IG), in which, for a constant strain rate, Young's modulus remains almost the same at different temperature and the yield limit decreases when the temperature increases.

Figure 27b highlights that at high temperature, the viscosity effect rate appears to be negligible.

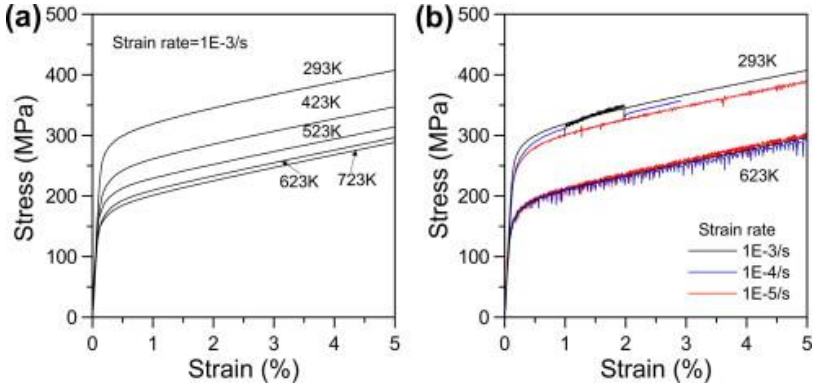

Figure 27 – Z2CND18 stainless steel tensile test' stress strain curves: (a) with fixed strain rate at 10^{-3} s and different temperature, (b) with different stress train rate for temperatures at 20ºC and 350 ºC (Chen, 2012).

Figure 28 shows monotonic and cyclic hardening curves at 20°C and 550°C for SS316L-SPH (from which the SS316L(N)-IG is derived) (Tavassoli, 1995). The monotonic data are extracted from the first quarter cycle, and the cyclic data from the half-life stress amplitude. It can be observed that the cyclic hardening is more pronounced for 550°C samples in comparison to room temperature samples. This difference can be explained by the fact that at 20°C, the initial yield strength is higher in comparison to high temperature cases.

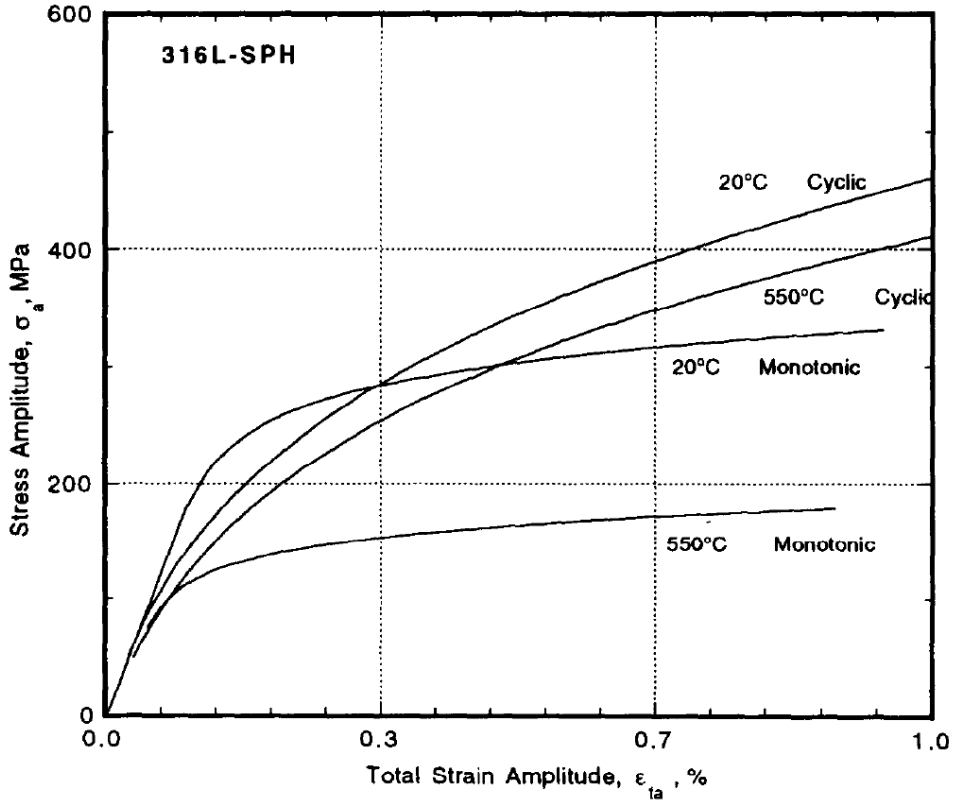

Figure 28 – Cyclic and monotonic hardening curves for similar material than SS316L(N)-IG at 20 ºC and 550 ºC (Tavassoli, 1995).

Figure 29 shows the S-N curve for SS316L(N)-IG extraxted from (AFCEN, 2007), at different temperature values: 20 ºC, 450 ºC, 550 º C & 650 º C. It can be observed the total number of cycles decrease under the temperture increase.

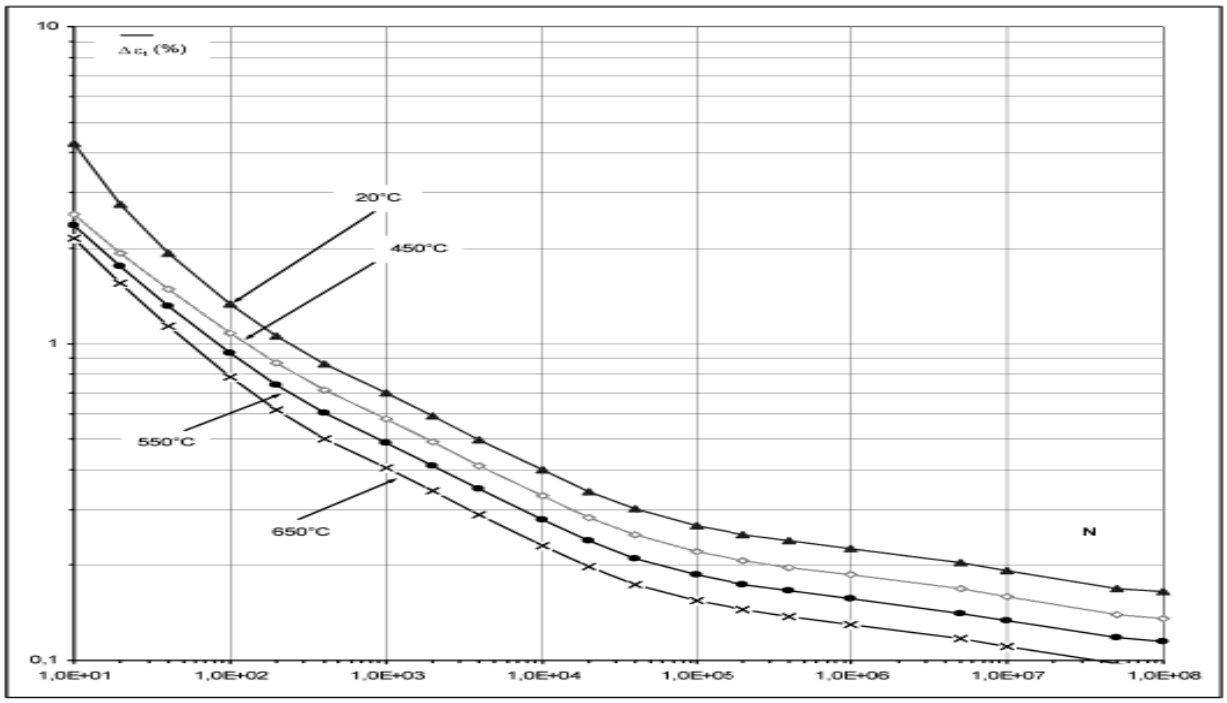

Figure 29 – Wöhler Curve (or S-N curve) for SS316L(N)-IG (AFCEN, 2007)

1.3.4.2. Combined cyclic thermal and mechanical loading

Figure 30 and Figure 31 show cyclic thermomechanical test performed on Z2CND18 stainless steel, for which imposed strain rate has been applied for ±6% and temperature amplitude between 150ºC and 550ºC has been applied for three different configurations (Chen, 2012). This test shows that at the initial state, when the temperature is not homogenised in the sample, the hardening is governed by the environment temperature whatever the compression or the tension state. In addition, this test also shows that after 100 cycles, when the temperature can be assumed homogenised, the stabilized hysteresis loops are almost identic in the three samples.

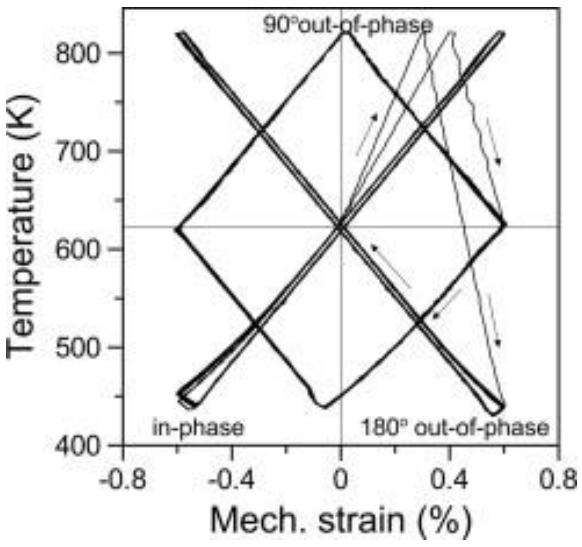

Figure 30 –Thermomechanical load for cyclic test on Z2CND18 stainless steel (Chen, 2012).

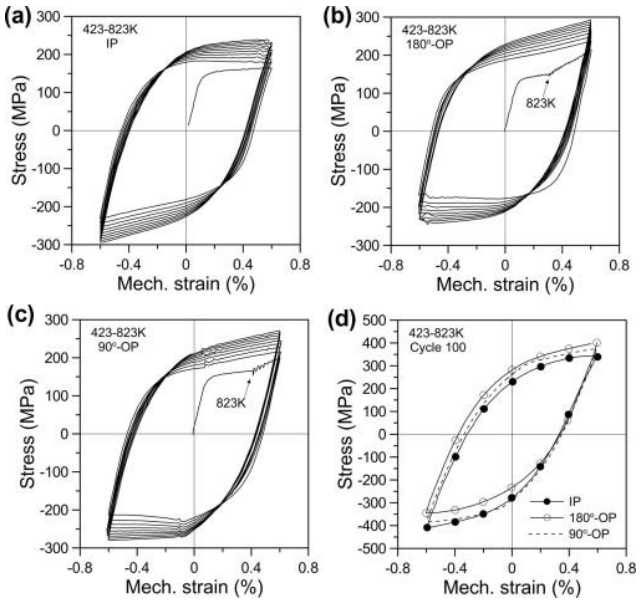

Figure 31 – Stress strain hysteresis loops for the first 10 cycles: (a) In phase, (b) 180º out of phase, (c) 90º out of phase and (d) stabilised loops after 100 cycles (Chen, 2012).

1.3.4.3. Bree cylinder test

The Bree cylinder test is a realistic representation of a Pressurised Nuclear Equipment (NPE), like the ITER Vacuum Vessel, under operational condition. The sample used in the Bree test is an axisymmetric tube. The loading is due to the superposition of a constant internal pressure and a cyclic temperature (Bree, 1967).

In nuclear codes, loads are dissociated in primary and secondary loads inducing respectively primary stress and secondary stress. The primary stress is defined as that portion of the total stress which is required to satisfy equilibrium with the applied loading and does not diminish after permanent deformation, (i.e. gravity earth, pressure, forces, etc), whereas secondary stress can be relaxed as a result of permanent deformation, i.e. thermal loads, imposed displacement, etc.

For structures under nuclear codes, the primary stress, which can lead to progressive deformation, has to remain below the yield limit of the material. In the Bree cylinder test, the water pressure applied inside the tube represents the primary load. The associated primary stress parameter used for building the Bree diagram is described in eq. (5), where σ_0 (in MPa) is the initial yield limit, and the maximum equivalent stress tensor in the sense of Von Mises for the primary stress is P_{max} (in MPa).

The secondary stress, which cannot lead to progressive deformation, is summed to the primary stress, and the total stress can reach the ultimate strength of the material. In the Bree cyclinder test, the secondary stress are obtained by applying cyclic thermal load. The second parameter of the Bree diagram is described in eq. (6) where the maximum equivalent stress tensor range in the sense of Von Mises for combined primary and secondary stress is $\Delta(P_{max} + Q)_{max}$ (in MPa).

X and Y (unitless) respectively correspond to the primary and secondary stress parameters i.e.:

$$X = \frac{P_{max}}{\sigma_0} \leq 1 \tag{5}$$

$$Y = \frac{\Delta(P + Q)_{max}}{\sigma_0} \tag{6}$$

The Bree diagram shows the different structural responses based on primary and secondary stress intensity, see Figure 32. As it shown in Figure 14, the following four states can occur:

- the elastic response (E),
- the elastic shakedown (S1 and S2),
- the plastic shakedown (P),
- the ratcheting (R1 and R2).

This test highlights that the ratcheting can occur under thermo-mechanical load application.

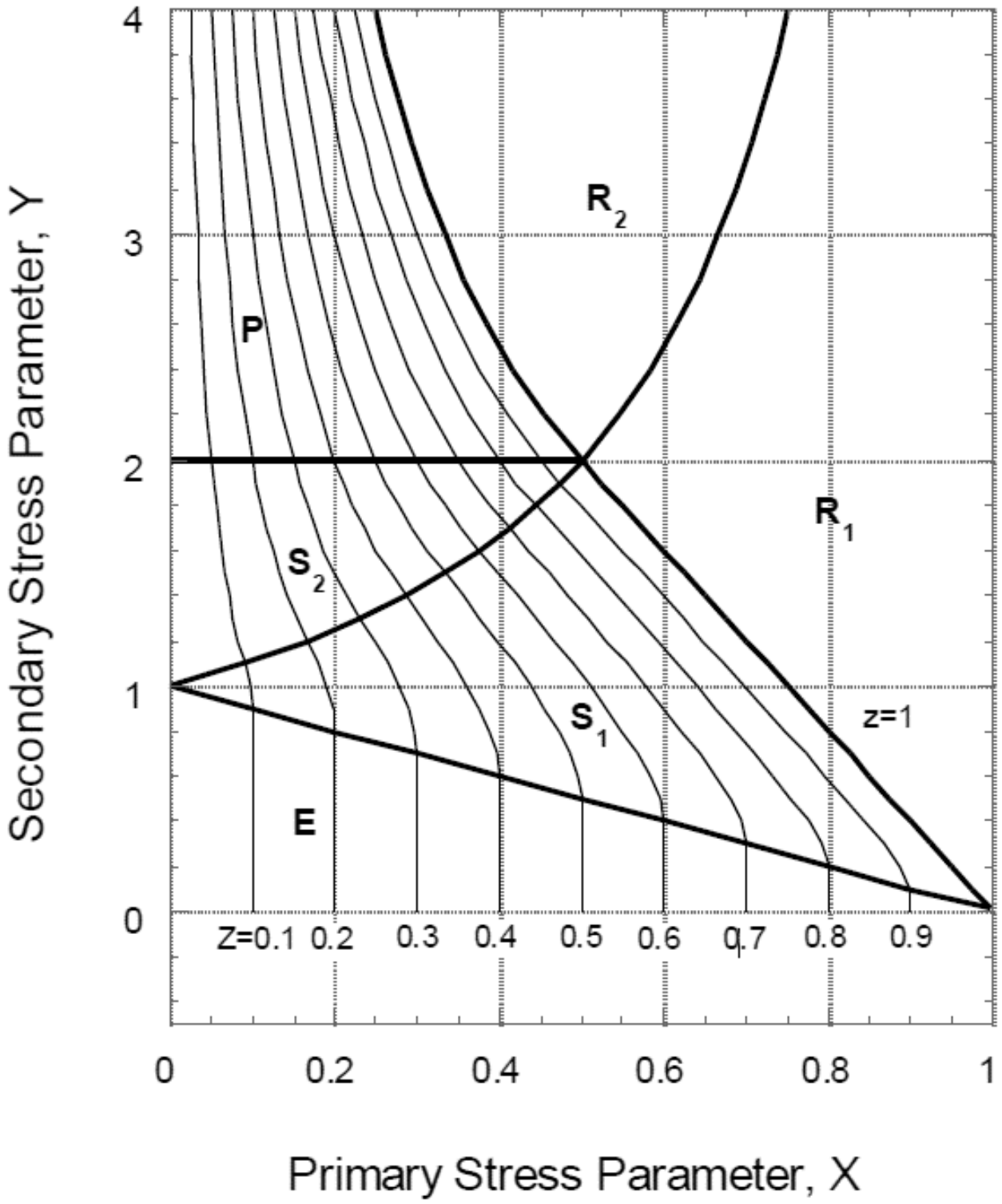

Figure 32 – Bree diagram (Bree, 1967) -material responses based on the ratio between primary and secondary stress parameters-

1.3.5. Effect of neutron irradiation

The ITER plasma-facing components and vacuum chamber are exposed to highly energetic neutron fluxes, generated during the Deuterium-Tritium fusion reaction. These neutron-structure interactions produces various types of secondary reactions, from which gamma rays and/or charged particles are created.

1.3.5.1. Physical phenomenon

The neutrons and photons, which are by definition electrically neutral, cross the magnetic confinement and penetrate deeply into the structural parts, converting their kinetic energy into thermal energy (Maki, 1999).

Based on this statement, the analysis software used in ITER for volume heating evaluation takes into account two contributors, which are: 1.the neutron source; 2.the photon source. Figure 33 shows an example of what a map of nuclear heating distribution on the ITER vacuum vessel could be.

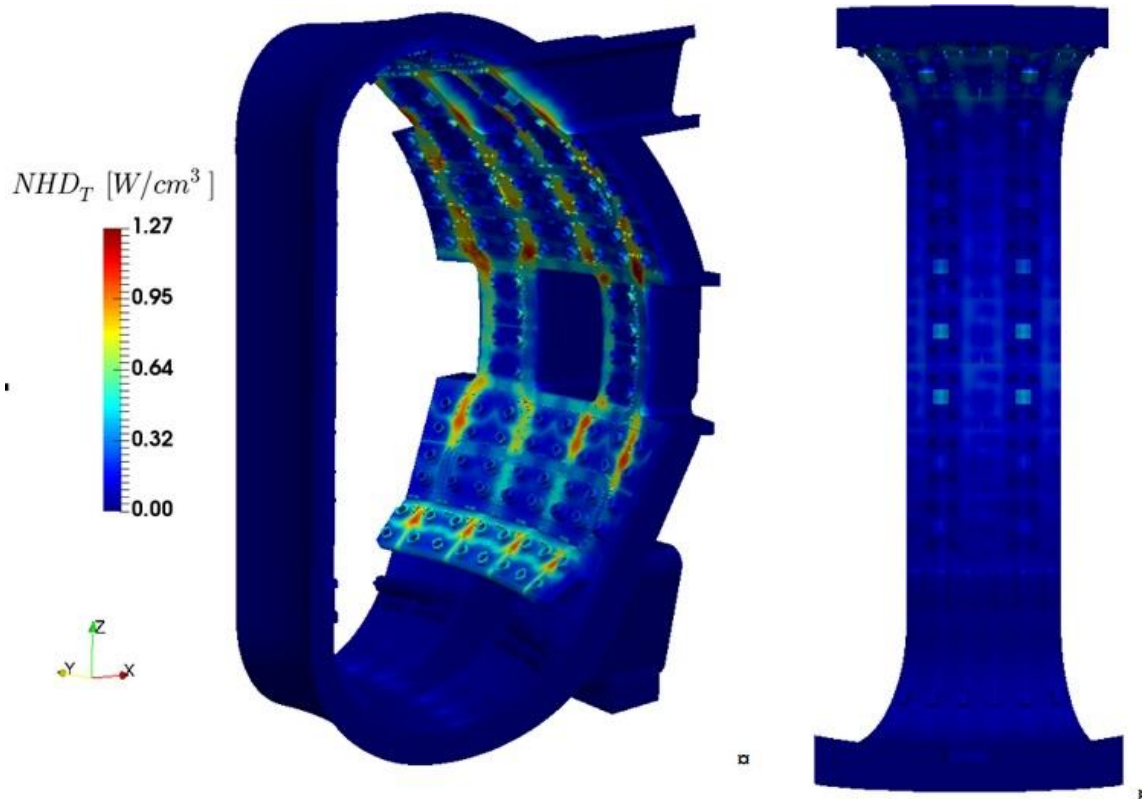

Figure 33 – ITER VV nuclear heating distribution map (Fabbri, 2018).

In addition to the heat power exchange, the neutron kinetic energy is so high that it allows atoms to move from their initial site. This results in a local displacement chain, limited in time and space, which modifies the crystalline structure of the material. Figure 34 shows a schematic representation of the displacement cascade induced after a Primary Knocked-on Atoms (PKA). This phenomenon is quantified in displacement per atoms (dpa). This means that for a material receiving a dose of 100 dpa, each atom moves 100 times (Boutard, 2014).

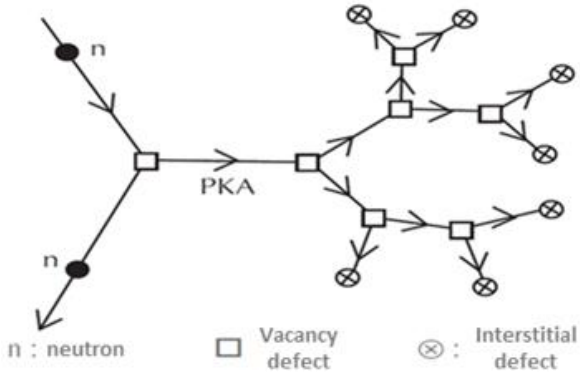

Figure 34 –Displacement cascade scheme (Boutard, 2014)

During the initial collision between neutron and atom (PKA), nuclear transmutation reactions occur. In nuclear fusion reactors, the worst reaction, which is the most sensitive for material damage, generates helium and hydrogen atoms. This atoms generation is made inside the steel structure with a rate of ~12 appmHe/dpa (12 10^{-6} atoms per dpa) for helium and ~45 appmH/dpa for hydrogen.

For ITER In Vessel components, which operate at temperature condition set as a maximum of 450ºC (below the thermal creep for the material), the expected peak damage in the steel would be about 2 dpa with a maximum helium generation of 55appm (Kalinin, 2001).

1.3.5.2. Degradation of mechanical properties

The irradiation affects the physical properties through generations of dpa and nuclear transmutation that can be grouped into two categories. The first covers various mechanical coefficients like yield strength, electrical resistivity and magnetic permeability, and the second covers density and Young's modulus.

For austenitic stainless steel, this damage results in an increase in the yield limit and a reduction in the plastic flow area. Figure 35 shows the design curves for the minimum yield strength of 316L (N)-IG steel as a function of neutron damage at a temperature range of 100–300 °C, and Figure 36 shows the minimum uniform elongation for different doses (Barabash, 2007).

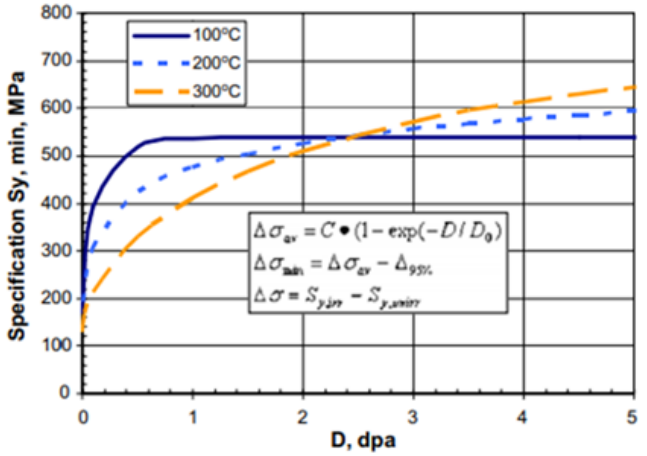

Figure 35 –Neutron irradiation effect on minimum yield strength (σ_0) of 316L(N)-IG steel (Barabash, 2007)

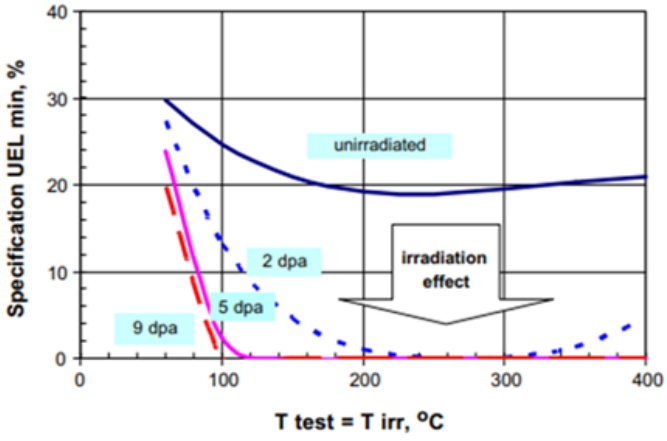

Figure 36 –Neutron irradiation effect on minimum elongation (UE) of 316L(N)-IG steel (Barabash, 2007).

Figure 37 and Figure 38 show respectively the superposition of unirradiated and irradiated fatigue test datas at low temperature (less than 325ºC) and high temperature (over 425ºC) for ITER VV material: SS316L(N)-IG. It can be observed that for low temperatures, irradiated data do not show a systematic deviation from the unirradiated data. And for the high temperature, irradiated data show a systematic deviation that remains very small considering the number of cycles. It can be noticed that all data (irradiated and unirradiated) are covered by the RCC-MR reference curve (described in Figure 29).

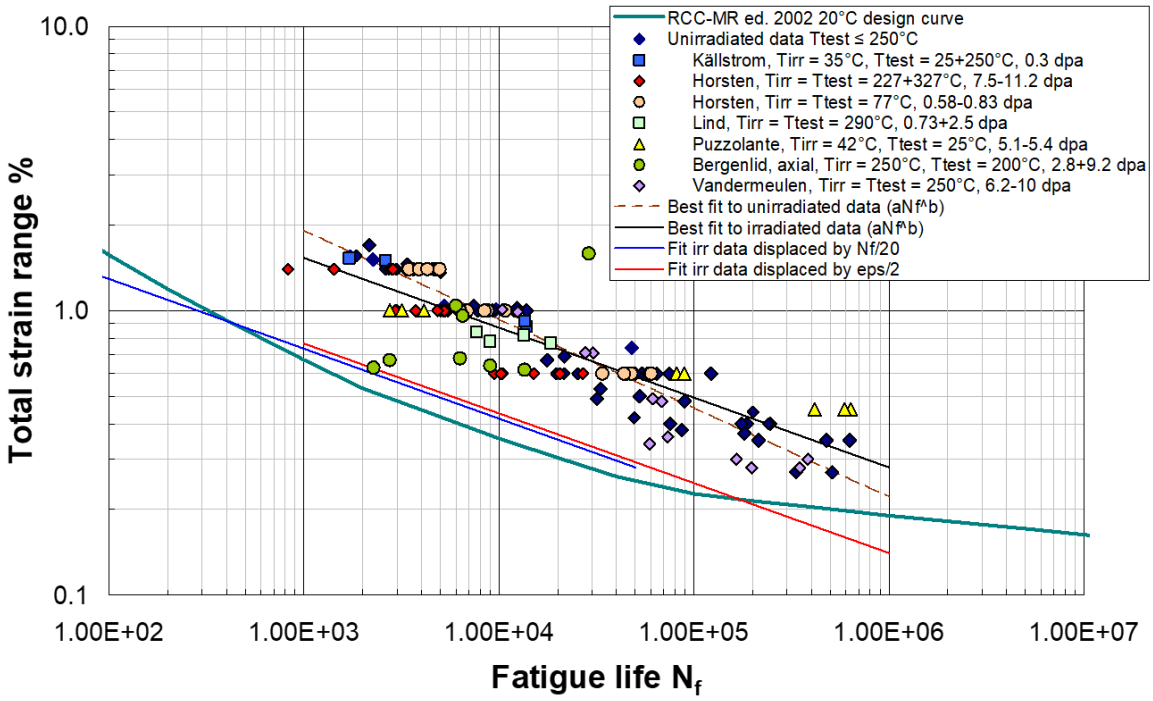

Figure 37 – Assessment of the effect of neutron irradiation on fatigue at temperatures less than 325ºC (Barabash, 2007).

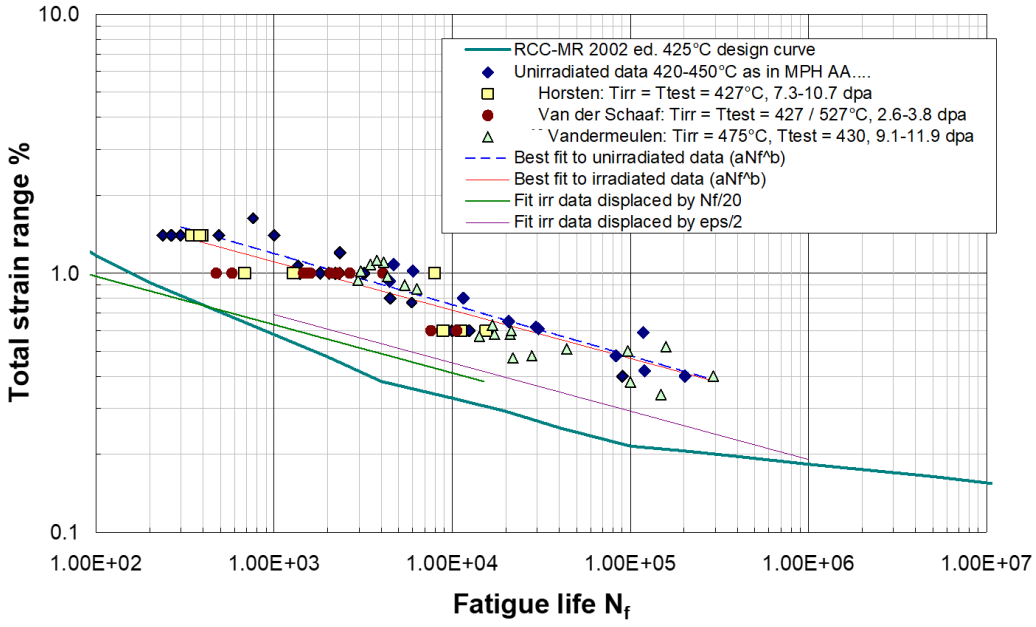

Figure 38 – Assessment of the effect of neutron irradiation on fatigue at temperatures over 425ºC (Barabash, 2007).

1.3.5.3. Swelling

The swelling phenomenon corresponds to a volume increase due to the accumulation of cavities and vacancies induced by neutron damage. Consequently, the density of the material decrease. Figure 39 shows the volume evolution between the initial coupon of CW 316 steel (close to ITER VV material) and the same coupon after irradiation up to 15 dpa at 533ºC (Klueh, 2008). It is important to note that this phenomenon is amplified at certain temperature range, generally close to the thermal creep temperature, see Figure 40. The swelling phenomenon could have an effect on the Young's modulus when large quantities of helium are formed due to the material effective cross section reduction.

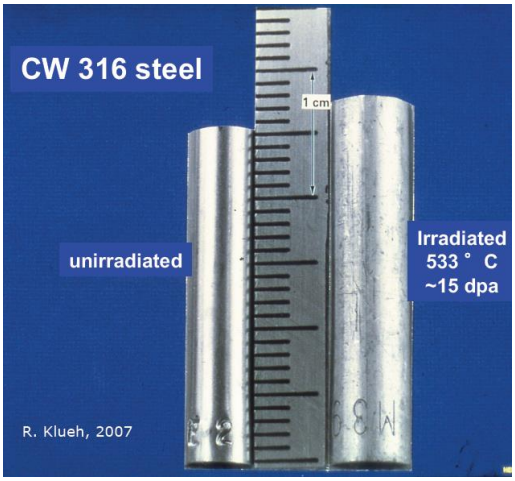

Figure 39 – Swelling (effect of vacancy clustering) of CW 316 steel (Klueh, 2008).

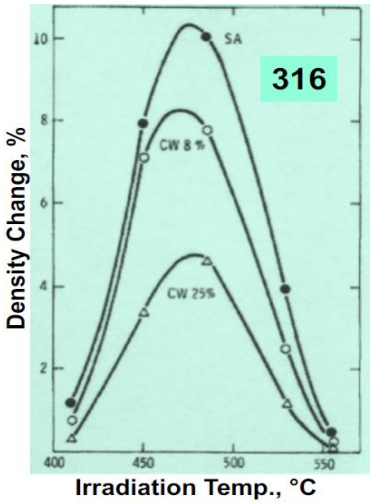

Figure 40 – Density evolution of CW 316 steel vs environment temperature (Klueh, 2008).

Figure 41 shows the swelling of SS316LN (close to ITER VV material) vs irradiation dose at temperature range where the phenomenon is amplified (412 ºC < T_{irr} < 545 ºC). Considering ITER operational conditions, this phenomenon will be negligeable.

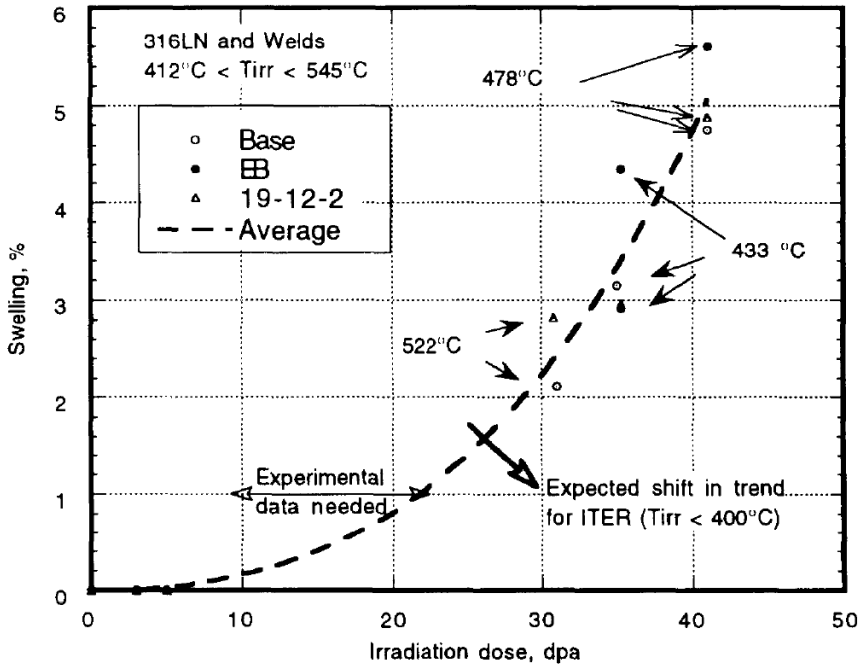

Figure 41 – Swelling of SS316LN vs irradiation dose (Tavassoli, 1995).

1.4. Modelling of metal plasticity

For the past decades, a lot of research has been led on analytical modelling of metals behaviour. Amongst the various existing approaches, two major classes of models emerge: multiscale based models (where microstructure and crystallography are involved) (Cailletaud, 1988) and phenomenological models (based on internal variables) (Coleman, et al., 1967).

The micro-macro models take into account physics and deformation mechanisms at the microscopic level and use mathematical techniques to transpose results from the microscopic level to the macroscopic one and vice versa. By definition, this type of modelling is more detailed, but may involve many internal variables, which requires a high computing time, not adapted to the structure design justification.

The phenomenological approach, which is indeed widely used in the industry, is based on variables which can be directly measured at the macroscopic scale, as the temperature and the total strain. Although this approach does not take into account the physical mechanism and deformation at the microscopic level, it requires few parameters identification and is better suited for design justification of a structure like the ITER vacuum Vessel.

1.4.1. Phenomenological approach

In the general thermo-mechanical case, two observables states variables, which can be directly measured on the tested sample, are the total stain ($\boldsymbol{\varepsilon}$) and the absolute temperature (T).

The internal variables, which cannot be directly identified, are generally defined by $\boldsymbol{\alpha}$, which corresponds to synthetic representation of a set of the internal variables. As an example, in case of a combined isotropic and kinematic hardening, the internal variables $\boldsymbol{\alpha}$ would be expressed as
$\boldsymbol{\alpha} = \{\boldsymbol{\varepsilon}^{\boldsymbol{p}}, \mathbf{X}, \mathrm{p}\}$.

1.4.1.1. Elasticity

Elasticity is the first and easiest mechanism of deformation that can be represented via the phenomenological methodology. By definition, after any loading and unloading, the structure is recovering its initial state. Depending on the material model to be developed, this elasticity can be anisotropic, non-linear, and/or thermally coupled.

For metal and alloy's modelisation, it is fundamental to state that this elasticity is linear isotropic as defined by Hooke's law.

$$\boldsymbol{\sigma} = (\lambda Tr(\boldsymbol{\varepsilon})\boldsymbol{G} + 2\boldsymbol{\varepsilon}) \tag{7}$$

Where Tr(.) is the trace operator, and where λ (in Pa) and μ (in Pa), first and second Lamé coefficients, are material parameters.

1.4.1.2. Multiaxial plasticity criteria

The transition between the reversible deformation and the permanent ones is defined via a scalar yield function defined as following:

$$f(\boldsymbol{\sigma}, \boldsymbol{\alpha}) \tag{8}$$

which defines a surface in the stress space where the multiaxial plasticity criterion is defined by:

$$\begin{array}{ll} f(\boldsymbol{\sigma}, \boldsymbol{\alpha})<0 & \text{elastic behaviour} \\ f(\boldsymbol{\sigma}, \boldsymbol{\alpha})=0 & \text{elastic limit (plastic behaviour)} \\ f(\boldsymbol{\sigma}, \boldsymbol{\alpha})>0 & \text{elasto-visco-plastic behaviour} \end{array} \tag{9}$$

The physical representation of this yield surface in a plane stress (inducing that $\sigma_3=0$) is described in Figure 42 with perfect plasticity (without hardening) where a plastic load increment produces a stress redistribution sliding along the yield surface. In the case where the model behaviour includes hardening, a load increment produces a stress distribution on the boundary defined by f=0 but this boundary will be shifted according to the hardening rule as described in Figure 43. Under unloading stage, the stress point moves from the boundary of the yield surface to the inside and thus, immediately recovers its elastic behaviour.

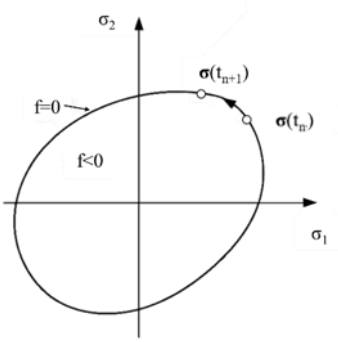

Figure 42 – Yield surface representation in a plane stress for prefect plasticity behaviour

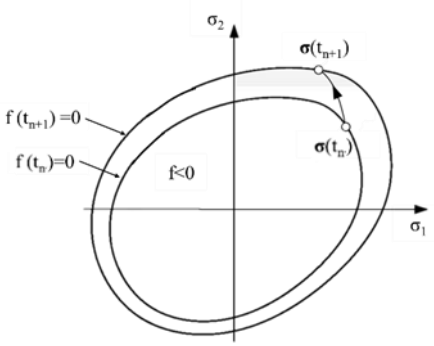

Figure 43 – Yield surface representation in a plane stress for plasticity including hardening behaviour

One of the simplest isotropic criterion for metal and alloy is the Tresca criterion which is based on the maximum shear stress. The yield function is defined in a given orthonormal basis ($\mathbf{e}_1$, $\mathbf{e}_2$, $\mathbf{e}_3$) as:

$$f = \max\left(\frac{1}{2}\left|\sigma_{ii} - \sigma_{jj}\right|\right) - \sigma_0 \tag{10}$$

where σ_0 (in MPa) is a material parameter which defines the initial yield limit.

The Von Mises criterion aims to improve the prediction of plasticity in metals. At the difference of the Tresca maximum shear criterion, it takes into account a combination of the three principal shear stresses. This is the most used criterion in industrial environment for design validation of structures. For ensuring analysis method coherence, the yield function of the model that we are proposing is based on the expression of the equivalent stress in the sense of Von Mises as:

$$f = \sqrt{\frac{3}{2}\left(\sigma_{ij} - \frac{1}{3}\sigma_{kk}\delta_{ij}\right) : \left(\sigma_{ij} - \frac{1}{3}\sigma_{kk}\delta_{ij}\right)} - \sigma_0 \tag{11}$$

The geometrical representation of the Von Mises yield surface in the plane stress case (σ_3=0) is an ellipse and the Tresca yield surface is represented as a prism of hexagonal base which is inscribed within the Von Mises cylinder, see Figure 44.

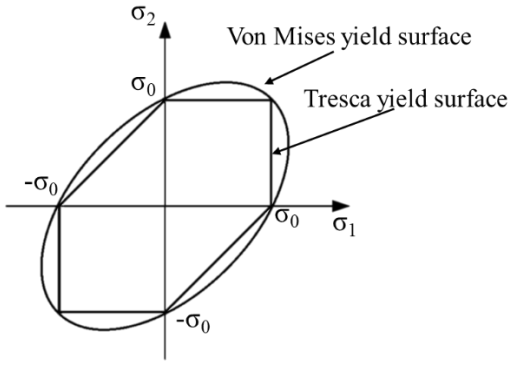

Figure 44 – Tresca and Von Mises yield surfaces representation in the plane stress (Chaboche, et al., 1988)

1.4.1.3. Hardening

Whatever the loading condition, in the elastic domain, the material exhibits a reversible behaviour. However, when the yield stress is passed, the hardening behavior can provide many different responses. In most of the cases, the hardening rules are formulated by a combination of two specific types of hardening: isotropic and kinematic.

When the material behaviour exceeds the elastic response, the total strain $\boldsymbol{\varepsilon}$ can be expressed as function of the reversible elastic stain $\boldsymbol{\varepsilon^e}$ and the plastic stain $\boldsymbol{\varepsilon^p}$:

$$\boldsymbol{\varepsilon} = \boldsymbol{\varepsilon^e} + \boldsymbol{\varepsilon^p} \tag{12}$$

The stress tensor $\boldsymbol{\sigma}$ is then supposed to linearly depend on the only elastic strain (see e.g. (Chaboche, et al., 1988)), i.e.:

$$\boldsymbol{\sigma} = \lambda Tr(\boldsymbol{\varepsilon} - \boldsymbol{\varepsilon^p})\boldsymbol{G} + 2\mu(\boldsymbol{\varepsilon} - \boldsymbol{\varepsilon^p}) \tag{13}$$

1.4.1.4. Isotropic hardening

The isotropic hardening is the simplest one, depending on a single scalar variable p ϵ R^+ (unitless).

Under tension/compression load, the compression curve which is subsequent to the initial tension loading can be obtained by a homothetic transformation with ratio of 1 and with the center at the point of the zero stress (point O in Figure 45).

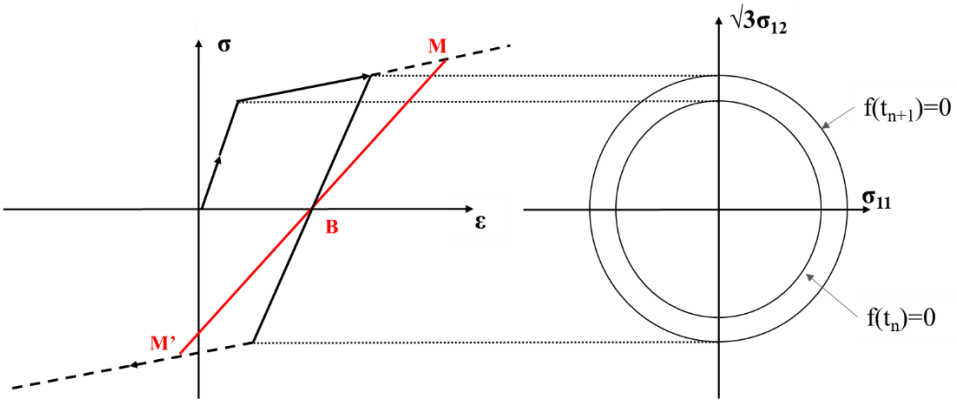

Figure 45 – Isotropic hardening (Chaboche, et al., 1988)

Taking into account the general expression of the isotropic hardening function R, the expression of the elastic threshold function appears as:

$$f = J(\boldsymbol{\sigma}) - R - \sigma_0 \quad (14)$$

where σ_0 (in MPa) is the initial yield limit and $J(.)$ is the expression of the equivalent stress in the sense of Von Mises.

In case of linear isotropic hardening, the isotropic function can be expressed as:

$$R = \mathrm{k}.\,\mathrm{p} \quad (15)$$

and for nonlinear approach, a multitude of expressions can be generated, where the most common being:

$$R = \mathrm{k}.\,p^m \quad (16)$$

$$R = k(1 - e^{-mp}) \quad (17)$$

where k and m are material parameters that have to be identified from experimental results.

1.4.1.5. Linear kinematic hardening (Prager model)

The linear kinematic hardening is directly linked to the plastic stain tensor $\boldsymbol{\varepsilon^p} \in R^3 \times R^3$ (unitless).

The linear kinematic hardening, in opposition to isotropic one, is able to take into account the influence of the loading path on the evolution of the yield surface. The center of the elastic domain (point B in Figure 46) represents the internal state of stress (or back stress).

In a tension/compression test, the compression curve which is subsequent to the initial tension loading, can be obtained by a homothetic transformation with ratio of -1 and with the center at the point of the back stress (point B in in Figure 46).

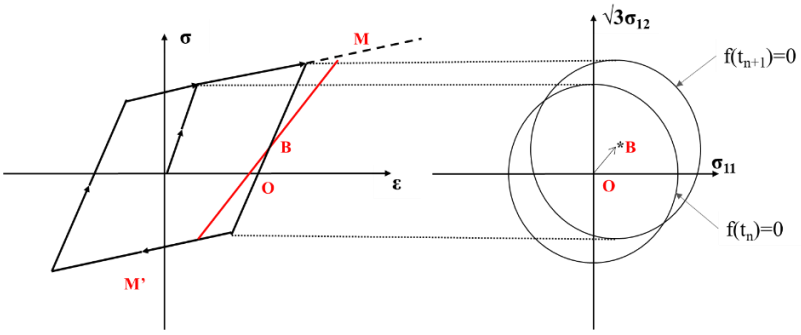

Figure 46 – Kinematic hardening (Chaboche, et al., 1988)

Taking into account the expression of linear kinematic function **B**, the expression of the elastic threshold function appears as:

$$f = J(\boldsymbol{\sigma} - \boldsymbol{B}) - \sigma_0 \quad (18)$$

where σ_0 (in MPa) is the initial yield limit.

An expression of linear kinematic function can be:

$$\mathbf{B} = b.\,\boldsymbol{\varepsilon^p} \quad (19)$$

where b is a material parameter that has to be identified from experimental results.

1.4.1.6. Non-Linear kinematic hardening

According to the expression of yield function with linear kinematic hardening described in eq.(19), it is by definition impossible to introduce nonlinearity by playing directly with the material parameters like it has been done for isotropic function.

The first nonlinear kinematic hardening model has been proposed by Armstrong and Frederick (Armstrong, et al., 1966). This model is not able to represent shakedown (plastic accommodation in this case), but it can generate ratcheting response.

The nonlinear kinematic hardening is managed with the plastic stain tensor $\boldsymbol{\varepsilon^p}$ and the kinematic hardening tensor $\mathbf{X}$.

Similarly to the linear kinematic hardening yield function expression described in eq.(18), the expression of the elastic threshold function with the expression of the equivalent stress appears as:

$$f = J(\boldsymbol{\sigma} - \mathrm{M}\mathbf{X}) - \sigma_0 \tag{20}$$

where σ_0 (in MPa) is the initial yield limit.

The evolution of the tensor variable of kinematic hardening ($\mathbf{X}$) is expressed as:

$$\dot{\boldsymbol{X}} = \dot{\boldsymbol{\varepsilon^p}} - \Lambda\Gamma\boldsymbol{X} \tag{21}$$

where Λ is the plastic multiplier.

1.4.1.7. Multiple hardening

In general, the model development is based on the superposition of several hardening functions in order to represent the complex phenomena that could be experimentally observed as described in §4. Table 2 shows the easiest combination that consists in superposing linear isotropic and linear kinematic hardening. However, this model is very limited and leads to an elastic shakedown after several cycles.

Table 2 – Model summary including linear kinematic hardening and linear isotropic hardening

Model	**Isotropic hardening**	**Linear Kinematic hardening**	**isotropic + linear kinematic hardening**
Stress tensor	$\boldsymbol{\sigma} = \lambda Tr(\boldsymbol{\varepsilon} - \boldsymbol{\varepsilon^p})\boldsymbol{G} + 2\mu(\boldsymbol{\varepsilon} - \boldsymbol{\varepsilon^p})$		
Elastic threshold function	$f = J(\boldsymbol{\sigma}) - R - \sigma_0$	$f = J(\boldsymbol{\sigma} - \boldsymbol{B}) - \sigma_0$	$f = J(\boldsymbol{\sigma} - \boldsymbol{B}) - R - \sigma_0$
Isotropic function	$R = \mathrm{k.p}$	Not applicable	$R = \mathrm{k.p}$
Kinematic function	Not applicable	$\mathbf{B} = b.\boldsymbol{\varepsilon^p}$	$\mathbf{B} = b.\boldsymbol{\varepsilon^p}$
Variable evolution	$\dot{\boldsymbol{\varepsilon^p}} = \Lambda\frac{3}{2.J(\boldsymbol{\sigma})}\boldsymbol{Dev}(\boldsymbol{\sigma})$	$\dot{\boldsymbol{\varepsilon^p}} = \Lambda\frac{3}{2.J(\boldsymbol{\sigma} - \boldsymbol{B})}\boldsymbol{Dev}(\boldsymbol{\sigma} - \boldsymbol{B})$	$\dot{\boldsymbol{\varepsilon^p}} = \Lambda\frac{3}{2.J(\boldsymbol{\sigma} - \boldsymbol{B})}\boldsymbol{Dev}(\boldsymbol{\sigma} - \boldsymbol{B})$
	$\dot{p} = \Lambda$		$\dot{p} = \Lambda$
Representation of the model behaviour by the Stress/Strain evolution under cyclic tension-compression load case	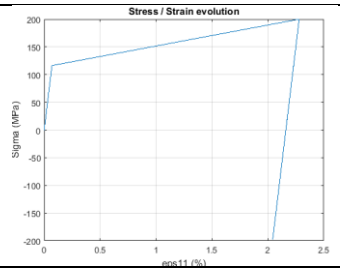	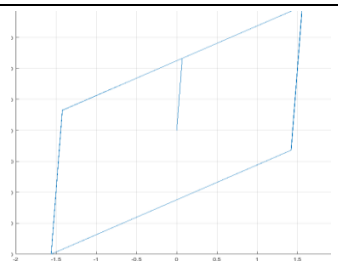	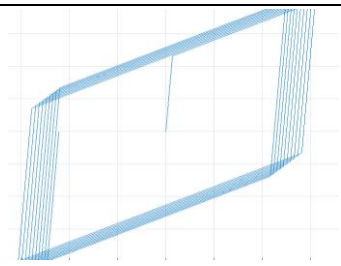

The nonlinear kinematic hardening model with only one kinematic hardening variable is very limited in the sense that it does not account shakedown and leads to ratcheting failure mode with a constant strain range after each cycle (Armstrong, et al., 1966). A way to limit this strain evolution is to combine it to a non-linear isotropic hardening which aims at reducing this strain range and reaching an elastic shakedown, see Table 3.

Table 3 – Model summary including nonlinear kinematic hardening and nonlinear isotropic hardening

Model	**non-linear kinematic hardening**	**isotropic + non-linear kinematic hardening**
Stress tensor		
Elastic threshold function	$f = J(\boldsymbol{\sigma} - M\boldsymbol{X}) - \sigma_0$	$f = J(\boldsymbol{\sigma} - M\boldsymbol{X}) - R - \sigma_0$
Isotropic function	Not applicable	$\mathrm{R} = k.(1 - e^{-mp})$
Kinematic function	$M\boldsymbol{X}$	$M\boldsymbol{X}$
Variable evolution	$\dot{\boldsymbol{\varepsilon}}^{\boldsymbol{p}} = \Lambda \frac{3}{2.J(\boldsymbol{\sigma} - M\boldsymbol{X})} .(\boldsymbol{s} - M\boldsymbol{x})$	$\dot{\boldsymbol{\varepsilon}}^{\boldsymbol{p}} = \Lambda \frac{3}{2.J(\boldsymbol{\sigma} - M\boldsymbol{X})} (\boldsymbol{s} - M\boldsymbol{x})$
	$\dot{\boldsymbol{X}} = \dot{\boldsymbol{\varepsilon}}^{\boldsymbol{p}} - \Lambda\Gamma\boldsymbol{x}$	$\dot{\boldsymbol{X}} = \dot{\boldsymbol{\varepsilon}}^{\boldsymbol{p}} - \Lambda\Gamma\boldsymbol{x}$
		$\dot{p} = \Lambda$
Representation of the model behaviour by the Stress/Strain evolution under cyclic tension-compression load case	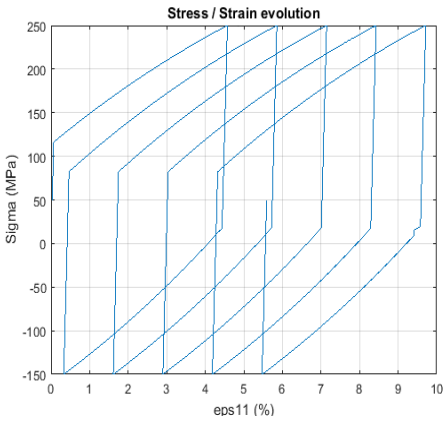	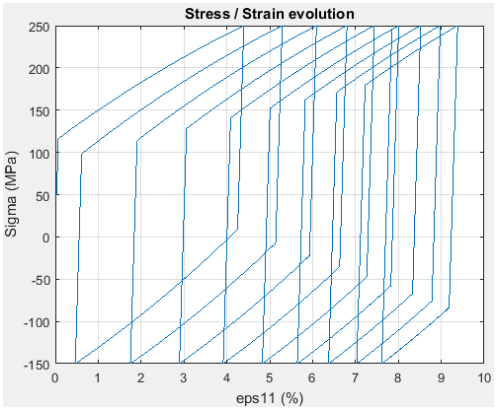

In the eighties, a lot of work has been done by combining different types of hardening, in particular nonlinear kinematic hardening (Chaboche, et al., 1989) (Chaboche, et al., 1989). The objective was to optimise the material response under cyclic loadings. It was proposed to introduce three kinematic hardening variables and to set one with linear behaviour as described in Figure 47. This combination results in a less pronounced ratcheting effect as it can be observed in Table 4.

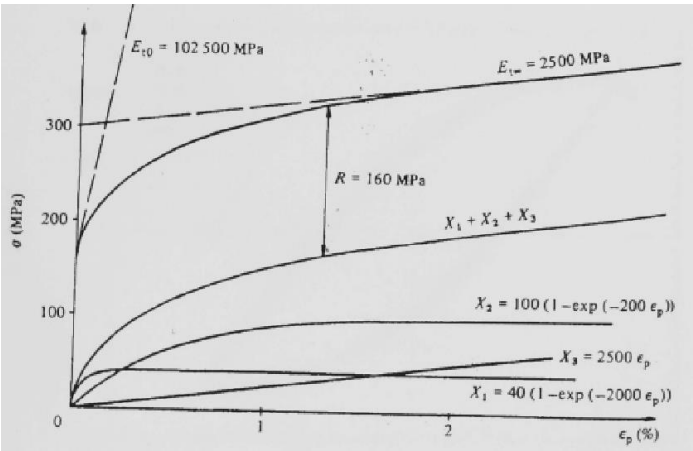

Figure 47 – Superposition of several kinematic hardening (Chaboche, et al., 1988)

Table 4 – Model summary including multi-nonlinear kinematic and nonlinear isotropic hardening

Model	**multi non-linear kinematic hardening**	**isotropic + multi non-linear kinematic hardening**
Stress tensor	$\boldsymbol{\sigma} = \lambda Tr(\boldsymbol{\varepsilon} - \boldsymbol{\varepsilon^p})\boldsymbol{G} + 2\mu(\boldsymbol{\varepsilon} - \boldsymbol{\varepsilon^p})$	
Elastic threshold function	$f = J\left(\boldsymbol{\sigma} - \sum_{i=1}^{n} M_i \boldsymbol{X}_i\right) - \sigma_0$	$f = J\left(\boldsymbol{\sigma} - \sum_{i=1}^{n} M_i \boldsymbol{X}_i\right) - R - \sigma_0$
Isotropic function	Not applicable	$\mathrm{R} = k.(1 - e^{-mp})$
Kinematic function	$\sum_{i=1}^{n} M_i \boldsymbol{X}_i$	$\sum_{i=1}^{n} M_i \boldsymbol{X}_i$
Variable evolution	$\dot{\boldsymbol{\varepsilon}}^{\boldsymbol{p}} = \Lambda \frac{3}{2.J(\boldsymbol{\sigma} - \sum_{i=1}^{n} M_i \boldsymbol{X}_i)} . \left(\boldsymbol{s} - \sum_{i=1}^{n} M_i \boldsymbol{x}_i\right)$	$\dot{\boldsymbol{\varepsilon}}^{\boldsymbol{p}} = \Lambda \frac{3}{2.J\left(\boldsymbol{\sigma} - \sum_{i=1}^{n} M_i \boldsymbol{X}_i\right)} . \left(\boldsymbol{s} - \sum_{i=1}^{n} M_i \boldsymbol{x}_i\right)$
	$\dot{\boldsymbol{X}}_n = \dot{\boldsymbol{\varepsilon}}^{\boldsymbol{p}} - \Lambda \Gamma_n \boldsymbol{x}_n$	$\dot{\boldsymbol{X}}_n = \dot{\boldsymbol{\varepsilon}}^{\boldsymbol{p}} - \Lambda \Gamma_n \boldsymbol{x}_n$
		$\dot{p} = \Lambda$
Representation of the model behaviour by the Stress/Strain evolution under cyclic tension-compression load case	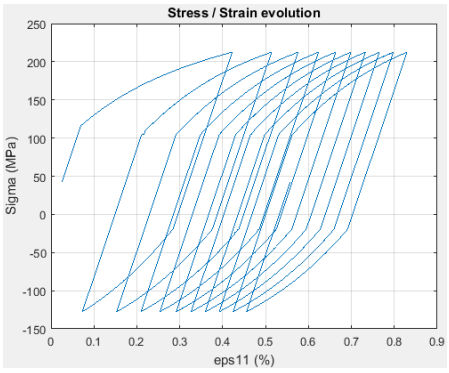	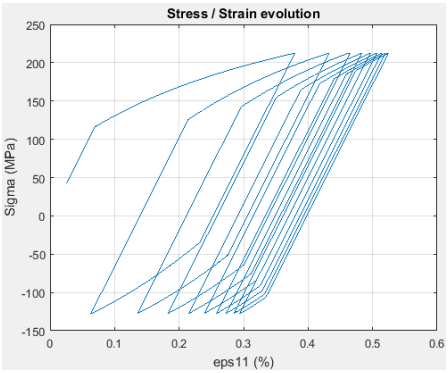

Another way to minimise this ratcheting effect was to introduce a second threshold function with a so called hardening memory variable (Chaboche, 1979). It results in a faster saturation of the isotropic hardening which leads to an elastic shakedown as described in Table 5.

Table 5 – Model summary including multi-nonlinear kinematic hardening and nonlinear isotropic hardening with memory effect

Model	**Non-linear isotropic + linear kinematic hardening with memory effect**	**Non-linear isotropic + non-linear kinematic hardening with memory effect**	**Non-linear isotropic + multi(x3)non-linear kinematic hardening with memory effect**
Stress tensor	$\boldsymbol{\sigma} = \lambda Tr(\boldsymbol{\varepsilon} - \boldsymbol{\varepsilon^p})\boldsymbol{G} + 2\mu(\boldsymbol{\varepsilon} - \boldsymbol{\varepsilon^p})$		
Elastic threshold function	$f = J(\boldsymbol{\sigma} - \boldsymbol{B}) - (\Pi.R) - \sigma_0$	$f = J(\boldsymbol{\sigma} - \boldsymbol{X}) - (\Pi.R) - \sigma_0$	$f = J\left(\boldsymbol{\sigma} - \sum_{i=1}^{n} M_i \boldsymbol{X}_i\right) - (\Pi.R) - \sigma_0$
Desaturation function	$F = J(\boldsymbol{\varepsilon^p} - \boldsymbol{E^p}) - \pi$		
Kinematic function	$\mathbf{B} = b.\boldsymbol{\varepsilon^p}$	MX	$\sum_{i=1}^{n} M_i \boldsymbol{X}_i$
Isotropic function	$\mathrm{R} = k.(1 - e^{-mp})$		
Isotropic saturation function	$\Pi = 1 + \beta\pi$		
Tensor normal to the elastic threshold function	$\boldsymbol{n} = \frac{3}{2J(\boldsymbol{\sigma} - \boldsymbol{B})}.\boldsymbol{Dev}(\boldsymbol{\sigma} - \boldsymbol{B})$	$\boldsymbol{n} = \frac{3}{2J(\boldsymbol{\sigma} - \boldsymbol{X})}(\boldsymbol{s} - M\boldsymbol{x})$	$\boldsymbol{n} = \frac{3}{2J(\boldsymbol{\sigma} - \sum_{i=1}^{n} M_i \boldsymbol{X}_i)}.\boldsymbol{Dev}\left(\boldsymbol{s} - \sum_{i=1}^{n} M_i \boldsymbol{x}_i\right)$
Tensor normal to the isotropic hardening desaturation function	$\boldsymbol{N} = \frac{2.(\boldsymbol{\varepsilon^p} - \boldsymbol{E^p})}{3.\boldsymbol{J}(\boldsymbol{\varepsilon^p} - \boldsymbol{E^p})}$		
Variable evolution	$\dot{\boldsymbol{\varepsilon}}^{\boldsymbol{p}} = \Lambda\frac{3}{2.J(\boldsymbol{\sigma} - \boldsymbol{B})}.\boldsymbol{Dev}(\boldsymbol{\sigma} - \boldsymbol{B})$	$\dot{\boldsymbol{\varepsilon}}^{\boldsymbol{p}} = \Lambda\frac{3}{2.J(\boldsymbol{\sigma} - M\boldsymbol{X})}.(\boldsymbol{s} - M\boldsymbol{x})$	$\dot{\boldsymbol{\varepsilon}}^{\boldsymbol{p}} = \Lambda\frac{3}{2.J(\boldsymbol{\sigma} - \sum_{i=1}^{n} M_i \boldsymbol{X}_i)}.\left(\boldsymbol{s} - \sum_{i=1}^{n} M_i \boldsymbol{x}_i\right)$
		$\dot{\boldsymbol{X}} = \dot{\boldsymbol{\varepsilon}}^{\boldsymbol{p}} - \Lambda\Gamma\boldsymbol{x}$	$\dot{\boldsymbol{X}}_n = \dot{\boldsymbol{\varepsilon}}^{\boldsymbol{p}} - \Lambda\Gamma_n\boldsymbol{x}_n$
	$\dot{p} = \Lambda$		
	$\dot{\pi} = \Lambda\frac{\langle \boldsymbol{n}:\boldsymbol{N}\rangle}{2}.\boldsymbol{H}(F)$		
	$\dot{\boldsymbol{E}}^{\boldsymbol{p}} = \Lambda\sqrt{\frac{3}{2}}.\frac{\langle \boldsymbol{n}:\boldsymbol{N}\rangle}{2}.\boldsymbol{N}.\boldsymbol{H}(F)$		
Representation of the model behaviour by the Stress/Strain evolution under cyclic tension-compression load case	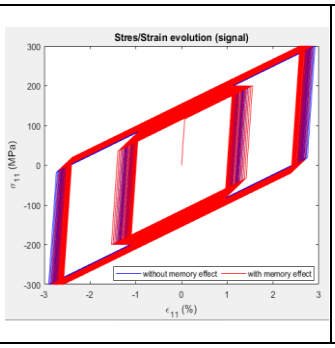	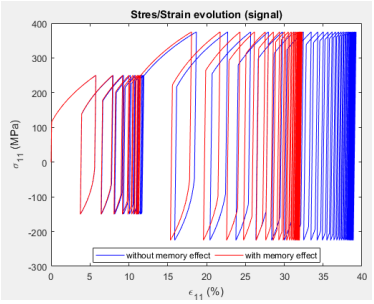	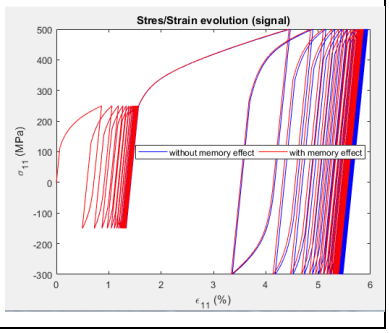

Another approach for minimising the ratcheting phenomenon aims to modify the second term of the kinematic hardening tensor evolution (Chaboche, 1991) (Ohno, et al., 1993) (Ohno, et al., 1993) (Jiang, et al., 1996) (Jiang, et al., 1996) (Abdel-Karim, et al., 2000) (Abdel-Karim, et al., 2000).

One of the most recent coupled model, appears as (Hassan, et al., 2002):

$$\dot{\boldsymbol{X}} = \frac{2}{3} M \dot{\boldsymbol{\varepsilon}}^{\boldsymbol{p}} - \Lambda\Gamma[\delta' \boldsymbol{X} + (1-\delta')(\boldsymbol{n}:\boldsymbol{X})\boldsymbol{n}] \langle 1 - \frac{X_l}{\|\boldsymbol{X}\|} \rangle \tag{22}$$

where M is characteristic coefficients of the material (unitless), X_l is characteristic coefficient of the material (MPa), δ' is characteristic coefficient of the material (unitless) comprised between 0 and 1, **n** is tensor normal to the elastic threshold function (MPa).

Although the present expression provides a more realistic representation of the material behaviour in ratcheting mode, it requires a complex material parameter identification.

1.4.2. Micro-macro approach

We propose to make the comparison between the phenomenological models described in previous sections with a micro-macro model presented in a PhD thesis report (Vincent, 2003). This polycrystalline plasticity model is based on a micro-macro transition approach, see Figure 48, in which two localisation steps and two homogenisation steps are used (macroscopic ↔ grain ↔ slip system) (Cailletaud, et al., 1994).

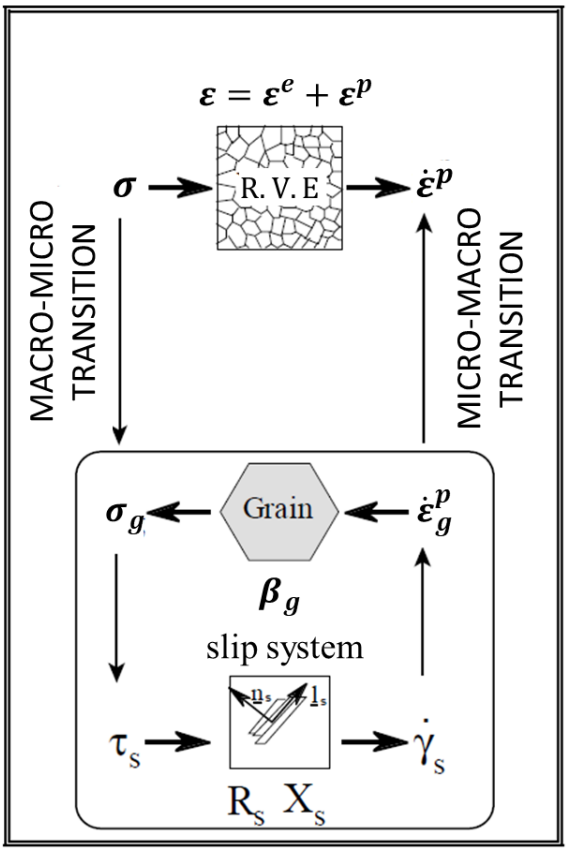

Figure 48 – Localisation and homogenisation scheme for polycrystalline model (Vincent, 2003)

1.4.2.1. The single crystal formulation

The model is based on the small perturbation theory, and an additive decomposition of the elastic and the viscoplastic strain. The so called resolved shear stress $\boldsymbol{\tau_s}$ acting on a particular slip system s is given by Schmid law:

$$\boldsymbol{\tau_s} = \boldsymbol{\sigma_g m_s} \tag{23}$$

where $\mathbf{m_s}$ is the orientation tensor attributed to the slip system s, described as follows:

$$\boldsymbol{m_s} = l_s \otimes n_s + n_s \otimes l_s \tag{24}$$

and where n_s and l_s are respectively the "slip plane" normal vector and the "slip direction" vector on this plane.

As for the macroscopic models, the yield function, at the level of the slip system s, which defines the transition between the reversible deformation and the permanent ones is expressed as follows:

$$f_s = |\boldsymbol{\tau_s} - \boldsymbol{X_s}| - R_s - \tau_0 \tag{25}$$

where the isotropic and kinematic hardening are represented by the internal variables R_s and $\mathbf{X_s}$, respectively, and τ_0 is a material parameter representing the initial slip limit in the slip system s.

For a time dependent material behaviour, the resolved shear stress $\boldsymbol{\tau_s}$ can be related to the corresponding shear rate $\dot{\boldsymbol{\gamma}}_{\boldsymbol{s}}$ via a power law expression:

$$\dot{\boldsymbol{\gamma}}_{\boldsymbol{s}} = \langle \frac{f_s}{K} \rangle^n \, sign(\boldsymbol{\tau_s} - \boldsymbol{X_s}) \tag{26}$$

where n an K are material parameters linked to the viscosity behaviour. This expression of the shear rate $\dot{\boldsymbol{\gamma}}_{\boldsymbol{s}}$ can be compared to a non-linear plastic flow multiplier expression in the case of viscoplastic model for phenomenological approach.

The non-linear evolution rule for isotropic hardening involves an integration matrix H_{sr} which represents self-hardening (diagonal terms) and latent hardening (non-diagonal terms) through:

$$R_s = R_0 + Q \sum_r H_{sr} q_r \tag{27}$$

where R_0 denotes the initial value of R_s, and the variable qr (in MPa) represents the isotropic hardening contribution of the slip system r. For austenistic stainless steel, which is made of FCC crystals (12 faces), the integration matrix H_{sr} is (12,12).

The isotropic variable evolution is defined by the following equation:

$$\dot{q}_r = b(1 - q_r)\dot{\boldsymbol{\gamma}}_{\boldsymbol{s}} \tag{28}$$

The kinematic hardening variable evolution follows the same methodology before proposed by Armstrong and Frederick (Armstrong, et al., 1966) for representing ratcheting, and it is expressed as:

$$\dot{\boldsymbol{X}}_{\boldsymbol{s}} = C\dot{\boldsymbol{\gamma}}_{\boldsymbol{s}} - D\boldsymbol{X_s}|\dot{\boldsymbol{\gamma}}_{\boldsymbol{s}}| \tag{29}$$

where C and D are material parameters.

1.4.2.2. Micro-macro transition and homogenisation

From this step, the equation can be solved for each crystal locally, and it is necessary to "redistribute" the information at the macroscopic level.

In the small strain and small rotation framework, the plastic strain tensor rate at grain level results from the slip occurring on each crystal face, and it is expressed as follows:

$$\dot{\boldsymbol{\varepsilon}}_{\boldsymbol{g}}^{\boldsymbol{p}} = \sum_s \boldsymbol{m_s}\dot{\boldsymbol{\gamma}}_{\boldsymbol{s}} \tag{30}$$

This Representative Volume Elementary (RVE) consists in a summation of grains with different orientation in such a way that the macroscopic plastic behaviour remains isotropic. On each grain, the macroscopic stress tensor $\boldsymbol{\sigma}$ is localised from the following law:

$$\boldsymbol{\sigma_g} = \boldsymbol{\sigma} + 2\mu(1-\beta)\left[\boldsymbol{B} - \boldsymbol{\beta_g}\right] \text{ with } \boldsymbol{B} = \sum_g f_g \boldsymbol{\beta_g} \tag{31}$$

where $\boldsymbol{\sigma_g}$ is the stress tensor in the grain g, μ is the shear modulus, β is a material constant, f_g is the volumic fraction of the grain g, and $\boldsymbol{\beta_g}$ is a variable representing the non-linear accommodation of intergranular plastic incompressibility. This variable evolution is expressed as follows:

$$\dot{\boldsymbol{\beta}}_{\boldsymbol{g}} = \dot{\boldsymbol{\varepsilon}}_{\boldsymbol{g}}^{\boldsymbol{p}} - \Delta\left[\boldsymbol{\beta}_{\boldsymbol{g}} - \delta\boldsymbol{\varepsilon}_{\boldsymbol{g}}^{\boldsymbol{p}}\right]\left\|\dot{\boldsymbol{\varepsilon}}_{\boldsymbol{g}}^{\boldsymbol{p}}\right\| \tag{32}$$

where Δ and δ are two material parameters and $\boldsymbol{\varepsilon}_{\boldsymbol{g}}^{\boldsymbol{p}}$ is the plastic strain tensor at grain level.

The macroscopic deformation is obtained from the mean of all plastic deformation per grain:

$$\dot{\boldsymbol{\varepsilon}}^{\boldsymbol{p}} = \sum_g f_g \boldsymbol{\varepsilon}_{\boldsymbol{g}}^{\boldsymbol{p}} \tag{33}$$

Finally, the stress tensor at the macroscopic level is expressed via the Hooke law as follow:

$$\boldsymbol{\sigma} = \sum_g f_g \boldsymbol{\sigma_g} = \frac{2\mu\upsilon}{1-2\upsilon} Tr(\boldsymbol{\varepsilon} - \boldsymbol{\varepsilon}^{\boldsymbol{p}})\boldsymbol{G} + 2\mu(\boldsymbol{\varepsilon} - \boldsymbol{\varepsilon}^{\boldsymbol{p}}) \tag{34}$$

where υ is the poisson coefficient.

There are a multitude of other plasticity models based on the micro-macro approach than the one presented above. Since they are based on physical phenomena at the microscopic level, these types of models are more promising than the phenomenological ones, where the physical mechanisms are taken at macroscopic level only.

1.5. Conclusion

The ITER Vacuum Vessel (VV), which is one of the main components, is the primary confinement barrier of the ITER nuclear installation. It shall withstand high heat loads, resist electromagnetic loads during disruptions, and shall be compatible with high vacuum operation.

The VV design is made according to nuclear code (i.e. RCC-MR), which provides detailed and basic rules for design, manufacturing, installation, commissioning and in-service inspection of nuclear plant devices. According to this code, the prevention of damage to guarantee the structural integrity has mainly two origins:

- prevention of damage originating from monotonic mechanical loads,
- prevention of damage originating from the progressive deformations, associated to repeated application of loads.

Among the different failure modes, the ratcheting is the most complex one to be simulated. Indeed, two types of ratcheting can be identified: material ratcheting, which is purely related to the material, and structural ratcheting (Hübel, 1996).

To assess ratcheting through the phenomenological approach, non-linear kinematic model was first introduced by Armstrong & Frederick (Armstrong, et al., 1966). In the eighties, a lot of works has been done by combining different type of hardening (Chaboche, et al., 1989) (Chaboche, et al., 1989) (Chaboche, 1991) (Chaboche, 1979), introducing time dependent variables (Chaboche, 1989) (Perzyna, 2005) (Nouailhas, 1988), with damage parameters (Lemaitre, 1985) (Rousselier, 1987), in the objective of optimising model behaviour response (Chaboche, 1989).

Since that time, a lot of work on mechanical testing (Haupt, et al., 1996) (Delobelle, et al., 1995), material parameters identification (Jiang, et al., 2008) (Kang, 2008) and model optimisation was done (Hassan, 1992) (Hassan, 1994), but the models remain valid only for restricted domain of loading.

Up to now, all the models linked to ratcheting phenomenon where only developed under isothermal assumption. Nevertheless, it has been demonstrated that the ratcheting phenomenon can occur under constant mechanical load with cyclic thermal loading (Bree, 1967) (Lee, 2003). Thermo-elastic behaviour model has already been developed in the past (Chaboche, et al., 1988), and some work on thermo-mechanical coupling for non-linear models have been initiated (Hyde, et al., 2010).

According to ITER community experts in materials and analyses, a thermo-mechanical behaviour model fitting the ITER Tokamak materials data will guarantee the best prediction of the damage considering nuclear and multi-physic loading conditions.

In the next chapter we present a non-linear behaviour model of vacuum vessel material with a strong thermomechanical coupling and a damage parameter to prevent crack initiation. More precisely, Chaboche's model available in the literature (elasto (visco) plasticity model with various types of hardening (Nouailhas, 1988) (Chaboche, 1979)) will be enriched in order to explicitly take into account the influence of temperature on the mechanical behaviour and reciprocally, the influence of the mechanical behaviour on temperature.

Chapter 2. Mechanical cyclic tests

2.1. Introduction

In the literature, a large amount of tensile-compression cyclic tests on stainless steel (i.e. type 316) exists, generally performed under imposed displacements. Nevertheless, to ensure a more precise material parameter identification, the mechanical tests presented in this chapter have been performed on sample machined from a 400x400x40mm^3 plate of the VV base material. Moreover, for cyclic tension-compression tests, the extensometer has been adapted for measuring the diameter evolution of the test specimen, which allows to measure the true stress during imposed force test and to pilot the test in imposed stress. Finally, cyclic torsion tests have been performed in imposed angle and imposed torque in low cycle fatigue area for which occurs the ratcheting failure mode.

This chapter describes the tensile test machine used, the geometry of the specimens and the different extensometer configurations. The first part corresponding to monotonic tensile tests aims to verify the isotropy of the material, the invariance of the young modulus under loading history and the viscosity response of the material for different test velocities. The second part of this chapter is dedicated to cyclic tensile-compression tests that have been performed in imposed force and imposed stress. For all tests, the true stress-strain curves and the engineering stress strain curves have been superposed in order to highlight the effect of the specimen diameter's evolution in this high stress range level, for which progressive deformation has been identified. Finally, cyclic torsion tests have been performed in imposed angle and imposed torque and reported in the last part of this chapter. The objectives were to reach similar material response than the cyclic tensile-compression tests, at the difference that the stress is by definition non homogeneously distributed.

2.2. Traction-torsion machine and extensometer

All experiments have been performed on two hydraulic machines MTS-322 100 kN for traction/compression tests and MTS-809 250kN/2200Nm for traction/compression/torsion equipped with an axial MTS extensometer, see Figure 49 and Figure 50. All tests have been achieved at "Laboratoire de Mécanique et d'Acoustique – LMA".

Figure 49 – MTS-322 Traction-compression machine

Figure 50 – Axial MTS extensometer

In the bibliography, numerous mechanical test results are available for type 316 stainless steel (Barabash, 2007) (Kalinin, 2000) (Kalinin, 1996) (Tavassoli, 1995). Nevertheless, to ensure more precise material parameter identification, mechanical tests have been performed on a sample machined from a 400x400x40mm^3 plate of the VV base material, see Figure 51.

Note that, due to the dimensions of the plate and for the sake of optimal use of the available material, the dimensions of the samples were not in agreement with the usual norms.

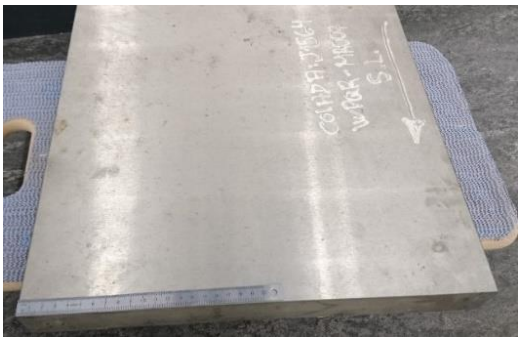

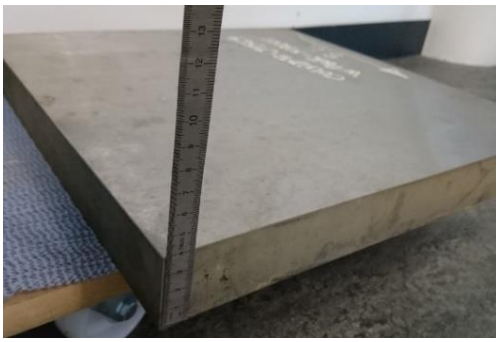

Figure 51 –Sample of SS316L(N)-IG plate 400x400x40 mm^3

For monotonic tensile tests, six specimens have been machined from the plate presented in Figure 51 with dimensions described in Figure 52. Before machining the specimens for cyclic loading, it is mandatory to ensure that the material is isotropic: for this reason, one-half of the specimens have been cut in the longitudinal part of the plate and the second half on the transversal part.

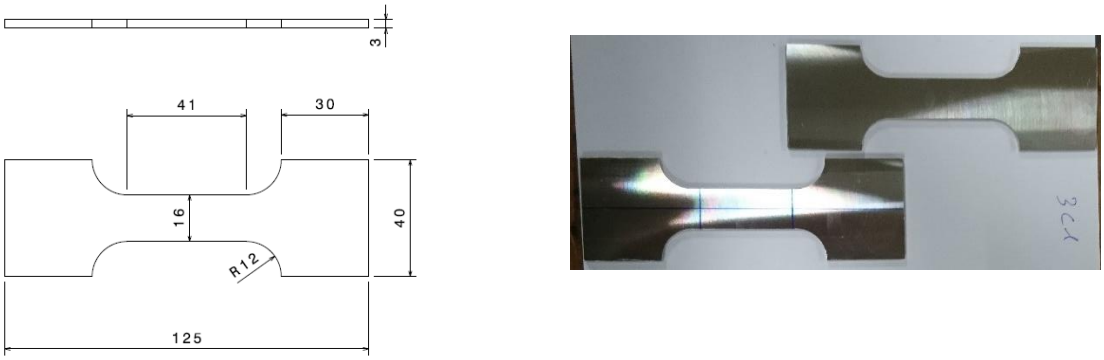

Figure 52 – specimen for monotonic tensile test.

After the confirmation of the isotropic characteristic of the plate material, 12 specimens have been prepared according to the dimensions described in Figure 53. Six have been used for cyclic tensile-compression tests and the others have been used for cyclic torsion tests.

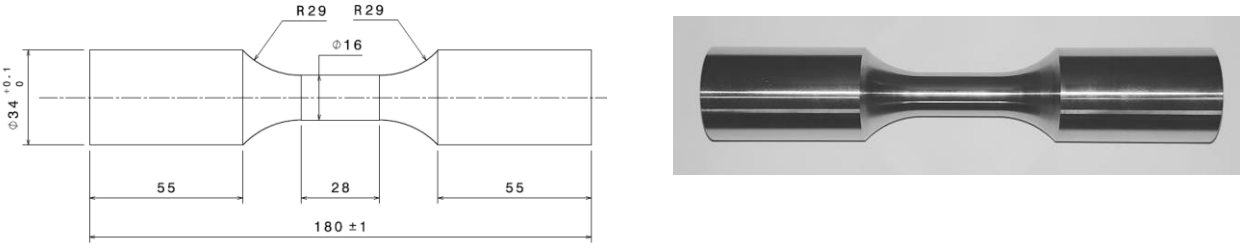

Figure 53 – specimen for cyclic test.

From the tensile-compression tests, two types of results can be reported: the engineering stress-strain curve, based on the initial cross-section, and the true stress-strain curve, based on the measured cross-section. For our experiments, the extensometer has been adapted for measuring the evolution of the test sample diameter, as shown in Figure 54. This configuration allows to measure the true stress during imposed force test, and to pilot the test in imposed stress.

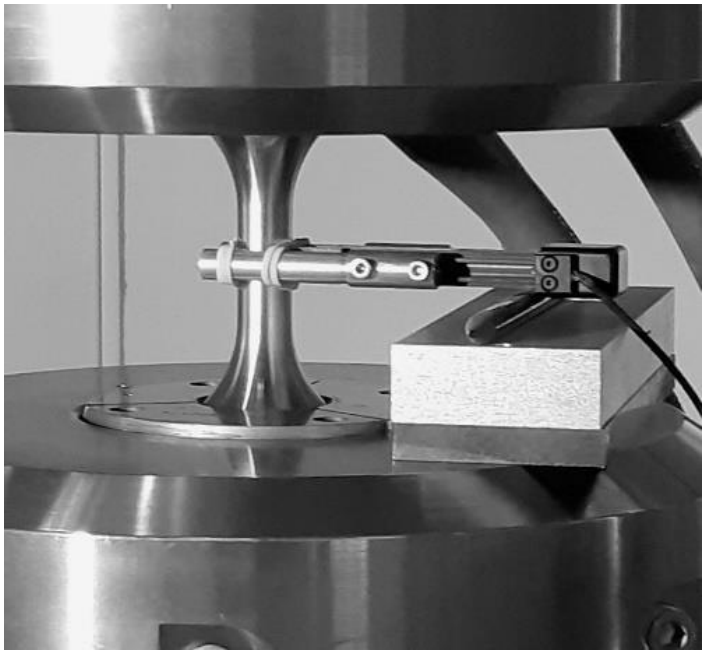

Figure 54 – Extensometer configuration for cyclic test.

2.3. Monotonic tensile test

The objectives of the monotonic tensile tests performed here are to confirm the basic mechanical properties of the studied austenitic stainless steel, i.e. SS316L(N)-IG (ITER VV structural material). In the following figures, Figure 55, Figure 58 and Figure 59, the variable on the y-axis is the so called engineering stress, i.e. computed from the actual force and the initial cross-section.

2.3.1. Verification of the isotropy of the material

The first two tensile tests have been performed in each direction (longitudinal and transversal) with imposed displacement rate of 1mm/min. It can be observed from Figure 55 that the two curves are perfectly superposed, which suggest that the material is isotropic (this isotropy assumption will be retained throughout the studies). Additionally, the rupture of the specimens occurs over 50% of strain, which is confirming the high ductility of the studied material.

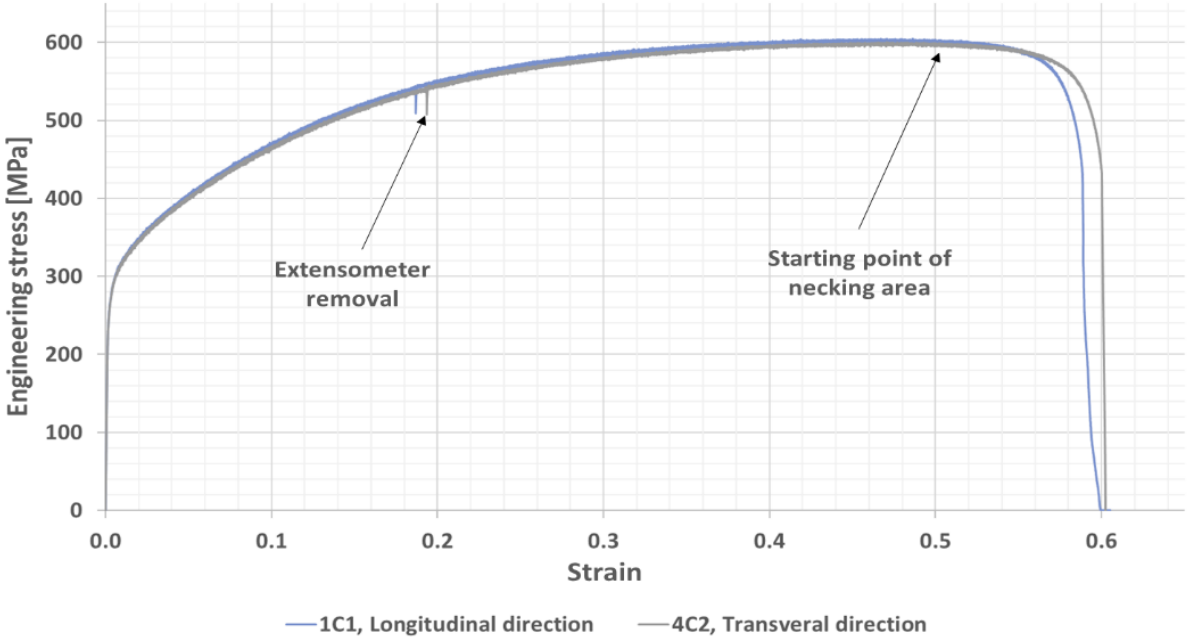

Figure 55 – Imposed displacement, 1mm/min rate

Figure 56 – Test monitoring

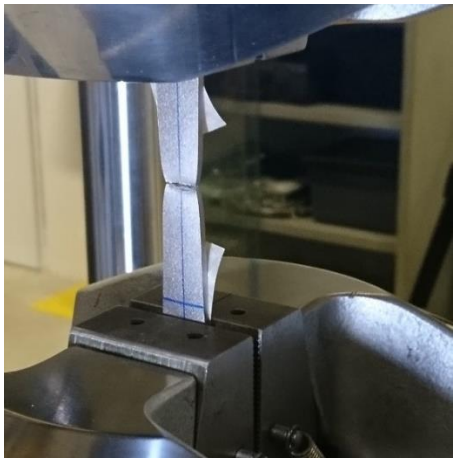

Figure 57 – Specimen 01 after failure

2.3.2. Invariance of the Young modulus verification

Two additional tensile tests in each direction (longitudinal and transversal) have been performed with the same rate of 1mm/min including four unloading steps every 14% of strain. The "unloading" step consists in a decreasing of the loading down to zero reaction force and restart loading with initial displacement rate. This type of test aims to identify any evolution of the Young's modulus during the test. The Figure 58 confirms that the Young modulus remains unchanged during the test and shows that the four curves are perfectly superposed except at the rupture area.

Finally, the specimens for which the four unloadings have been applied broke before the others. This observation indicates that the loading history is of the utmost importance on the mechanical behaviour of the material.

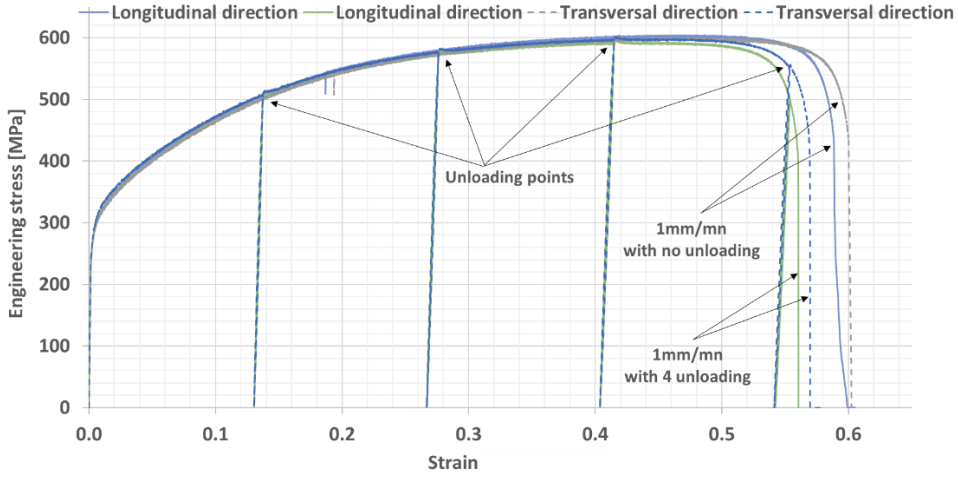

Figure 58 – Comparison between tensile tests with unloading (#4) and reloading (#4) in transverse and longitudinal directions.

2.3.3. Viscosity of the material verification

The last three specimens have been tested at different displacement rates: 1mm/min, 10 mm/min and 100mm/min. The results presented in Figure 59 show that the material is lightly viscous (difference around 10% at the level of the yield strength limit and the plastic response). Nevertheless, it can be observed that at low velocity (1 mm/min), the ultimate strength is 30% higher in comparison with other tests performed.

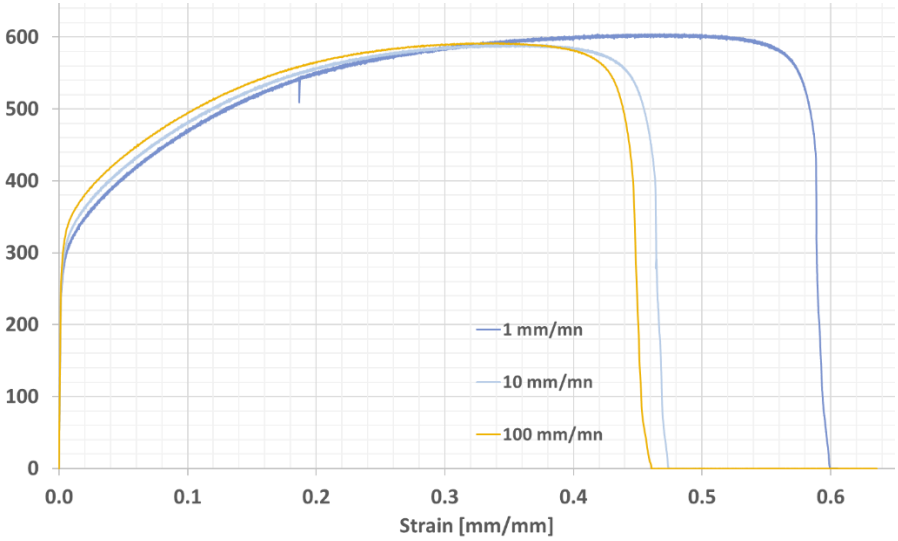

Figure 59 – Comparison between monotonic tensile tests at different velocities.

2.4. Tension-compression cyclic test

In the literature, most of the cyclic tests are performed with imposed displacements which is not representative of the ITER VV load applications. The following tests have been carried out in imposed force and imposed stress with an amplitude range allowing the occurrence of the ratcheting failure mode. Moreover, the true stress-strain curves and the engineering stress-strain curves have been superposed for all tests, in the objective of highlighting the effect of the specimen diameter's evolution in this high stress range level for which progressive deformation has been identified.

2.4.1. Imposed force cyclic tests

2.4.1.1. Identification of force range for low cycle fatigue (Cylinder-01)

The first specimen has been tested under cyclic loading with imposed force at different amplitudes up to observe ratcheting failure mode. The objective is to identify the force range level for which the low cycle fatigue occurs (less than 10 000 cycles).

The force was imposed following the sinusoidal evolution described in eq.(35), where F_{moy} is the mean force, ΔF the force range and f=0.3Hz, the frequency.

$$F(t) = F_{moy} + \frac{\Delta F}{2} \sin(2\,\pi\, f\, t) \quad (35)$$

$$Fmoy = \frac{Fmax + Fmin}{2} \quad (36)$$

$$\Delta F = Fmax - Fmin \quad (37)$$

For each test, the machine reaches gradually the nominal value, by applying an initial 10 cycles sequence. In all the following curves, the area for which the nominal value is reached, will be noted "point A". Note that the results interpretation is made beyond this point.

For this first test, we have noted that the high strain range does not allow to use the extensometer in the configuration described in Figure 50. That is why the curve presented in Figure 60 represents the force evolution along the displacement, directly extracted from the machine sensors. Despite this technical issue, it can be observed that the shakedown occurs for the two first force amplitudes (80/-20kN during 2352 cycles and 100/-40kN during 1000 cycles) and the ratcheting occurs for the last one (105/-45kN) up to the break after 178 cycles over the previous ones. Based on this results, we have adapted the force range to be studied for the other cylinders which corresponds to $90<F_{max}<100$kN and $-30<F_{min}<-40$kN.

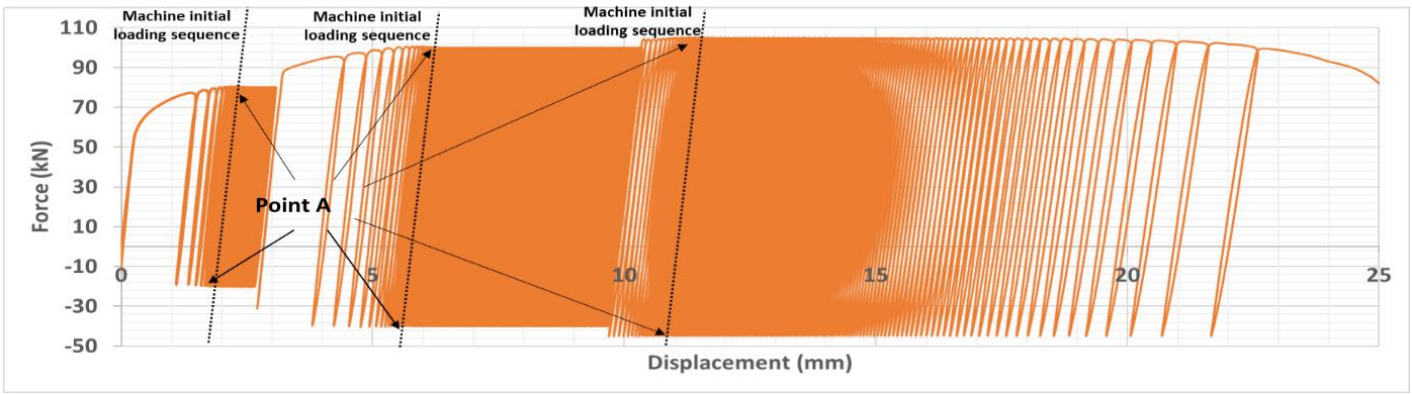

Figure 60 – Results of cyclic test on cylinder 01 with imposed force loading

2.4.1.2. Reference imposed force test: F_{max}=100kN, F_{min}=-40kN (cylinder-02)

For the following tests, the extensometer configuration has been modified for measuring the diameter evolution of the specimen as described in Figure 54. That is why in the following figures, two types of results are reported: the engineering stress-strain curve (in orange) based on the initial cross-section (200mm^2), and the true stress-strain curve (in blue), which is based on the measured cross-section.

The test result for cylinder-02 presented in Figure 61 has been realised with cyclic force load considering F_{max}=100kN and F_{min}=-40kN. The force was imposed following the sinusoidal evolution described in eq. (35), where mean force F_{moy}= 30kN, the force range ΔF=140kN and the frequency f=0.3Hz. Failure appears after 3574 cycles.

Figure 61 shows that since the beginning of the test, the strain has evolved from 0.07 to 0.27 after each cycles during ~3540cycles, which corresponds to a mean rate of 5.65 10^{-7} per cycle. It is only at the end of the test that the strain rate is accelerating up to the rupture of the specimen. Effectively, the specimen strain has increased by 0.08 in 24 cycles which corresponds to a mean strain rate of 3.2 10^{-3}, about 200 times higher to the previous one. Additionally, it can be observed from the true stress-strain curve that the cross-section of the specimen decreases continuously until a limit is reached close to the rupture.

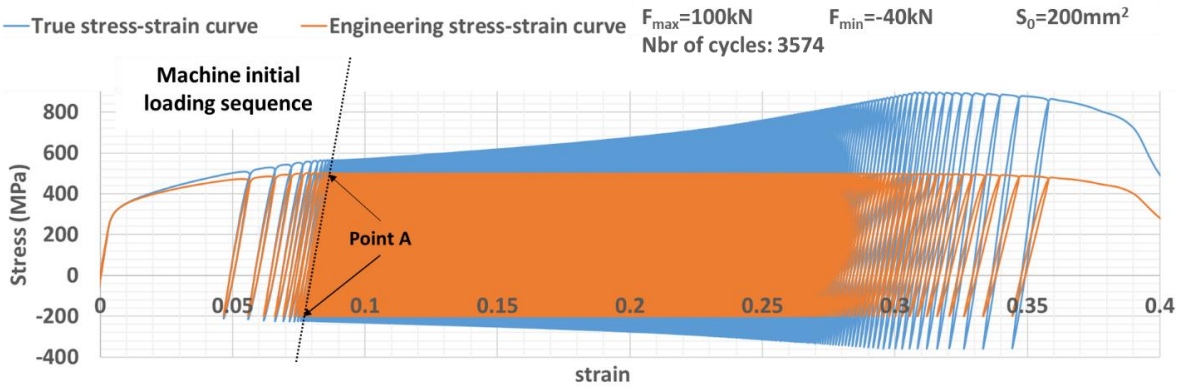

Figure 61 – Results of cyclic test on cylinder 02 with imposed force loading

By definition, shakedown appears when the strain evolution between two cycles is equal or close to zero. However, the results show that the strain increases continuously after each cycles.

That is why, to dissociate shakedown and ratcheting, we proposed to plot the strain evolution along the cumulative cycles, as it is shown in Figure 62.

The dashed black line represents the strain evolution with an affine function, for which the slope coefficient provides information on the ratcheting rate. Indeed, when the slope is close to infinite, plastic shakedown occurs, otherwise, this slope is as small as the ratcheting stain is pronounced, see Figure 62.

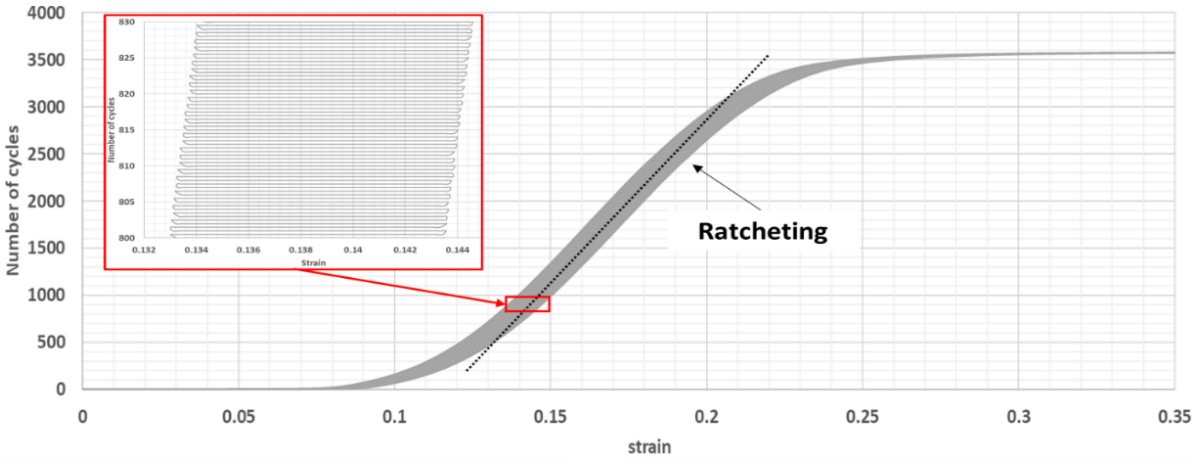

Figure 62 – Cumulative number of cycles along the strain for cylinder 02

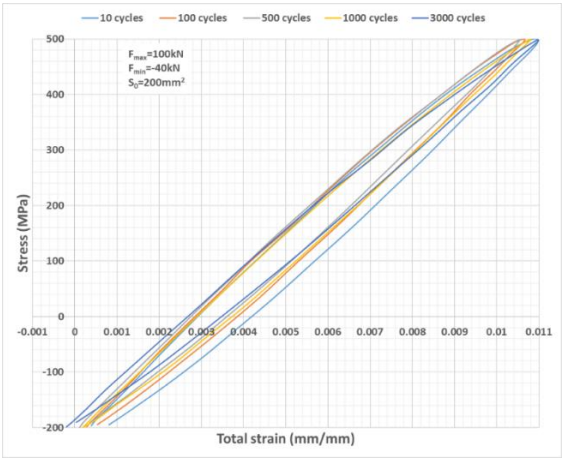

Figure 63 –Hysteresis loop at different cycles extracted from imposed cyclic force loading test performed on cylinder

The macroscopic views of the cylinder 02 after break presented in Figure 64 show a ductile fracture pattern on the periphery and a brittle one in the center. The fracture occurred after 3574 cycles.

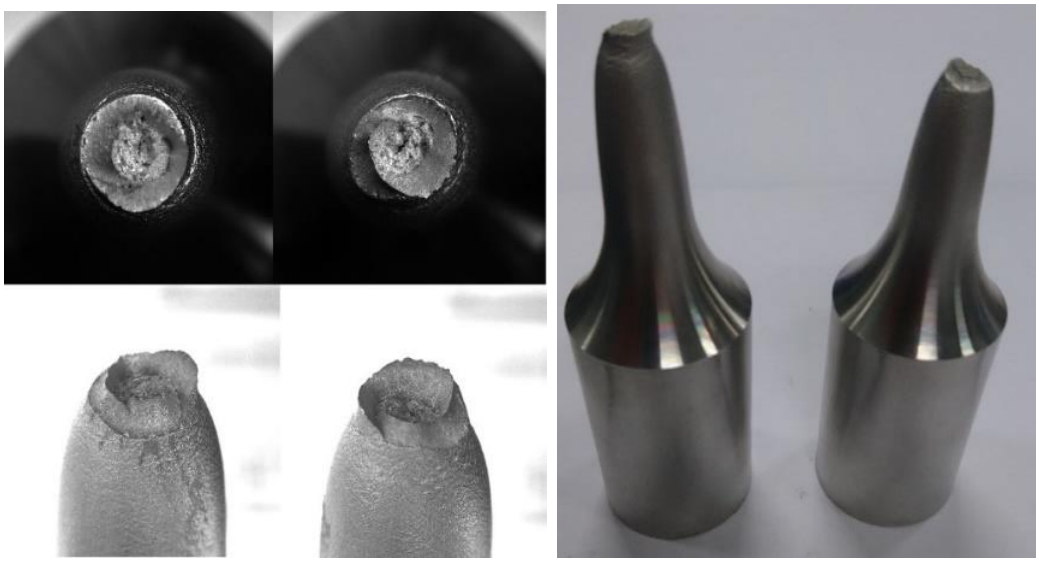

Figure 64 – Cylinder 02 after failure

2.4.1.3. Force range decrease with same mean force (cylinder-03)

The test for cylinder-03, see result in Figure 65, has been realised with cyclic force load considering F_{max}=80kN and F_{min}=-20kN up to reaching stabilised strain after 27100 cycles. Then, the amplitude force ΔF has been increased considering F_{max}=90kN and F_{min}=-30kN. The test sample presented in Figure 67 after 48652 cycles shows that the rupture does not occur at the level of the extensometer. For this reason, the true stress-strain curve does not present exploitable results for the second cyclic load. In addition, the position and the shape of the rupture area suggest that the failure mode was induced by a defect probably introduced during the specimen manufacturing.

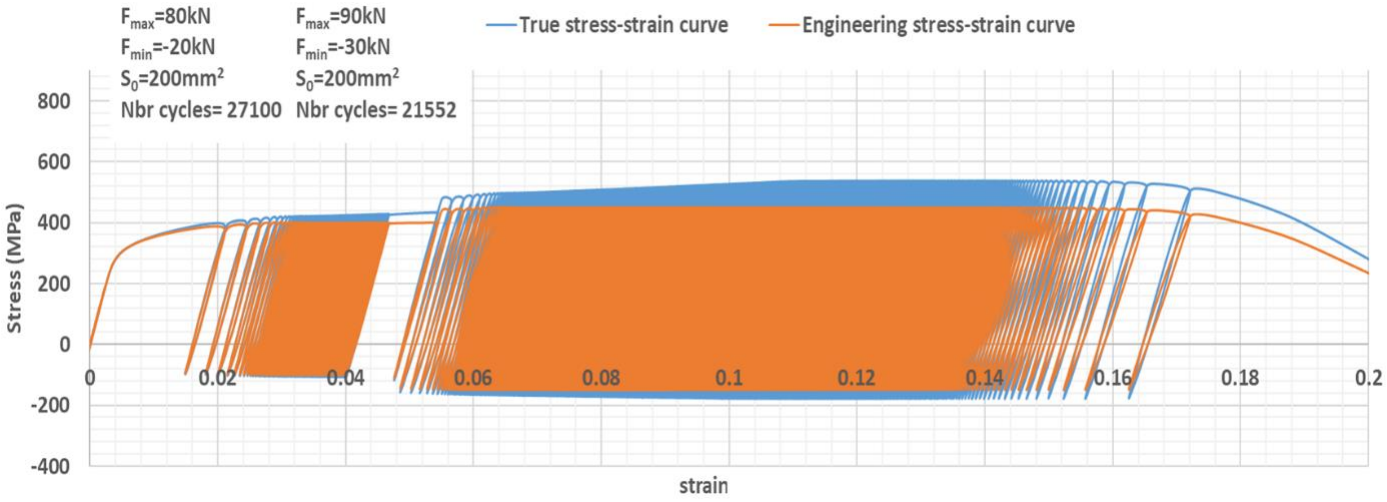

Figure 65 – **Results of cyclic test on cylinder 03 with imposed force loading**

Figure 66 illustrates the cumulative number of cycles along the strain evolution. For the first loading sequence where the shakedown response has been reached, the cumulative number of cycle shows a quasi-vertical evolution, while for the second one where the ratcheting appears, this evolution is more pronounced.

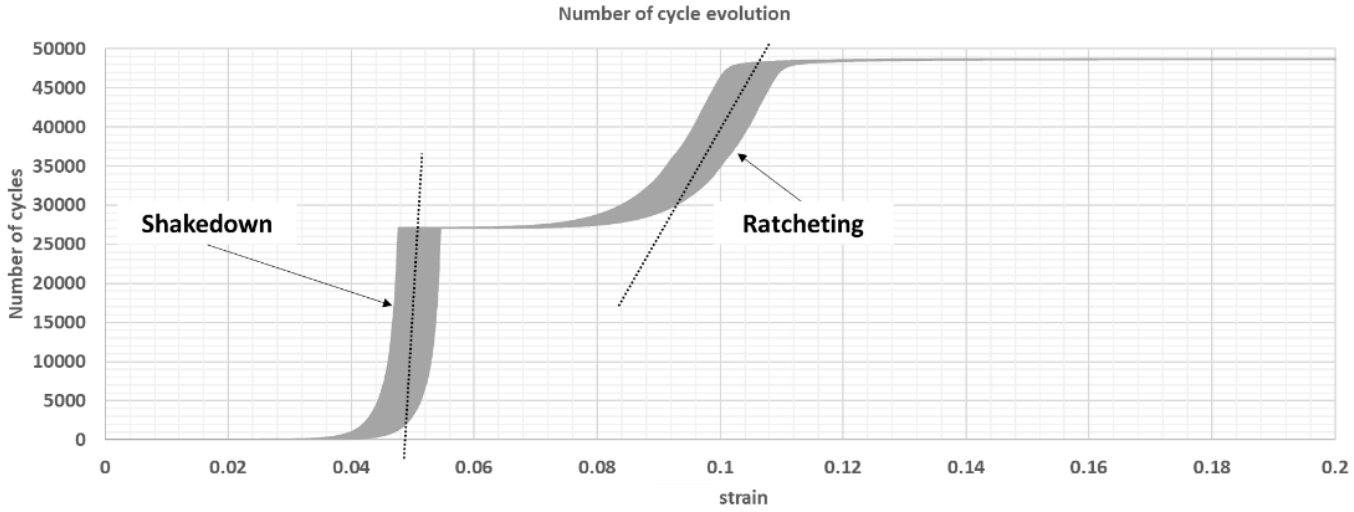

Figure 66 – Cumulative number of cycles along the strain for cylinder 03

Figure 67 – Cylinder 03 after failure

2.4.1.4. Comparison of specimen deformation evolution for different force ranges with same mean forces

Figure 68 reports the three tests results performed in imposed force where different forces ranges have been tested while maintaining the same mean force. It represents the cumulative number of cycles along the strain evolution and make it possible to identify shakedown and ratcheting.

It can be observed that after each cycle the strain increases and its rate is amplified with the force amplitude. Moreover, it can be conclude that the ratcheting failure mode is amplified by a high force range with high mean force.

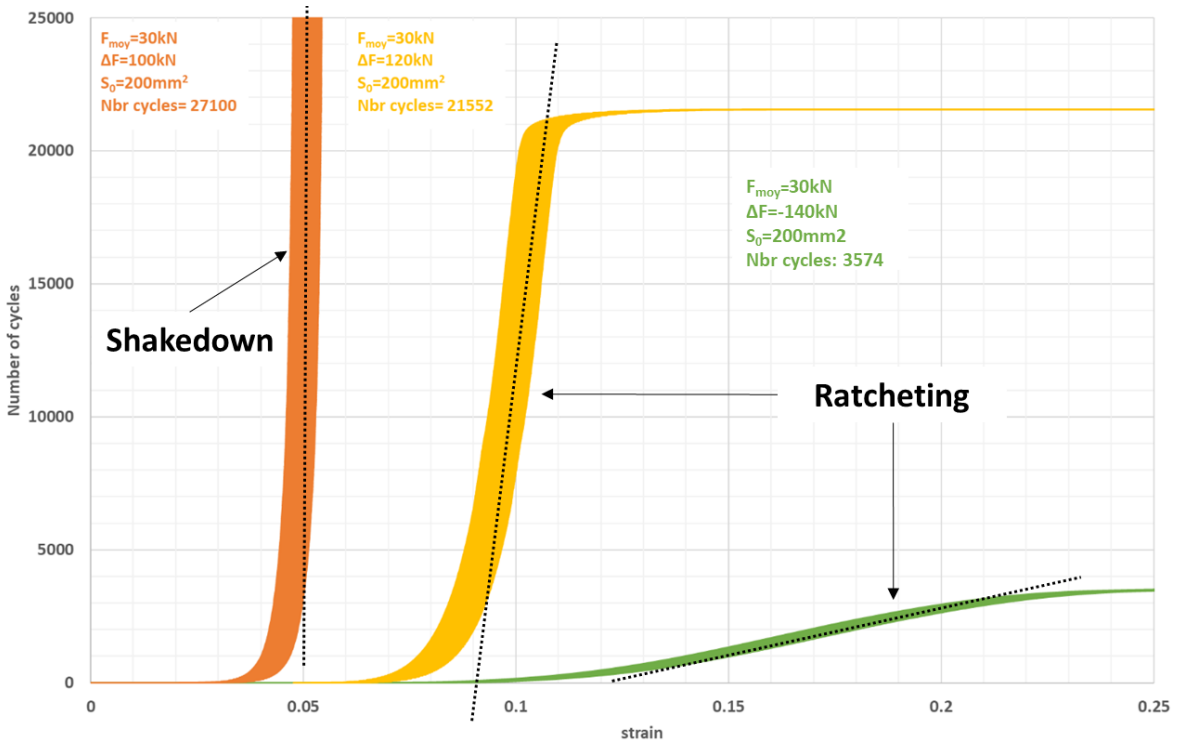

Figure 68 – Strain evolution along the test cycles for different force ranges and mean stress

2.4.2. Imposed stress cyclic tests

As described in Chapter I, the nuclear codes dissociate the loads in primary loads and secondary loads. Since the ratcheting is associated to a failure mode to be checked under secondary loading, we are proposing here to monitor the test in imposed stress. By definition, since the stress remains constant, no evolution of the strain should be observed.

2.4.2.1. Reference imposed stress test: σ_{max}=730MPa, σ_{min}=-250MPa (cylinder-04)

The stress is imposed following the same sinusoidal evolution as described in eq.(38), where σ_{moy} is the mean stress, $\Delta\sigma$ is the stress range and f=0.3Hz the frequency.

$$\sigma(t) = \sigma_{moy} + \frac{\Delta\sigma}{2}\sin(2\,\pi\,f\,t) \tag{38}$$

$$\sigma_{moy} = \frac{\sigma_{max} + \sigma_{min}}{2} \tag{39}$$

$$\Delta\sigma = \sigma_{max} - \sigma_{min} \tag{40}$$

The test for cylinder-04, see result in Figure 69, has been realised with cyclic stress load considering σ_{max}=730MPa and σ_{min}=-250MPa. The stress has been imposed following the same sinusoidal evolution as described in eq.(38), where the mean stress σ_{moy}= 490MPa, the stress range $\Delta\sigma$=1080MPa and the frequency f=0.3Hz. Failure appears after 15830 cycles.

Obviously, a similar material behaviour than the one for the imposed force test on cyclinder-02 can be observed. This time, however, we have plotted the ratcheting strain ($\delta\varepsilon$), see Figure 25 along the strain from the point A to the end of the test, as reported in Figure 70. It shows an exponential evolution that increases rapidly during the last 10 cycles.

A second phenomenon that was also observed for imposed force condition, which is reported for this type of loading on the engineering stress-strain curve, is that the stress decreases to a stabilised stress range, see Figure 69.

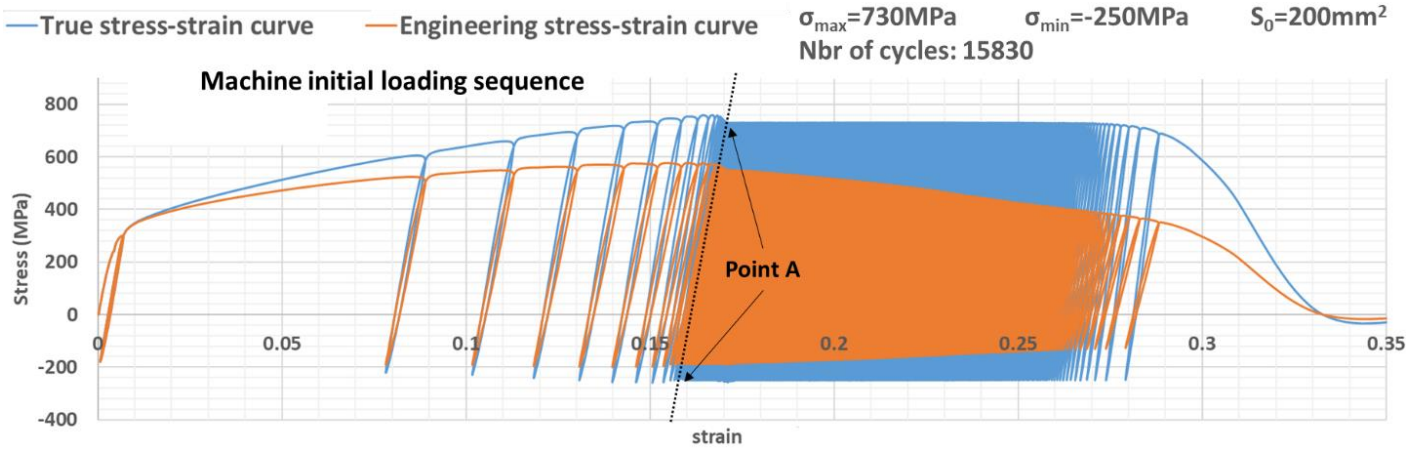

Figure 69 – Results of cyclic test on cylinder 04 with imposed stress loading

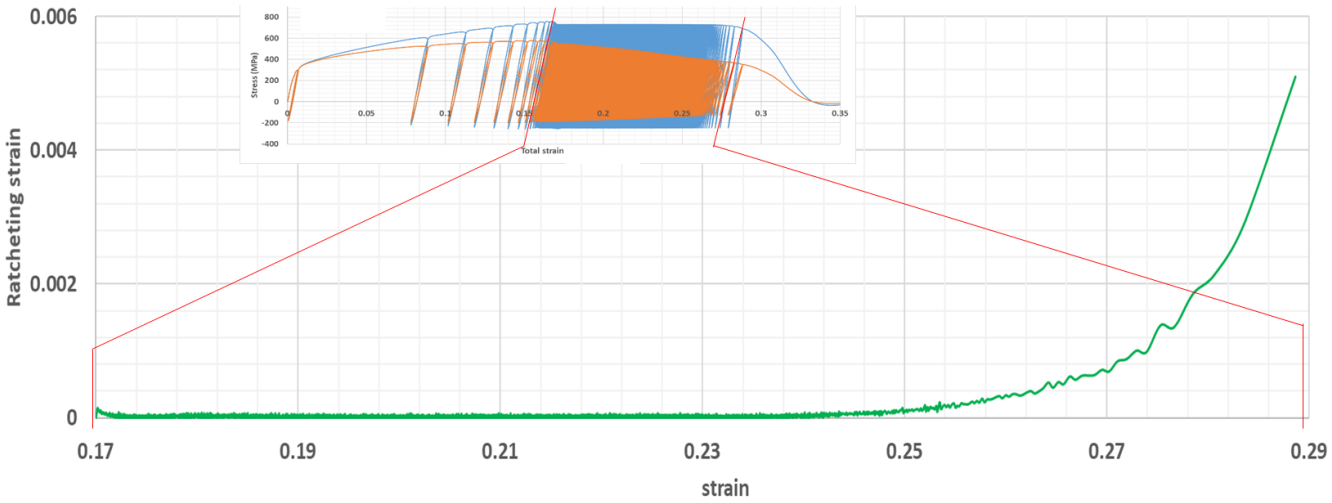

Figure 70 – Ratcheting strain along the strain for cylinder 04

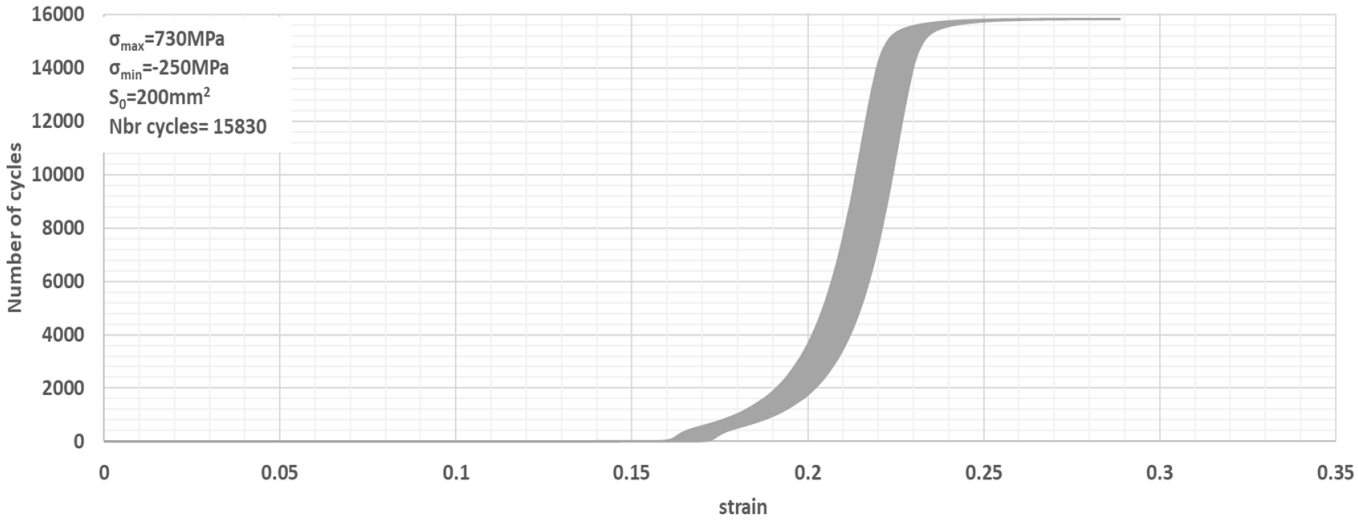

Figure 71 – Cumulative number of cycles along the strain for cylinder 04

2.4.2.2. Mean stress increase with same stress range (Cylinder-05)

The test for cylinder-05, see result in Figure 72, has been realised with cyclic stress load considering σ_{max}=780MPa and σ_{min}=-300MPa. The stress was imposed following the same sinusoidal evolution as described in eq.(38), where the mean stress σ_{moy}= 540MPa, the stress range $\Delta\sigma$=1080MPa and the frequency f=0.3Hz. Failure appears after 7632 cycles.

In comparison to the test performed on cylinder 04, the stress range has been kept at the same value, and the mean stress has been increased. In that case, the overall number of cycles has been reduced by a factor of 2.

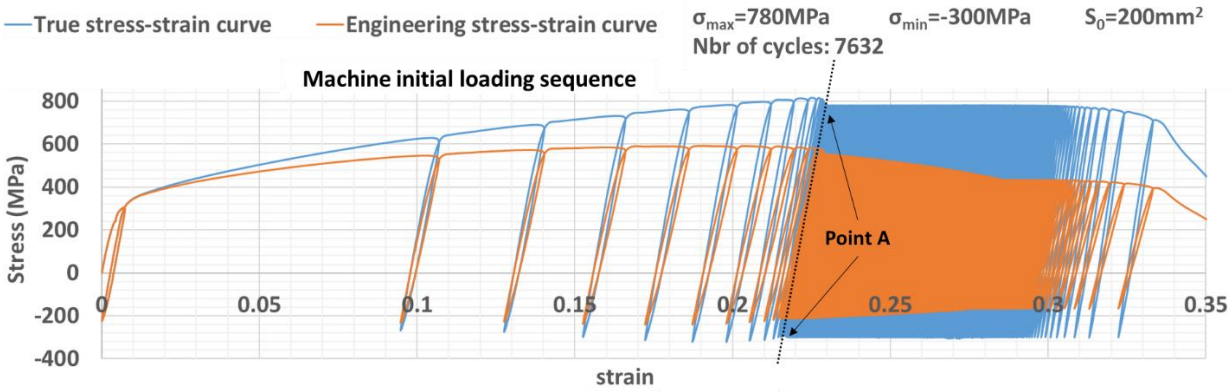

Figure 72 – Results of cyclic test on cylinder 05 with imposed stress loading

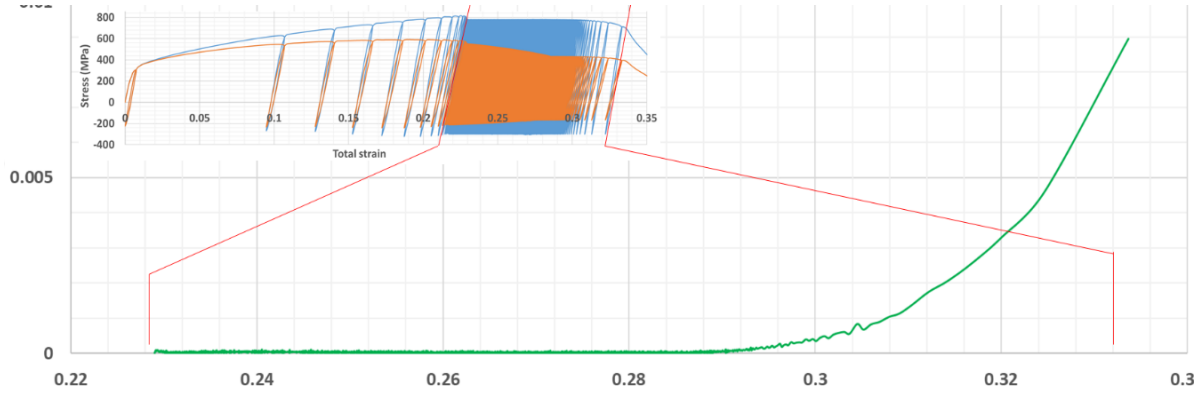

Figure 73 – Ratcheting strain along the strain for cylinder 05

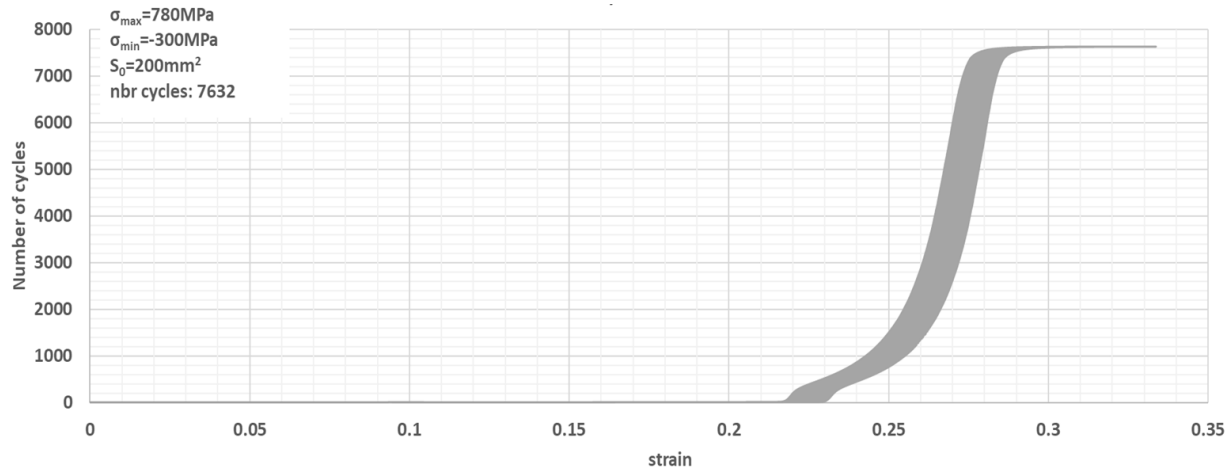

Figure 74 – Cumulative number of cycles along the strain for cylinder 05

2.4.2.3. Stress range decrease with same mean stress (cylinder-06)

The test for cylinder-06, see result in Figure 75, has been realised with cyclic stress load considering σ_{max}=680MPa and σ_{min}=-300MPa. The stress has been imposed following the same sinusoidal evolution as described in eq.(38), where the mean stress σ_{moy}= 490MPa, the stress range $\Delta\sigma$=980MPa and the frequency f=0.3Hz. Failure appears after 10424 cycles.

In comparison to the test performed on cylinder 04, the mean stress has been kept at the same value, and the stress range has been reduced. In that case, the overall number of cycles has been increased.

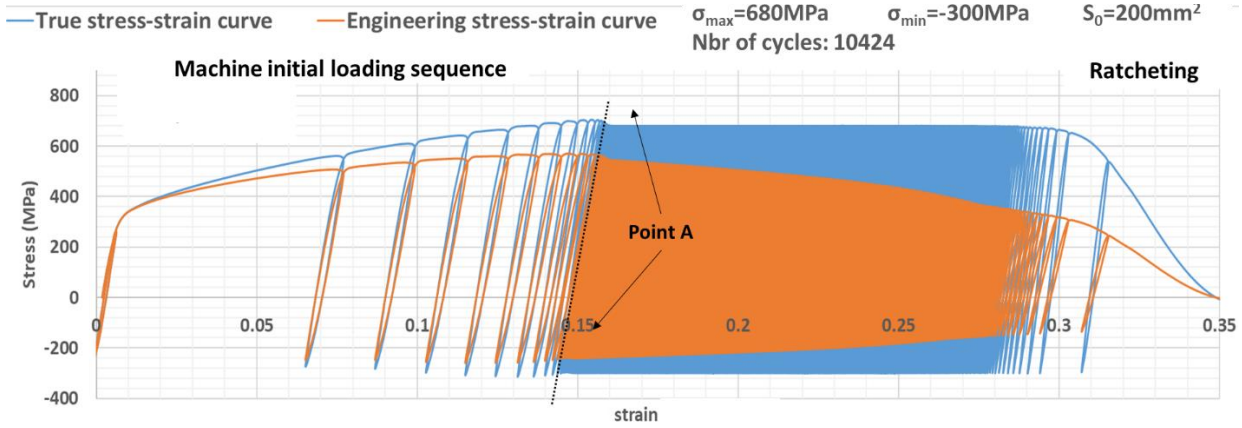

Figure 75 – **Results of cyclic test on cylinder 06 with imposed stress loading**

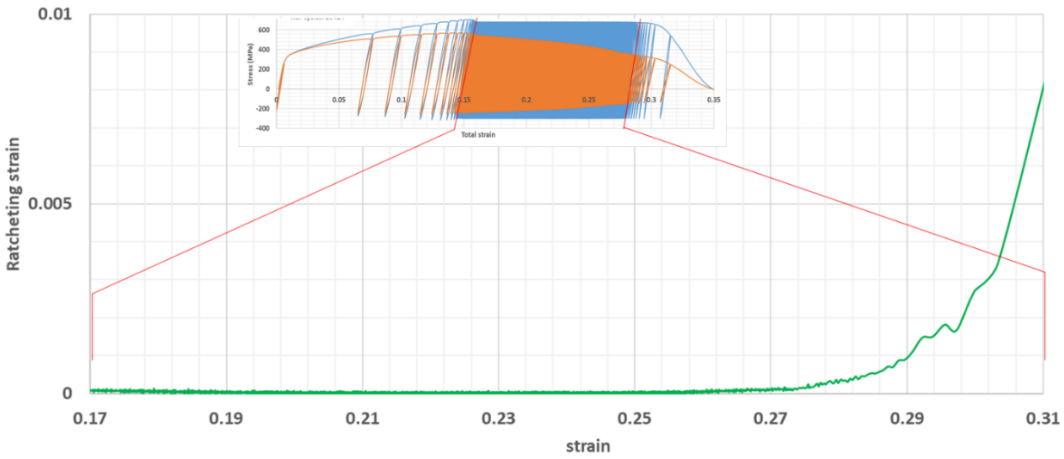

Figure 76 – Ratcheting stain along the strain for cylinder 06

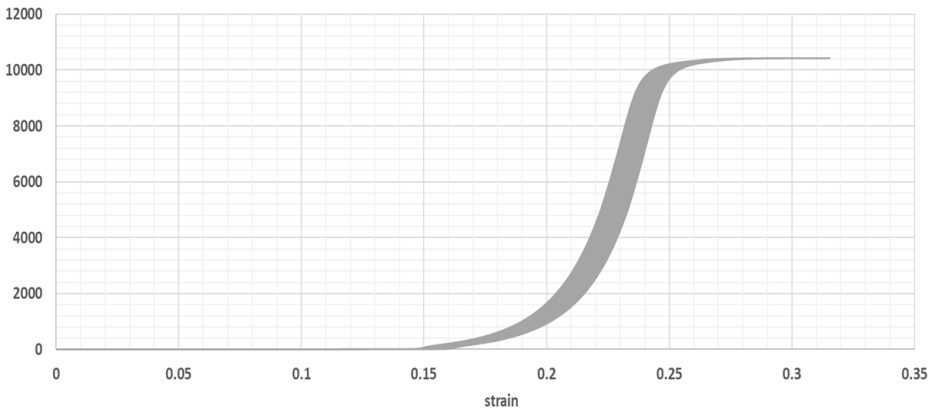

Figure 77 – Evolution of strain amplitude along the strain for cylinder 06

2.4.2.4. Comparison of specimen deformation evolution for different stress ranges and mean stress

Figure 78 reports the three tests results performed in imposed stress where different stress ranges and mean stress have been tested. It represents the cumulative number of cycles along the strain evolution and make it possible to identify ratcheting for the three tests.

The tests have confirmed the effect of the stress range and the mean stress on the ratcheting response, where this failure mode is amplified by a high stress range with high mean stress.

Similar conclusion than imposed force test can be done, where the ratcheting failure mode is amplified by a high stress range with high mean stress.

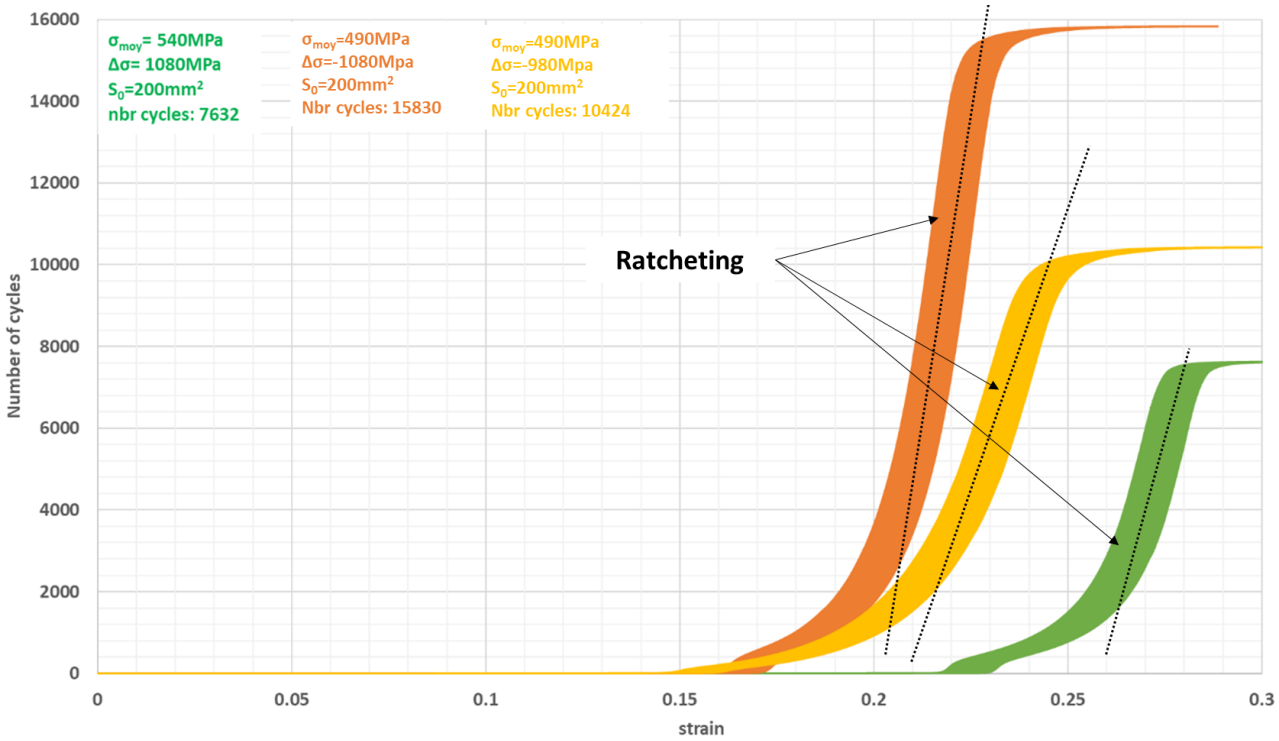

Figure 78 – Strain evolution along the test cycles for different stress ranges and mean stress

2.5. Monotonic torsion test

At the difference of the tensile-compression test, the torsion test does not provide a uniform distribution of the stress. Additionally, the variations of the radius and of the overall length level are very small. In that case, experiment has been performed with no extensometer and the presented results are expressed in torque (in N.m) function of deformation angle (in radians).

The test has been performed in imposed angle rate of 1.7π/360 radians /min including 5 unloading steps every π/9 radians. The angle range of the machine is comprised between -5π/18 radians and 5π/18 radians. In that case, when the limit value is reached, the test is stopped and the position of the machine is reinitialised at -5π/18 radians. Finally the test is restarted.

Figure 79 shows that the specimen undergoes a twist of approximately 4x2π before breaking, which shows that the material is very ductile. The maximum torque reached is 580 N.m.

Figure 80 shows the superposition of the last unloading and reloading sequence before the re-initialisation of the machine. The slight difference between the trends of the two dashed lines can be linked to a small evolution of the specimen's radius.

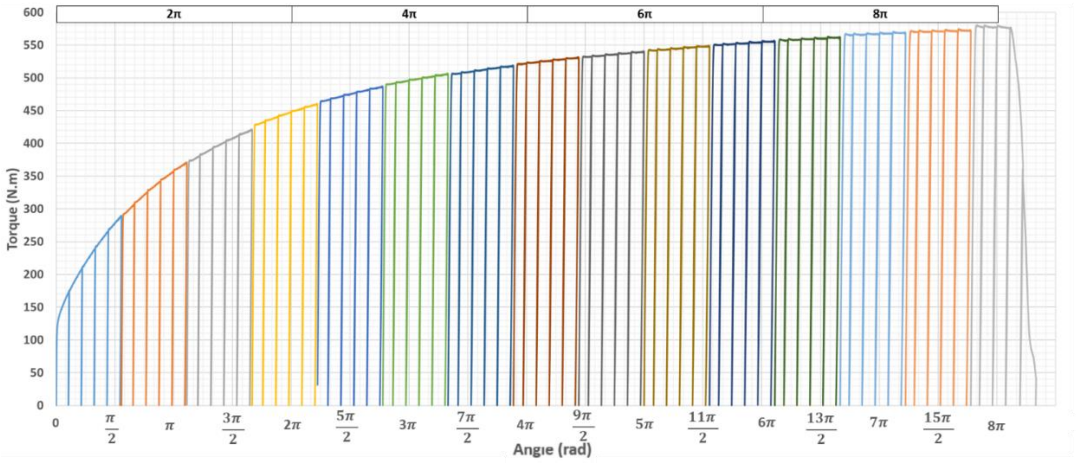

Figure 79 – Results of torsion test on cylinder 12 with imposed angle loading

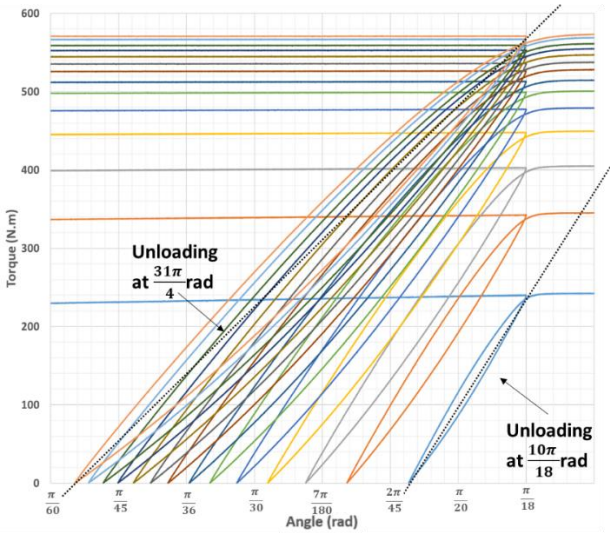

Figure 80 – Results of torsion test on cylinder 12 with imposed angle loading

2.6. Torsion cyclic test results

Similarly to the tension –compression cyclic test, the aim here is to identify the ratcheting phenomena during torsional tests.

The torsion loading generates non uniform distribution of stress where the maximum values occur at the external surface of the cylinder. In that case the first crack occurs in this area. That is why each cyclic test performed during this campaign has been stopped at the apparition of the first detectable surface crack (in the order of mm).

2.6.1. Imposed angle cyclic tests results

2.6.1.1. Identification of angle range for low cycle fatigue: $\alpha_{max}=2\pi/45$ rad, $\alpha_{min}=-\pi/45$ rad (cylinder-07)

The first cyclic torsion test has been performed on the cylinder 07 with imposed angle. In the objective of identifying ratcheting phenomenon, different scenarios have been tested up to reach a low cycle fatigue domain, below 10^4 cycles.

The angle is imposed following the sinusoidal evolution as described in eq.(41), where α_{moy} is the mean angle (in rad), $\Delta\alpha$ is the angle range (in rad) and f=0.3Hz the frequency.

$$\alpha(t) = \alpha_{moy} + \frac{\Delta\alpha}{2}\sin(2\,\pi\,f\,t) \tag{41}$$

$$\alpha_{moy} = \frac{\alpha_{max} + \alpha_{min}}{2} \tag{42}$$

$$\Delta\alpha = \alpha_{max} - \alpha_{min} \tag{43}$$

We remind that for each test, the machine reaches gradually the nominal value, by applying an initial 10 cycles sequence.

Figure 81 illustrates the stabilised responses of the specimen for the three tested configurations. The yellow curve is that obtained for the first cyclic loading, with $\alpha_{max}= \pi/360$ radians, $\alpha_{min}= -\pi/720$ radians (33637 cycles); The blue curved is obtained considering $\alpha_{max}=\pi/90$ radians, $\alpha_{min}=-\pi/180$ radians (23974 cycles); the orange curve is obtained considering $\alpha_{max}=\pi/45$ radians, $\alpha_{min}=-\pi/90$ radians. Since no noticeable evolution has been observed on this third sequence, the test was stopped after 16568 cycles. At his stage, the specimen reached 74179 cycles.

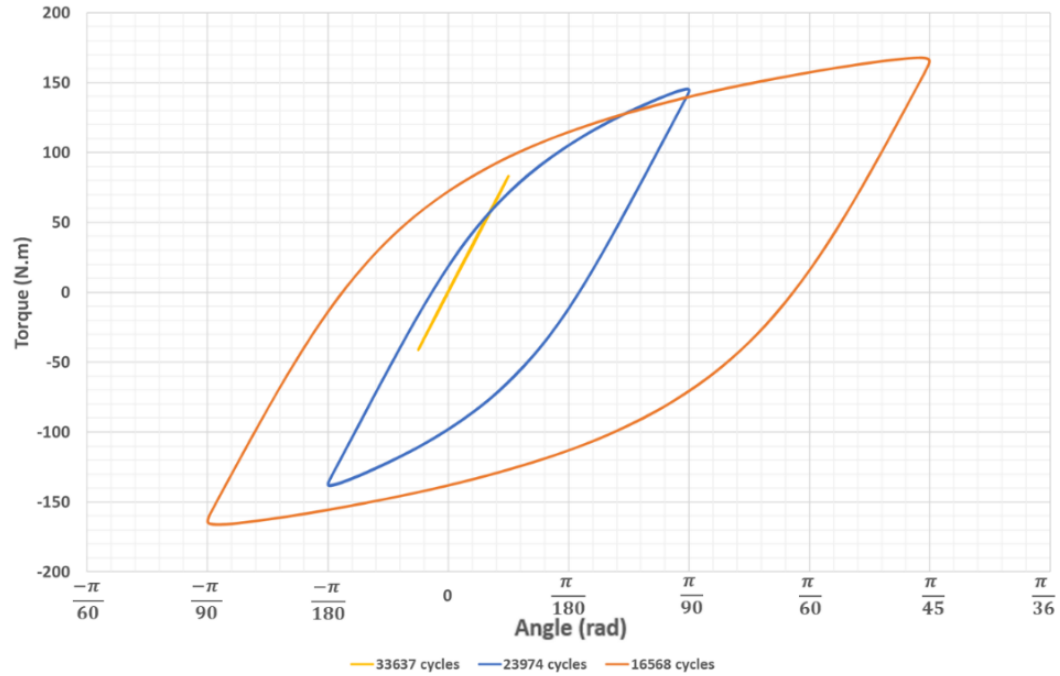

Figure 81 –Results of cyclic test on cylinder 07 with imposed angle loading up to +$\frac{\pi}{45}$/-$\frac{\pi}{90}$ radians

For the last sequence, with $\alpha_{max}=2\pi/45$ radians and $\alpha_{min}=-\pi/45$ radians, the test has been stopped after 3500 cycles, at the apparition of the first visible crack, see plotted results on Figure 82.

For the tension-compression test in imposed displacements (or strain), the ratcheting is traduced by a relaxion of the mean stress.

In the present test result, we can notice in the first cycle a hardening response which can be explained by the non-homogeneous distribution of the stress that requires some cycles to be stabilised. After this point, the hysteresis loop is stabilised and after a certain number of cycles (around 1500 in this case), the reaction torque decreases, which corresponds to a ratcheting failure mode.

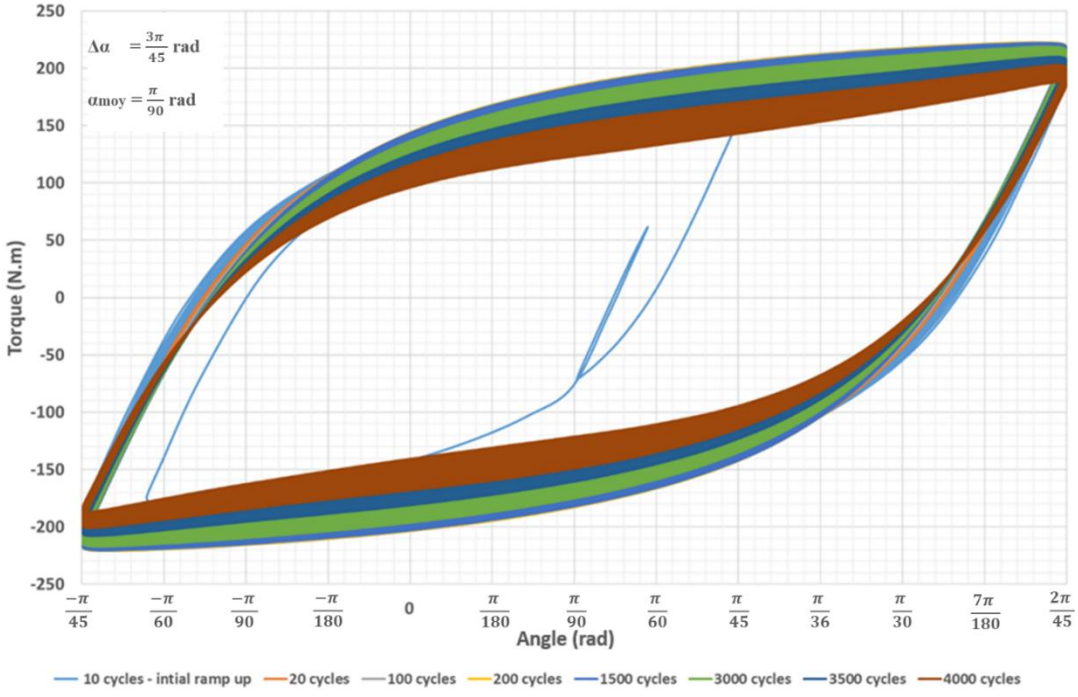

Figure 82 –Results of cyclic test on cylinder 07 with imposed angle loading +$\frac{2\pi}{45}$/-$\frac{\pi}{45}$ radians

Similar to tension-compression tests results, Figure 83 shows the reaction torque evolution along the test cycles for the last two sequences of the test, in which the difference between shakedown and ratcheting can be easily identified.

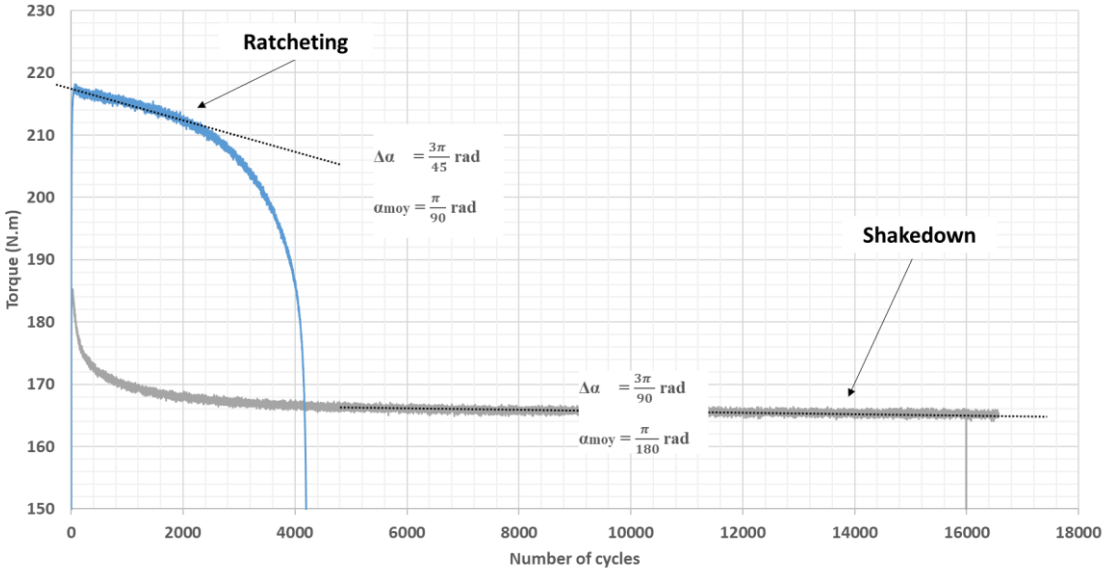

Figure 83 – Reaction torque evolution along the test cycles

2.6.1.2. Decrease of angle range and mean angle (cylinder-08)

For cylinder 08, two sequences achieved such that $\alpha_{max}=\pi/45$ radians, $\alpha_{min}=-\pi/90$ radians during 23126 cycles (first sequence) and $\alpha_{max}=\pi/30$ radians, $\alpha_{min}=-\pi/60$ radians during 6795 cycles (second sequence).

In comparison to the test performed on cylinder 07, the angle range and the mean angle have been decreased. As it can be expected, the overall number of cycles have been increased, see Figure 86.

Figure 84 shows a softening of the material during the first 1500 cycles up to reach a stabilised hysteresis loop already observed with cylinder 07.

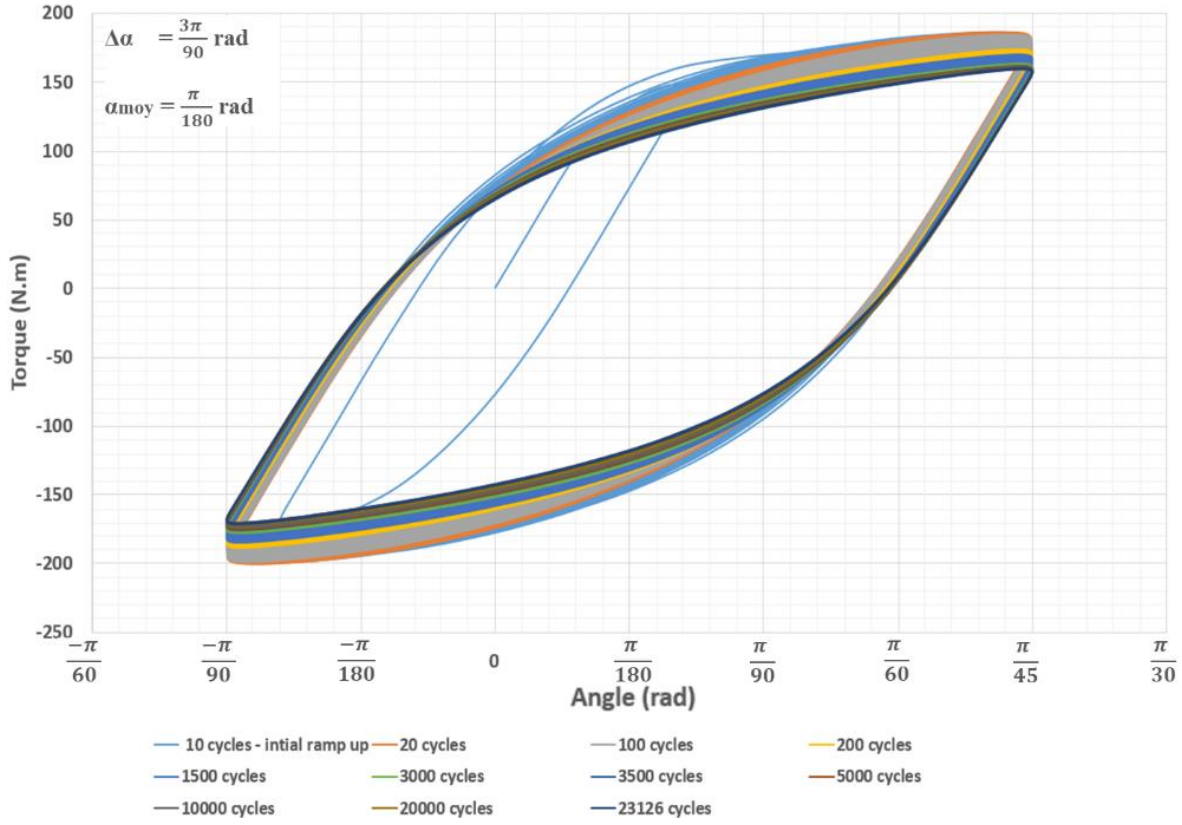

Figure 84 – Results of cyclic test on cylinder 08 with imposed angle loading +$\frac{\pi}{45}$/-$\frac{\pi}{90}$ radians (23126 cycles)

For the second sequence, with $\alpha_{max}= \pi/30$ radians and $\alpha_{min}= -\pi/60$ radians, see Figure 85, the material adopt a hardening response for the first 100 cycles. Then, it adopts a stabilised response up to 3000 cycles, and finally ratchets until the first crack appearance (6000 cycles).

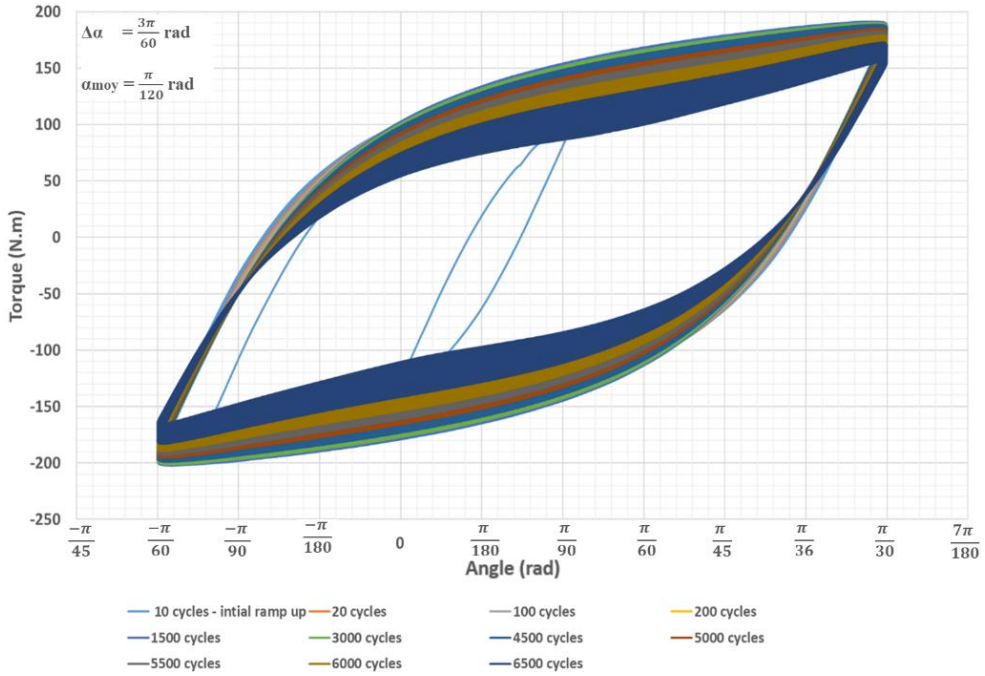

Figure 85 –Results of cyclic test on cylinder 08 with imposed angle loading +$\frac{\pi}{30}$/-$\frac{\pi}{60}$ radians (6500 cycles)

Figure 86 shows that the loading history has an impact on the results (here the reaction torques), see orange and yellow curve, where only for cylinder 07, two load sequences were performed before. However, since the test was stopped before reaching a first crack initiation, the effect on the total number of cycles cannot be verified.

As experimentally observed for tension-compression imposed force test, the failure is amplified by a high angle range with high mean angle.

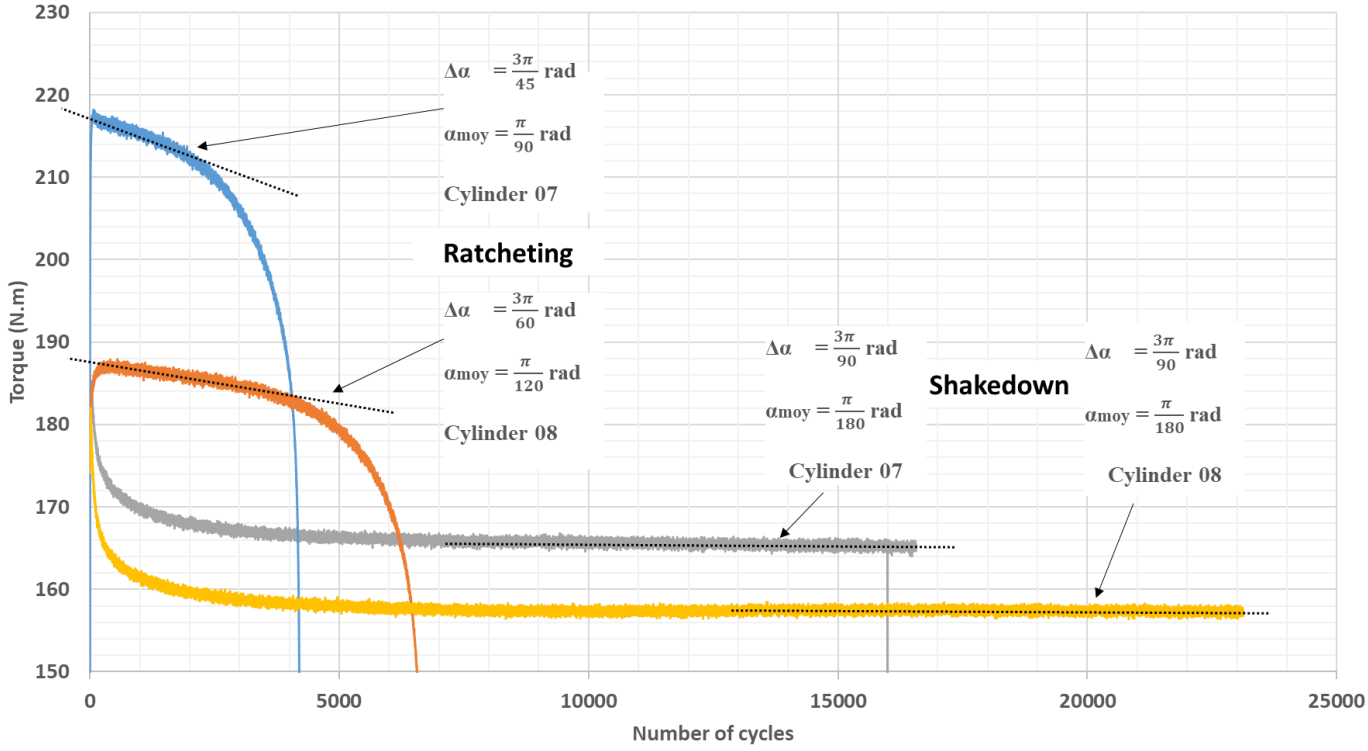

Figure 86 – Reaction torque evolution along the test cycles for different angle ranges and mean angles

2.6.2. Imposed torque cyclic tests results

According to the nuclear codes load decomposition, the torsion test carried out in imposed angle is classified as secondary load and the one carried out in imposed torque as primary load.

2.6.2.1. Identification of torque range for low cycle fatigue: M_{max}=300 N.m, M_{min}=-150 N.m (Cylinder-09)

For this test campaign, the torque has been imposed following the sinusoidal evolution described in eq.(44), where M_{moy} is the mean torque, ΔM is the torque range and f=0.3Hz the frequency.

$$M(t) = M_{moy} + \frac{\Delta M}{2} \sin(2\,\pi\,f\,t) \tag{44}$$

$$M_{moy} = \frac{M_{max} + M_{min}}{2} \tag{45}$$

$$\Delta M = M_{max} - M_{min} \tag{46}$$

Different scenarios have been tested by gradually increasing the torque range up to reaching the ratcheting failure mode. The Figure 87 represents the stabilised responses of the specimen under the five first tested configurations. The clear blue curve is that obtained for the first cyclic loading, with M_{max}=100 N.m and M_{min}=-50 N.m (26632 cycles); the orange curve is that obtained for the second cyclic loading, with M_{max}=150 N.m and M_{min}=-75 N.m (62270 cycles); the yellow curve is that obtained for the third cyclic loading, with M_{max}=160 N.m and M_{min}=-80 N.m, (19481 cycles); the dark blue curve is that obtained for the fourth cyclic loading with M_{max}=180 N.m and M_{min}=-90 N.m (25587 cycles); the green curve is that obtained for the fifth cyclic loading, with M_{max}=220 N.m and M_{min}=-110 N.m. At this stage the specimen reached 139804 cycles.

We can notice from **Figure 87** & **Figure 88** that the specimen is requiring some cycles before reaching stabilised hyteresis mode.

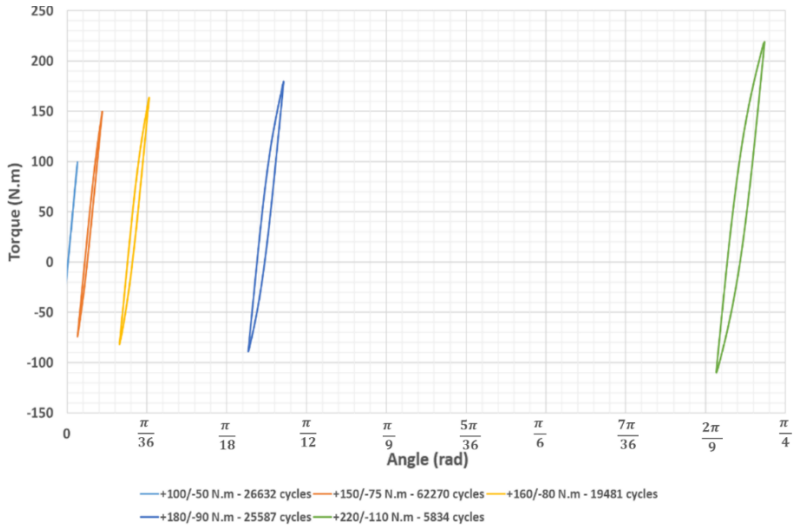

Figure 87 – Results of cyclic test on cylinder 09 with imposed torque loading at different values

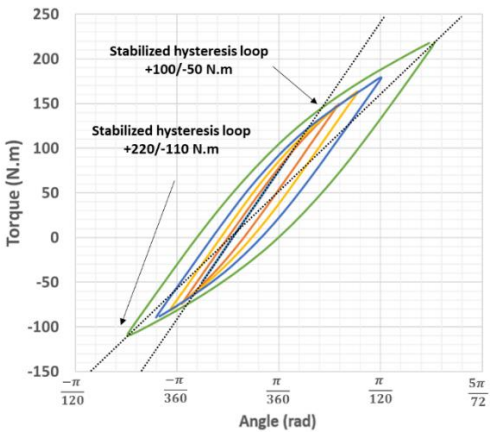

Figure 88 – Stabilised hysteresis loop from results of cyclic test on cylinder 09 with imposed torque loading at different values

The last sequence (sixth) of cylinder-09, see result Figure 89 & Figure 90, has been realised with cyclic torque load considering M_{max}=300 N.m and M_{min}=-150 N.m. The torque was imposed following the same sinusoidal evolution as described in eq.(44), where the mean torque M_{moy}= 75 N.m, the torque range ΔM=450 N.m and the frequency f=0.3Hz. First surface crack appears after 30266 cycles, in addition to the 145638 cycles reached for lower torque amplitude.

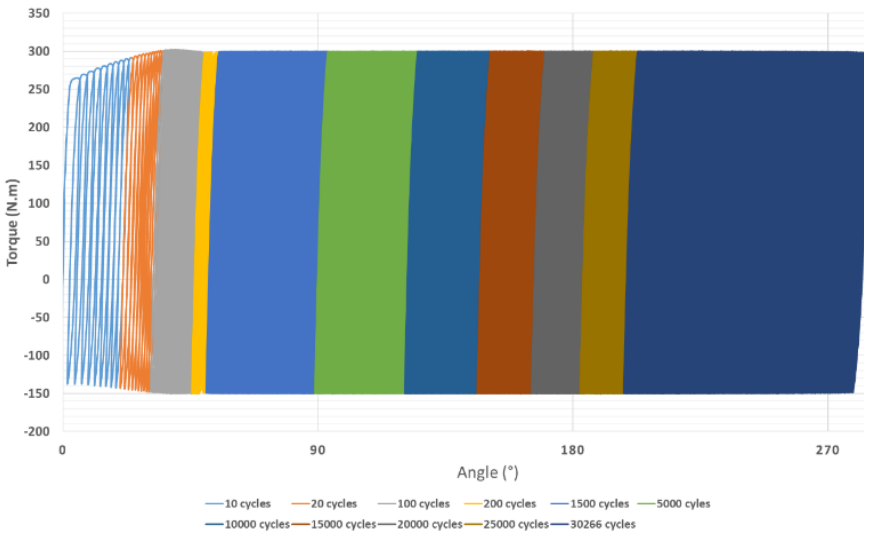

Figure 89 – Results of cyclic test on cylinder 09 with imposed torque loading at +300/-150 N.m

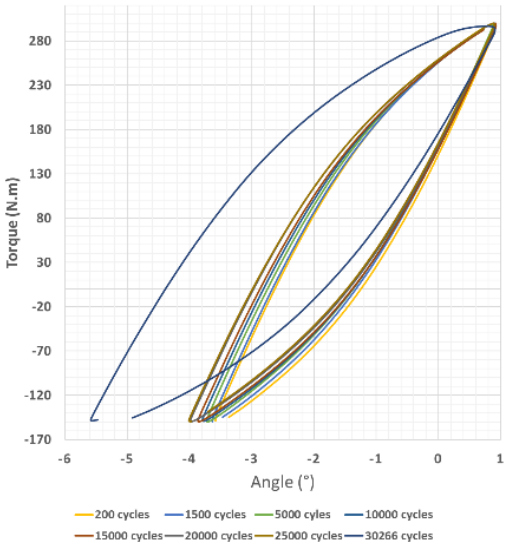

Figure 90 – Stabilised hysteresis loop from imposed loading +300/-150 N.m

Figure 90 shows that the hysteresis loop area increases along the test, suggesting that internal phenomena are occurring, including ratcheting.

At the end of the test, the angle exceeded 3π/2 radians, which confirms the ductility of the material. Figure 91 shows the angle evolution along the cumulative cycles, which has a shape similar to that of the tension-compression tests, see Figure 62.

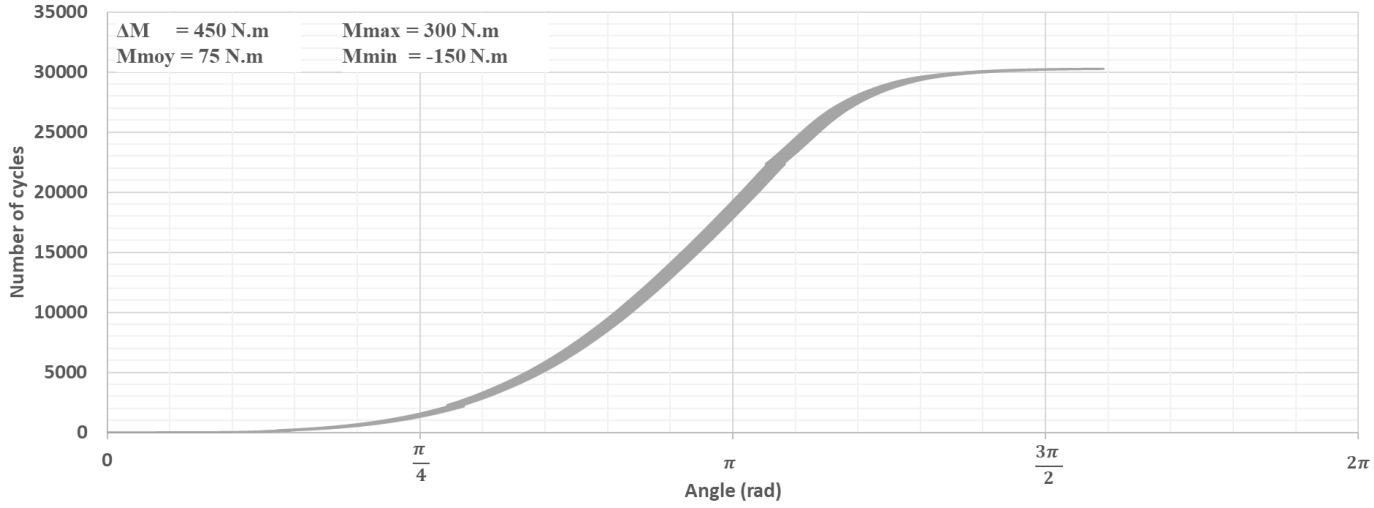

Figure 91 – Angle evolution along the cumulative cycles for cylinder 09 (350/-150 N.m)

2.6.2.2. Torque range increase with same mean torque (cylinder-10)

The test for the sequence of cylinder-10, see result in Figure 92 & Figure 93, has been realised with cyclic torque load considering M_{max}=350 N.m and M_{min}=-200 N.m. The torque was imposed following the same sinusoidal evolution as described in eq.(44), where the mean torque M_{moy}= 75 N.m, the torque range ΔM=550 N.m and the frequency f=0.3Hz. First surface crack appears after 30266 cycles when the specimen has made more than 3 turns, see Figure 94.

In comparison to the test performed on cylinder 09, the mean torque has been kept at the same value, and the torque range has been increased. In that case, the overall number of cycles decreased.

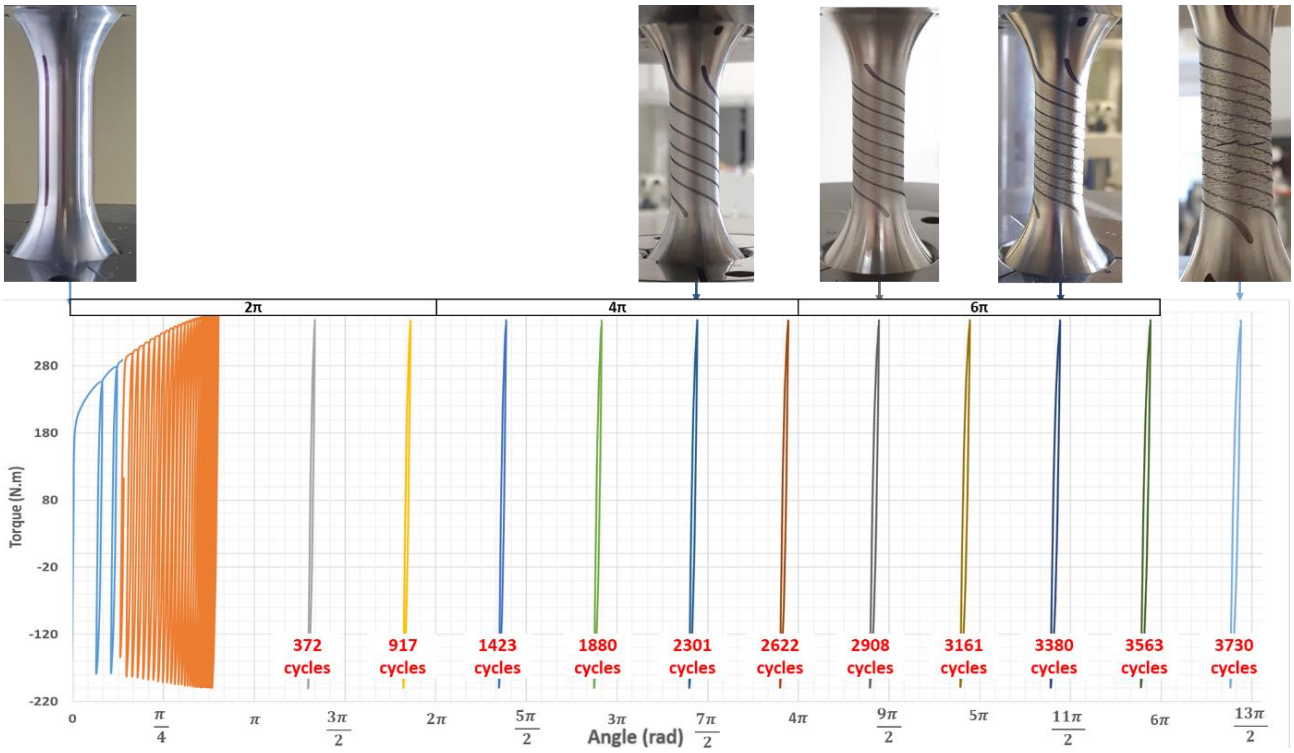

Figure 92 – Results of cyclic test on cylinder 10 with imposed torque loading at (350/-200 N.m)

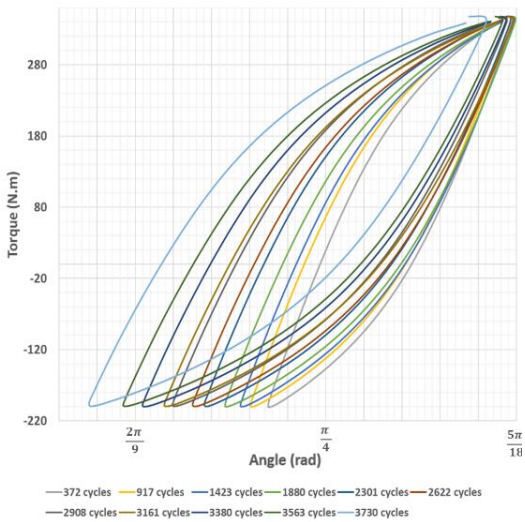

Figure 93 –Cylinder 10 hysteresis loop relative to the number of cycles

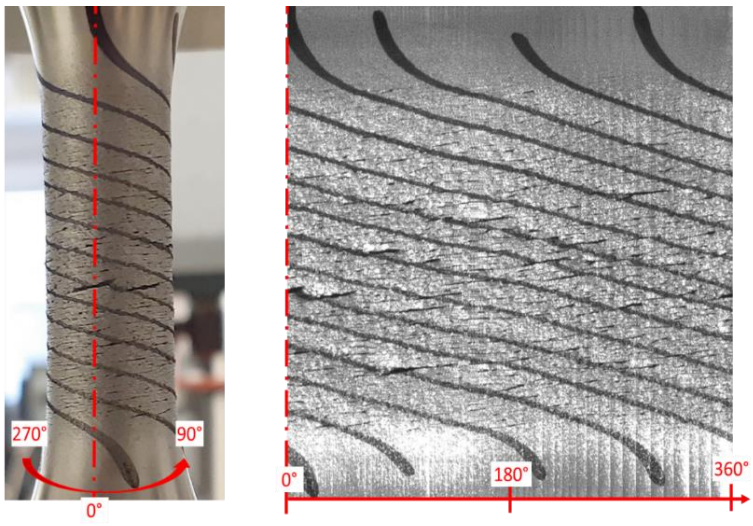

Figure 94 –Cylinder 10 after 3730 cycles

Due to the large deformation angle associated to the applied torque range, the test had to be stopped and restarted every ±5π/18 radians. In addition, the machine gradually reaches the nominal value, by applying an initial 10 cycles for each new sequence. In that case, Figure 95, which represents the evolution of the angle along the cumulative cycles, does not have a smooth shape. However, a shape similar to the one already observed can be recognised, which justifies ratcheting.

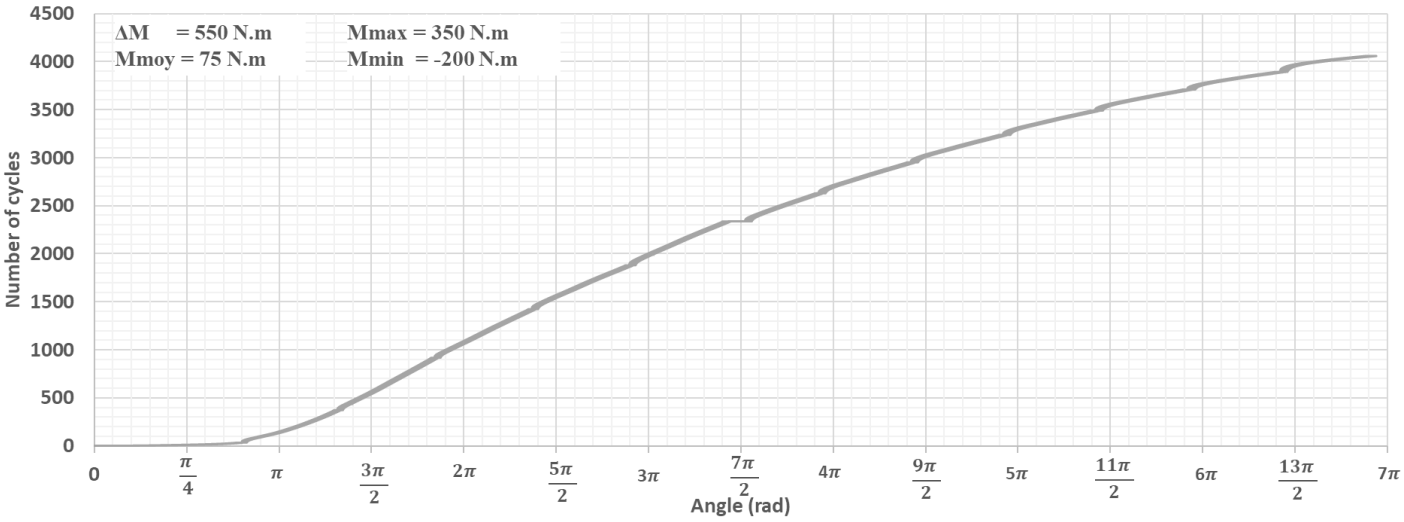

Figure 95 – Angle evolution along the cumulative cycles for cylinder 10 (350/-200 N.m

2.6.2.3. Mean torque increase with same torque range (cylinder-11)

The test for the sequence of cylinder-11, see result in Figure 96 & Figure 97, has been realised with cyclic torque load considering M_{max}=315 N.m and M_{min}=-135 N.m. The torque was imposed following the same sinusoidal evolution as described in eq.(44), where the mean torque M_{moy}= 90 N.m, the torque range ΔM=450 N.m and the frequency f=0.3Hz. First surface crack appears after 42183 cycles, see Figure 98.

In comparison to the test performed on cylinder 09, the torque range has been kept at the same value, and the mean torque has been decreased. In that case, the overall number of cycles decreased.

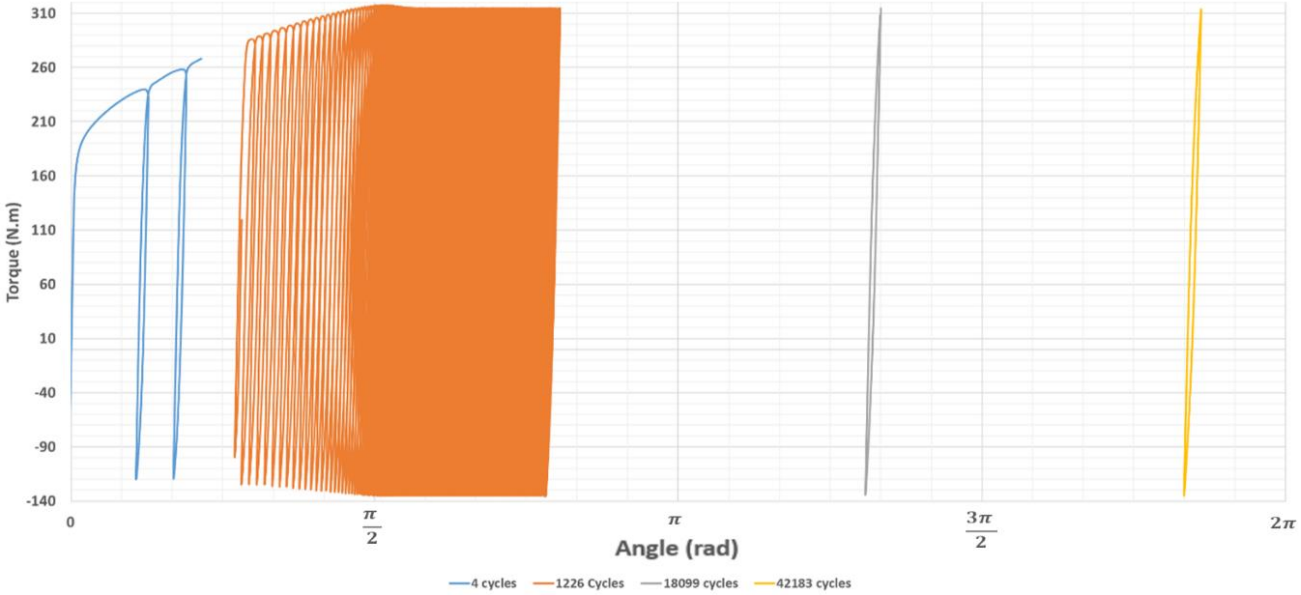

Figure 96 – Imposed torque cylinder 11

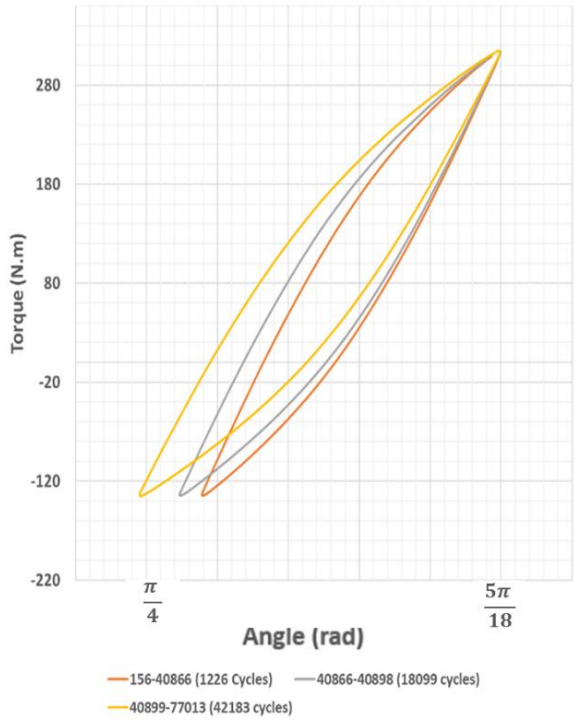

Figure 97 – Cylinder 11 hysteresis loops relative to the number of cycles

Figure 98 – Cylinder 11 after 42183 cycles

Figure 99 shows the angle evolution along the cumulative cycles.

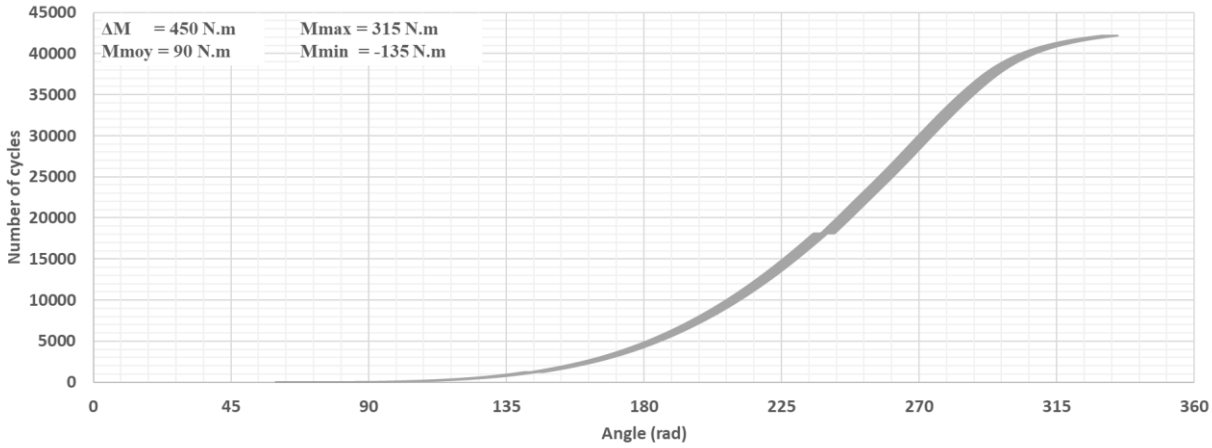

Figure 99 – Angle evolution along the cumulative cycles for cylinder 11 (315/-135 N.m)

2.6.2.4. Comparison of specimen deformation evolution torque ranges and mean torques

Figure 100 reports the three tests results performed in imposed torque where different torque ranges and mean torque have been tested. It represents the angle evolution along the cumulative cycles and make it possible to identify ratcheting for the three tests.

The tests have confirmed the effect of the stress range and the mean stress on the ratcheting response, where this failure mode is amplified by a high stress range with high mean stress.

A similar response can be observed for tension-compression tests.

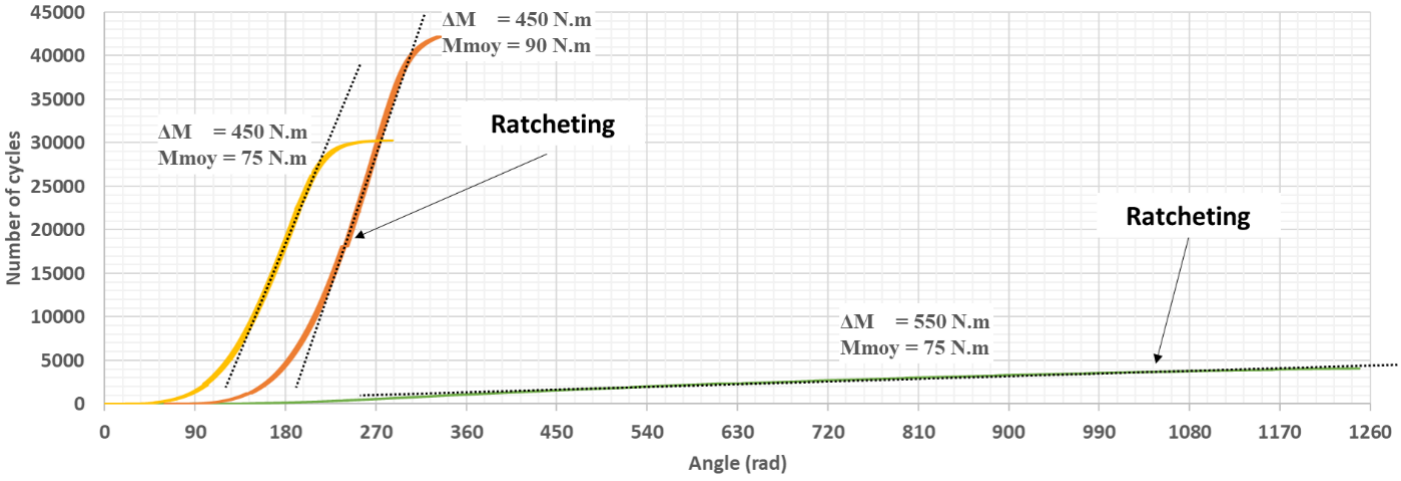

Figure 100 –Angle evolution along the test cycles for different torque ranges and mean torques

2.7. Conclusion

The results of monotonic tests confirm the isotropy of the material and show few viscosity response. Additionally, the comparison made between a tensile test with unloading sequence and purely monotonic one shows that the history of load have an impact on the ultimate strength.

The tension-compression tests, performed under imposed stress and imposed force show a similar behaviour of the material. First of all, at each cycle of the test, we can notice a strain evolution, also for stabilised hysteresis where ratcheting strain ($\delta\varepsilon$), is close to 10^{-5}. Additionally for specimen that have reached ratcheting failure mode, we can notice an exponential evolution of this strain range which occur during the last 20 cycles.

Finally, the tests have confirmed the effect of the stress range and the mean stress on the ratcheting response, where this failure mode is amplified by a high stress range with high mean stress.

The monotonic test shows that the total elongation can reach 50% of strain at low velocity, what was confirmed by the monotonic torsion test results for which a twist of approximately $4x2\pi$ was necessary before the specimen breaks.

For the cyclic torsion test performed with imposed angle, we can notice in the first cycle a hardening response which can be explained by the non-homogeneous distribution of the stress that requires some cycles to be stabilised. After this point the hysteresis loop is stabilised and after a certain number of cycles, the material starts to soften up to crack initiation on the surface.

Concerning the imposed torque test, similar responses than the tension-compression test have been observed where the “strain” is increasing at each cycle up to an increase of the strain range evolution leading to ratcheting failure mode. Also, for the torsional tests, we have compared test at different torque amplitude and mean torque giving the same conclusion than for the tension compression test.

It can be noticed that the mechanical test results presented in this chapter should have been carried out under vacuum conditions, considering minimised radiation heat exchange with appropriate temperature monitoring, to observe the temperature evolution during the work hardening.

Chapter 3. Thermomechanical model

3.1. Introduction

Our objective is to develop a model reliable enough for determining if a structure adopts or not a stabilised response under cyclic loading. In the purpose of industrial use, this model has to be simple regarding its development and material parameter identification.

Knowing the large amount of experiments and modelling performed on austenistic stainless steels, we propose a model development based on the superposition of several hardening functions to represent the following hardening behaviours: Bauschinger effect, cyclic softening and hardening, shakedown (elastic and/or plastic), and the ratcheting.

Considering the experimental results, we propose to take into account in our development the ductile fracture mechanism resulting of the formation, growth and coalescence of microcavities (micropores). In that case, our model is based on the general framework of continuum damage mechanics for which the ductile fracture results from the competition between hardening and damage.

The stress decomposition made by the nuclear codes implies to study the behaviour of a structure under cyclic loading where the secondary stress (generally induced by thermal loads) is dominant in comparison to other loads. We propose to solve the problem through a strong thermomechanical coupling that requires to solve the heat equation (related to the considered model) together with the balance of linear momentum.

In a few words, the Chaboche's models available in the literature (elasto-(visco)-plasticity models, with various types of hardening coupled with damage) have been enriched in order to explicitly take into account the influence of the temperature on the mechanical behaviour and, reciprocally, the influence of the mechanical behaviour on the temperature.

3.2. Thermomechanical model: state variables & constitutive equations

Although the strain levels recorded during the experimental tests exceed 50%, the hypothesis of infinitesimal strains is retained. According to nuclear design rules, it is excluded that the VV structural material undergoes large deformations, which are not required for plastic shakedown and ratcheting. The stress and strain fields in the VV under normal operation conditions are heterogeneous, and this heterogeneity may be sufficient to trigger these phenomena, even though the deformations remain, globally, well below 50%.

3.2.1. State variables & state potentials

The two basic state variables that should necessarily be considered when dealing with thermomechanical problems are the absolute temperature $T \in R^+$ (in K) and, in the cases where the deformations of the material remain "small", the infinitesimal strain tensor $\boldsymbol{\varepsilon}$ (unitless).

Additionally, for representing the basic hardening mechanisms occurring on austenistic stainless steel under cyclic loading, which are Bauschinger effect, cyclic softening and hardening, and shakedown (elastic and/or plastic), the following internal variables are used for this study:

- plastic strain tensor $\boldsymbol{\varepsilon}^p$ (unitless),
- isotropic hardening variable $p \geq 0$ (unitless).

The different previous studies showed the benefit of superposing several nonlinear kinematic hardening variables (Chaboche, et al., 1989) (Chaboche, et al., 1989), that is why we choose to include in the present model several kinematic hardening tensors $\mathbf{X_i}$ (unitless).

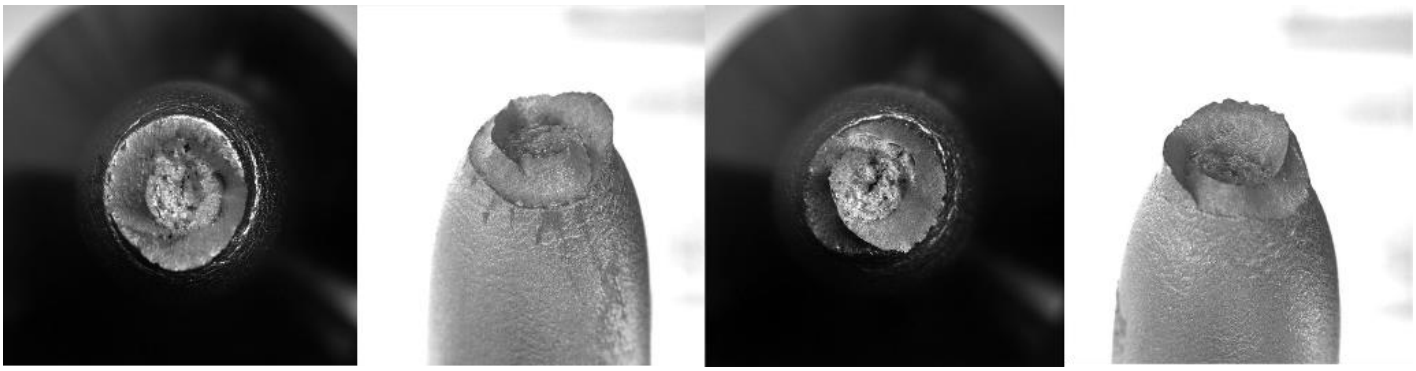

Figure 101 – Macroscopic views of the cylinder 02 after fracture showing a ductile fracture on the periphery

Finally, for modelling the ductile fracture, see Figure 101, in the framework of continuum damage mechanics, the last internal variable that is considered is the damage variable $d \in [0,1]$ (unitless) (Lemaitre, 1985).

We also assume that the plastic flow is incompressible, therefore $Tr(\boldsymbol{\varepsilon}^{\mathbf{p}})=0$ and $Tr(\mathbf{X_i})=0$.

Helmholtz free energy density Ψ (in J/kg) is taken as thermodynamic potential, corresponding to a function of all state variables. We assume the following expression for the development of the constitutive model:

$$\begin{aligned}\Psi(T,\boldsymbol{\varepsilon},\boldsymbol{\varepsilon^p},\boldsymbol{X_i},\mathrm{p},\mathrm{d}) = \\ +\frac{1}{2\rho_0}\lambda\left(Tr(\boldsymbol{\varepsilon}-\boldsymbol{\varepsilon^p})\right)^2+\frac{1}{\rho_0}\mu(\boldsymbol{\varepsilon}-\boldsymbol{\varepsilon^p}):(\boldsymbol{\varepsilon}-\boldsymbol{\varepsilon^p}) \\ -\frac{1}{\rho_0}(3\lambda+2\mu)\gamma Tr(\boldsymbol{\varepsilon}-\boldsymbol{\varepsilon^p})(T-T_0) \\ -\frac{\mathrm{C}_\varepsilon(T-T_0)^2}{2T_0} \\ +\frac{1}{\rho_0}k(1-d)\left(p+\frac{1}{m}e^{-mp}\right) \\ +\frac{1}{2\rho_0}\sum_{i=1}^{N_{kh}}M_i\,\boldsymbol{X_i}:\boldsymbol{X_i}\end{aligned} \tag{47}$$

where ρ_0 (in kg.m^{-3}) is the initial density, T_0 is the initial temperature and Tr(.) is the trace operator. λ, μ, γ, C_ε, M_i, k and m are material parameters (temperature dependent), which should be identified from experimental results, such as monotonic and cyclic tests results.

The first part of the free energy represents the mechanical part of the linear elastic deformation which includes the material parameters λ (in Pa) and μ (in Pa), first and second Lamé coefficients.

$$\rho_0\bar{\Psi}^1_{\varepsilon^e}(\boldsymbol{\varepsilon},\boldsymbol{\varepsilon^p})=\frac{\lambda}{2}\left(Tr(\boldsymbol{\varepsilon}-\boldsymbol{\varepsilon^p})\right)^2+\mu Tr\left((\boldsymbol{\varepsilon}-\boldsymbol{\varepsilon^p}).(\boldsymbol{\varepsilon}-\boldsymbol{\varepsilon^p})\right) \tag{48}$$

Obviously, plastic strain $\boldsymbol{\varepsilon}^{\mathbf{p}}$, elastic strain $\boldsymbol{\varepsilon}^{\mathbf{e}}$ (unitless) and total strain $\boldsymbol{\varepsilon}$ are linked via the following equation:

$$\boldsymbol{\varepsilon}=\boldsymbol{\varepsilon}^{\boldsymbol{e}}+\boldsymbol{\varepsilon}^{\boldsymbol{p}} \tag{49}$$

The second part of the free energy represents the thermoelastic part where γ (in K^{-1}) is the thermal expansion parameter:

$$\rho_0\bar{\Psi}^2_{\varepsilon^e}(\boldsymbol{\varepsilon},\boldsymbol{\varepsilon}^{\mathbf{p}},\mathrm{T})=-(3\lambda+2\mu)\gamma\mathrm{Tr}(\boldsymbol{\varepsilon}-\boldsymbol{\varepsilon}^{\mathbf{p}})(\mathrm{T}-\mathrm{T}_0) \tag{50}$$

The purely thermal effects are obviously taken into account in the model, via the third part of the free energy, including the heat capacity C_ε at constant volume (in J/kg.K):

$$\bar{\Psi}_T(T)=-\frac{\mathrm{C}_\varepsilon(T-T_0)^2}{2T_0} \tag{51}$$

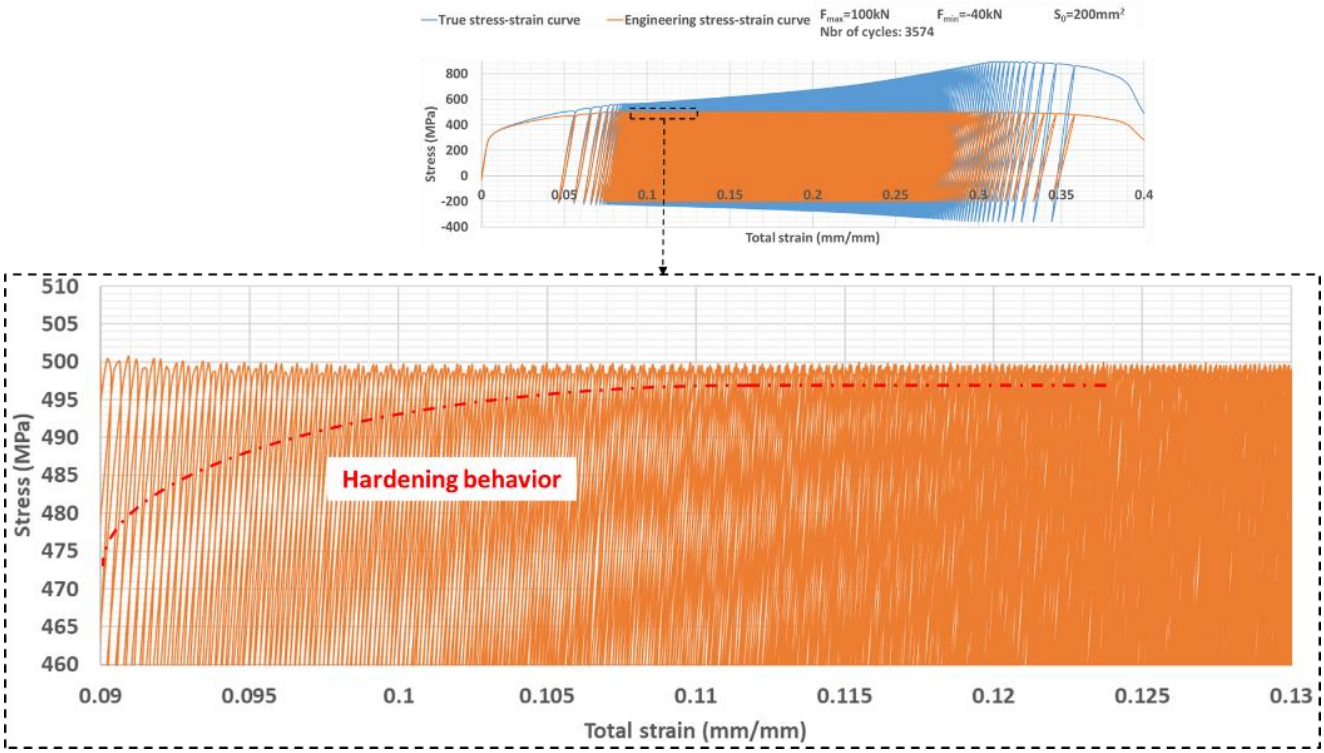

Figure 102 – Engineering stress strain curve showing the hardening of the material extracted from imposed cyclic force loading test performed on cylinder 02 (see Ch.II, §4.1.2)

It has been observed from the cyclic tension-compression tests that the material exhibits a hardening behaviour with a logarithmic trend, see Figure 102. We propose a non-linear expression of the isotropic hardening (Nouailhas, 1988), where m (unitless) and k (in Pa) are two characteristic coefficients of the material. For an undamaged material, the expression of the free energy representing the isotropic hardening can be defined as:

$$\rho_0 \overline{\Psi}_p(p) = k\left(p + \frac{1}{m}e^{-mp}\right) \tag{52}$$

The modelling of ductile fracture in the framework of continuum damage mechanics is resulting from the competition between hardening and damage. The damage variable is based on the concept that ductile fracture results from the formation, growth and coalescence of cavities, see Figure 103 (Rousselier, 1987). Despite the complexity of this damage mechanism, the chosen hypothesis assumes only one single type of cavity with isotropic evolution.

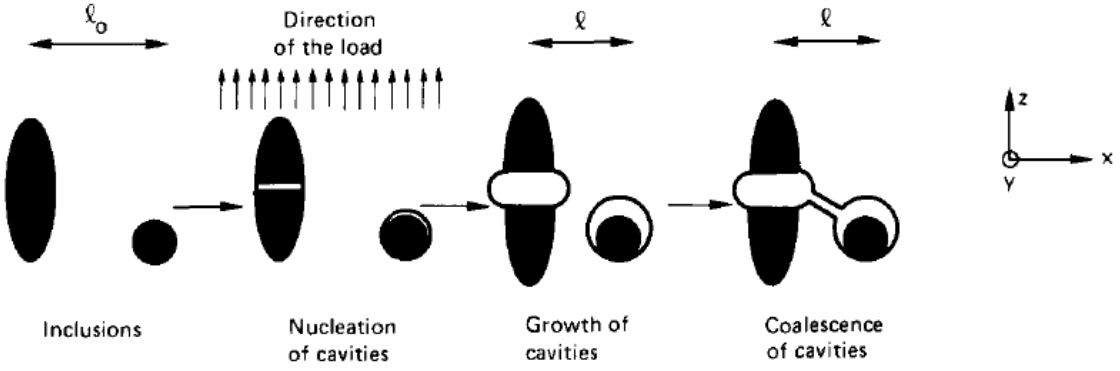

Figure 103 – Ductile crack growth at micro scale (Rousselier, 1987).

On the assumption that this phenomenon is isotropic, the volume ratio of these microcracks and microcavities can be represented by a scalar variable d, where d=0 in the undamaged state and d=1 when the exhaustion of ductility is reached (Rousselier, 1987). Figure 104 illustrates an example of the damage variable evolution (Lemaitre, 1985).

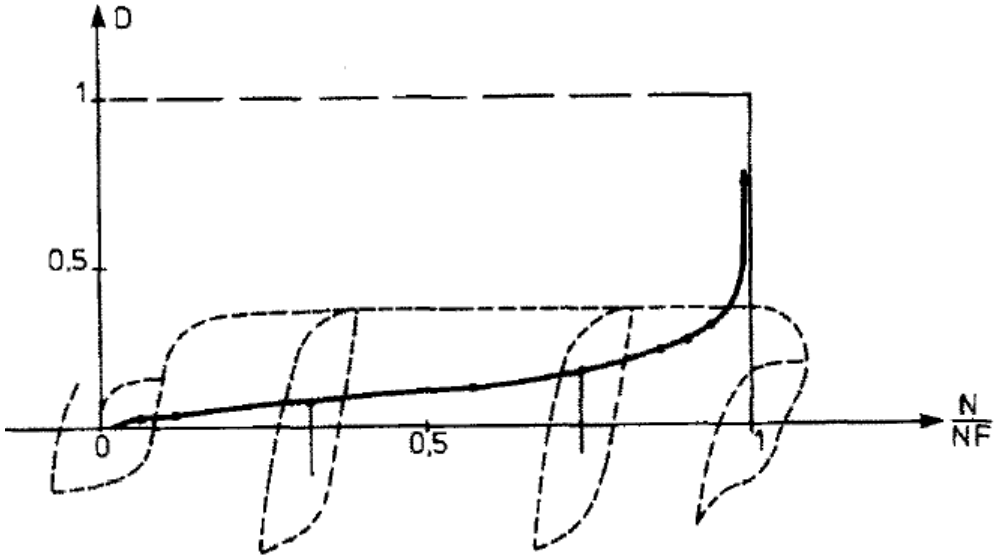

Figure 104 –Example of the damage variable evolution (Lemaitre, 1985)

For a damaged material, a competition is assumed to exist between plasticity (tendency to harden) and damage (tendency to soften). Consequently, eq.(52) is modified in the following way:

$$\rho_0 \overline{\Psi}_p(p,d) = (1-d)k\left(p + \frac{1}{m}e^{-mp}\right) \tag{53}$$

The kinematic hardening represents the non-homogeneous plastic deformation linked to the characteristic coefficient of the material M_i (in Pa). The kinematic hardening is commonly represented by summing several tensorial variables X_i (where N_{kh}=2 or 3 in most cases) aiming at smoothing the plastic behaviour in order to obtain a better agreement with experiments. The superposition of kinematic variables is made by summing the different terms as follows, which is the fifth part of the free energy (Nouailhas, 1988):

$$\rho_0 \overline{\Psi}_{\boldsymbol{X}}(\boldsymbol{X_i}) = \frac{1}{2}\sum_{i=1}^{N_{kh}} M_i \, \boldsymbol{X_i}\!:\boldsymbol{X_i} \tag{54}$$

3.2.2. Intrinsic dissipation

The first law of the thermodynamics first postulates that an internal energy, e, can be defined for all thermodynamics systems and, secondly, that the variation of this internal energy is ever equal to that of energy supplied to the system as heat (thermal part) and work (mechanical part). Furthermore, the definition of the free energy allows to relate the internal energy and the entropy, s:

$$\Psi = e - Ts \tag{55}$$

Inserting the previous relation in the energy conservation, the first principle takes the following local form:

$$\rho_0 T\dot{s} + div(\boldsymbol{q}) - r^v = \boldsymbol{\sigma}:\dot{\boldsymbol{\varepsilon}} - \rho_0\dot{\Psi} - \rho_0 s\dot{T} \tag{56}$$

where s is the entropy density (J/kg.K), $\boldsymbol{q}$ is the the surface heat fluxes (W/m^2), and r^v is the external heat source (W/m^3).

The second law of thermodynamics states that the variation of the entropy is ever greater or equal to that of the surroundings of the system. In continuum thermodynamics, it reads (local version at a material point):

$$\rho\dot{s} + div\left(\frac{\boldsymbol{q}}{T}\right) - \frac{r^v}{T} \geq 0 \tag{57}$$

Combining the first and the second thermodynamics principle, one can express the Clausius-Duhem inequality which can be interpreted as the sum of the thermal dissipation (heat conduction) and the intrinsic dissipation, which are both assumed positive or null. The expression of intrinsic dissipation $\emptyset_{int}$ (W/m^3) is function of the expression of the free energy derivative, expressed as (see (Coleman, et al., 1967)):

$$\emptyset_{\boldsymbol{int}} = \left(\boldsymbol{\sigma} - \rho_0\frac{\partial\Psi}{\partial\boldsymbol{\varepsilon}}\right):\dot{\boldsymbol{\varepsilon}} - \rho_0\left(s + \frac{\partial\Psi}{\partial T}\right)\dot{T} - \rho_0\frac{\partial\Psi}{\partial\boldsymbol{\alpha}}.\dot{\boldsymbol{\alpha}} \geq 0 \tag{58}$$

where $\boldsymbol{\alpha}$ is a synthetic representation of the set of internal variables (p, d, $\boldsymbol{\varepsilon^p}$ and $\mathbf{X}_i$, in the present study).

The thermal dissipation is defined from:

$$\emptyset_{\boldsymbol{therm}} = \left(-\frac{\mathbf{grad}\,T}{T}\right).\mathbf{q} \geq 0 \tag{59}$$

In the present case, the partial derivative of Ψ, with respect to the internal variables, can be developed as:

$$\rho_0\frac{\partial\Psi}{\partial\boldsymbol{\alpha}}:\dot{\boldsymbol{\alpha}} = \rho_0\frac{\partial\Psi}{\partial p}\dot{p} + \rho_0\frac{\partial\Psi}{\partial d}\dot{d} + \rho_0\frac{\partial\Psi}{\partial\boldsymbol{\varepsilon^p}}:\dot{\boldsymbol{\varepsilon}}^{\boldsymbol{p}} + \rho_0\sum_{i=1}^{N_{kh}}\frac{\partial\Psi}{\partial\boldsymbol{X}_i}:\dot{\boldsymbol{X}}_i \tag{60}$$

Due to the fact that the entropy density is a state function and as we consider that irreversible phenomena are due only to the evolution of the internal variables or to heat conduction, a first condition for the non negativity of the intrinsic dissipation, see eq.(58) is:

$$s = -\frac{\partial \Psi(\mathrm{T}, \boldsymbol{\varepsilon}, \boldsymbol{\alpha})}{\partial T} \tag{61}$$

With a similar reasoning as for the entropy, and assuming that there are no supplementary irreversible phenomena due to the evolution of the strain, the stress tensor $\boldsymbol{\sigma}$ can be written as follows:

$$\boldsymbol{\sigma} = \rho_0 \frac{\partial \Psi(\mathrm{T}, \boldsymbol{\varepsilon}, \boldsymbol{\alpha})}{\partial \boldsymbol{\varepsilon}} \tag{62}$$

Consequently, the expression of the intrinsic dissipation is:

$$\emptyset_{\boldsymbol{int}} = \rho_0 \frac{\partial \Psi}{\partial p}\dot{p} + \rho_0 \frac{\partial \Psi}{\partial d}\dot{d} + \rho_0 \frac{\partial \Psi}{\partial \boldsymbol{\varepsilon^p}} : \dot{\boldsymbol{\varepsilon}}^{\boldsymbol{p}} + \rho_0 \sum_{i=1}^{N_{kh}} \frac{\partial \Psi}{\partial \boldsymbol{X}_\mathrm{i}} : \dot{\boldsymbol{X}}_\mathrm{i} \geq 0 \tag{63}$$

According to the definition of the entropy density described in eq.(61) and considering the fact that all material parameters can be temperature dependent, the partial derivative of Ψ, with respect to the temperature T, appears as:

$$\begin{gathered} s = -\frac{\partial \Psi}{\partial T} = \\ \frac{1}{2\rho_0}\left(Tr(\boldsymbol{\varepsilon} - \boldsymbol{\varepsilon^p})\right)^2 \frac{\partial \lambda}{\partial T} - \frac{1}{\rho_0}\left((\boldsymbol{\varepsilon} - \boldsymbol{\varepsilon^p}) : (\boldsymbol{\varepsilon} - \boldsymbol{\varepsilon^p})\right)\frac{\partial \mu}{\partial T} \\ + \frac{1}{\rho_0}(3\lambda + 2\mu)\gamma Tr(\boldsymbol{\varepsilon} - \boldsymbol{\varepsilon^p}) + \frac{1}{\rho_0}(3\lambda + 2\mu)Tr\left((\boldsymbol{\varepsilon} - \boldsymbol{\varepsilon^p})\right)(T - T_0)\frac{\partial \gamma}{\partial T} \\ + \frac{1}{\rho_0}\left(3\frac{\partial \lambda}{\partial T} + 2\frac{\partial \mu}{\partial T}\right)\gamma(T)Tr(\boldsymbol{\varepsilon} - \boldsymbol{\varepsilon^p})(T - T_0) \\ \frac{C_\varepsilon(T - T_0)}{T_0} + \frac{(T - T_0)^2}{2T_0}\frac{\partial \mathrm{C}_\varepsilon}{\partial T} \\ -\frac{1}{2\rho_0}\sum_{i=1}^{N_{kh}} (\boldsymbol{X_i} : \boldsymbol{X_i})\frac{\partial M_i}{\partial T} \\ -\frac{1}{\rho_0}.(1 - d)\left(p + \frac{1}{m}e^{-mp}\right)\frac{\partial k}{\partial T} + \frac{1}{\rho_0}k(1 - d)\left(p + \frac{1}{m}\right)\left(\frac{1}{m}e^{-mp}\right)\frac{\partial m}{\partial T} \end{gathered} \tag{64}$$

Nevertheless, to simplify the equation of the entropy density, the material parameters temperature dependence is neglected on the hypothesis that the temperature range studied has no significant effect. The expression of the entropy density then becomes:

$$s = -\frac{\partial \Psi}{\partial T} = \frac{C_\varepsilon(T - T_0)}{T_0} + \frac{(3\lambda + 2\mu)\gamma Tr(\varepsilon - \varepsilon^p)}{\rho_0} \tag{65}$$

Note that, in order to simplify the writing of some equations, the state function associated with the temperature, $\mathrm{A^T}$, will be expressed as:

$$A^T = -\rho_0 \frac{\partial \Psi}{\partial T} = \rho_0 s \tag{66}$$

The expression of the partial derivative of Ψ, with respect to the plastic strain ($\boldsymbol{\varepsilon^p}$), gives the thermodynamical force $\boldsymbol{A^{\varepsilon^p}}$ associated with the plastic strain (the minus sign is conventional):

$$\boldsymbol{A^{\varepsilon^p}} = -\rho_0 \frac{\partial \Psi}{\partial \boldsymbol{\varepsilon^p}} = \rho_0 \frac{\partial \Psi}{\partial \boldsymbol{\varepsilon}} = \boldsymbol{\sigma} \tag{67}$$

According to the definition of the stress tensor described in eq.(62), it appears as:

$$\boldsymbol{\sigma} = \lambda Tr(\boldsymbol{\varepsilon} - \boldsymbol{\varepsilon^p})\boldsymbol{G} + 2\mu(\boldsymbol{\varepsilon} - \boldsymbol{\varepsilon^p}) - (3\lambda + 2\mu)\gamma(T - T_0)\boldsymbol{G} \tag{68}$$

This stress tensor can be dissociated in pure thermoelastic part, $\boldsymbol{\sigma^T}$, and a mechanical part, $\boldsymbol{\sigma^M}$, which are defined by the following equations :

$$\boldsymbol{\sigma^T} = -(3\lambda + 2\mu)\gamma(T - T_0)\boldsymbol{G} \tag{69}$$

$$\boldsymbol{\sigma^M} = \lambda Tr(\boldsymbol{\varepsilon} - \boldsymbol{\varepsilon^p})\boldsymbol{G} + 2\mu(\boldsymbol{\varepsilon} - \boldsymbol{\varepsilon^p}) \tag{70}$$

where **G** is the metric tensor (in any orthonormal basis, $G_{ij}=\delta_{ij}$ where δ_{ij} represents the Kronecker delta).

The expression of the partial derivative of Ψ, with respect to the i^{th} tensor variable of kinematic hardening (X_i), gives the i^{th} thermodynamical force, $\boldsymbol{A^{X_i}}$, associated with the kinematic hardening:

$$\boldsymbol{A^{X_i}} = -\rho_0 \frac{\partial \Psi}{\partial \boldsymbol{X_i}} = -M_i \boldsymbol{X_i} \tag{71}$$

The isotropic function including the damage variable is defined by the partial derivative of Ψ with respect to the isotropic variable p:

$$A^p = -\rho_0 \frac{\partial \Psi}{\partial p} = -k(1 - \mathrm{d})(1 - e^{-mp}) \tag{72}$$

The partial derivative of Ψ with respect to the damage variable d is:

$$A^d = -\rho_0 \frac{\partial \Psi}{\partial d} = k\left(p + \frac{1}{m}e^{-mp}\right) \tag{73}$$

With all these expressions, we are now in position to formulate evolution equations which have to fulfil the requirement of the non negativity of the intrinsic dissipation whatever the evolution of the thermodynamical system ($\dot{T}$, $\dot{\boldsymbol{\varepsilon}}$, $\dot{\boldsymbol{\varepsilon^p}}$, $\dot{\boldsymbol{X_i}}$, $\dot{\mathrm{p}}$, $\dot{\mathrm{d}}$)

3.2.3. Plasticity and damage: yield surface

In industrial nuclear environments such as ITER, the nuclear design codes require the use of isotropic yield surface for steel structure to identify the transition between elastic response and irreversible deformations. Moreover, the Von Mises yield surface is one of the most used criterion for the prediction of plasticity in metals. That is why, for ensuring a coherence in the analysis method, the yield function of the model is based on the expression of the Von Mises equivalent stress, i.e.:

$$f(\boldsymbol{\sigma}, \boldsymbol{A^{X_i}}, A^p) = J\left(\boldsymbol{\sigma} + \sum_{i=1}^{N_{kh}} \boldsymbol{A^{X_i}}\right) + A^p - \sigma_0 \tag{74}$$

The results of cyclic tension/compression tests, conducted in imposed stress, show that the material undergoes elastic shakedown at low stress amplitude and plastic shakedown up to ratcheting at higher stress amplitude. We propose to implement the damage variable also in the kinematic hardening part of the yield function, in such a way that isotropic and kinematic hardening work in opposition: in the low damage state, the isotropic hardening is dominant whereas in a higher damage state, the kinematic hardening becomes dominant. Keeping the objective of a simple model development, the damage coupling with kinematic hardening is identical for all the variables.

Consequently, eq.(74) is modified in the following way:

$$f(\boldsymbol{\sigma}, \boldsymbol{A^{X_i}}, A^p, d) = J\left(\boldsymbol{\sigma} + \mathrm{d}\sum_{i=1}^{N_{kh}} \boldsymbol{A^{X_i}}\right) + A^p - \sigma_0 \tag{75}$$

It is important to note that the hypothesis chosen here are strong. During the first cycles (d ≈0), the proposed model is not able to represent plastic shakedown as it was experimentally observed, see Figure 63 from chapter-II.

Alternatively using internal variables instead of thermodynamical forces, the yield function appears as:

$$f(\boldsymbol{\sigma}, \boldsymbol{X_i}, \mathrm{p}, \mathrm{d}) = J\left(\boldsymbol{\sigma} - \mathrm{d}\sum_{i=1}^{N_{kh}} M_i \boldsymbol{X_i}\right) - k(1-\mathrm{d})(1-e^{-mp}) - \sigma_0 \tag{76}$$

where σ_0 (in MPa) is the initial yield limit, and the Von Mises equivalent stress is expressed as:

$$J(\boldsymbol{\sigma}) = \sqrt{\frac{3}{2}\boldsymbol{Dev}(\boldsymbol{\sigma}) : \boldsymbol{Dev}(\boldsymbol{\sigma})} = \sqrt{\frac{3}{2}\boldsymbol{s} : \boldsymbol{s}} \tag{77}$$

where **Dev(.)** is the deviatoric operator defined as:

$$\boldsymbol{Dev}(\boldsymbol{\sigma}) = \boldsymbol{s} = \boldsymbol{\sigma} - \frac{1}{3}\mathrm{Tr}(\boldsymbol{\sigma})\mathbf{G} \tag{78}$$

3.2.4. Plasticity and damage: evolution equations

The evolution equations of the internal variables must be such that the inequality concerning the intrinsic dissipation, see eq.(63), is ever satisfied. The framework of the so called generalised standard materials, see e.g. (Germain, et al., 1983), allows the systematic verification of this constraint. It is based on two assumption, namely:

i) a plastic multiplier Λ can be defined, which cannot be negative,
ii) at least one plastic flow potential can be defined, whose partial derivative fix the direction for the evolution of the internal variables.

As a consequence of i) and ii), the evolution equations for the set of internal variables $\boldsymbol{\alpha}$, see eq.(58), read:

$$\dot{\boldsymbol{\alpha}} = \Lambda \frac{\partial g}{\partial \boldsymbol{A}^{\boldsymbol{\alpha}}} \tag{79}$$

In these study, due to the fact that plasticity and damage are irreversible phenomena that can evolve in very different ways, two flow potentials are clearly distinguished, one for the plasticity, g, and one for the damage, g^d. The intrinsic dissipation then reads:

$$\emptyset_{int} = -\rho_0 \left(\frac{\partial \Psi}{\partial \boldsymbol{\varepsilon^p}} : \Lambda \frac{\partial g}{\partial \boldsymbol{\sigma}} + \frac{\partial \Psi}{\partial p} \Lambda \frac{\partial g}{\partial A^p} + \sum_{i=1}^{N_{kh}} \left(\frac{\partial \Psi}{\partial \boldsymbol{X}_i} \right) : \Lambda \frac{\partial g}{\partial \boldsymbol{A}^{\boldsymbol{X}_i}} + \frac{\partial \Psi}{\partial d} \Lambda \frac{\partial g^d}{\partial A^d} \right) \tag{80}$$

For representing the ratcheting response, the equation setting requires the use of a non-associative model where the plastic flow potential g is not only defined by the expression of the elastic threshold function eq.(75), but also with an additional term initially described by Armstrong and Frederick as follow (Armstrong, et al., 1966):

$$g(\boldsymbol{\sigma}, \boldsymbol{A}^{\boldsymbol{X}_i}, A^p\ d) = f(\boldsymbol{\sigma}, \boldsymbol{A}^{\boldsymbol{X}_i}, A^p d) + \sum_{i=1}^{N_{kh}} \left(\frac{\Gamma_i}{2M_i} \left(\boldsymbol{Dev}(\boldsymbol{A}^{\boldsymbol{X}_i}) : \boldsymbol{Dev}(\boldsymbol{A}^{\boldsymbol{X}_i}) \right) \right) \tag{81}$$

where Γ_i are unitless material parameters linked to the non-linear kinematic hardening behaviour, and $\boldsymbol{Dev}(\boldsymbol{A}^{\boldsymbol{X}_i}) = \boldsymbol{A}^{\boldsymbol{X}_i}$.

This additional term, which is linked to the ratcheting strains, see Figure 105, is too pronounced, and most of the past studies performed in the objective of minimising this material response have led to the introduction of additional parameters inducing a more complex elaboration of the material behaviour law. See (Chaboche, 1991), (Ohno, et al., 1993), (Ohno, et al., 1993), (Jiang, et al., 1996), (Jiang, et al., 1996), (Abdel-Karim, et al., 2000) and (Abdel-Karim, et al., 2000).

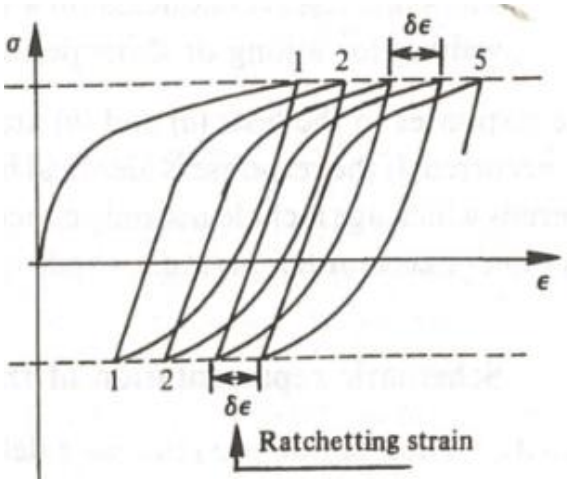

Figure 105 – Ratcheting with imposed stress (Chaboche, et al., 1988)

We have observed during the mechanical test campaign that after each cycle, the specimen is evolving, and the only difference between the stabilised response and the ratcheting is the ratcheting strain value ($\delta\boldsymbol{\varepsilon}$) between each cycle. Moreover, for tension-compression tests conducted in imposed stress, we have observed that the ratcheting strain have an exponential evolution that increases rapidly during the last 10 cycles, as it is described in Figure 106.

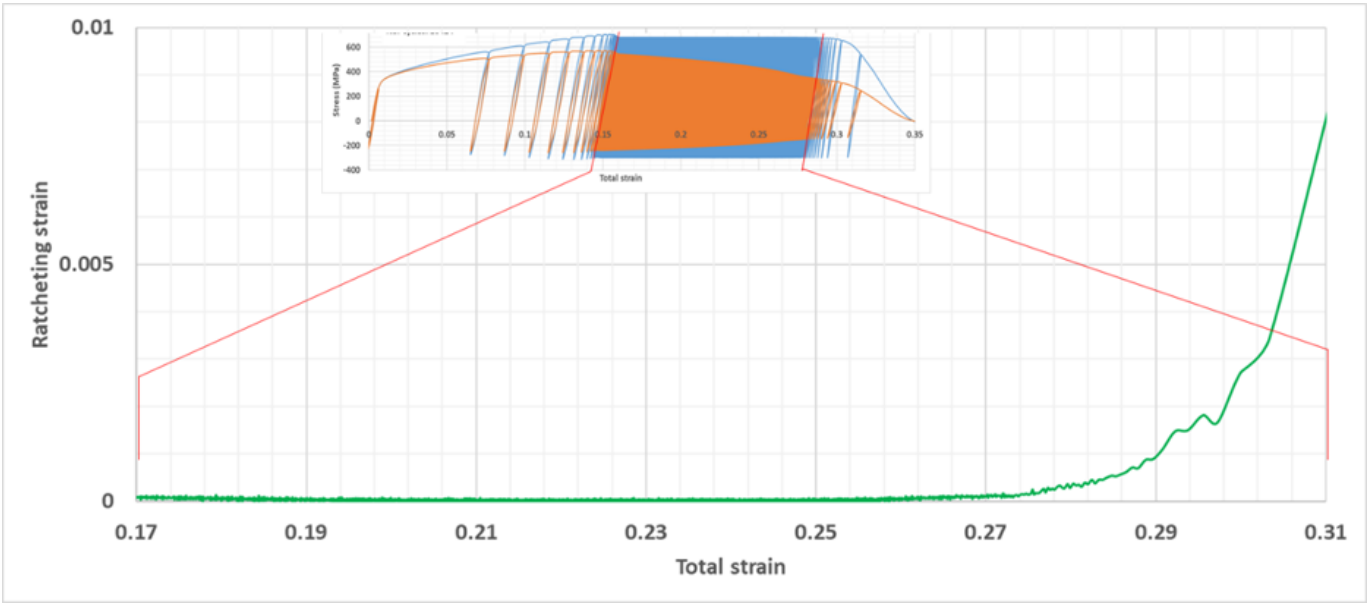

Figure 106 – Evolution of ratcheting strain along the total strain extracted from imposed cyclic stress loading test performed on cylinder 06 (see Ch.II, §4.2.3)

As the ratcheting failure mode is induced by a ductile fracture, and as the damage variable evolution proposed by Lemaitre (Lemaitre, 1985) and Rousselier (Rousselier, 1987) in continuum damage mechanics adopts an exponential behaviour similar to the one experimentally observed in Figure 104, we propose a coupling between the damage variable and the plastic flow potential as follows:

$$g(\boldsymbol{\sigma}, \boldsymbol{A}^{\boldsymbol{X}_\mathrm{i}}, A^p, \mathrm{d}) = f(\boldsymbol{\sigma}, \boldsymbol{A}^{\boldsymbol{X}_\mathrm{i}}, A^p d) + d\sum_{i=1}^{N_{kh}} \left(\frac{\Gamma_i}{2M_i} (\boldsymbol{A}^{\boldsymbol{X}_\mathrm{i}} : \boldsymbol{A}^{\boldsymbol{X}_\mathrm{i}}) \right) \tag{82}$$

This additional coupling with the damage variable ensures that ratcheting strain evolution is minimised at low damage mode, i.e. when d is close to 0, whereas when d is close to 1, $\delta\boldsymbol{\varepsilon}$ is high enough to generate ratcheting response.

The second flow potential g^d is dedicated to the damage variable evolution and decoupled from main plastic flow potential g. On the assumption that the microcrack propagation is isotropic and the growth of cavities depends on the tensile loading only, this plastic flow is function of the positive part of the stress tensor and the damage variable. This flow potential is adjusted by a characteristic coefficient of the material, n (in Pa). Finally, to ensure that the variable d will not exceed 1, we have introduced the term (1-d) that sets the variable evolution to zero as soon as d=1. The flow potential g^d can be expressed as follows:

$$g^d = \frac{d}{n}(1-d)\langle Tr(\boldsymbol{\sigma})\rangle A^d \tag{83}$$

In eq.(83), the Mc Cauley brackets are defined by:

$$\langle Tr(\boldsymbol{\sigma})\rangle = \begin{cases} 0 & if\ Tr(\boldsymbol{\sigma}) < 0 \\ Tr(\boldsymbol{\sigma}) & if\ Tr(\boldsymbol{\sigma}) \geq 0 \end{cases} \tag{84}$$

Let us express the evolution of all variables based on the partial derivatives of the plastic flow potential g, starting with the plastic strain rate $\dot{\boldsymbol{\varepsilon}}^{\boldsymbol{p}}$:

$$\dot{\boldsymbol{\varepsilon}}^{\boldsymbol{p}} = \Lambda \frac{\partial\left(f(\boldsymbol{\sigma}, \boldsymbol{A}^{\boldsymbol{X}_i}, A^p d) + d\sum_{i=1}^{N_{kh}}\left(\frac{\Gamma_i}{2M_i}\boldsymbol{A}^{\boldsymbol{X}_i} : \boldsymbol{A}^{\boldsymbol{X}_i}\right)\right)}{\partial \boldsymbol{A}^{\boldsymbol{\varepsilon}^{\boldsymbol{p}}}} \tag{85}$$

After several calculations, it appears that:

$$\dot{\boldsymbol{\varepsilon}}^{\boldsymbol{p}} = \Lambda\left(\frac{3}{2J\left(\boldsymbol{\sigma} - \mathrm{d}\sum_{i=1}^{N_{kh}} M_i\, \boldsymbol{X}_{\boldsymbol{i}}\right)}\right)\left(\boldsymbol{s} - \mathrm{d}\sum_{i=1}^{N_{kh}} M_i\, \boldsymbol{X}_{\boldsymbol{i}}\right) \tag{86}$$

The evolution equation of the kinematic hardening variable $\mathbf{X_i}$ reads:

$$\dot{\boldsymbol{X}}_{\boldsymbol{i}} = \Lambda \frac{\partial\left(f(\boldsymbol{\sigma}, \boldsymbol{A}^{\boldsymbol{X}_i}, A^p d) + d\sum_{i=1}^{N_{kh}}\left(\frac{\Gamma_i}{2M_i}\boldsymbol{A}^{\boldsymbol{X}_i} : \boldsymbol{A}^{\boldsymbol{X}_i}\right)\right)}{\partial \boldsymbol{A}^{\boldsymbol{X}_{\boldsymbol{i}}}} \tag{87}$$

After several calculations, it appears that:

$$\dot{\boldsymbol{X}}_{\boldsymbol{i}} = \Lambda\left(\frac{3}{2J\left(\boldsymbol{\sigma} - \mathrm{d}\sum_{i=1}^{N_{kh}} M_i\, \boldsymbol{X}_{\boldsymbol{i}}\right)}\right)\left(\boldsymbol{s} - \mathrm{d}\sum_{i=1}^{N_{kh}} M_i\, \boldsymbol{X}_{\boldsymbol{i}}\right) + \Lambda \mathrm{d}\frac{\Gamma_i}{M_i}\left(-M_i \boldsymbol{X}_{\boldsymbol{i}}\right) \tag{88}$$

$$\dot{\boldsymbol{X}}_{\boldsymbol{i}} = \boldsymbol{d}\dot{\boldsymbol{\varepsilon}}^{\boldsymbol{p}} - d\Lambda\Gamma_i \boldsymbol{X}_{\boldsymbol{i}} \tag{89}$$

The evolution of the isotropic variable p reads:

$$\dot{p} = \Lambda \frac{\partial g}{\partial A^p} = \Lambda \tag{90}$$

Finally, the evolution equation of the damage variable d is defined by the following equation:

$$\dot{d} = \Lambda \frac{\partial g^d}{\partial A^d} = \Lambda \frac{d(1-d)}{n} \langle Tr(\boldsymbol{\sigma}) \rangle \tag{91}$$

A strictly positive value is required for the internal damage variable to initiate damage evolution (from eq.(91) we see that $\dot{d} = 0$ if d(t=0)=d_0=0) . It is proposed to set the parameter d_0 at a value between 10^{-4} and 10^{-5}, which corresponds to the initial fraction of cavities. The evolution of the cavities will mainly be driven by the plastic flow multiplier Λ and it will be adjusted by a characteristic coefficient of the material, n (in Pa)

All the terms of the expression of the intrinsic dissipation, see eq.(63), have at now been developed. It is mandatory to demonstrate that the proposed model is admissible by verifying the positivity of the intrinsic dissipation, thus satisfying the second principle of the thermodynamics.

Eventually, the intrinsic dissipation reads:

$$\emptyset_{int} = \begin{pmatrix} \boldsymbol{\sigma} : \Lambda \dot{\boldsymbol{\varepsilon}}^{\boldsymbol{p}} \\ -\sum_{i=1}^{N_{kh}} M_i \boldsymbol{X_i} : \left(\mathrm{d}\Lambda \dot{\boldsymbol{\varepsilon}}^{\boldsymbol{p}} - \Lambda \mathrm{d}\Gamma_i \boldsymbol{X_i} \right) \\ -k(1-\mathrm{d})(1-e^{-mp})\Lambda \\ +k\left(p + \frac{1}{m}e^{-mp}\right)\Lambda \frac{d(1-d)}{n} \langle Tr(\boldsymbol{\sigma}) \rangle \end{pmatrix} \tag{92}$$

Or, in the case when Λ≥0:

$$\begin{gathered} \frac{1}{\Lambda}\emptyset_{int} = \\ \boldsymbol{\sigma} : \dot{\boldsymbol{\varepsilon}}^{\boldsymbol{p}} - \mathrm{d}\sum_{i=1}^{N_{kh}} M_i \boldsymbol{X_i} : \dot{\boldsymbol{\varepsilon}}^{\boldsymbol{p}} + d\sum_{i=1}^{N_{kh}} M_i \boldsymbol{X_i} : \sum_{i=1}^{N_{kh}} \Gamma_i \boldsymbol{X_i} \\ -k(1-\mathrm{d})(1-e^{-mp}) + k\left(p + \frac{1}{m}e^{-mp}\right)\frac{d(1-d)}{n}\langle Tr(\boldsymbol{\sigma}) \rangle \end{gathered} \tag{93}$$

It can be observed that $\boldsymbol{\sigma} : \dot{\boldsymbol{\varepsilon}}^{\boldsymbol{p}} = \boldsymbol{s} : \dot{\boldsymbol{\varepsilon}}^{\boldsymbol{p}}$ (due to the fact that $Tr(\dot{\boldsymbol{\varepsilon}}^{\boldsymbol{p}})$**=0**), and according to the expression of the Von Mises equivalent stress, eq.(77), it then appears that:

$$\boldsymbol{s} : \boldsymbol{s} = \frac{2}{3} J(\boldsymbol{\sigma})^{\mathbf{2}} \tag{94}$$

From which we get:

$$\begin{aligned}\emptyset_{int} = & \left(\frac{2J\left(\boldsymbol{\sigma} - \mathrm{d}\sum_{i=1}^{N_{kh}} M_i\,\boldsymbol{X_i}\right)^2}{3}\right)\left(\frac{3}{2J\left(\boldsymbol{\sigma} - \mathrm{d}\sum_{i=1}^{N_{kh}} M_i\,\boldsymbol{X_i}\right)}\right)\Lambda \\ & + d\sum_{i=1}^{N_{kh}} M_i\,\boldsymbol{X_i} : \sum_{i=1}^{N_{kh}} M_i\,\boldsymbol{X_i} \\ & - k\Lambda(1-\mathrm{d})(1-e^{-mp}) \\ & + k\left(p + \frac{1}{m}e^{-mp}\right)\Lambda\frac{d(1-d)}{n}\langle Tr(\boldsymbol{\sigma})\rangle\end{aligned} \tag{95}$$

Finally, the expression of the intrinsic dissipation reduced to:

$$\emptyset_{int} = \Lambda\begin{pmatrix} J\left(\boldsymbol{\sigma} - \mathrm{d}\sum_{i=1}^{N_{kh}} M_i\,\boldsymbol{X_i}\right) - k(1-\mathrm{d})(1-e^{-mp}) \\ + d\sum_{i=1}^{N_{kh}} M_i\,\Gamma_i\boldsymbol{X_i} : \boldsymbol{X_i} + \left(k\left(p + \frac{1}{m}e^{-mp}\right)\right)\frac{d(1-d)}{n}\langle Tr(\boldsymbol{\sigma})\rangle \end{pmatrix} \tag{96}$$

It can be easily seen that the term at the first line of the previous equation is always positive as $J\left(\boldsymbol{\sigma} - \mathrm{d}\sum_{i=1}^{N_{kh}} M_i\,\boldsymbol{X_i}\right)$- $k(1-\mathrm{d})(1-e^{-mp}) > \sigma_0$ in the case of a plastic flow. Other terms are always positive whatever is the evolution. The proposed model is therefore thermodynamically admissible.

We furthermore assume that the flow is viscoplastic. The expression of the plastic multiplier Λ is therefore given by:

$$\Lambda = \frac{1}{\eta\sigma_0}\left\langle J\left(\boldsymbol{\sigma} - \mathrm{d}\sum_{i=1}^{N_{kh}} M_i\boldsymbol{X_i}\right) - k(1-\mathrm{d})(1-e^{-mp}) - \sigma_0\right\rangle \tag{97}$$

where η (in s) is a characteristic coefficients of the material.

3.2.5. Heat equation

The thermal conduction in a homogeneous volume could be expressed with the Fourier's law, which states that the internal heat generation flux is proportional to the temperature gradient. According to the isotropic Fourier's law, this flux distribution is expressed as follow:

$$div(\boldsymbol{q}) = -k.\,div\big(grad(T)\big) = -k_T \Delta T \tag{98}$$

where k_T is the heat conductivity coefficient.

In the case where the temperature range studied has no significant effect on the material parameters, the hypothesis that the material temperature dependence is neglected can be applied. Starting from the expression of the entropy density, which is described in eq.(65), the evolution of the entropy density is simplified as follows:

$$\dot{s} = \mathrm{C}_{\varepsilon}\frac{\dot{T}}{T_0} + \frac{(3\lambda + 2\mu)\gamma Tr(\dot{\boldsymbol{\varepsilon}})}{\rho_0} \tag{99}$$

Starting from eq.(56), and eq.(57), and taking into account the expression of the intrinsic dissipation, eq.(96), the isothermal entropy density evolution, eq.(99), the flux distribution, eq.(98), the heat equation for the proposed model finally reads:

$$\begin{aligned}
&\frac{\rho_0 C_{\varepsilon}}{T_0} T\dot{T} - k_T \Delta T - r^v = \\
&-(3\lambda + 2\mu)\gamma Tr(\dot{\boldsymbol{\varepsilon}})T \\
&+\Lambda J\big(\boldsymbol{\sigma} - \mathrm{d}\textstyle\sum_{i=1}^{N_{kh}} M_i\, \boldsymbol{X_i}\big) \\
&+d\Lambda \sum_{i=1}^{N_{kh}} M_i\, \Gamma_i \boldsymbol{X_i} : \boldsymbol{X_i} \\
&+k\Lambda(1-\mathrm{d})(1-e^{-mp}) \\
&+k\left(p + \frac{1}{m}e^{-mp}\right)\Lambda\frac{d(1-d)}{n}\langle Tr(\boldsymbol{\sigma})\rangle
\end{aligned} \tag{100}$$

Remark:

The evolution of the entropy density, taking into account the material parameters temperature dependence, is expressed as follow:

$$
\begin{aligned}
\dot{s} = \\
&\frac{1}{2\rho_0}\frac{\partial^2\lambda}{\partial T^2}\dot{T}\big(Tr(\boldsymbol{\varepsilon}-\boldsymbol{\varepsilon^p})\big)^2+\frac{1}{\rho_0}\frac{\partial\lambda}{\partial T}Tr(\dot{\boldsymbol{\varepsilon}})\\
&-\frac{\partial^2\mu}{\partial T^2}\big((\boldsymbol{\varepsilon}-\boldsymbol{\varepsilon^p}):(\boldsymbol{\varepsilon}-\boldsymbol{\varepsilon^p})\big)\dot{T}-\frac{\partial\mu}{\partial T}\big(2(\dot{\boldsymbol{\varepsilon}}-\dot{\boldsymbol{\varepsilon}}^{\boldsymbol{p}}):(\boldsymbol{\varepsilon}-\boldsymbol{\varepsilon^p})\big)\\
&+\frac{1}{\rho_0}\left(3\frac{\partial\lambda}{\partial T}+2\frac{\partial\mu}{\partial T}\right)\dot{T}\gamma Tr(\boldsymbol{\varepsilon}-\boldsymbol{\varepsilon^p})+\frac{1}{\rho_0}(3\lambda+2\mu)\frac{\partial\gamma}{\partial T}\dot{T}Tr(\boldsymbol{\varepsilon}-\boldsymbol{\varepsilon^p})+\frac{1}{\rho_0}(3\lambda+2\mu)\gamma Tr(\dot{\boldsymbol{\varepsilon}})\\
&+\frac{1}{\rho_0}\left(3\frac{\partial\lambda}{\partial T}+2\frac{\partial\mu}{\partial T}\right)\dot{T}\frac{\partial\gamma}{\partial T}Tr(\boldsymbol{\varepsilon}-\boldsymbol{\varepsilon^p})(T-T_0)+\frac{1}{\rho_0}(3\lambda+2\mu)\frac{\partial^2\gamma}{\partial T^2}\dot{T}Tr(\boldsymbol{\varepsilon}-\boldsymbol{\varepsilon^p})(T-T_0)\\
&+\frac{1}{\rho_0}(3\lambda+2\mu)\frac{\partial\gamma}{\partial T}Tr(\dot{\boldsymbol{\varepsilon}})(T-T_0)+\frac{1}{\rho_0}(3\lambda+2\mu)\frac{\partial\gamma}{\partial T}Tr(\boldsymbol{\varepsilon}-\boldsymbol{\varepsilon^p})\dot{T}\\
&+\frac{1}{\rho_0}\left(3\frac{\partial^2\lambda}{\partial T^2}+2\frac{\partial^2\mu}{\partial T^2}\right)\dot{T}\gamma Tr(\boldsymbol{\varepsilon}-\boldsymbol{\varepsilon^p})(T-T_0)+\frac{1}{\rho_0}\left(3\frac{\partial\lambda}{\partial T}+2\frac{\partial\mu}{\partial T}\right)\dot{T}\frac{\partial\gamma}{\partial T}Tr(\boldsymbol{\varepsilon}-\boldsymbol{\varepsilon^p})(T-T_0)\\
&+\frac{1}{\rho_0}\left(3\frac{\partial\lambda}{\partial T}+2\frac{\partial\mu}{\partial T}\right)\gamma Tr(\dot{\boldsymbol{\varepsilon}})(T-T_0)+\frac{1}{\rho_0}\left(3\frac{\partial\lambda}{\partial T}+2\frac{\partial\mu}{\partial T}\right)\gamma Tr(\boldsymbol{\varepsilon}-\boldsymbol{\varepsilon^p})\dot{T}\\
&+\frac{\partial \mathrm{C}_\varepsilon}{\partial T}\dot{T}\frac{(T-T_0)}{T_0}+\frac{\mathrm{C}_\varepsilon}{T_0}\dot{T}+\frac{\partial^2\mathrm{C}_\varepsilon}{\partial T^2}\dot{T}\frac{(T-T_0)^2}{2T_0}+\frac{\partial \mathrm{C}_\varepsilon}{\partial T}\frac{(T-T_0)}{T_0}\dot{T}\\
&-\frac{1}{2\rho_0}\dot{T}\sum_{i=1}^{N_{kh}}\frac{\partial^2\mathrm{M}_i}{\partial T^2}\,\boldsymbol{X_i}:\boldsymbol{X_i}-\frac{1}{\rho_0}\sum_{i=1}^{N_{kh}}\frac{\partial\mathrm{M}_i}{\partial T}\,\boldsymbol{X_i}:\dot{\boldsymbol{X}}_{\boldsymbol{i}}\\
&+\frac{1}{\rho_0}\left(p+\frac{1}{m}e^{-mp}\right)\frac{\partial k}{\partial T}\dot{d}\\
&-\frac{1}{\rho_0}(1-d)\left(\dot{p}-\frac{1}{m}e^{-mp}\left(m\dot{p}+\frac{\partial m}{\partial T}\dot{T}p\right)-\frac{1}{m^2}\frac{\partial m}{\partial T}\dot{T}e^{-mp}\right)\frac{\partial k}{\partial T}\\
&-\frac{1}{\rho_0}.(1-d)\left(p+\frac{1}{m}e^{-mp}\right)\frac{\partial^2 k}{\partial T^2}\dot{T}\\
&+\frac{1}{\rho_0}\frac{\partial k}{\partial T}\dot{T}(1-d)\left(p+\frac{1}{m}\right)\left(\frac{1}{m}e^{-mp}\right)\frac{\partial m}{\partial T}\\
&-\frac{1}{\rho_0}k\dot{d}\left(p+\frac{1}{m}\right)\left(\frac{1}{m}e^{-mp}\right)\frac{\partial m}{\partial T}\\
&+\frac{1}{\rho_0}k(1-d)\left(\dot{p}+\frac{1}{m^2}\frac{\partial m}{\partial T}\dot{T}\right)\left(\frac{1}{m}e^{-mp}\right)\frac{\partial m}{\partial T}\\
&-\frac{1}{\rho_0}k(1-d)\left(p+\frac{1}{m}\right)\left(\begin{matrix}\frac{1}{m}e^{-mp}\cdot\left(m\dot{p}+\frac{\partial m}{\partial T}\dot{T}p\right)\\+\frac{1}{m^2}\frac{\partial m}{\partial T}\dot{T}e^{-mp}\end{matrix}\right)\frac{\partial m}{\partial T}\\
&+\frac{1}{\rho_0}k(1-d)\left(p+\frac{1}{m}\right)\left(\frac{1}{m}e^{-mp}\right)\frac{\partial^2 m}{\partial T^2}\dot{T}
\end{aligned}
\tag{101}
$$

3.3. Model predictions for some simple loading cases

The proposed model has been tested on homogeneous problem to illustrate its ability to represent specific characteristic for which it was developed. We considered the case of a cyclic homogeneous uniaxial tensile test with a strong thermo-mechanical coupling. For this, all variables involved in non-linear ordinary differential equations (ODE)s were solved using Matlab® software.

3.3.1. Uniaxial tensile test: hypotheses

In order to simplify the resolution of the heat and mechanical equations, the following hypotheses have been made:

- no body forces: $\mathbf{f^v}=0$,
- uniform stress distribution: $\mathbf{div}(\boldsymbol{\sigma})=0$,
- uniform temperature distribution: grad(T)=0,
- no volumic heat generation applied: $r^v=0$,
- uniaxial loading: $\sigma_{22}= \sigma_{33}=0$ and $\varepsilon_{22}= \varepsilon_{33}$,

For this simulation, only two kinematic hardening variables were taken into account.

3.3.1.1. Imposed stress hypothesis

The input signal is an imposed stress along the direction $\mathbf{e_1}$ where the stress tensor is defined in a given orthonormal basis ($\mathbf{e}_1$, $\mathbf{e}_2$, $\mathbf{e}_3$) as:

$$[\sigma(t)] = \begin{bmatrix} \sigma_{11}(t) & 0 & 0 \\ 0 & 0 & 0 \\ 0 & 0 & 0 \end{bmatrix} \tag{102}$$

From eq.(68), the stress tensor components can be expressed as:

$$\begin{cases} \sigma_{11} = \lambda Tr(\boldsymbol{\varepsilon}) - \lambda Tr(\boldsymbol{\varepsilon^p}) + 2\mu(\varepsilon_{11}) - 2\mu\varepsilon_{11}^p - Th \\ 0 = \lambda Tr(\boldsymbol{\varepsilon}) - \lambda Tr(\boldsymbol{\varepsilon^p}) + 2\mu(\varepsilon_{22}) - 2\mu\varepsilon_{22}^p - Th \\ 0 = \lambda Tr(\boldsymbol{\varepsilon}) - \lambda Tr(\boldsymbol{\varepsilon^p}) + 2\mu(\varepsilon_{33}) - 2\mu\varepsilon_{33}^p - Th \end{cases} \tag{103}$$

where:

$$Th = (3\lambda + 2\mu)\gamma(T - T_0) \tag{104}$$

The plastic incompressibility, simply reads:

$$Tr(\boldsymbol{\varepsilon^p}) = \varepsilon_{11}^p + \varepsilon_{22}^p + \varepsilon_{33}^p = 0 \tag{105}$$

Starting from the expression of the stress tensor components described in eq.(103), it appears that:

$$\begin{cases} Tr(\boldsymbol{\varepsilon}) = \dfrac{\sigma_{11}}{\lambda} - \dfrac{2\mu}{\lambda}\varepsilon_{11} + \dfrac{2\mu}{\lambda}\varepsilon_{11}^p + \dfrac{1}{\lambda}Th \\ Tr(\boldsymbol{\varepsilon}) = -\dfrac{2\mu}{\lambda}\varepsilon_{22} + \dfrac{2\mu}{\lambda}\varepsilon_{22}^p + \dfrac{1}{\lambda}Th \\ Tr(\boldsymbol{\varepsilon}) = -\dfrac{2\mu}{\lambda}\varepsilon_{33} + \dfrac{2\mu}{\lambda}\varepsilon_{33}^p + \dfrac{1}{\lambda}Th \end{cases} \tag{106}$$

Then, by combining these equations, the expression of the trace of strain tensor appears as follows:

$$Tr(\boldsymbol{\varepsilon}) = \frac{1}{3\lambda + 2\mu}\sigma_{11} + 3\gamma(T - T_0) \tag{107}$$

By introducing Tr(**ε**) from eq.(107) in the expression of the stress tensor components along the direction $\mathbf{e_1}$ described in eq.(103), the following expression of the strain tensor components can be deduced:

$$\varepsilon_{11} = \frac{(\lambda+\mu)}{\mu(3\lambda+2\mu)}\sigma_{11} + \gamma(T-T_0) + \varepsilon_{11}^p \tag{108}$$

and

$$\varepsilon_{22} = \frac{-\lambda}{2\mu(3\lambda+2\mu)}\sigma_{11} + \gamma(T-T_0) - \frac{\varepsilon_{11}^p}{2} \tag{109}$$

Note: $\sigma_{11} = \mu\frac{3\lambda+2\mu}{\lambda+\mu}\varepsilon_{11}$ correspond to Hooke's law knowing that the Young modulus can be expressed as $E = \mu\frac{3\lambda+2\mu}{\lambda+\mu}$

Starting from eq. (107), the expression of the trace of strain tensor evolution required in the heat equation, eq.(100), appears as follows:

$$Tr(\dot{\varepsilon}) = \frac{1}{3\lambda+2\mu}\dot{\sigma}_{11} + 3\gamma\dot{T} \tag{110}$$

Starting from the expression of the temperature evolution where:

$$\dot{T} = A - \frac{(3\lambda+2\mu)\gamma Tr(\dot{\boldsymbol{\varepsilon}})T_0}{\rho \mathrm{C}_\varepsilon} \tag{111}$$

$$\begin{aligned} \mathrm{A} = {} & \left(\frac{T_0}{\rho_0 T \mathrm{C}_\varepsilon}\right) r^v + \left(\frac{T_0}{\rho_0 T \mathrm{C}_\varepsilon}\right)\Lambda J\left(\boldsymbol{\sigma} - \mathrm{d}\sum_{i=1}^{N_{kh}} M_i\,\boldsymbol{X_i}\right) \\ & + \left(\frac{T_0}{\rho_0 T \mathrm{C}_\varepsilon}\right)\Lambda\left(d\sum_{i=1}^{N_{kh}} M_i\,\Gamma_i \boldsymbol{X_i}\!:\!\boldsymbol{X_i} + k(1-\mathrm{d})(1-e^{-mp})\right) \\ & + \left(\frac{T_0}{\rho_0 T \mathrm{C}_\varepsilon}\right)\Lambda k\left(p + \frac{1}{m}e^{-mp}\right)\frac{d(1-d)}{n}\langle Tr(\boldsymbol{\sigma})\rangle \end{aligned} \tag{112}$$

it appears that :

$$\dot{T} = A - \frac{(3\lambda+2\mu)\gamma T_0}{\rho \mathrm{C}_\varepsilon}\left(\frac{1}{3\lambda+2\mu}\dot{\sigma}_{11} + 3\gamma\dot{T}\right) \tag{113}$$

$$\dot{T} = \left(A - \frac{\dot{\sigma}_{11}\gamma T_0}{\rho \mathrm{C}_\varepsilon}\right)\left(\frac{\rho \mathrm{C}_\varepsilon}{\rho \mathrm{C}_\varepsilon + 3(3\lambda+2\mu)\gamma^2 T_0}\right) \tag{114}$$

For a monotonic loading, we can propose a linear expression of σ_{11} with associated stress evolution along the the direction $\mathbf{e_1}$:

$$\sigma_{11} = at \tag{115}$$
$$\dot{\sigma}_{11} = a \tag{116}$$

For a cyclic loading, we can propose a sinosidal expression of σ_{11} with associated stress evolution along the direction $\mathbf{e_1}$:

$$\sigma_{11} = \alpha\sin(2\pi \mathrm{t}) \tag{117}$$
$$\dot{\sigma}_{11} = 2\alpha\pi.\cos(2\pi \mathrm{t}) \tag{118}$$

3.3.1.2. Imposed strain hypothesis

The input signal is an imposed strain along the direction $\mathbf{e_1}$ where the strain tensor is defined in a given orthonormal basis ($\mathbf{e}_1$, $\mathbf{e}_2$, $\mathbf{e}_3$) as:

$$[\varepsilon\ (t)] = \begin{bmatrix} \varepsilon_{11}(t) & 0 & 0 \\ 0 & \varepsilon_{22}(t) & 0 \\ 0 & 0 & \varepsilon_{22}(t) \end{bmatrix} \tag{119}$$

Starting from the expression of the strain tensor in the case of imposed stress hypothesis described in eq.(108), the expression of the stress tensor appears as:

$$\sigma_{11} = \mu \frac{3\lambda + 2\mu}{\lambda + \mu} \left(\varepsilon_{11} - \varepsilon_{11}^{p} - \gamma (T - T_0) \right) \tag{120}$$

Starting from the expression of the trace of the strain tensor in the case of imposed stress hypothesis described in eq.(107), the expression the trace of the strain tensor appears as:

$$Tr(\boldsymbol{\varepsilon}) = \frac{\mu}{\lambda + \mu} \left(\varepsilon_{11} - \varepsilon_{11}^{p} \right) + \left(3 - \frac{\mu}{\lambda + \mu} \right) \gamma (T - T_0) \tag{121}$$

Then, the expression of the trace of strain tensor evolution required in the heat equation, eq.(100), appears as follows:

$$Tr(\dot{\varepsilon}) = \frac{\mu}{\lambda + \mu} \dot{\varepsilon}_{11} + \left(3 - \frac{\mu}{\lambda + \mu} \right) \gamma \dot{T} \tag{122}$$

Starting from the expression of the temperature evolution recalled in eq.(111) and eq.(112) , it appears that:

$$\dot{T} = A - \frac{(3\lambda + 2\mu)\gamma T_0}{\rho \mathrm{C}_{\varepsilon}} \left(\frac{\mu}{\lambda + \mu} \dot{\varepsilon}_{11} + \left(3 - \frac{\mu}{\lambda + \mu} \right) \gamma \dot{T} \right) \tag{123}$$

$$\dot{T} = \left(A - \frac{\mu (3\lambda + 2\mu)\gamma T_0 \dot{\varepsilon}_{11}}{(\lambda + \mu)\rho \mathrm{C}_{\varepsilon}} \right) \left(\frac{(\lambda + \mu)\rho \mathrm{C}_{\varepsilon}}{(\lambda + \mu)\rho \mathrm{C}_{\varepsilon} + (3(\lambda + \mu) - \mu)(3\lambda + 2\mu)\gamma^2 T_0} \right) \tag{124}$$

For a monotonic loading, we can propose a linear expression of ε_{11} with associated strain evolution along the the direction $\mathbf{e_1}$:

$$\varepsilon_{11} = at \tag{125}$$
$$\dot{\varepsilon}_{11} = a \tag{126}$$

For a cyclic loading, we can propose a sinosidal expression of ε_{11} with associated strain evolution along the direction $\mathbf{e_1}$:

$$\varepsilon_{11} = \alpha \sin(2\pi t) \tag{127}$$
$$\dot{\varepsilon}_{11} = 2\alpha\pi . \cos(2\pi t) \tag{128}$$

3.3.2. Internal variables: evolution equations

The plastic strain tensor evolution along the axial and transversal axis are respectively defined by the following differential equations:

$$\dot{\varepsilon^p}_{11} = \frac{3}{2J(\boldsymbol{\sigma} - d\sum_{i=1}^{2} M_i \boldsymbol{X}_i)} \cdot \left(s_{11} - d\sum_{i=1}^{2} M_i x_{(i)_{11}} \right) \dot{p} \tag{129}$$

$$\dot{\varepsilon^p}_{22} = \frac{3}{2J(\boldsymbol{\sigma} - d\sum_{i=1}^{2} M_i \boldsymbol{X}_i)} \cdot \left(s_{22} - d\sum_{i=1}^{2} M_i x_{(i)_{22}} \right) \dot{p} \tag{130}$$

The kinematic hardening evolution along the $\mathbf{e}_1$ axis and the $\mathbf{e}_2$ axis are respectively defined by the following differential equations:

$$\dot{X}_{(i)11} = \dot{\varepsilon^p}_{11} - \dot{p} d\Gamma_i X_{(i)_{11}} \tag{131}$$

$$\dot{X}_{(i)22} = \dot{\varepsilon^p}_{22} - \dot{p} d\Gamma_i X_{(i)_{22}} \tag{132}$$

The isotropic hardening evolution is defined by the following differential equation:

$$\dot{p} = \frac{1}{\eta\sigma_0} \langle J\left(\boldsymbol{\sigma} - \mathrm{d}\sum_{i=1}^{2} M_i \boldsymbol{X}_i \right) - k(1-\mathrm{d})(1-e^{-mp}) - \sigma_0 \rangle \tag{133}$$

The damage variable evolution is defined by the following differential equation:

$$\dot{d} = \dot{p}\frac{d}{n}(1-d)\langle \sigma_{11}(t) \rangle \tag{134}$$

The temperature evolution $\dot{T}$ which is dependent of the type of loading is described in eq.(114) and eq.(124), respectively for imposed stress and imposed strain loading.

When all variable evolution equations have been set, see eqs. (129) to (134), this system of first order differential equations is solved using the non-linear ordinary differential equation solver ODE23, with pre-set options, from Matlab® software.

3.3.3. Material parameters: identification

The identification of the material parameters has been made following a heuristic method (i.e. with identification by hands) of "increasing complexity". In the first step, the only internal variable taken into account is this of isotropic hardening, from which the associated material parameters are identified, on the basis of experimental results, see Chapter II.

In the second step, the damage variable is also taken into account, and in the third and last step, the kinematic hardening variables. Note that all the numerical simulation (Matlab®) have been made assuming that the material parameters do not depend on the temperature.

We start first by using the linear elastic material parameters, extracted from the RCC-MR nuclear code:

- density, ρ_0=7930 kg/m^3,
- mean thermal expansion coefficient, γ=15.3.10^{-6} K^{-1},
- material specific heat, C_ε=472 J/kg.K,
- Lamé coefficients λ =115.384 GPa and μ =76.923 GPa, (E=200 GPa and υ=0.3)
- yield limit, σ_0=220 MPa.

Considering the simplest model simulation, the material parameters associated with the non-linear kinematic hardening (M_i, Γ_i) and the damage (n, d_0) are set to 0. Additionally, the strong thermal coupling is not activated, meaning that the temperature evolution does not affect the mechanical behaviour.

Figure 107 shows the superposition of the reference tensile curve (solid blue line) described in chapter II, and the stress strain curve as predicted by the model with imposed stress (dashed blue line) where k=100MPa, m=10 and imposed strain (dash-dotted red line) where k=350MPa, m=50.

The exponential behaviour of the isotropic hardening allows an easier setting of the parameter k, which corresponds to the difference between the maximum stress and the yield stress. The parameter m provides a smoother transition between σ_0 and the maximum stress.

It can be noted that the yield limit for the reference material curve is lower than the one provided by the nuclear code. Additionally, the transition between elastic and plastic response is non smooth for the phenomenological model.

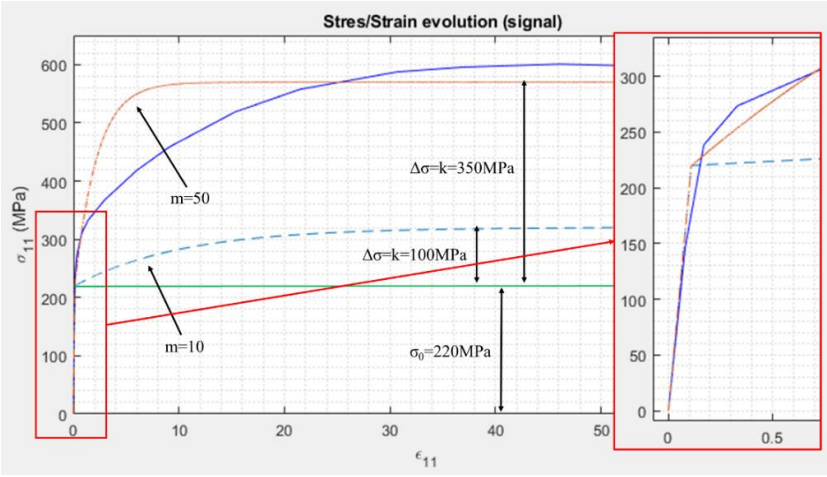

Figure 107 – Stress/strain curve: influence of isotropic hardening parameters m and k.

After several iterations, the parameters k and m have been respectively set to 320MPa and 10, which corresponds to the best fitting in terms of plastic hardening shape observed during the test, see imposed stress curve (dashed blue line) in Figure 108. In the case of the imposed strain curve (dash-dotted red line), the yield limit has been shifted by 60MPa upward, which provides a good fitting between the experimental and simulated results.

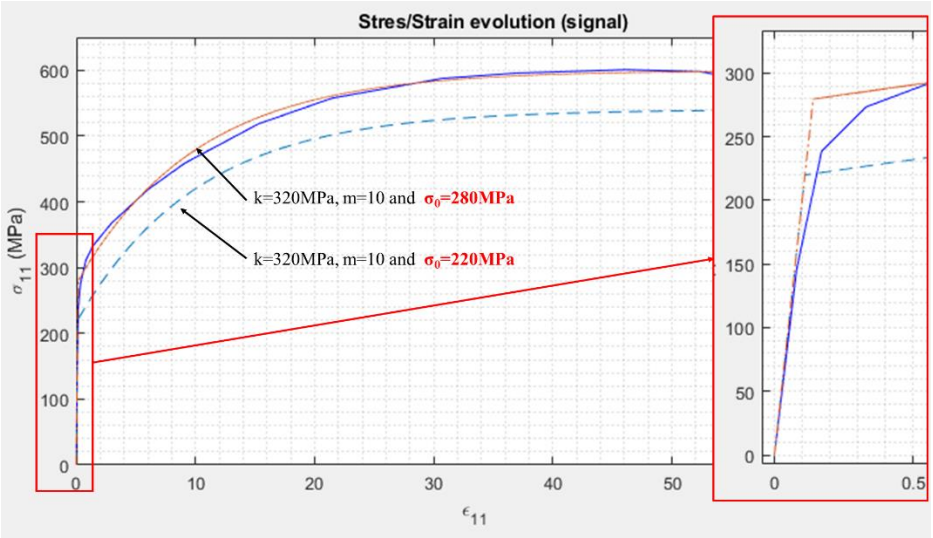

Figure 108 – Stress/strain curve: influence yield limit parameter σ_0.

The viscosity parameter η helps smoothing the transition between elastic and plastic behaviours, and slightly increases the yield limit as observed in Figure 109. For the proposed model, this parameter is set to 0.1^{s-1}.

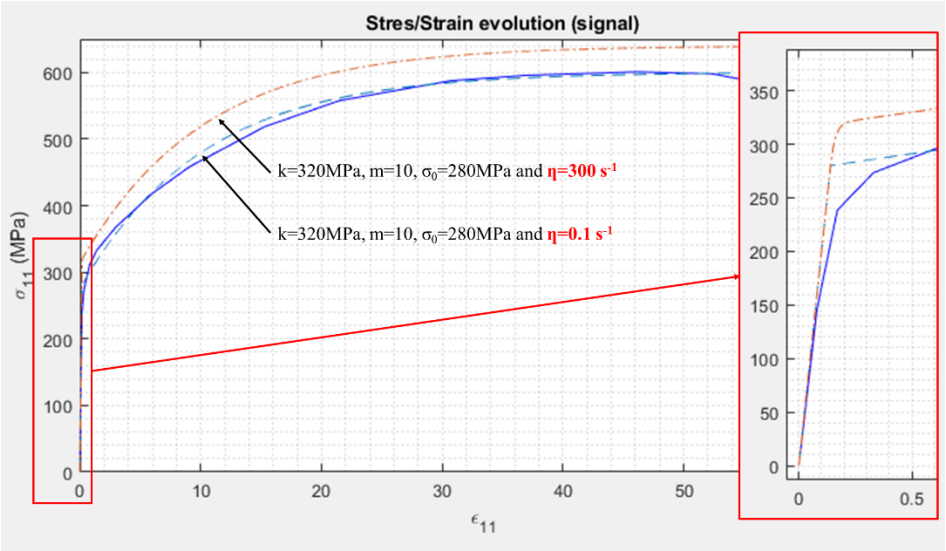

Figure 109 – Stress/strain curve: influence of viscosity parameter η.

At this stage, we propose to activate the damage variable evolution, which introduces two new parameters: the initial fraction of cavities d_0 (unitless) and a dedicated characteristic coefficient of the material n (in MPa).

Figure 109 shows the results of four simulations for which different values have been set for these two material parameters. We recall that the solid blue line corresponds to the reference tensile curve, and that the dashed blue and red lines correspond respectively to the calculated curves for imposed stress and strain.

The damage parameters are adjusted in such a way that the point A, which corresponds to the yield of the so-called damage zone, coincides with the specimen necking of the reference curve. According to the expression of the damage evolution in eq. (91), these two parameters work in opposition. Indeed, an increase of the ratio of cavities or a decrease of coefficient n achieves faster the damage zone.

After several iterations, we have chosen to fix the initial fraction of cavities to 10^{-5} and parameter n to 31 MPa.

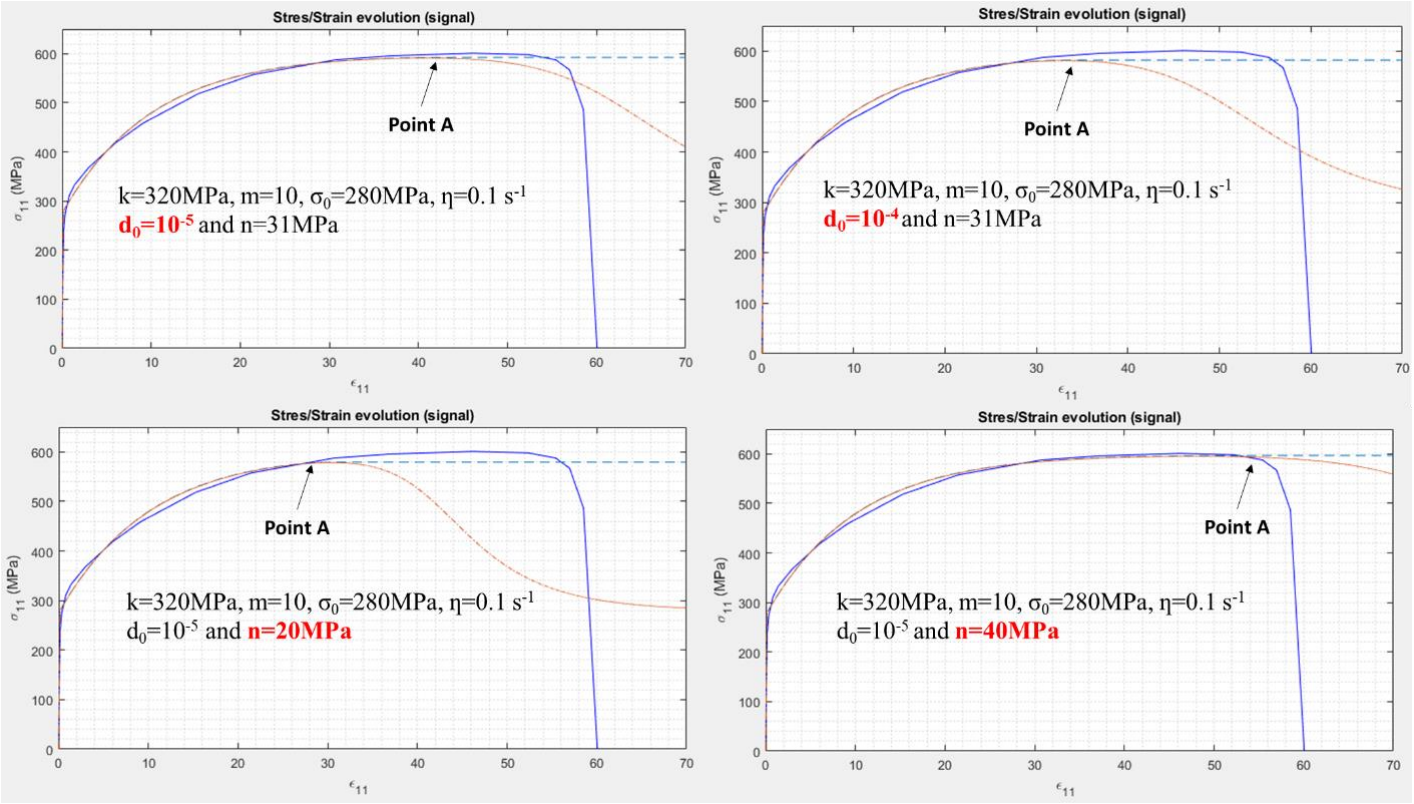

Figure 110 – Stress/strain curves: influence of damage parameters n and d_0.

For this last stage, the two kinematic hardening variables are added, corresponding to four new parameters. This second hardening type, which is also coupled with damage, see eq.(82), drives the ratcheting. We carried out the parameter identification in the two following steps: first, the raw values are defined under monotonic loading, and then, these values are refined under cyclic loading.

Concerning the monotonic loading, due to the coupling with damage, the kinematic hardening modifies the material behaviour when the stress intensity becomes higher, close to the ultimate strength, see Figure 111. The expression of the plastic flow potential in eq.(82), links the two kinematic hardening parameters by the ratio Γ/M. An increase in this ratio reaches more quickly the damage zone.

The kinematic hardening parameters are now set with M_1=100 MPa, Γ_1=5, M_2=7.5 MPa and Γ_2=0.5 for monotonic loading.

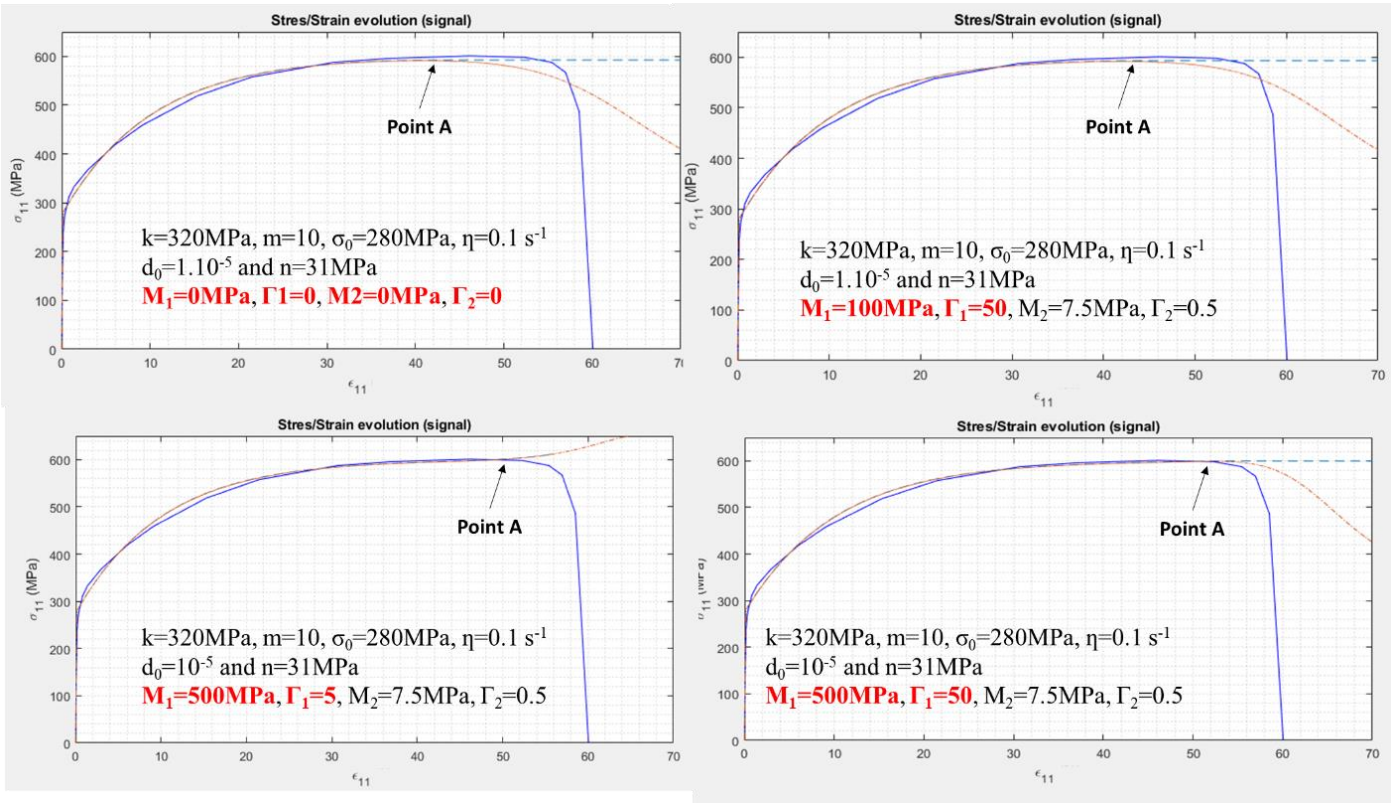

Figure 111 – Stress/strain curves: influence of kinematic hardening parameters M and Γ.

Considering the second step of the parameter identification, the Matlab® file has been updated for simulating simultaneously the mechanical model under monotonic and cyclic loadings.

In the graph on top of Figure 112, the dashed red and blue lines correspond respectively to the reference engineering monotonic tensile and cyclic curve, the solid red and blue lines correspond respectively to the simulated curves.

The graph at the bottom of Figure 112 represents the cumulative cycles along the simulation relative to the total strain tensor. We recall that for this imposed force test, 3574 cycles were reached during the reference test.

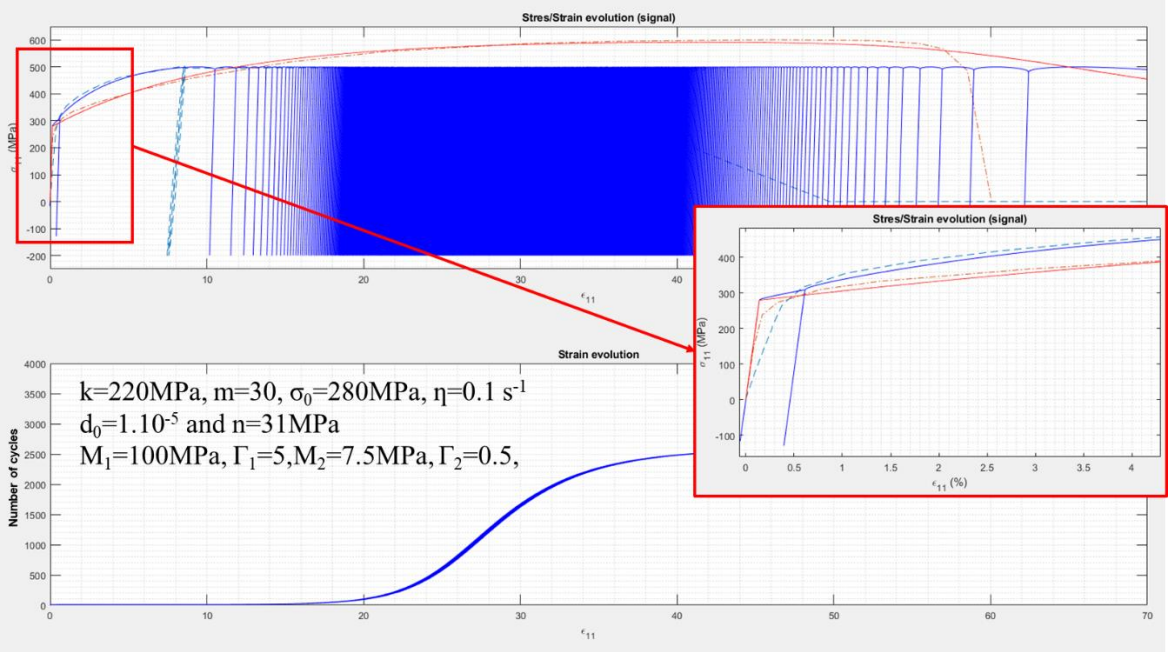

Figure 112 – Stress/strain curves: comparison between monotonic and cyclic loading.

As it was described in Chapter I, the cyclic hardening curves provide different hardening shapes than monotonic ones. In that case, the isotropic parameters have been updated to fit with reference curve shape for the first 10% of total strain (k=220MPa, and m=30), see graph in red square on Figure 112. Despite this modification, all the other parameters settings have been conserved, and Figure 112 shows good results for cyclic loading in terms of total strain and total number of cycles.

Now, the objective is to adjust the parameters in order to recover, in the same order of magnitude, the maximum total strain and the associated numbers of cycles reached during the reference test. Figure 113 to Figure 117 show the effect of the various parameters on the simulation results under cyclic loading.

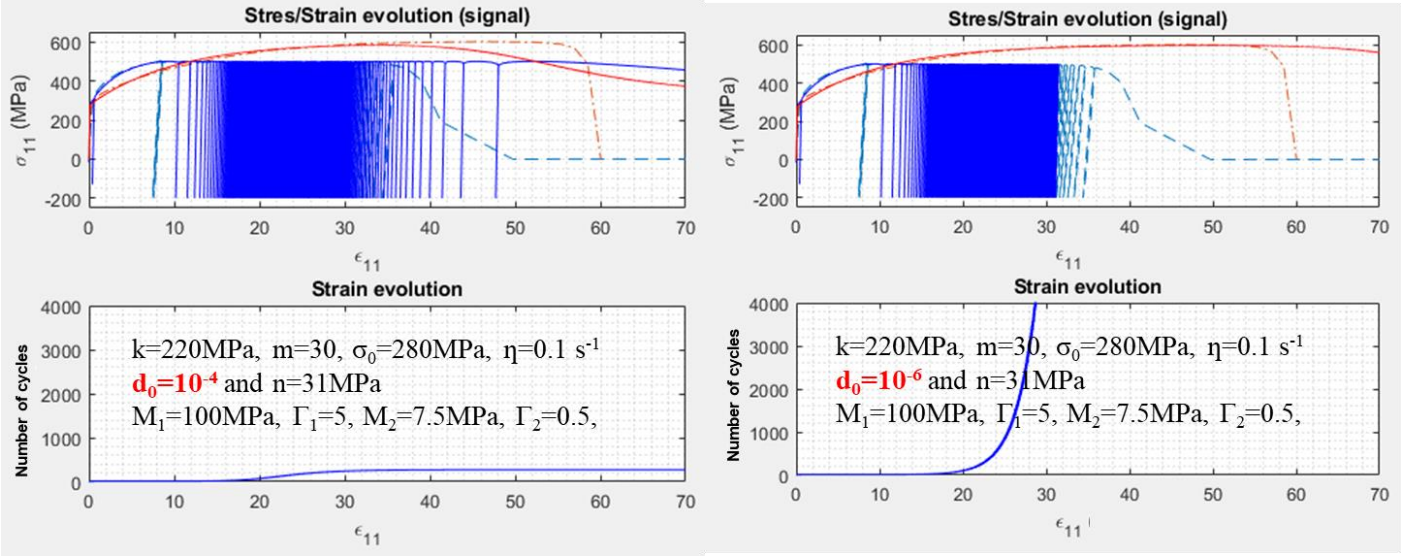

Figure 113 – Stress/strain curves: effect of the initial fraction of cavities d_0

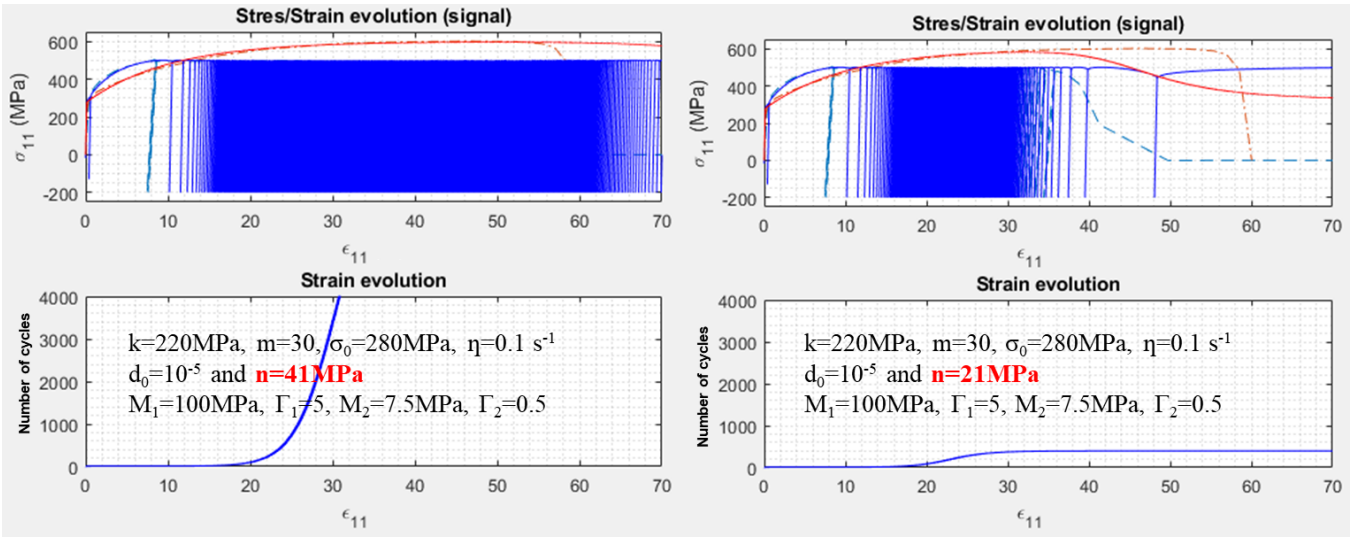

Figure 114 – Effect of the damage parameter n

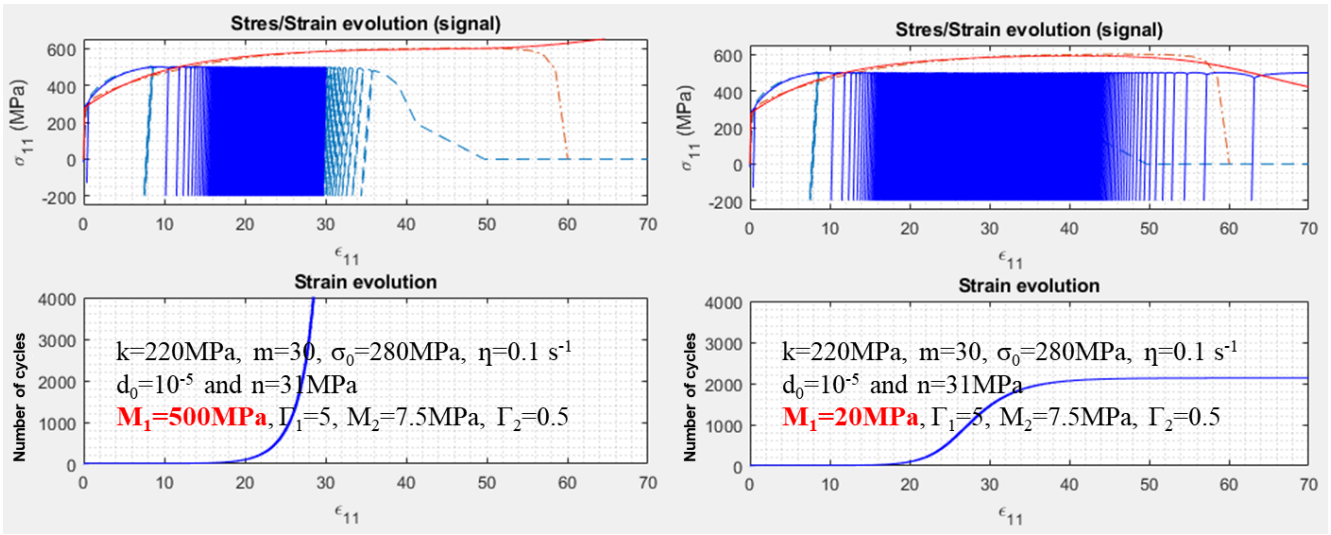

Figure 115 – Effect of the kinematic hardening parameter M

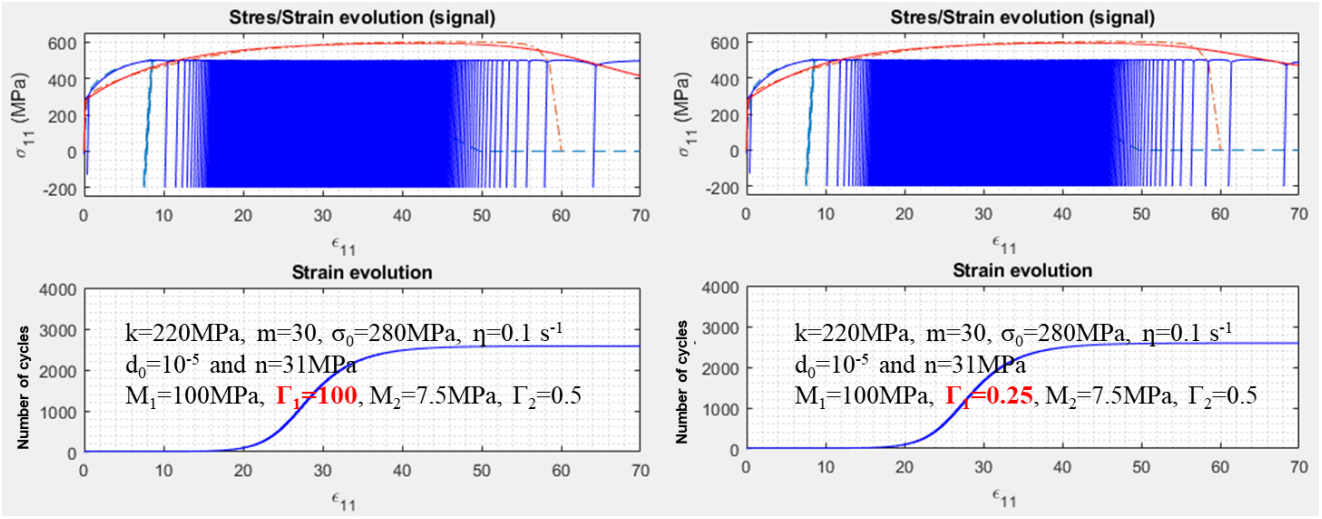

Figure 116 – Effect of the kinematic hardening parameter Γ

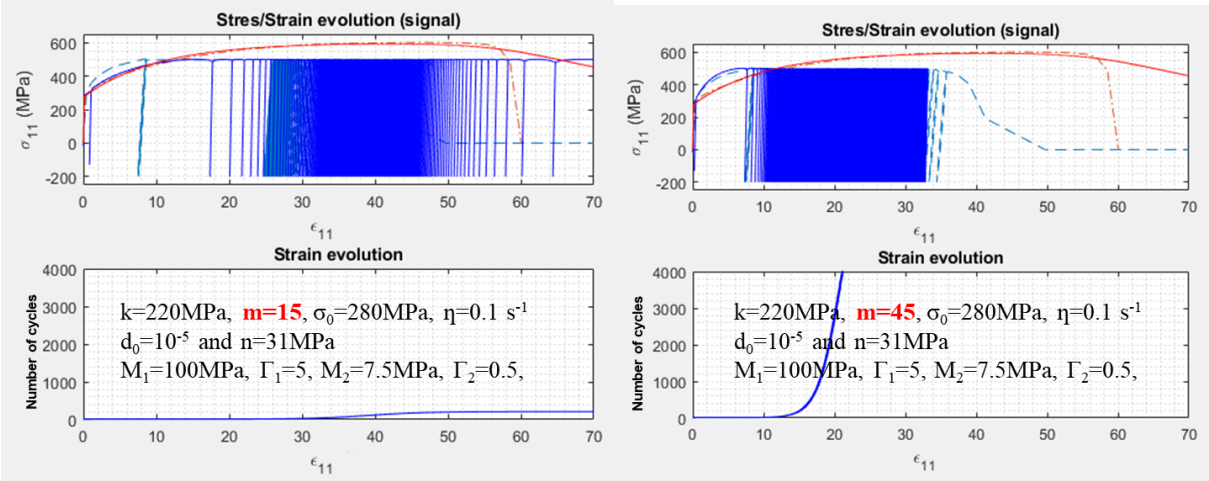

Figure 117 – Effect of the isotropic hardening parameter m

After several iterations, we propose 3 different parameters settings providing a similar solution which are summarised in Figure 118. It can be observed that these three responses show different total strain evolution and different damage evolution.

Finally, we have chosen the parameters set summarised in Table 8, which corresponds to the simulated curves in the red box of Figure 118.

It must be noted that the set of parameters proposed here, was chosen by the physical interpretation of the mechanical test performed at ambient temperature.

Table 6 – Material parameters set for model interpretation

Initial elastic yield limit	σ_0=280MPa
Viscosity parameter	η=0.1 s^{-1}
Isotropic hardening parameters	k=220MPa, m=30
Kinematic hardening parameters	M_1=400MPa, $\Gamma_1=10^3$, M_2=15MPa, Γ_2=0
Damage parameters	$d_0=1.7\ 10^{-6}$, n=20MPa

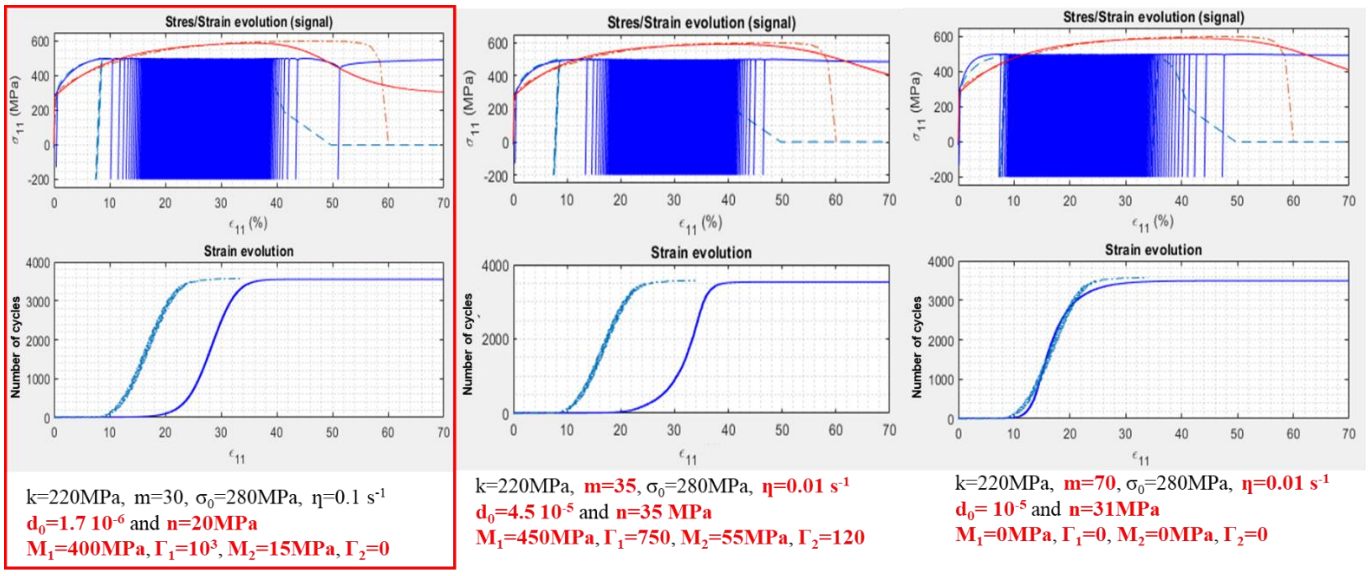

Figure 118 – Effect of parameters set on the stress-strain evolution

3.3.4. Monotonic loading: results

To interpret results of the numerical simulation, we have introduced the strong thermomechanical coupling by taking into account the temperature evolution in the stress tensor expression.

Figure 119 represents the simulation in imposed stress with a rate of 35MPa/min (dashed blue line) and the one in imposed strain with a rate of 1 mm/mn (dashed red line), in accordance to the reference test (solid blue line).

After point A , see Figure 119, which corresponds to the yield of the so-called damage zone, the two curves are no longer coincident. This phenomenon can be explained by the relation between the damage variable and the expression of the isotropic function described in eq.(53), in which the stress-strain evolution results from a competition between hardening and damage. In imposed strain simulation, when the damage zone is reached, the stress decreases down to zero, whereas in imposed stress simulation, the algorithm diverges in the damage zone.

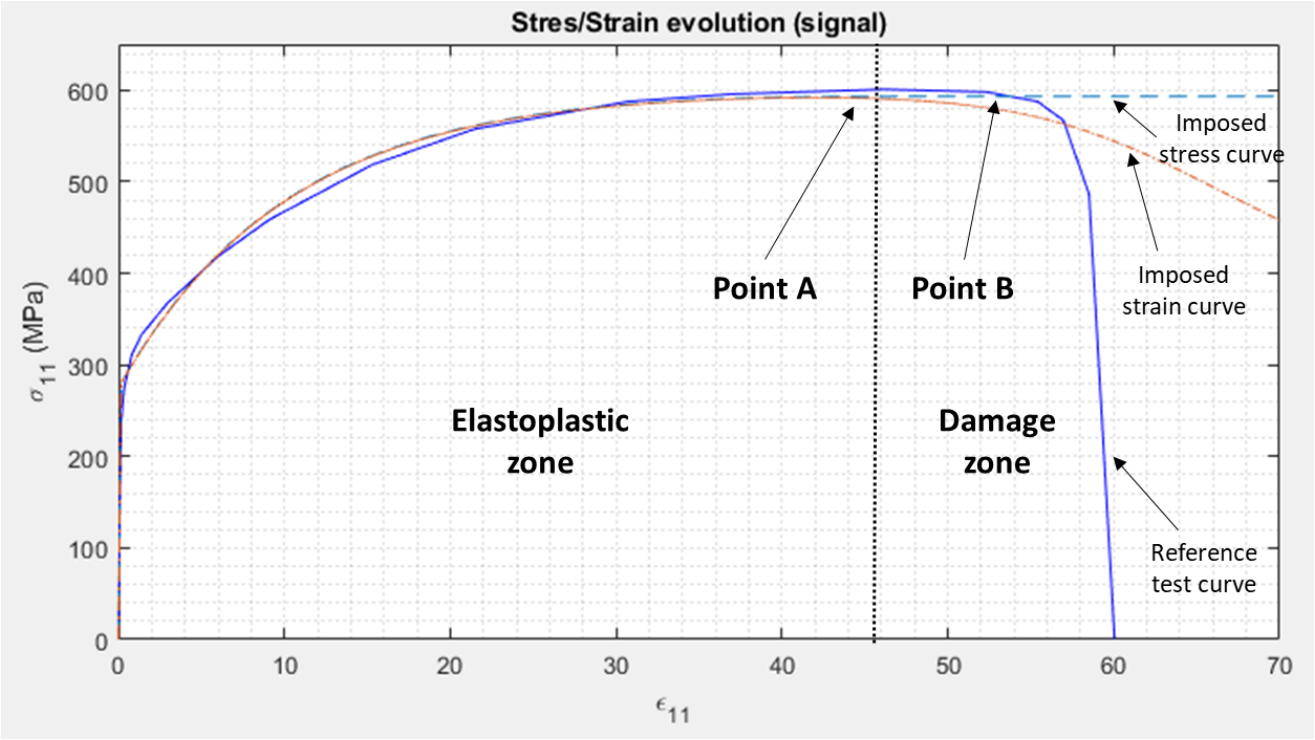

Figure 119 – Comparison of stress/strain evolution between imposed stress & imposed strain simulations and reference engineering stress-strain curve.

Figure 120 shows the damage variable evolution, which is defined in eq. (91). By comparing this evolution to the stress tensor evolution from Figure 119, we can observe that the damage variable remains close to zero up to 40% of strain. Beyond this value, the damage variable starts increasing, impacting the stress-strain evolution, see point A in the two figures. The value of d=1 is reached at 100% of strain, far from the ultimate strength observed during the experimental test, which occurs around 58% of strain, see point B in Figure 119.

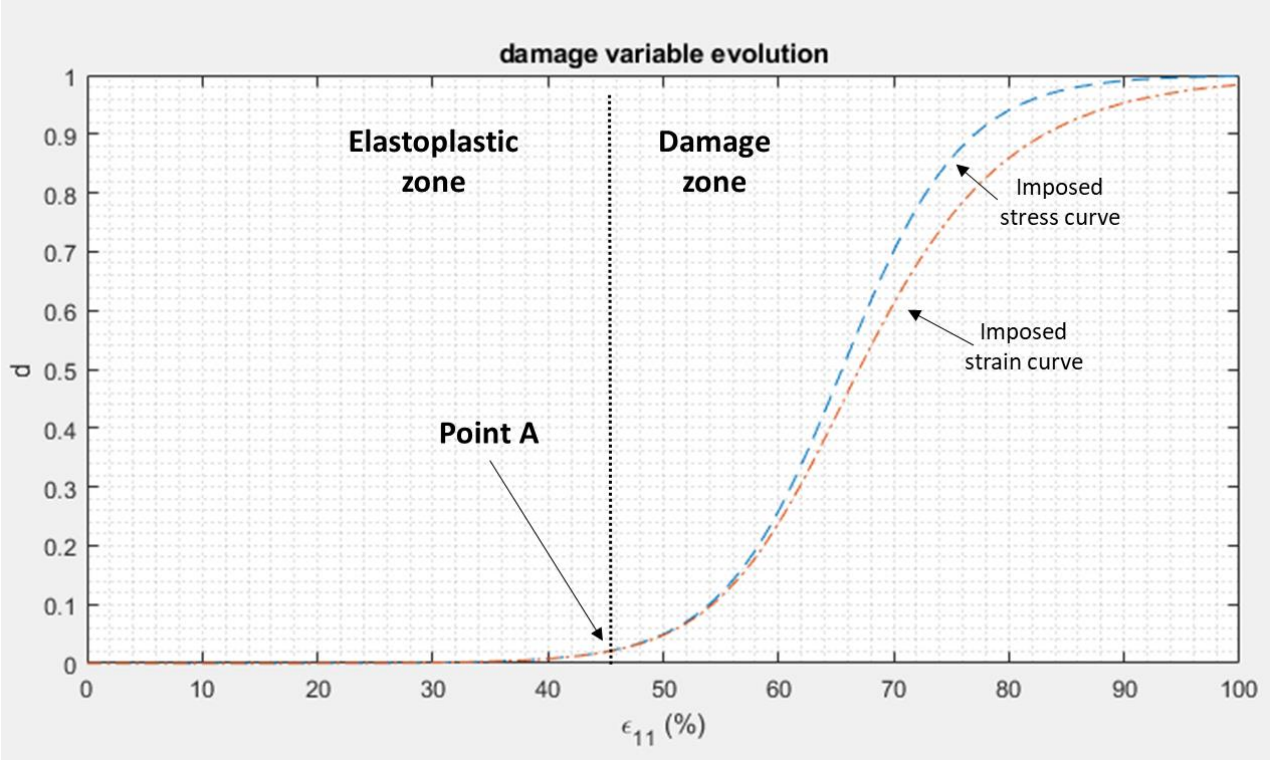

Figure 120 – Comparison of damage variable evolution between imposed stress & imposed strain simulations

When the damage variable is around 10^{-2}, see point A in Figure 120, meaning that the collapse is imminent, the total strain evolution and that of the internal variables diverge. Beyond this critical point, the computed values of the different variables are physically meaningless.

To validate the temperature evolution, the mechanical test results presented in chapter II should have been carried out under vacuum conditions, considering minimised radiation heat exchange and minimised heat conduction between the specimen and the testing machine with appropriate temperature monitoring. Due to this lack of experimental data, the temperature evolution curve presented in Figure 121 cannot be superposed to any reference curve.

The heat equation as given by eq. (100), shows that the temperature evolution is dependent of the trace of the strain tensor evolution. In the elastic domain, where all the internal variables are equal to 0, a decrease of temperature is observed, which is in agreement with classical results in thermoelasticity, see e.g. (Moreau, 2005) . When the yield strength is reached, the temperature evolution depends on dissipation mechanisms (hardening and damage) which become higher than the thermoelastic mechanism and result in an increase in temperature.

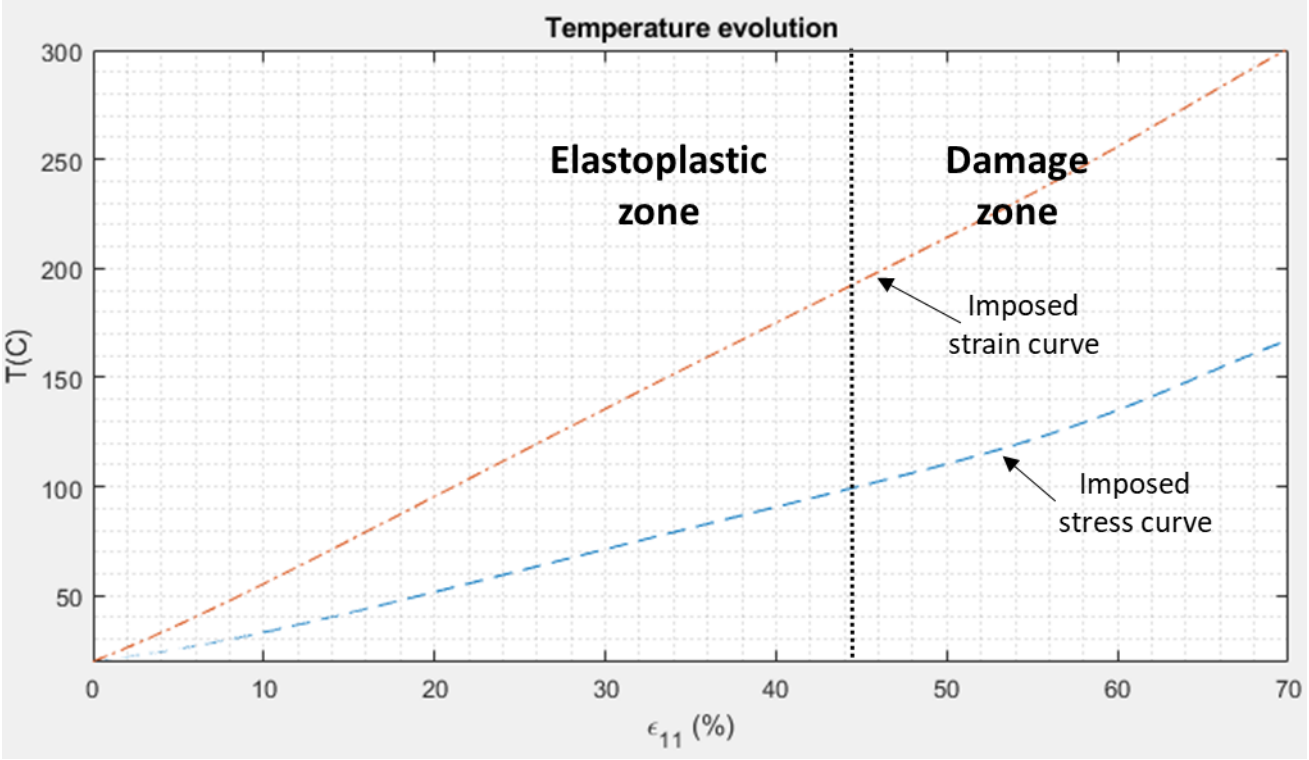

Figure 121 – Comparison of temperature evolution between imposed stress & imposed strain simulations

Note also that the strain rate difference for the two simulations, which is reported in Figure 122, justifies the temperature evolution discrepancy between the two loading configuration.

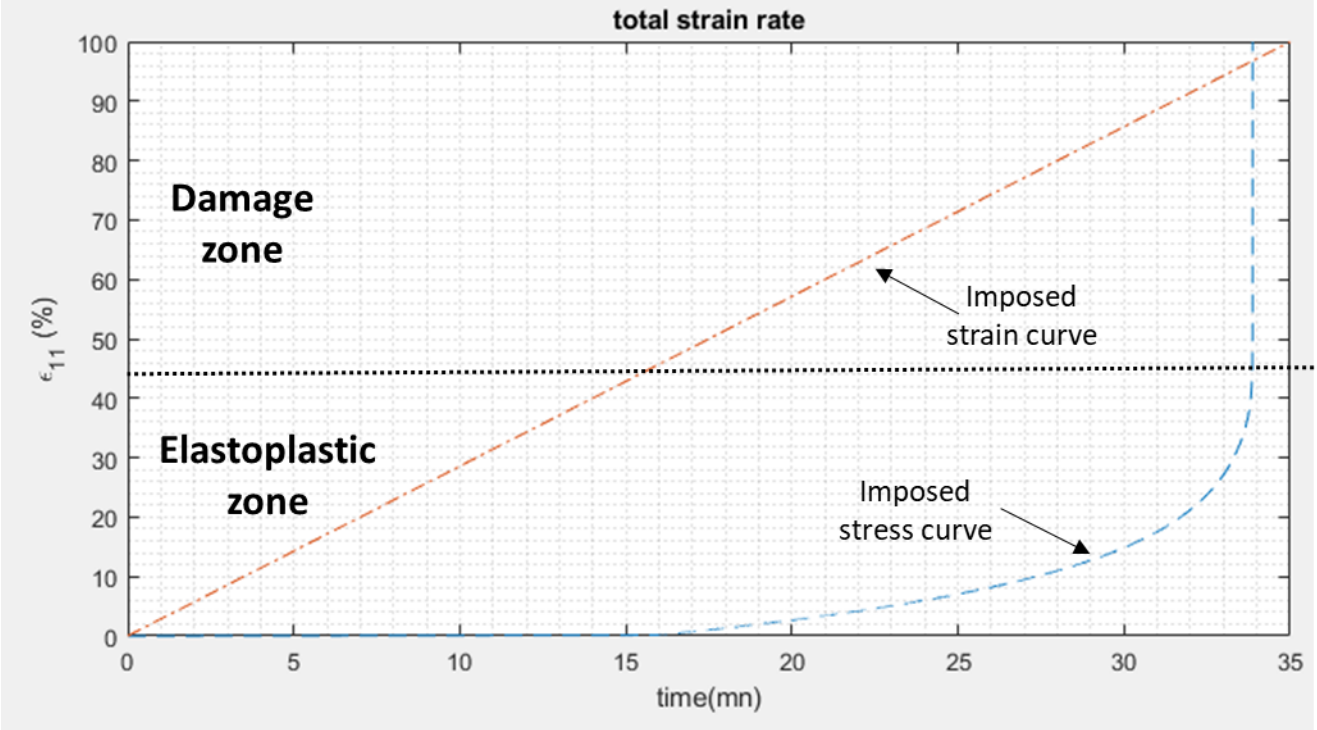

Figure 122 – Comparison of total strain evolution between imposed stress & imposed strain simulations

3.3.5. Cyclic loading: results

For the cyclic simulations, the strong thermomechanical coupling have been removed, but the temperature evolution according to the heat equation has been conserved.

Figure 123 shows the superposition of the reference engineering stress-strain curve (dashed line) obtained in the case of cyclic imposed force described in chapter II, and the simulated stress-strain evolution curve in imposed stress assumption (solid line).

The simulated curve was obtained following the sinusoidal evolution described in eq.(38), where σ_{moy} is the mean stress, $\Delta\sigma$ is the stress range and f=0.3Hz the frequency, and considering σ_{max}=500MPa and σ_{min}=-200MPa.

$$\sigma(t) = \sigma_{moy} + \frac{\Delta\sigma}{2}\sin(2\,\pi\,f\,t) \tag{135}$$

$$\sigma_{moy} = \frac{\sigma_{max} + \sigma_{min}}{2} \tag{136}$$

$$\Delta\sigma = \sigma_{max} - \sigma_{min} \tag{137}$$

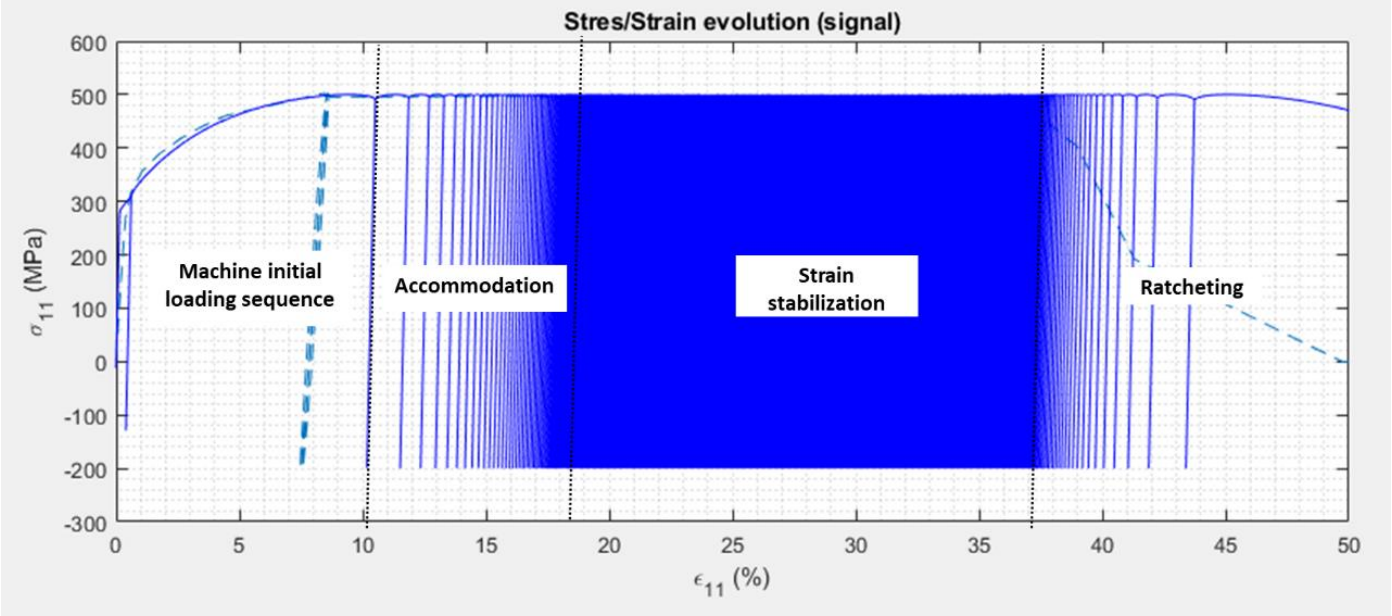

Figure 123 – Stress/strain evolution: cyclic loading with imposed stress signal

As in the experimental study, the first ten cycles correspond to the initial sequence which gradually reaches the nominal stress value, around 10% of strain. From this point up to 18% of deformation, an accommodation linked to the isotropic hardening is observed. Then, from 18% up to 37% of deformation, the evolution of the strain is almost constant: in this zone, the isotropic hardening has reached its maximum value. The last part of the curve shows the ratcheting response up to the model divergence (d=1). Beyond this critical point, the computed values of the different variables are physically meaningless.

Figure 124 gives the cumulated number of cycles with respect to the total strain evolution, where the blue dashed curve represents the 3574 cycles achieved during the reference test, and the dark blue

one the simulated one. Although the chosen parameters allow to retrieve the same number of cycle, the simulated response has an offset of 10% in strain.

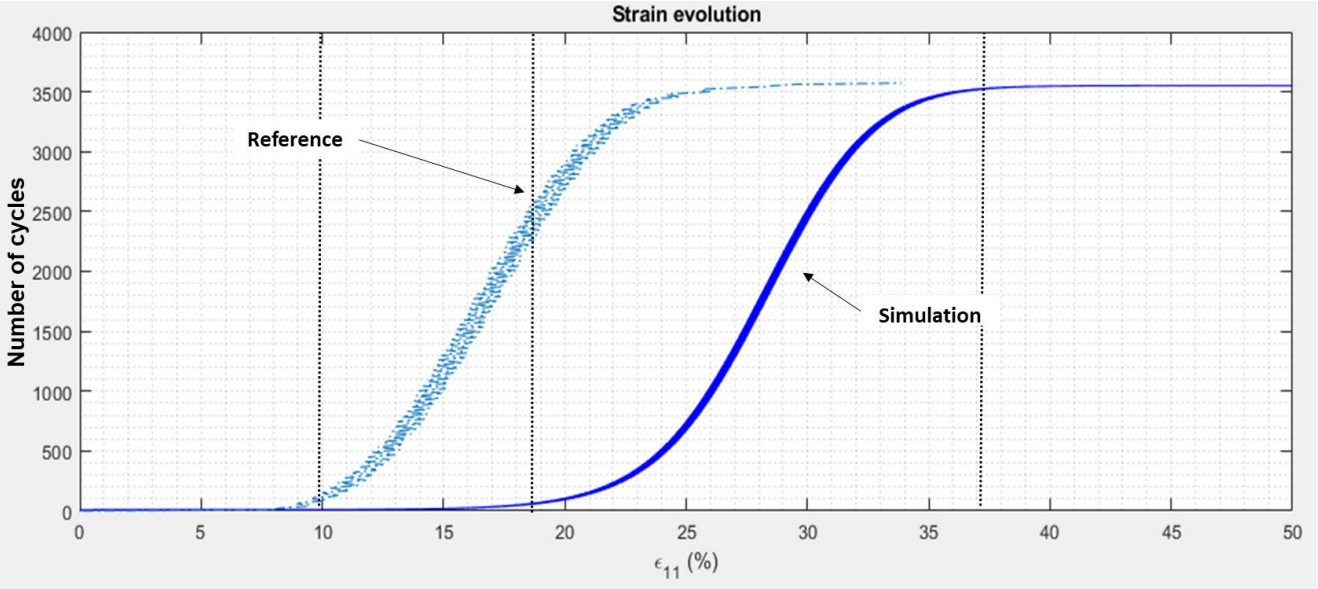

Figure 124 – Total strain state relative to cumulative number of cycles

As it has been already observed for the monotonic simulation, when the damage evolution becomes fast, the ratcheting phenomenon is triggered. In Figure 124, the total number of cycles stops growing at 35% of total strain, which corresponds to the change of slope for the damage variable, see Figure 125. Contrary to what was expected, the algorithm diverges at value of d around 0.02, far from maximum admissible value (d=1).

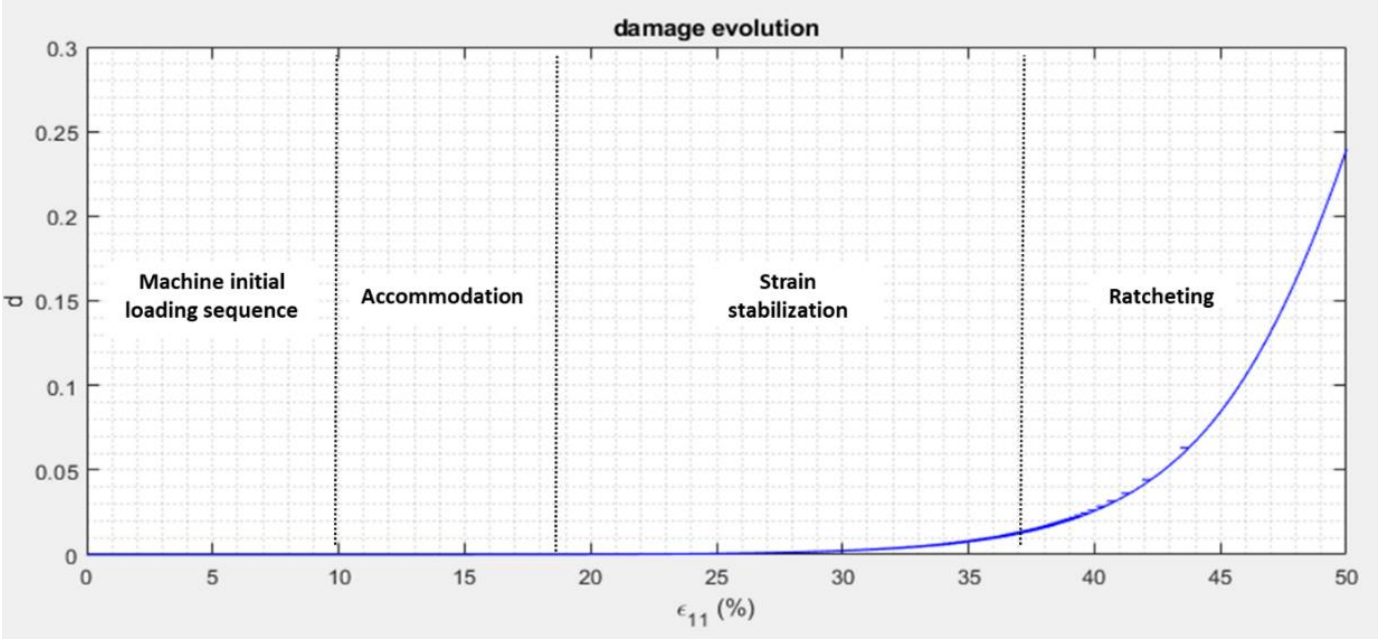

Figure 125 – Damage variable evolution

Figure 126 shows the temperature evolution linked to the mechanical behavior via eq.(100). The adiabatic hypothesis underlying the simulations does not allow any thermal dissipation, resulting in an unrealistic temperature range.

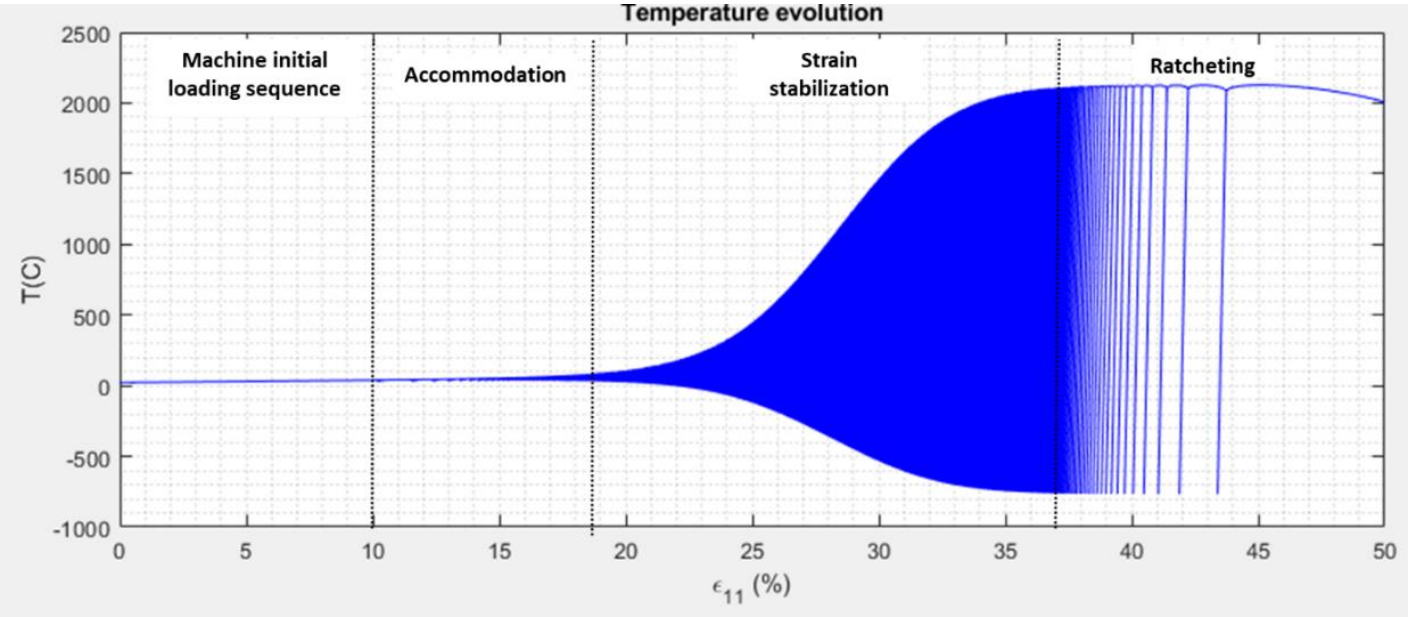

Figure 126 – Temperature evolution

Finally, the input signal has been modified by ±60MPa. The results are reported in Figure 127 and Figure 128. Compared to the reference simulation where Δσ=700MPa (blue curve), a decrease in the signal amplitude (pink curve) increases the number of cycles and reduces the total strain while an amplitude increase of the signal (red curve) induces the opposite response. From these three simulations it can be observed an elastic shakedown (small stress amplitude), a strain evolution up to ratcheting (reference signal) and a pure ratcheting response (high stress amplitude signal). Thus, the model demonstrates its ability to account for different phenomena, such as shakedown and ratcheting, depending on the stress intensity.

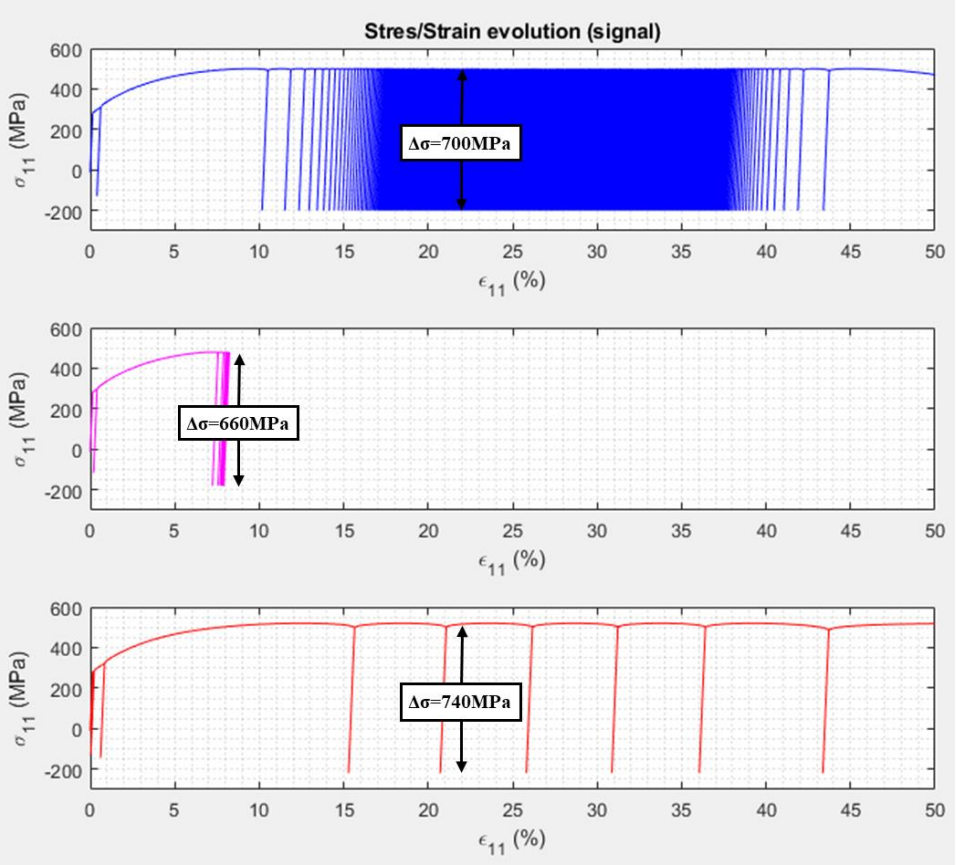

Figure 127 – Model predictions: comparison for different input signals

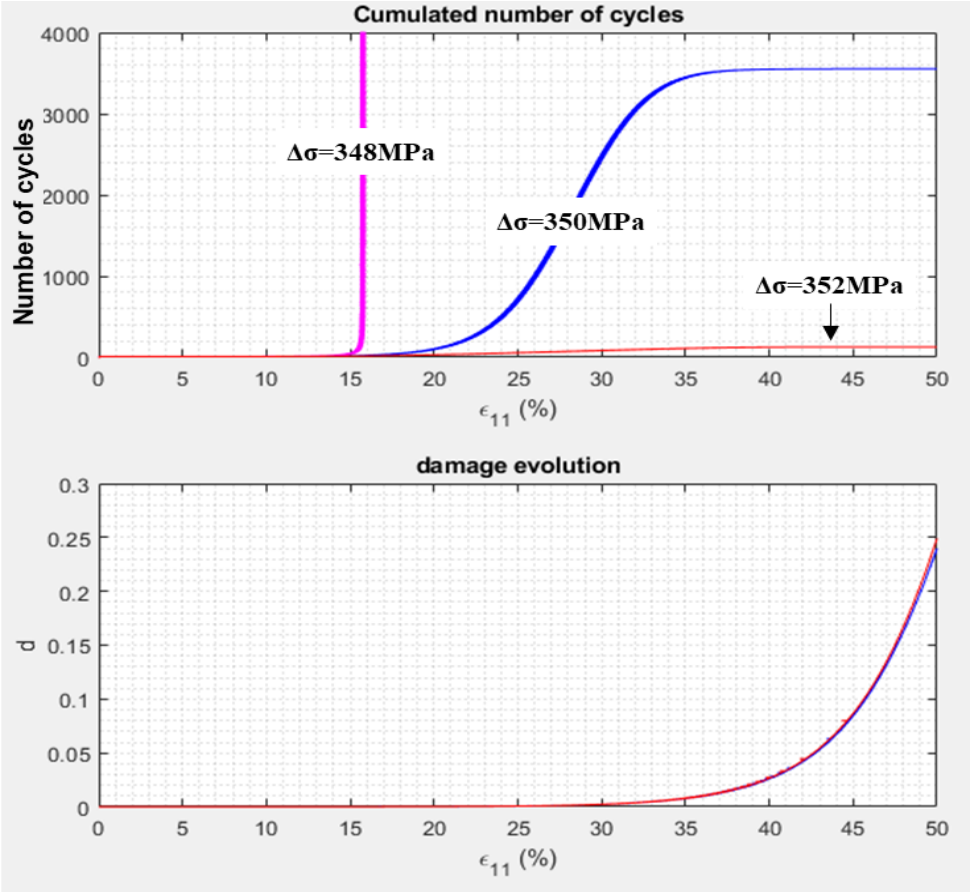

Figure 128 – Model predictions: comparison for different input signals

3.4. Conclusion

In order to take into account the temperature effect on the mechanical response, and vice-versa, the model requires two additional terms in the Helmholtz free energy ψ, which are linked to the thermal expansion and the specific heat of the material.

The hypothesis that all material parameters are temperature dependent, as it could be experimentally observed, gives a more complex expression of the entropy density, which is deduced from the partial derivative of ψ with respect to the temperature, see eq. (64). This complexity is then amplified for the development of the heat equation that requires to derivate the entropy density by time. In our case, to simplify the equations, the material parameters temperature dependence has been neglected and only the two additional terms including directly the temperature variable have been kept.

In the framework of continuum damage mechanics, for the modelling of the ductile fracture, we have proposed to couple the damage evolution with both the isotropic and the kinematic hardenings. We kept the competition between damage and isotropic hardening, but for the second one, we proposed a coupling where the hardening is amplified by the damage evolution. It results in two hardening working in opposite way, and in an expression of the Von Mises equivalent stress including damage. The model is summarised in Table 7.

The model has been tested on a homogeneous uniaxial tensile test case with strong thermomechanical coupling using Matlab® software. The identification of material parameters has been made through a heuristic method by fitting the results from the mechanical test campaign.

The results show a reliable fitting with the experimental engineering stress strain curve for the monotonic loading. We have also observed a temperature evolution dependent on the strain tensor evolution, highlighting the influence of the mechanical behaviour on the temperature. Nevertheless, the adiabatic hypothesis combined with the lack of experimental data do not allow to justify temperature variable evolution. We have also observed that the isotropic hardening response is dominant in comparison to the kinematic hardening one. This phenomena can be justified by the hypothesis made on the coupling with damage which is probably too strong. In addition, the exponential trend of the damage evolution induces a very sensitive response of the material, which also depends on the parameters set, especially during the transition between ratcheting and shakedown.

For cyclic loadings, the thermal hypothesis, which does not allow thermal dissipations, induces unrealistic temperature variation. For ensuring a more reasonable model interpretation, we have decoupled the thermal part from the mechanical one in cyclic loading condition. Under these conditions, the proposed model leads to a positive hardening for the first cycles up to a stabilisation of the strain rate and finally triggers ratcheting as observed experimentally. When the load is modified with diminution of the amplitude stress, the number of cycles increases, whereas an increase of the amplitude stress generates ratcheting. Nevertheless, the isotropic hardening dominance does not allow plastic shakedown and Baushinger effect. To improve this results, it is proposed to reduce the damage part in the coupling with kinematic hardening.

Finally, it can be concluded that the developed model, whose main objectives were to take into account a strain stabilisation or a ratcheting failure mode with simple development, meets our expectation. More complex cases (non-homogeneous stress distribution in structural problems) require the implementation of the constitutive model into a finite element software. This software must have be able to solve simultaneously heat equation and motion equation for a more realistic temperature evolution.

Table 7 – Model summary for thermo(visco)plastic model including Non-linear isotropic + multi(x3)non-linear kinematic hardening with damage

Model	**Non-linear isotropic + multi(x3)non-linear kinematic hardening with damage**
Stress tensor	$\boldsymbol{\sigma} = \lambda Tr(\boldsymbol{\varepsilon} - \boldsymbol{\varepsilon^p})\boldsymbol{G} + 2\mu(\boldsymbol{\varepsilon} - \boldsymbol{\varepsilon^p}) - (3\lambda + 2\mu)\gamma(T - T_0)\boldsymbol{G}$
Elastic threshold function	$f = J\left(\boldsymbol{\sigma} - \mathrm{d}\sum_{i=1}^{N_{kh}} M_i \boldsymbol{X_i}\right) - k(1-\mathrm{d})(1-e^{-mp}) - \sigma_0$
Isotropic function	$k(1-\mathrm{d})(1-e^{-mp})$
Kinematic function	$\mathrm{d}\sum_{i=1}^{n} M_i \boldsymbol{X}_i$
Variables evolution	$\dot{\boldsymbol{\varepsilon^p}} = \Lambda\left(\frac{3}{2J\left(\boldsymbol{\sigma} - \mathrm{d}\sum_{i=1}^{N_{kh}} M_i \boldsymbol{X_i}\right)}\right)\left(\boldsymbol{s} - \mathrm{d}\sum_{i=1}^{N_{kh}} M_i \boldsymbol{X_i}\right)$
	$\dot{\boldsymbol{X}}_{\boldsymbol{i}} = \boldsymbol{d}\dot{\boldsymbol{\varepsilon}}^{\boldsymbol{p}} - d\Lambda\Gamma_i \boldsymbol{X_i}$
	$\dot{p} = \Lambda$
	$\dot{d} = \Lambda\frac{d(1-d)}{n}\langle Tr(\boldsymbol{\sigma})\rangle$
	$= \frac{1}{\eta\sigma_0}\langle J\left(\boldsymbol{\sigma} - \mathrm{d}\sum_{i=1}^{N_{kh}} M_i \boldsymbol{X_i}\right) - k(1-\mathrm{d})(1-e^{-mp}) - \sigma_0\rangle$
Heat equation	$\frac{\rho_0 C_\varepsilon}{T_0} T\dot{T} - k_T \Delta T - r^v = -(3\lambda + 2\mu)\gamma T Tr(\dot{\boldsymbol{\varepsilon}})T + \Lambda J\left(\boldsymbol{\sigma} - \mathrm{d}\sum_{i=1}^{N_{kh}} M_i \boldsymbol{X_i}\right) + d\Lambda\sum_{i=1}^{N_{kh}} M_i \Gamma_i \boldsymbol{X_i}:\boldsymbol{X_i} + k\Lambda(1-\mathrm{d})(1-e^{-mp}) + k\left(p + \frac{1}{m}e^{-mp}\right)\Lambda\frac{d(1-d)}{n}\langle Tr(\boldsymbol{\sigma})\rangle$

Chapter 4. Numerical application

4.1. Introduction

We were able to demonstrate, on a homogeneous uniaxial tensile test, that the model can adopt different response, more precisely, ratcheting and/or shakedown depending of the cyclic load intensity. At this stage, it is mandatory to implement the proposed model in a Finite Element (FE) software and test it on more complex cases (non-homogeneous stress distribution in structural problems). This is why we propose to model an ITER VV welded support subject to representative plasma scenario comprising: cyclic thermal loads (secondary loads) and static mechanical loads (primary loads).

In this chapter, we first recall the basic FE resolution for a thermomechanical problem. This FE implementation is done in Abaqus® and is based on a variational formulation of the thermomechanical problem, which cannot be solved directly. In that case, we have made a local integration of internal variables at each Gauss point, which is commonly done using the return radial method. Due to the thermomechanical coupling and the damage variable, we had to modify the return radial method to adapt it to our model.

We present here in details the implementation of the modified radial return method and we also discuss the obtention of consistant tangent operators that are required for an integration in Abaqus® user subroutines.

In a second stage we have tested the FE formulation by simulating a cyclic tension-compression test and a cyclic torsion test, which have been compared to the reference curves presented in chapter-II.

Finally, a simplified VV geometry that is the VV “rails” was tested under thermomechanical cyclic loading.

4.2. Finite element formulation

There are many paper that discuss about FEM implementation of viscoplastic model (Kullig, et al., 2006), some other paper compares the fully thermomechanical coupling with complete dissociated analysis like (Benaarbia, et al., 2018). However, papers discussing about fully coupled thermomechanical resolution are few, and in the following paragraph, we will try to develop the FE formulation for our model.

4.2.1. Variational formulation of the thermomechanical problem

In the case of a thermomechanical coupling, we consider a closed domain, Ω, which is stress free in the initial configuration at the initial temperature, T_0. Mechanical boundary conditions apply onto $\partial\Omega_u$ for displacements and $\partial\Omega_\sigma$ for forces. Thermal boundary conditions apply onto $\partial\Omega_T$ for temperature and $\partial\Omega_q$ for thermal flux (Hugues, 1987).

The strong formulation of this thermomechanical coupling, see (Rothe, 2015), requires to find the displacement u(x,t), and the associated temperature, T(x,t), by solving together :

- the balance of linear momentum (Cauchy's first law of motion or motion equations), which can be also expressed as:

$$\boldsymbol{Div}\big(\boldsymbol{\sigma}(x,t)\big) + \boldsymbol{f^v}(x,t) = \mathbf{0} \qquad \forall\, x \in \Omega \tag{138}$$

where $\boldsymbol{f^v}$ are the body forces.

In can be noted that the stress tensor, $\boldsymbol{\sigma}$, can be dissociated in pure thermoelastic part, $\boldsymbol{\sigma^T}$, and a mechanical part, $\boldsymbol{\sigma^M}$, as it is described in chapter-III eq.(69) & eq.(70), and expressed as:

$$\boldsymbol{\sigma}(x,t) = \boldsymbol{\sigma^M}(x,t) + \boldsymbol{\sigma^T}(x,t), \tag{139}$$

- the heat equation for the proposed model, defined in chapter-III eq.(100), can be written as follows:

$$\frac{\rho_0 C_\varepsilon}{T_0} T\dot{T} = \emptyset_{int} + \boldsymbol{\sigma}:\dot{\boldsymbol{\varepsilon}} - div\ \boldsymbol{q} + r^v \qquad \forall\, x \in \Omega \tag{140}$$

Where $\emptyset_{int}$ is the intrinsic dissipation, $\boldsymbol{q}$ is the heat flux, and r^v is the external heat source.

In addition to this two equations, the following boundary conditions (BC) can be taken into account:

- the surface heat flux is applied onto the external surface, where it appears:

$$\boldsymbol{q} = \boldsymbol{q^s} \qquad \text{onto } \partial\Omega q \tag{141}$$

- the temperature is applied onto the external surface, where it appears:

$$\boldsymbol{T} = \boldsymbol{T}_u \qquad \text{onto } \partial\Omega T \tag{142}$$

where this two domain are linked by the following properties $\partial\Omega q \cap \partial\Omega T = 0$ and $\partial\Omega q \cup \partial\Omega T = d\Omega$

- the imposed displacement is set as follow:

$$\boldsymbol{u} = \boldsymbol{u}_0 \qquad \text{onto } \partial\Omega u \tag{143}$$

- the force is applied normal to the external surface:

$$\boldsymbol{\sigma}.\boldsymbol{n} = t \qquad \text{onto } \partial\Omega\sigma \tag{144}$$

where this two domain are linked by the following property $\partial\Omega u \cap \partial\Omega\sigma = 0$ and $\partial\Omega u \cup \partial\Omega\sigma = d\Omega$

Finally, for the initial conditions (IC):

- the initial temperature is set as:

$$T(x, T = 0) = T_0 \tag{145}$$

- the initial stress state is set as:

$$\boldsymbol{\sigma}(x, T = 0) = 0 \tag{146}$$

This set of equations (from eq.(138) to eq.(146)), used for the strong formulation, cannot be solved directly. In that case we are proposing a finite element resolution using the weak formulation of the thermomechanical problem.

At small strain, we consider the following weak formulation of the mechanical problem to be solved, taking into account the initial and boundary condition described above, find $(\boldsymbol{u}, T)$ such that $\forall(\boldsymbol{\delta u}, \boldsymbol{\delta} T)$:

$$\begin{cases} \int_\Omega (\boldsymbol{\sigma^T} + \boldsymbol{\sigma^M}) : \left(\boldsymbol{grad}\ (\delta \boldsymbol{u})\right)_{sym} d\Omega - \int_{\partial\Omega\sigma} \left((\boldsymbol{\sigma^T} + \boldsymbol{\sigma^M}).\boldsymbol{n}\right).\delta \boldsymbol{u} ds - \int_\Omega f^v.\delta \boldsymbol{u}\, d\Omega = 0 \\ \int_\Omega \left(\frac{\rho_0 C_\varepsilon}{T_0} T\dot{T}\delta T - T\left(\frac{\boldsymbol{\partial}(\boldsymbol{\sigma^T} + \boldsymbol{\sigma^M})}{\partial T} : \dot{\boldsymbol{\varepsilon}}\right)\delta T - \emptyset_{int}\delta T - r^v \delta T \right. \\ \left. -\boldsymbol{q}.\boldsymbol{grad}\ \delta T\right) d\Omega + \int_{\partial\Omega q} (\boldsymbol{q^s}.\boldsymbol{n})\delta T ds = 0 \end{cases} \tag{147}$$

This is a coupled nonlinear problem formulated in displacement and temperature. $\boldsymbol{\sigma}$ as unknown variable have to be calculated knowing the strain tensor $\boldsymbol{\varepsilon}$ (function of the displacement $\mathbf{u}$) and the temperature T. In addition, this problem is time dependent that is why to solve it, it is necessary to:

- make a local integration of the internal variables of constitutive model,
- adopt a global time discretisation scheme,
- linearize the problem around a known solution.

4.2.2. Local integration of internal variables: return radial method

For the internal variables local integration, we consider a time interval $[t_n;t_{n+1}]$, all quantities are known t_n and we assume that we have predictive values for $\mathbf{u}_{n+1}$ and T_{n+1} at time t_{n+1}. Therefore, we need to compute the evolution of the internal variables during the time interval knowing their values at a previous time increment and having a prediction of the current strain value $\boldsymbol{\varepsilon}_{n+1}$ and temperature T_{n+1} locally at each Gauss point. Where the indice n and n+1 denote values at time t_n and t_{n+1}. In this work, we follow the return mapping approach as earlier proposed by NGuyen Quoc Son in his PhD thesis (1973), and used later by several authors (see for instance (Hughes, et al., 2000) (Adam, et al., 2005) (Benaarbia, et al., 2018)), for which global flow chart is given in Figure 129.

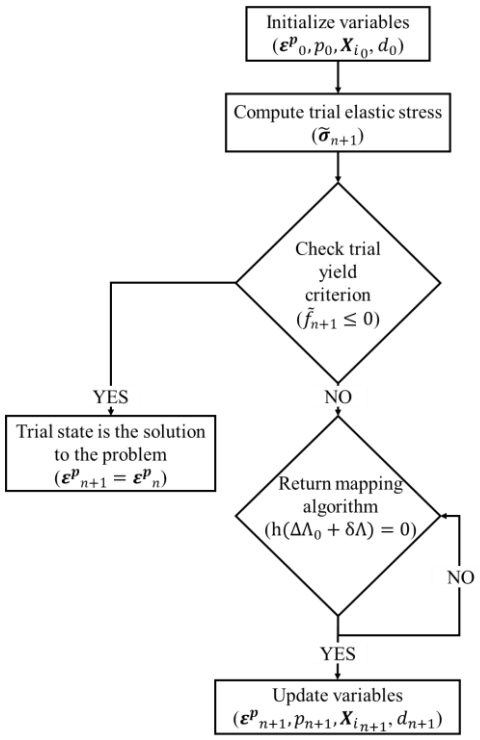

Figure 129 – Flow chart for the return-mapping algorithm (Hughes, et al., 2000)

We are looking for the evolution of stress tensor which corresponds of solving the following expression:

$$\boldsymbol{\sigma}_{n+1} = \lambda Tr(\boldsymbol{\varepsilon}_{n+1} - \boldsymbol{\varepsilon}^{\boldsymbol{p}}{}_{n+1})\boldsymbol{G} + 2\mu(\boldsymbol{\varepsilon}_{n+1} - \boldsymbol{\varepsilon}^{\boldsymbol{p}}{}_{n+1}) - (3\lambda + 2\mu)\gamma(T_{n+1} - T_0)\boldsymbol{G} \tag{148}$$

From this expression $\boldsymbol{\varepsilon}_{n+1}$, T_{n+1}, correspond to predicted value defined by global Newton Raphson scheme. $\boldsymbol{\varepsilon}^{\boldsymbol{p}}{}_{n+1}$ is the unknown variable to be defined.

The return mapping algorithm is based on the definition of a trial state for which the plastic flow and other internal state variables are frozen. We therefore assume that the trial state at time t_{n+1}, is equal to the last converged value, so that:

$$\begin{aligned} \tilde{\boldsymbol{\varepsilon}}^{\boldsymbol{p}}{}_{n+1} &= \boldsymbol{\varepsilon}^{\boldsymbol{p}}{}_n \\ \tilde{\boldsymbol{X}}_{(i)n+1} &= \boldsymbol{X}_{(i)n} \quad \forall \boldsymbol{i} \\ \tilde{p}_{n+1} &= p_n \\ \tilde{d}_{n+1} &= d_n \end{aligned} \tag{149}$$

We can therefore define a trial stress tensor $\tilde{\boldsymbol{\sigma}}_{n+1}$, for which the plastic flow is frozen (we use the incompressibility of the plastic flow: Tr($\boldsymbol{\varepsilon}^{\mathrm{p}}$)=0)such that:

$$\tilde{\boldsymbol{\sigma}}_{n+1} = \lambda Tr(\boldsymbol{\varepsilon}_{n+1})\boldsymbol{G} + 2\mu(\boldsymbol{\varepsilon}_{n+1} - \boldsymbol{\varepsilon^p}_n) - (3\lambda + 2\mu)\gamma(T_{n+1} - T_0)\boldsymbol{G} \quad (150)$$

We recall here the main equations describing the model that we have developed:

Elastic threshold function $$f = \mathrm{J}(\boldsymbol{S}) - k(1-\mathrm{d})(1 - e^{-mp}) - \sigma_0 \quad (151)$$

Von Mises equivalent stress $$\mathrm{J}(\boldsymbol{S}) = \sqrt{\frac{3}{2}}\left\| \boldsymbol{Dev}\left(\boldsymbol{\sigma} - d\sum_{i=1}^{N_{kh}} M_i \boldsymbol{X_i}\right)\right\| \quad (152)$$

Plastic strain tensor evolution $$\dot{\boldsymbol{\varepsilon^p}} = \sqrt{\frac{3}{2}}\mathbf{n}\Lambda \quad (153)$$

Plastic flow direction $$\mathbf{n} = \frac{\boldsymbol{S}}{\|\mathbf{S}\|} \quad (154)$$

Kinematic hardening tensor evolution $$\boldsymbol{X_i} = d\dot{\boldsymbol{\varepsilon^p}} - d\Lambda\Gamma_i \boldsymbol{Dev}(\boldsymbol{X}_\mathrm{i}) \quad (155)$$

Isotropic hardening variable evolution $$\dot{p} = \Lambda \quad (156)$$

Damage variable evolution $$\dot{d} = \Lambda\frac{d(1-d)}{n}\langle Tr(\boldsymbol{\sigma})\rangle \quad (157)$$

Plastic multiplier (viscoplastic model) $$\Lambda = \frac{1}{\eta\sigma_0}\langle f\rangle \quad (158)$$

The expression of the isotropic hardening variable evolution according to the numerical approach, could be discretise by using the backward Euler approximation on the interval $\Delta t \in [t_n; t_{n+1}]$, as follow:

$$\dot{p} = \frac{p_{n+1} - p_n}{\Delta t} \quad (159)$$

$$\Delta \mathrm{t} = \mathrm{t}_{n+1} - \mathrm{t}_n \quad (160)$$

Since $p_{n+1}$is an unknown variable, it is possible of expressing the isotropic hardening variable evolution ($\dot{p}$) via the Backward Euler method resolution which induces that:

$$\frac{p_{n+1} - p_n}{\Delta t} = \Lambda_{n+1} \quad (161)$$

Since the plastic flow multiplier (Λ) is directly linked to the isotropic hardening variable evolution, it could be deduced its evolution ($\Delta\Lambda$) via the backward Euler method resolution as follow:

$$\Delta\Lambda = p_{n+1} - p_n = \Delta t\,\Lambda_{n+1} = \Delta t\frac{1}{\eta\sigma_0}\langle f_{n+1}\rangle \quad (162)$$

Following the same methodology, the expression of other variables evolution could be defined as:

$$\boldsymbol{\varepsilon^p}_{n+1} - \boldsymbol{\varepsilon^p}_n = \sqrt{\frac{3}{2}}\mathbf{n}_{n+1}\Delta\Lambda \quad (163)$$

$$\boldsymbol{X}_{(i)n+1} - \boldsymbol{X}_{(i)n} = d_{n+1}\sqrt{\frac{3}{2}}\mathbf{n}_{n+1}\Delta\Lambda - d_{n+1}\Gamma_i \boldsymbol{X}_{(i)n+1}\Delta\Lambda \quad (164)$$

$$d_{n+1} - d_n = \Delta\Lambda\,\frac{d_{n+1}(1-d_{n+1})}{n}\langle Tr(\boldsymbol{\sigma}_{n+1})\rangle \quad (165)$$

Additionally to the expression of trial stress tensor $\tilde{\boldsymbol{\sigma}}_{n+1}$ defined in eq.(150), the return radial method requires the definition of a trial elastic threshold that is described for this model as:

$$\tilde{f}_{n+1} = \sqrt{\frac{3}{2}}\|\tilde{\mathbf{S}}_{n+1}\| - \mathrm{R}(\mathrm{p}_n, \mathrm{d}_n) - \sigma_0 \tag{166}$$

where the expression of the isotropic function including damage variable, $\mathrm{R}(\mathrm{p_n},\mathrm{d_n})$, is described as follows:

$$\mathrm{R}(\mathrm{p}_n, \mathrm{d}_n) = -k(1-d_n)(1-e^{-m\mathrm{p}_n}) \tag{167}$$

And the trial deviatoric stress tensor ($\tilde{\mathbf{S}}_{n+1}$) is expressed as follows:

$$\tilde{\mathbf{S}}_{n+1} = \boldsymbol{Dev}\left(\tilde{\boldsymbol{\sigma}}_{n+1} - d_n \sum_{i=1}^{N_{kh}} M_i \boldsymbol{X}_{(i)n}\right) \tag{168}$$

If the expression of the new yield criterion based on elastic prediction is below zero ($\tilde{\mathrm{f}}_{\mathrm{n+1}} \leq 0$), which could correspond to an elastic deformation then it appears:

$$\boldsymbol{\varepsilon^p}_{n+1} = \boldsymbol{\varepsilon^p}_n \tag{169}$$
$$p_{n+1} = p_n \tag{170}$$
$$\boldsymbol{X}_{(i)n+1} = \boldsymbol{X}_{(i)n} \tag{171}$$
$$d_{n+1} = d_n \tag{172}$$

In that case, the mechanical part of the expression of $\boldsymbol{\sigma}_{n+1}$ described in eq.(148) could be solved.

Otherwise, if the trial elastic threshold is above zero ($\tilde{\mathrm{f}}_{\mathrm{n+1}} > 0$), which means that plastic deformations has occurred. We have to find a solution to $\boldsymbol{\varepsilon}^{\mathbf{p}}{}_{\mathrm{n+1}}$, which is defined as:

$$\boldsymbol{\varepsilon^p}_{n+1} = \sqrt{\frac{3}{2}}\mathbf{n}_{n+1}\,\Delta t\,\frac{1}{\eta\sigma_0}\langle \mathrm{J}(\mathbf{S}_{n+1}) - \mathrm{R}(\mathrm{p}_{n+1}, \mathrm{d}_{n+1}) - \sigma_0\rangle + \boldsymbol{\varepsilon^p}_n \tag{173}$$

From the eq.(173), the remaining unknown variables are:

- plastic flow direction $\mathbf{n}_{n+1}$,
- Von Mises equivalent stress $\mathrm{J}(\mathbf{S}_{n+1})$
- isotropic hardening function $\mathrm{R}(\mathrm{p}_{n+1}, \mathrm{d}_{n+1})$.

The radial return method or closest point projection consists in having an expression of $\boldsymbol{\varepsilon}^{\mathbf{p}}{}_{\mathrm{n+1}}$ function of trial expressions, variables at time increment $\mathrm{t_n}$ and $\Delta\Lambda$ (Hughes, et al., 2000). In our model, the isotropic hardening is coupled with damage, which does not allow a direct resolution as for simpler models.

Lets start from the expression of $\boldsymbol{\sigma}_{\mathrm{n+1}}$ described in eq.(148) for expressing the deviatoric stress tensor $\mathbf{S}_{n+1}$:

$$\boldsymbol{Dev}(\boldsymbol{\sigma}_{n+1}) = 2\mu\boldsymbol{Dev}(\boldsymbol{\varepsilon}_{n+1} - \boldsymbol{\varepsilon^p}_{n+1}) \tag{174}$$

$$\boldsymbol{Dev}(\boldsymbol{\sigma}_{n+1}) = 2\mu\boldsymbol{Dev}\big(\boldsymbol{\varepsilon}_{n+1} - \boldsymbol{\varepsilon^p}_{n+1} + (\boldsymbol{\varepsilon^p}_n - \boldsymbol{\varepsilon^p}_n)\big) \tag{175}$$

By using the same method, we can also express the deviatoric trial stress tensor, as follow:

$$\boldsymbol{Dev}(\tilde{\boldsymbol{\sigma}}_{n+1}) = 2\mu \boldsymbol{Dev}(\boldsymbol{\varepsilon}_{n+1} - \boldsymbol{\varepsilon^p}_n) \tag{176}$$

In that case, the deviatoric stress tensor could be express function of its trial definition as follow:

$$\boldsymbol{Dev}(\boldsymbol{\sigma}_{n+1}) = \boldsymbol{Dev}(\tilde{\boldsymbol{\sigma}}_{n+1}) - 2\mu \boldsymbol{Dev}(\boldsymbol{\varepsilon^p}_{n+1} - \boldsymbol{\varepsilon^p}_n) \tag{177}$$

According to the expression of the plastic strain tensor evolution described in eq.(163), it appears:

$$\boldsymbol{Dev}(\boldsymbol{\sigma}_{n+1}) = \boldsymbol{Dev}(\tilde{\boldsymbol{\sigma}}_{n+1}) - 2\mu \boldsymbol{Dev}\left(\sqrt{\frac{3}{2}}\mathbf{n}_{n+1}\Delta\Lambda\right) \tag{178}$$

Let's continue from the expression of the kinematic strain tensor $\mathbf{X}_{(i)n+1}$ described in eq.(164), which could be rewritten as follow:

$$\boldsymbol{X}_{(i)n+1} = \left(d_{n+1}\sqrt{\frac{3}{2}}\mathbf{n}_{n+1}\Delta\Lambda + \boldsymbol{X}_{(i)n}\right)\frac{1}{(1 + d_{n+1}\Gamma_i\Delta\Lambda)} \tag{179}$$

Let's defined the new variable δ function of ΔΛ and d_{n+1} as follow:

$$\delta_{(i)n+1} = \frac{1}{(1 + d_{n+1}\Gamma_i\Delta\Lambda)} \tag{180}$$

Starting from eq.(179), the expression of the deviatoric part of the kinematic stress tensor appears as:

$$\begin{gathered}\boldsymbol{Dev}\left(\sum_{i=1}^{N_{kh}} M_i \boldsymbol{X}_{(i)n+1}\right) = \\ \boldsymbol{Dev}\left(d_{n+1}^2 \sum_{i=1}^{N_{kh}} M_i \delta_{(i)n+1}\sqrt{\frac{3}{2}}\mathbf{n}_{n+1}\Delta\Lambda\right) + \boldsymbol{Dev}\left(d_{n+1}\sum_{i=1}^{N_{kh}} M_i \boldsymbol{X}_{(i)n}\delta_{(i)n+1}\right)\end{gathered} \tag{181}$$

By combining the eq.(178) and the eq.(181), we can retrieve a part of the expression of deviatoric stress $\mathbf{S}_{n+1}$ as follow:

$$\begin{gathered}\mathbf{S}_{n+1} = \\ \boldsymbol{Dev}(\tilde{\boldsymbol{\sigma}}_{n+1}) - 2\mu \boldsymbol{Dev}\left(\sqrt{\frac{3}{2}}\mathbf{n}_{n+1}\Delta\Lambda\right) \\ -\boldsymbol{Dev}\left(d_{n+1}^2 \sum_{i=1}^{N_{kh}} M_i \delta_{(i)n+1}\sqrt{\frac{3}{2}}\mathbf{n}_{n+1}\Delta\Lambda\right) - \boldsymbol{Dev}\left(d_{n+1}\sum_{i=1}^{N_{kh}} M_i \boldsymbol{X}_{(i)n}\delta_{(i)n+1}\right)\end{gathered} \tag{182}$$

That could also be expressed as:

$$\begin{gathered}\mathbf{S}_{n+1} = \\ \boldsymbol{Dev}(\tilde{\boldsymbol{\sigma}}_{n+1}) - d_{n+1}\sum_{i=1}^{N_{kh}} M_i \boldsymbol{X}_{(i)n}\delta_{(i)n+1} \\ -\left(2\mu + d_{n+1}^2 \sum_{i=1}^{N_{kh}} M_i \delta_{(i)n+1}\right)\left(\sqrt{\frac{3}{2}}\mathbf{n}_{n+1}\Delta\Lambda\right)\end{gathered} \tag{183}$$

Let's defined the new variable ξ function of ΔΛ and δ as follow:

$$\xi_{(i)n+1} = \sqrt{\frac{3}{2}}\Delta\Lambda\left(2\mu + d_{n+1}^2\sum_{i=1}^{N_{kh}} M_i\delta_{(i)n+1}\right) \tag{184}$$

At this stage, it remains to define an expression of the plastic flow direction $\mathbf{n}_{n+1}$ as a function of ΔΛ and d_{n+1}. Since the plastic flow direction is function of deviatoric stress $\mathbf{S}_{n+1}$, see eq.(154) , the eq. (183) can be developed as follow:

$$\mathbf{S}_{n+1} = \boldsymbol{Dev}(\widetilde{\boldsymbol{\sigma}}_{n+1}) - d_{n+1}\sum_{i=1}^{N_{kh}} M_i\boldsymbol{X}_{(i)n}\delta_{(i)n+1} - \frac{\mathbf{S}_{n+1}}{\|\mathbf{S}_{n+1}\|}\xi_{n+1} \tag{185}$$

That could also be expressed as:

$$\mathbf{S}_{n+1}\left(\frac{\|\mathbf{S}_{n+1}\| + \xi_{n+1}}{\|\mathbf{S}_{n+1}\|}\right) = \boldsymbol{Dev}(\widetilde{\boldsymbol{\sigma}}_{n+1}) - d_{n+1}\sum_{i=1}^{N_{kh}} M_i\boldsymbol{X}_{(i)n}\delta_{(i)n+1} \tag{186}$$

Computing the norm of eq.(186), it can be obtained the following expression:

$$\|\mathbf{S}_{n+1}\| + \|\xi_{n+1}\| = \left\|\boldsymbol{Dev}(\widetilde{\boldsymbol{\sigma}}_{n+1}) - d_{n+1}\sum_{i=1}^{N_{kh}} M_i\boldsymbol{X}_{(i)n}\delta_{(i)n+1}\right\| \tag{187}$$

Knowing that ξ_{n+1} being strictly positive, let's introduce the expression of $\left\|\boldsymbol{S}_{n+1}^{*}\right\|$ from eq.(187) as follow:

$$\|\mathbf{S}_{n+1}\| = \left\|\boldsymbol{S}_{n+1}^{*}\right\| - \xi_{n+1} \tag{188}$$

Where

$$\left\|\boldsymbol{S}_{n+1}^{*}\right\| = \left\|\boldsymbol{Dev}(\widetilde{\boldsymbol{\sigma}}_{n+1}) - d_{n+1}\sum_{i=1}^{N_{kh}} M_i\boldsymbol{X}_{(i)n}\delta_{(i)n+1}\right\| \tag{189}$$

Finally, the viscoplastic tensor flow direction $\mathbf{n}_{n+1}$ can be expressed as:

$$\mathbf{n}_{n+1} = \frac{\boldsymbol{Dev}(\widetilde{\boldsymbol{\sigma}}_{n+1}) - d_{n+1}\sum_{i=1}^{N_{kh}} M_i\boldsymbol{X}_{(i)n}\delta_{(i)n+1}}{\left\|\boldsymbol{Dev}(\widetilde{\boldsymbol{\sigma}}_{n+1}) - d_{n+1}\sum_{i=1}^{N_{kh}} M_i\boldsymbol{X}_{(i)n}\delta_{(i)n+1}\right\|} = \frac{\boldsymbol{S}_{n+1}^{*}}{\left\|\boldsymbol{S}_{n+1}^{*}\right\|} \tag{190}$$

At this stage, all unknown variable from eq.(173) have been expressed using ΔΛ, d_{n+1} and variable at the time increment t_n. To compute this values, the following non-linear system (that comes from eqs.(162), (165) requires to be solved:

$$r(\Delta\Lambda, d_{n+1})\begin{cases}\Delta\Lambda - \Delta t\dfrac{1}{\eta\sigma_0}\left\langle\sqrt{\dfrac{3}{2}}\left(\left\|\boldsymbol{S}_{n+1}^{*}\right\| - \xi_{n+1}\right) - \mathrm{R}(\mathrm{p}_{n+1}, \mathrm{d}_{n+1}) - \sigma_0\right\rangle = 0 \\ d_{n+1} - d_n - \Delta\Lambda\,\dfrac{d_{n+1}(1-d_{n+1})}{n}\langle Tr(\widetilde{\boldsymbol{\sigma}}_{n+1})\rangle = 0\end{cases} \tag{191}$$

Due to the plastic incompressibility, it can be demonstrated that:

$$Tr(\boldsymbol{\sigma}_{n+1}) = Tr(\widetilde{\boldsymbol{\sigma}}_{n+1}) \tag{192}$$

And we recall the expression of the isotropic hardening combined with the damage variable from eq.(167), as follow:

$$\mathrm{R}(\mathrm{p}_{n+1}, \mathrm{d}_{n+1}) = -k(1-d_{n+1})\left(1-e^{-m(\Delta\Lambda+\mathrm{p}_n)}\right) \tag{193}$$

The previous system, eq.(191), can be linearized and solved with a local Newtown scheme.

It is proposed at this stage to use a Taylor development, starting from a known points $\Delta\Lambda$, d_{n+1} and looking for the increment ($\delta\Lambda$, $\delta\mathrm{d}$) for solving the following system equations:

$$\mathrm{r}(\Delta\Lambda+\delta\Lambda, d_{n+1}+\delta\mathrm{d}\,) = 0 \tag{194}$$

We make a serial development and it appears:

$$\mathrm{r}(\Delta\Lambda+\delta\Lambda, d_{n+1}+\delta\mathrm{d}) = \mathrm{r}(\Delta\Lambda, d_{n+1}) + \mathrm{K}.(\delta\Lambda, \delta\mathrm{d})^{\mathrm{T}} + \mathrm{o}(\delta\Lambda, \delta\mathrm{d}) \tag{195}$$

We iterate in the local newton scheme:

$$\begin{bmatrix}\delta\Lambda\\ \delta\mathrm{d}\end{bmatrix} = -\mathrm{K}^{-1}.\,\mathrm{r}(\Delta\Lambda, d_{n+1}) \tag{196}$$

until

$$\|\mathrm{r}(\Delta\Lambda+\delta\Lambda, d_{n+1}+\delta\mathrm{d}\,)\| < 10^{-8} \tag{197}$$

Where the local tangent operator is:

$$K = \begin{bmatrix} \dfrac{\partial r_1(\Delta\Lambda, d_{n+1})}{\partial\Delta\Lambda} & \dfrac{\partial r_1(\Delta\Lambda, d_{n+1})}{\partial \mathrm{d}_{n+1}} \\ \dfrac{\partial r_2(\Delta\Lambda, d_{n+1})}{\partial\Delta\Lambda} & \dfrac{\partial r_2(\Delta\Lambda, d_{n+1})}{\partial \mathrm{d}_{n+1}} \end{bmatrix} \tag{198}$$

The computation of following derivatives are requested to express the local tangent operator K:

$$\begin{aligned} \frac{\partial\xi_{n+1}}{\partial\Delta\Lambda} &= \frac{\partial}{\partial\Delta\Lambda}\left(\sqrt{\frac{3}{2}}\Delta\Lambda\left(2\mu + d_{n+1}^2\sum_{i=1}^{N_{kh}} M_i\delta_{(i)n+1}\right)\right) \\ &= \frac{\xi_{n+1}}{\Delta\Lambda} - \sqrt{\frac{3}{2}}\Delta\Lambda d_{n+1}^3\sum_{i=1}^{N_{kh}} M_i\Gamma_i\delta_{(i)n+1}^2 \end{aligned} \tag{199}$$

$$\begin{aligned} \frac{\partial\left\|\boldsymbol{S}_{n+1}^{*}\right\|}{\partial\Delta\Lambda} &= \frac{\partial}{\partial\Delta\Lambda}\left\|\boldsymbol{Dev}(\widetilde{\boldsymbol{\sigma}}_{n+1}) - d_{n+1}\sum_{i=1}^{N_{kh}} M_i\boldsymbol{X}_{(i)n}\delta_{(i)n+1}\right\| \\ &= d_{n+1}^2\sum_{i=1}^{N_{kh}} M_i\Gamma_i\delta_{(i)n+1}^2\boldsymbol{X}_{(i)n} : \mathbf{n}_{n+1} \end{aligned} \tag{200}$$

$$\begin{aligned} \frac{\partial\mathrm{R}(\mathrm{p}_{n+1}, \mathrm{d}_{n+1})}{\partial\Delta\Lambda} &= \frac{\partial}{\partial\Delta\Lambda}\left(k(1-d_{n+1})\left(1-e^{-m(\Delta\Lambda+\mathrm{p}_n)}\right)\right) \\ &= -mk(1-d_{n+1})e^{-m(\Delta\Lambda+\mathrm{p}_n)} \end{aligned} \tag{201}$$

$$\frac{\partial\xi_{n+1}}{\partial\mathrm{d}_{n+1}} = \frac{\partial}{\partial\mathrm{d}_{n+1}}\left(\sqrt{\frac{3}{2}}\Delta\Lambda\left(2\mu + d_{n+1}^2\sum_{i=1}^{N_{kh}} M_i\delta_{(i)n+1}\right)\right) \tag{202}$$

$$= \sqrt{\frac{3}{2}}\Delta\Lambda\left(\sum_{i=1}^{N_{kh}} M_i\delta_{(i)n+1} - d_{n+1}\Delta\Lambda\sum_{i=1}^{N_{kh}} M_i\Gamma_i\delta_{(i)n+1}^2\right)$$

$$\frac{\partial\left\|\boldsymbol{S}_{n+1}^{*}\right\|}{\partial \mathrm{d}_{n+1}} = \frac{\partial}{\partial \mathrm{d}_{n+1}}\left\|\boldsymbol{Dev}(\widetilde{\boldsymbol{\sigma}}_{n+1}) - d_{n+1}\sum_{i=1}^{N_{kh}} M_i\boldsymbol{X}_{(i)n}\delta_{(i)n+1}\right\| \qquad (203)$$

$$= \left(\sum_{i=1}^{N_{kh}} d_{n+1}\,\Delta\Lambda\,M_i\Gamma_i\delta_{(i)n+1}^2\boldsymbol{X}_{(i)n} - M_i\delta_{(i)n+1}\boldsymbol{X}_{(i)n}\right):\mathbf{n}_{n+1}$$

$$\frac{\partial \mathrm{R}(\mathrm{p}_{n+1},\mathrm{d}_{n+1})}{\partial \mathrm{d}_{n+1}} = \frac{\partial}{\partial \mathrm{d}_{n+1}}\left(k(1-d_{n+1})\left(1-e^{-m(\Delta\Lambda+\mathrm{p}_n)}\right)\right) \qquad (204)$$

$$= k\left(1-e^{-m(\Delta\Lambda+\mathrm{p}_n)}\right)$$

The local tangent operator reads:

$$K = \begin{bmatrix} \sqrt{\frac{3}{2}}\left(\frac{\partial\left\|\boldsymbol{S}_{n+1}^{*}\right\|}{\partial\Delta\Lambda} - \frac{\partial\xi_{n+1}}{\partial\Delta\Lambda}\right) + \frac{\partial \mathrm{R}(\mathrm{p}_{n+1},\mathrm{d}_{n+1})}{\partial\Delta\Lambda} - \frac{\eta}{\Delta t} & \sqrt{\frac{3}{2}}\left(\frac{\partial\left\|\boldsymbol{S}_{n+1}^{*}\right\|}{\partial \mathrm{d}_{n+1}} - \frac{\partial\xi_{n+1}}{\partial \mathrm{d}_{n+1}}\right) + \frac{\partial \mathrm{R}(\mathrm{p}_{n+1},\mathrm{d}_{n+1})}{\partial \mathrm{d}_{n+1}} \\ -\frac{d_{n+1}(1-d_{n+1})}{n}\langle Tr(\widetilde{\boldsymbol{\sigma}}_{n+1})\rangle & 1-\Delta\Lambda\frac{d_{n+1}(1-2d_{n+1})}{n}\langle Tr(\widetilde{\boldsymbol{\sigma}}_{n+1})\rangle \end{bmatrix} \qquad (205)$$

The method for defining all variables evolution from which σ depends has been defined. We are now able to give σ(x,T) which is required for the finite element formulation.

In comparison to linear kinematic and/or linear isotropic models, which can be solved with an explicit resolution, the present model requires having a local newton resolution.

4.2.3. Implementation in Abaqus®: user subroutine

The finite element software Abaqus® has been selected for the implementation of our model, because it implements the previously presented two field weak formulation and we can use subroutines to define the mechanical and thermal contributions.

4.2.3.1. Global time discretisation scheme

Abaqus® uses a backward-difference scheme that consists in the following approximations: $\dot{T} = (T(t_{n+1}) - T(t_n))/\Delta t$ and $\dot{\boldsymbol{u}} = (\boldsymbol{u}(t_{n+1}) - \boldsymbol{u}(t_n))/\Delta t$. We note T_{n+1} the temperature at time t_{n+1} and we note T_n the temperature at time t_n (same notation for **u**). Therefore, the time discretisation of the system eq. (147), on a time interval $[t_n, t_{n+1}]$, find $(\boldsymbol{u}_{n+1}, T_{n+1})$ knowing $(\boldsymbol{u}_n, T_n)$ such that $\forall(\boldsymbol{\delta u}_{n+1}, \boldsymbol{\delta} T_{n+1})$, appears as:

$$\begin{cases} \int_\Omega (\boldsymbol{\sigma}^{\boldsymbol{T}}_{n+1} + \boldsymbol{\sigma}^{\boldsymbol{M}}_{n+1}) : \left(\boldsymbol{grad}(\delta \boldsymbol{u}_{n+1})\right)_{sym} d\Omega - \int_{\partial\Omega\sigma} \left((\boldsymbol{\sigma}^{\boldsymbol{T}}_{n+1} + \boldsymbol{\sigma}^{\boldsymbol{M}}_{n+1})\boldsymbol{n}_{n+1}\right) \delta \boldsymbol{u}_{n+1} ds \\ \qquad - \int_\Omega \boldsymbol{f}^{\boldsymbol{v}} \boldsymbol{u}_{n+1}\, d\Omega = 0 \\ \int_\Omega \left(\frac{\rho_0 C_\varepsilon}{T_0} T_{n+1} \frac{(T_{n+1} - T_n)}{\Delta t} \delta T_{n+1} - T_{n+1} \left(\frac{\boldsymbol{\partial}(\boldsymbol{\sigma}^{\boldsymbol{T}}_{n+1} + \boldsymbol{\sigma}^{\boldsymbol{M}}_{n+1})}{\partial T_{n+1}} : \frac{(\boldsymbol{\varepsilon}_{n+1} - \boldsymbol{\varepsilon}_n)}{\Delta t} \right) \delta T_{n+1} \right) d\Omega \\ \int_\Omega (-r^v \delta T_{n+1} - \emptyset_{int} \delta T_{n+1} - \boldsymbol{q_{n+1}}.\, \boldsymbol{grad}\, \delta T_{n+1}) d\Omega + \int_{\partial\Omega q} (\boldsymbol{q}^{\boldsymbol{s}}.\, \boldsymbol{n}_{n+1}) \delta T_{n+1} ds = 0 \end{cases} \quad (206)$$

4.2.3.2. Problem linearization: global Newton Raphson scheme

At this stage the problem has been discretise in time, but it remain nonlinear, see system eq. (206). It is a common practice to linearize the problem by using a Newton Raphson scheme for having the following formulation:

$$\begin{pmatrix} K_{\boldsymbol{uu}} & K_{\boldsymbol{u}T} \\ K_{T\boldsymbol{u}} & K_{TT} \end{pmatrix} \begin{pmatrix} \Delta_{\boldsymbol{u}} \\ \Delta_T \end{pmatrix} = \begin{pmatrix} f(\boldsymbol{u}_{n+1}) \\ f(T_{n+1}) \end{pmatrix} \quad (207)$$

Where K represent the tangent operator, $f(\boldsymbol{u}_{n+1})$ and $f(T_{n+1})$ are defined in the system eq. (206), and $\Delta_{\mathbf{u}}$ and Δ_T are respectively the displacement and the temperature increment.

For this problem formulation, Abaqus® proposes different subroutines. In our case we have selected the:

- UMAT subroutine, which is dedicated to the mechanical part only, and for which we need to compute: the mechanical part of the stress tensor $\boldsymbol{\sigma}^{\boldsymbol{M}}$**,** the intrinsic dissipation $\emptyset_{int}$ and the latent heat term $T\left(\frac{\boldsymbol{\partial}\boldsymbol{\sigma}^{\boldsymbol{M}}}{\partial T} : \dot{\boldsymbol{\varepsilon}}\right)$,
- UMATHT subroutine, which is dedicated to the thermal part only, and for which we need to compute: the heat capacity $\rho_0 C_\varepsilon (T/T_0) T$ and the thermal conductivity **q**.

Note that the previous expression have been extracted from the system eq. (206), and for the sake of simplicity, we have noted all quantities at time t_{n+1} without indexes.

Furthermore, the thermal part of the stress tensor $\boldsymbol{\sigma^T}$ can be taken into account with the expansion material property that can be defined independently of UMAT and UMATHT subroutine. In this case the strain passed as argument in UMAT is only the mechanical strain (expansion contribution is previously removed).

For defining the tangent operator K, previously introduced in eq.(207), we need to define the following expressions:

- The variation of the stress increment with respect to the strain increment, which is required in all the analysis. In Abaqus®, this variable is denominated as DDS DDE and is described as follow:

$$\frac{\partial \boldsymbol{\sigma}^{\boldsymbol{M}}_{n+1}}{\partial \boldsymbol{\varepsilon}_{n+1}} \tag{208}$$

- The variation of the heat generation increment (caused by the mechanical working of the material) with respect to the strain increment, which is required for thermomechanical coupling only and noted as DRPL DE:

$$\frac{\partial \emptyset_{int}}{\partial \boldsymbol{\varepsilon}_{n+1}} + \left(\frac{\partial \boldsymbol{\sigma}^{\boldsymbol{M}}_{n+1}}{\partial \boldsymbol{\varepsilon}_{n+1}} : \frac{(\boldsymbol{\varepsilon}_{n+1} - \boldsymbol{\varepsilon}_n)}{\Delta t} \right) \tag{209}$$

- The variation of the stress increment with respect to the temperature, (required for thermomechanical coupling only) and noted as DDS DDT:

$$\frac{\partial \boldsymbol{\sigma}^{\boldsymbol{M}}_{n+1}}{\partial T_{n+1}} \tag{210}$$

- The variation of the heat generation increment (mechanical work) with respect to the temperature, (required for thermomechanical coupling only) and noted as DRPL DT:

$$\frac{\partial \emptyset_{int}}{\partial T_{n+1}} + \left(\frac{\partial \boldsymbol{\sigma}^{\boldsymbol{M}}_{n+1}}{\partial T_{n+1}} : \frac{(\boldsymbol{\varepsilon}_{n+1} - \boldsymbol{\varepsilon}_n)}{\Delta t} \right) \tag{211}$$

Since the thermal part of the stress tensor is solved independently, and taking into account the hypothesis we did, where the material parameter are not temperature dependent, it can deduced that DDS DDT=0 and DRPL DT=0.

Let's develop the expression of the variation of the stress increment with respect to the strain increment (DDS DDE):

$$\frac{\partial \boldsymbol{\sigma}^{\boldsymbol{M}}_{n+1}}{\partial \boldsymbol{\varepsilon}_{n+1}} = \frac{\partial \boldsymbol{\sigma}^{\boldsymbol{M}}_{n+1}}{\partial \boldsymbol{\varepsilon}_{n+1}} + \frac{\partial \boldsymbol{\sigma}^{\boldsymbol{M}}_{n+1}}{\partial \boldsymbol{\varepsilon}^{\boldsymbol{p}}_{n+1}} \frac{\partial \boldsymbol{\varepsilon}^{\boldsymbol{p}}_{n+1}}{\partial \boldsymbol{\varepsilon}_{n+1}} \tag{212}$$

From this new expression we need to develop the expression of $\mathrm{d}\boldsymbol{\varepsilon}^{\boldsymbol{p}}_{n+1}$, starting from eq.(163), we can deduce:

$$\mathrm{d}\boldsymbol{\varepsilon}^{\boldsymbol{p}}_{n+1} = \left(\sqrt{\frac{3}{2}} \mathbf{n}_{n+1} \right) \mathrm{d}\Delta\Lambda + \left(\sqrt{\frac{3}{2}} \Delta\Lambda \right) \mathrm{d}\mathbf{n}_{n+1} \tag{213}$$

Following the same methodology, we start from eq.(190) and we find the following expression of $\mathrm{d}\mathbf{n}_{n+1}$:

$$\mathrm{d}\mathbf{n}_{n+1} = \frac{1}{\left\|\boldsymbol{S}^{*}_{n+1}\right\|}(\mathbb{I}_{\mathbf{4}} - \mathbf{n}_{n+1}\otimes\mathbf{n}_{n+1}):\mathrm{d}\boldsymbol{S}^{*}_{n+1} \tag{214}$$

The deviatoric projector is defined as follow:

$$\mathbb{P} = \mathbb{I}_{\mathbf{4}} - \frac{1}{3}\boldsymbol{G}\otimes\boldsymbol{G} \tag{215}$$

where $\mathbb{I}_{\mathbf{4}}$ is the 4th identity tensor.

According to the similar expression, let's simplify the eq. (214) as follow:

$$\mathrm{d}\mathbf{n}_{n+1} = \mathbb{P}_{\boldsymbol{S}}:\mathrm{d}\boldsymbol{S}^{*}_{n+1} \tag{216}$$

Starting from mechanical part of the stress tensor defined in eq.(148), we obtain the following equation:

$$\mathrm{d}\boldsymbol{\sigma}^{\boldsymbol{M}}_{n+1} = (2\mu\mathbb{P} + \lambda\boldsymbol{G}\otimes\boldsymbol{G}):\mathrm{d}\boldsymbol{\varepsilon}_{n+1} - 2\mu\mathbb{P}\mathrm{d}\boldsymbol{\varepsilon}^{\boldsymbol{p}}_{n+1} \tag{217}$$

$$\mathrm{d}\boldsymbol{\sigma}^{\boldsymbol{M}}_{n+1} = \mathbb{C}:\mathrm{d}\boldsymbol{\varepsilon}_{n+1} - 2\mu\mathbb{P}\mathrm{d}\boldsymbol{\varepsilon}^{\boldsymbol{p}}_{n+1} \tag{218}$$

where $\mathbb{C}$ is the Hooke's fourth order tensor.

Similarly, starting from the mechanical part of the deviatoric stress tensor defined in eq.(150), we obtain the following equation:

$$\mathrm{d}\widetilde{\boldsymbol{\sigma}}^{\boldsymbol{M}}_{n+1} = \mathbb{C}:\mathrm{d}\boldsymbol{\varepsilon}_{n+1} \tag{219}$$

Still following the same approach, we start from eq.(189) and we find the expression of $\mathrm{d}\boldsymbol{S}^{*}_{n+1}$:

$$\mathrm{d}\boldsymbol{S}^{*}_{n+1} = \mathbb{P}:\mathrm{d}\widetilde{\boldsymbol{\sigma}}^{\boldsymbol{M}}_{n+1} - \left(\sum_{i=1}^{N_{kh}} M_i\boldsymbol{X}_{(i)n}\delta_{(i)n+1}\right)\mathrm{d}d_{n+1} - \left(\sum_{i=1}^{N_{kh}} M_i\boldsymbol{X}_{(i)n}d_{n+1}\right)\mathrm{d}\delta_{(i)n+1} \tag{220}$$

For simplifying the expression of the tangent matrix, which is defined later in this chapter, let's define $\mathbf{R}_1$ and $\mathbf{R}_2$ as follow:

$$\boldsymbol{R}_1 = \sum_{i=1}^{N_{kh}} M_i\boldsymbol{X}_{(i)n}\delta_{(i)n+1} \tag{221}$$

$$\boldsymbol{R}_2 = \sum_{i=1}^{N_{kh}} M_i\boldsymbol{X}_{(i)n}d_{n+1} \tag{222}$$

Let's continue from eq.(180) and define the expression of $\mathrm{d}\delta_{(i)n+1}$:

$$\mathrm{d}\delta_{(i)n+1} = \left(-\left(\delta_{(i)n+1}\right)^2\Gamma_i\Delta\Lambda\right)\mathrm{d}d_{n+1}\left(-\left(\delta_{(i)n+1}\right)^2\Gamma_i d_{n+1}\right)\mathrm{d}\Delta\Lambda \tag{223}$$

We note the expression R_3 and R_4 as follow:

$$R_3 = -\left(\delta_{(i)n+1}\right)^2\Gamma_i\Delta\Lambda \tag{224}$$

$$R_4 = -\left(\delta_{(i)n+1}\right)^2\Gamma_i d_{n+1} \tag{225}$$

Numerical application

To obtain the expression of the variation operator $\mathrm{d}d_{n+1}$ and $\mathrm{d}\Delta\Lambda$, we have to differentiate the non-linear system defined in eq.(196), that can be developed as follow:

$$\begin{cases} K_{11}\mathrm{d}\Delta\Lambda + K_{12}\mathrm{d}d_{n+1} + + \overbrace{\left(\sqrt{\frac{3}{2}}\mathbf{n}_{n+1}:\mathbb{P}:\mathbb{C}\right)}^{\boldsymbol{H_1}}:\mathrm{d}\boldsymbol{\varepsilon}_{n+1} = 0 \\ K_{21}\mathrm{d}\Delta\Lambda + K_{22}\mathrm{d}d_{n+1} + \overbrace{\left(\Delta\Lambda\,\frac{d_{n+1}(1-d_{n+1})}{n}\langle Tr(\widetilde{\boldsymbol{\sigma}}_{n+1})\rangle 3\lambda\boldsymbol{G}\right)}^{\boldsymbol{H_2}}:\mathrm{d}\boldsymbol{\varepsilon}_{n+1} = 0 \end{cases} \tag{226}$$

It can be noticed that the expression of the tangent matrix operators K_{11}, K_{12}, K_{21}, K_{22} are given from the local integration solution.

From the previous system eq.(226), it can be obtained the expression of $\mathrm{d}\Delta\Lambda$ and $\mathrm{d}d_{n+1}$:

$$\begin{cases} \mathrm{d}\Delta\Lambda = \dfrac{K_{12}\boldsymbol{H_2} - K_{22}\boldsymbol{H_1}}{\det(K)}:\mathrm{d}\boldsymbol{\varepsilon}_{n+1} \\ \mathrm{d}d_{n+1} = \dfrac{K_{21}\boldsymbol{H_1} - K_{11}\boldsymbol{H_2}}{\det(K)}:\mathrm{d}\boldsymbol{\varepsilon}_{n+1} \end{cases} \tag{227}$$

From these expression of $\mathrm{d}\Delta\Lambda$ and $\mathrm{d}d_{n+1}$, we can now develop the expression $\mathrm{d}\mathbf{n}_{n+1}$, previously described in eq.(214), and we obtain the following equation:

$$\mathrm{d}\mathbf{n}_{n+1} = \mathbb{P}_{\boldsymbol{S}}:\begin{pmatrix} \mathbb{P}:\mathrm{d}\widetilde{\boldsymbol{\sigma}}^{\boldsymbol{M}}_{n+1} - \boldsymbol{R}_1\left(\dfrac{K_{21}\boldsymbol{H_1} - K_{11}\boldsymbol{H_2}}{\det(K)}:\mathrm{d}\boldsymbol{\varepsilon}_{n+1}\right) \\ -\boldsymbol{R_2}R_3\left(\dfrac{K_{21}\boldsymbol{H_1} - K_{11}\boldsymbol{H_2}}{\det(K)}:\mathrm{d}\boldsymbol{\varepsilon}_{n+1}\right) \\ -\boldsymbol{R_2}R_4\left(\dfrac{K_{12}\boldsymbol{H_2} - K_{22}\boldsymbol{H_1}}{\det(K)}:\mathrm{d}\boldsymbol{\varepsilon}_{n+1}\right) \end{pmatrix} \tag{228}$$

$$\mathrm{d}\mathbf{n}_{n+1} = \underbrace{\mathbb{P}_{\boldsymbol{S}}:\left(\mathbb{P}:\mathbb{C} - (\boldsymbol{R}_1 + \boldsymbol{R_2}R_3)\otimes\left(\frac{K_{21}\boldsymbol{H_1} - K_{11}\boldsymbol{H_2}}{\det(K)}\right) - (\boldsymbol{R_2}R_4)\otimes\left(\frac{K_{12}\boldsymbol{H_2} - K_{22}\boldsymbol{H_1}}{\det(K)}\right)\right):\mathrm{d}\boldsymbol{\varepsilon}_{n+1}}_{\mathbb{C}_N} \tag{229}$$

Finally, by introducing eq.(229) in eq.(218), it appears:

$$\mathrm{d}\boldsymbol{\sigma}^{\boldsymbol{M}}_{n+1} = \left(\mathbb{C} - \sqrt{6}\mu\mathbb{P}:\left(\mathbf{n}_{n+1}\otimes\frac{K_{12}\boldsymbol{H_2} - K_{22}\boldsymbol{H_1}}{\det(K)}\right) - \sqrt{6}\mu\mathbb{P}:\mathbb{C}_N\right):\mathrm{d}\boldsymbol{\varepsilon}_{n+1} \tag{230}$$

Similar development is done for DRPL DE.

4.3. Numerical tests application

For checking the numerical implementation of our model, we have first simulated a 0D analysis case and compared it to the Matlab® simulations. This method, which is based on a single element, allows verifying the model response independently to the geometry and the mesh configuration. We have then modelled the cylinder specimens used for the test campaign and simulated two representative cyclic load cases. Finally, a real geometry that is the ITER Vacuum Vessel rail, have been modelled and tested under thermomechanical scenario.

For the following FE simulations, we have used the material parameters defined in the Chapter-III with the "0D simulations".We recall the linear elastic material parameters, extracted from the RCC-MR nuclear code:

- density, ρ_0=7930 kg/m^3,
- mean thermal expansion coefficient, γ=15.3.10^{-6} K^{-1},
- material specific heat, C_ε=472 J/kg.K,
- Lamé coefficients, λ =115.384 GPa and μ =76.923 GPa, (E=200 GPa and υ=0.3)
- yield limit, σ_0=220 MPa.
-

And the non-linear parameters defined with Matlab®:

- initial elastic yield limit, σ_0=280MPa,
- viscosity parameter, η=0.1 s^{-1},
- isotropic hardening parameters, k=220MPa and m=30,
- kinematic hardening parameters, M_1=400MPa, Γ_1=10^3, M_2=15MPa and Γ_2=0,

damage parameters, d_0=1.7 10^{-6} and n=20MPa.

4.3.1. Model validation with 0D analysis

The model validation was made on a single element, see Figure 132, loaded by a cyclic imposed stress sinusoidal evolution described in eq.(38), where σ_{moy} is the mean force, $\Delta\sigma$ is the force range and f=0.3Hz the frequency, and considering σ_{max}=500MPa and σ_{min}=-200MPa.

The comparison between the Matlab and the Abaqus simulations, presented in Figure 130 and Figure 131, validates the numerical implementation.

At the end of the damage evolution, see Figure 131, it can be observed a small deviation, which is justified by the solver differences between the two softwares.

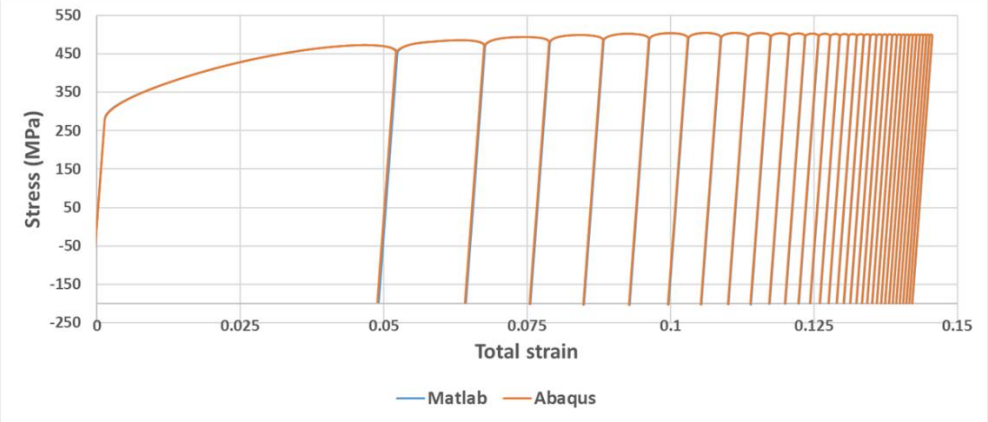

Figure 130 – Stress/strain evolution: comparison between Matlab® simulation and Abaqus® simulation

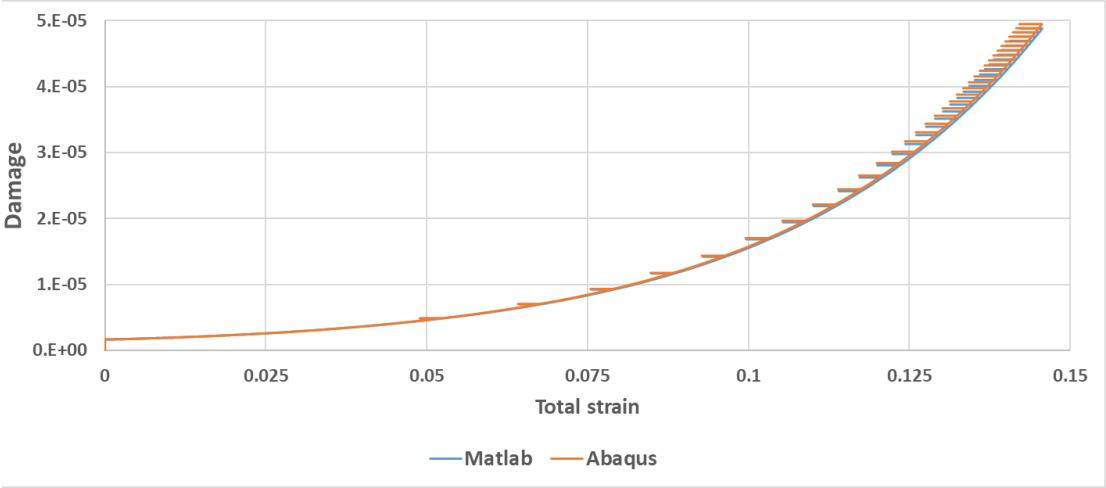

Figure 131 – Damage evolution: comparison between Matlab® simulation and Abaqus® simulation

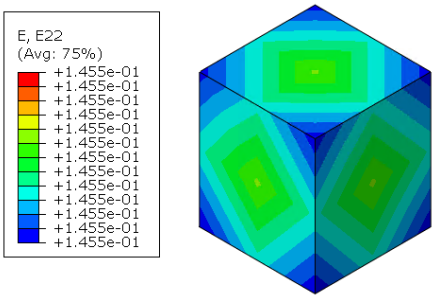

Figure 132 –Strain map at the end of the simulation

4.3.2. Comparison between FE simulations and mechanical tests

The second step of the model validation was made on a cyclic tension-compression test with imposed force, and on cyclic torsion test, both are non-homogeneous cases. The geometry is based on the cylinder described in chapter-II, see Figure 53, and it was meshed with quadratic hexahedron elements of 5mm size, type C3D20 for mechanical analysis and C3D20T for thermomechanical ones, see Figure 133. It can be noticed that no mesh sensitivity was done for this study since we have not observed strong localization effect in the stress and/or strain fields.

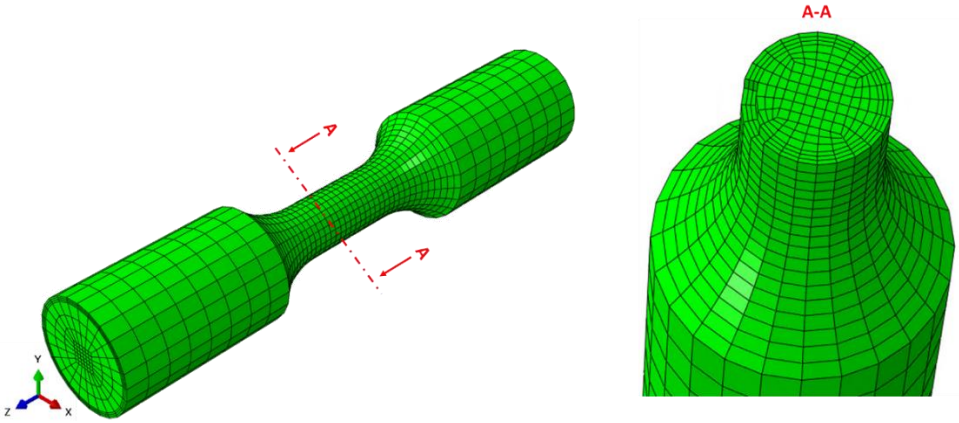

Figure 133 – Meshed geometry in Abaqus® for model validation

For non-coupled analysis, the environment temperature is set at 20ºC, and the two extremity of the specimen are piloted by a key node located at the center of the external face of the cylinder, see Figure 134. For the two simulations, one node is fixed and the load is applied to the second one. It can be noticed that the cylinder revolution axis is aligned with the Z-axis, and its centroid is coincident with coordinate system origin.

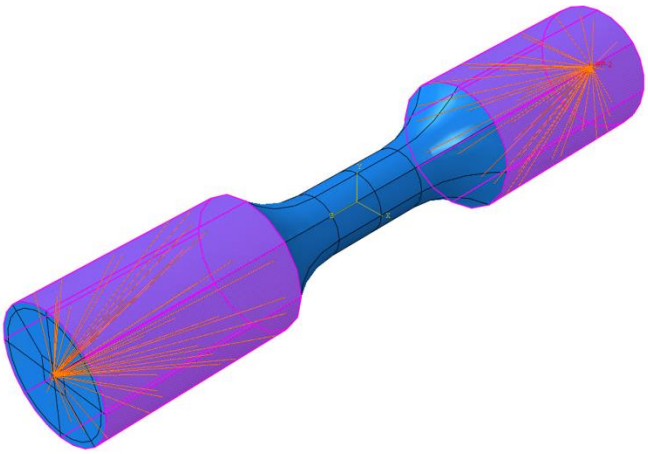

Figure 134 – Boundary condition: external surfaces piloted by a key node.

4.3.2.1. Mechanical simulation: Cyclic tensile test

This simulation is based on the mechanical test made in imposed force and presented in chapter II, see §2.4.1.2. The load was applied according to the sinusoidal evolution described in eq.(35), where F_{moy} is the mean force, ΔF is the force range and f=0.3Hz the frequency, and considering F_{max}=100kN and F_{min}=-40kN.

Figure 135 shows the comparison between the cyclic test results presented in chapter-II and the Abaqus® simulation.

It can be observed a difference of the Young Modulus between the two curves. To obtain the test curve, we had to recalculate the strain based on the displacement, and some error was introduced.

However, the stress intensity looks to be in the same range and we can observe that the simulated curve adopt an accommodation response from 0% to 20% of strain. Over this point, the strain has a constant rate up to the end of the simulation, which have been stopped for computing time purpose. In the case where the simulation would have continued, the damage variable evolution presented in Figure 136, lets predict that a ratcheting response would have occurred (as observed for the 0D analysis in §3.3.5).

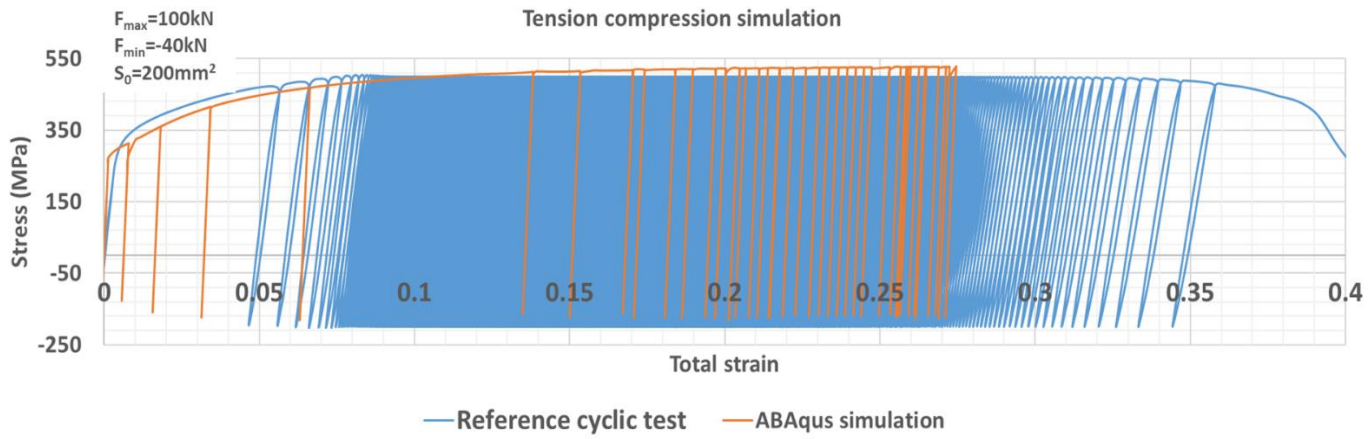

Figure 135 – Comparison between mechanical test result (blue curve) and Abaqus® simulation (orange curve) for cyclic tension compression test with imposed force loading 100kN/-40kN

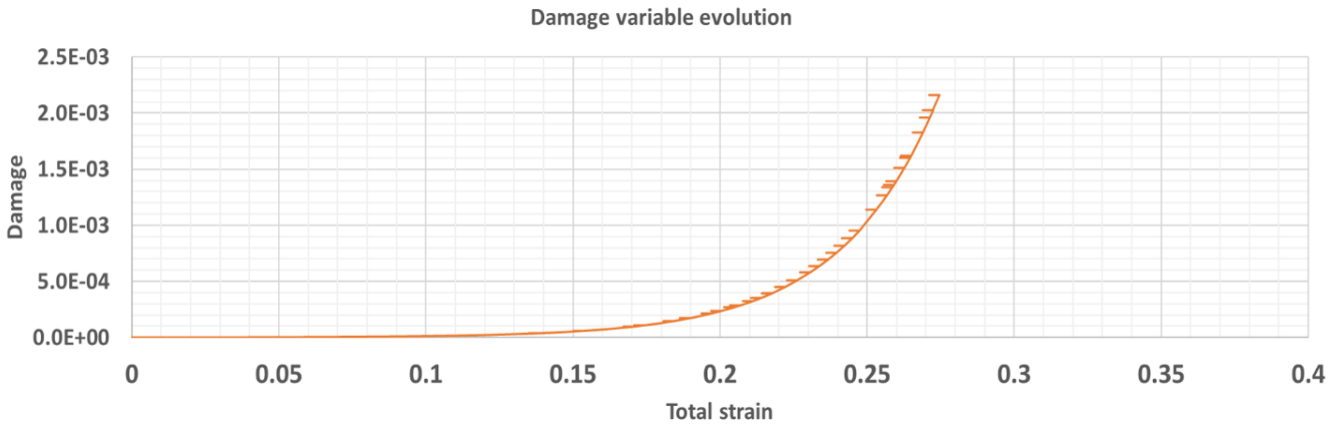

Figure 136 – Damage variable evolution for imposed force loading 100kN/-40kN

As expected for a tensile-compression test simulation, Figure 137 shows that the strain is homogeneously distributed in the cross-section of the specimen central zone. However, Figure 138, which refers to the damage distribution, shows that its distribution is non-homogeneous and it is maximised in the center part of the cross-section. This results can be compared to the macroscopic view of the cylinder 02 after break, see Figure 139, where the ductile fracture has occurred on the periphery and the a brittle one in the center.

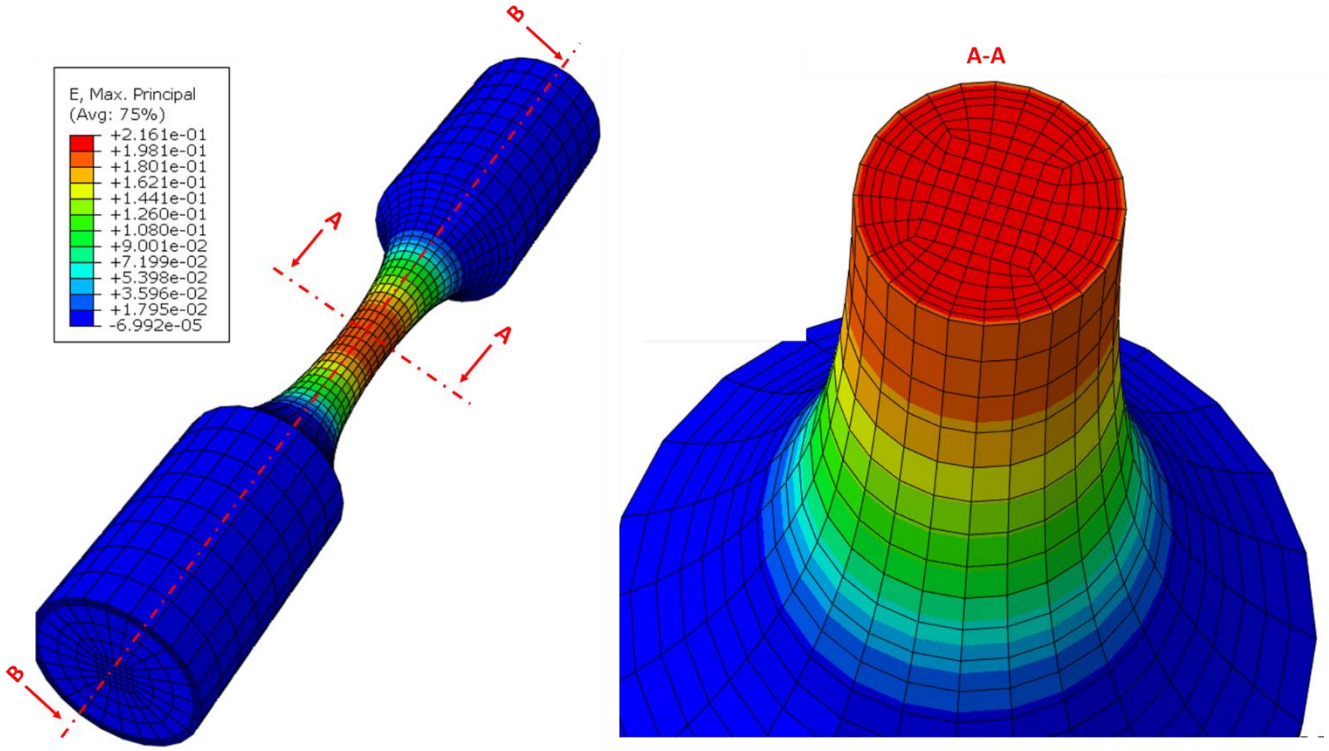

Figure 137 – Maximum principal strain map

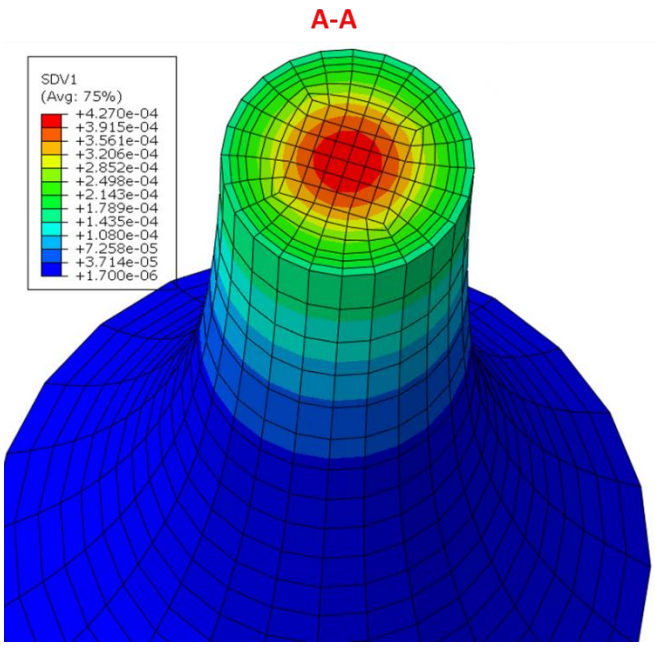

Figure 138 – Damage map

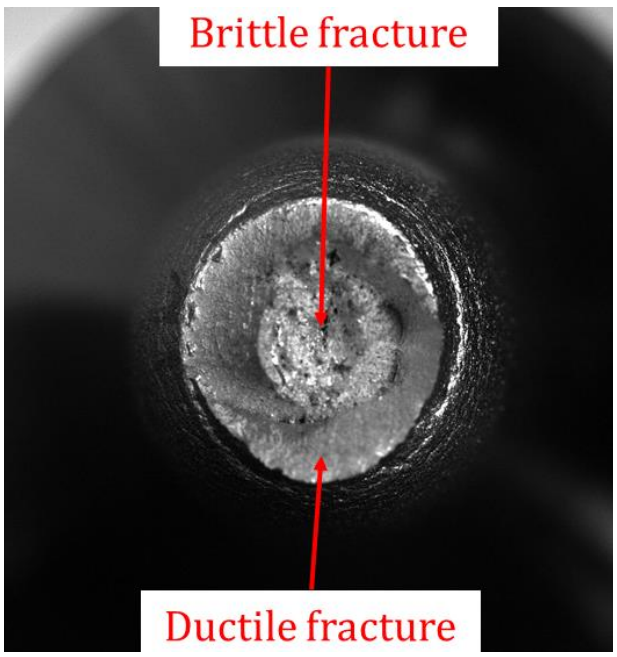

Figure 139 – Macroscopic views of the cylinder 02 after break, see §2.4.1.2

In addition to Figure 138, Figure 141 shows the damage map at the end of the simulation in the longitudinal cross-section of the cylinder (B-B).

For justifying this non-homogeneous distribution, which is maximised in the specimen central zone, we first recall that the damage variable evolution is function of the positive part of the stress tensor, as described in eq.(83). Then, we have extracted the stress map at different loading values (F_{max}, F_{min} and F_{moy}), as reported in Figure 140. It can be observed that the stress is homogenously distributed, in the cross-section of the specimen's useful part, only at the maximum and minimum values of the sinusoid (F_{max} and F_{min}). During the transition phase (F_{moy}), the stress intensity remains positive in the core of the cylinder.

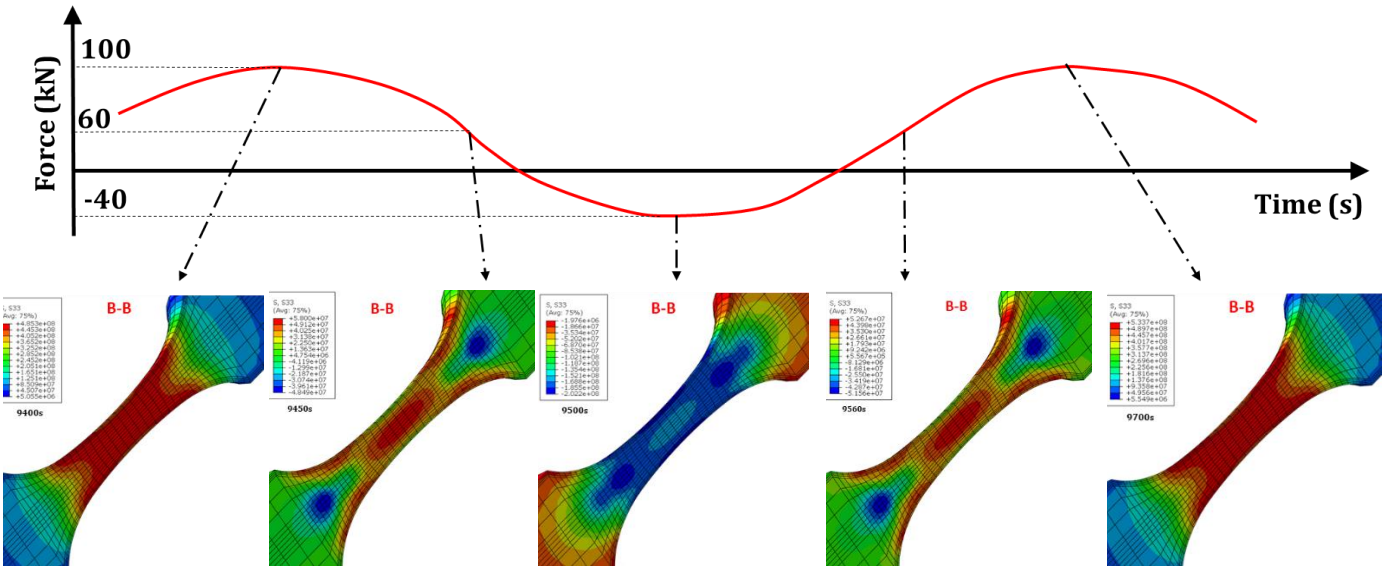

Figure 140 – Stress map evolution along the sinusoidal force signal (from 9400s to 9700s)

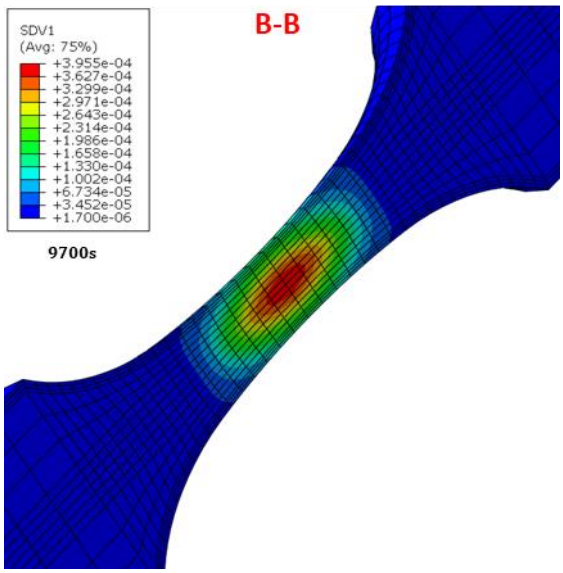

Figure 141 – damage map at the end of the simulation (9700s)

4.3.2.2. Mechanical simulation: Cyclic torsion test

This simulation is based on the mechanical test made in imposed angle and presented in chapter II, see §2.6.1.2. The load was applied according to the sinusoidal evolution described in eq.(41), where α_{moy} is the mean angle (in rad), $\Delta\alpha$ is the angle range (in rad) and f=0.3Hz the frequency, and considering $\alpha_{max}=\pi/45$ radians, $\alpha_{min}=-\pi/90$ radians.

Even if the comparison made between the simulation and the reference test, see Figure 142, shows discrepancies in the material response and the reaction torque amplitude, a softening of the material can be observed for the two curves.

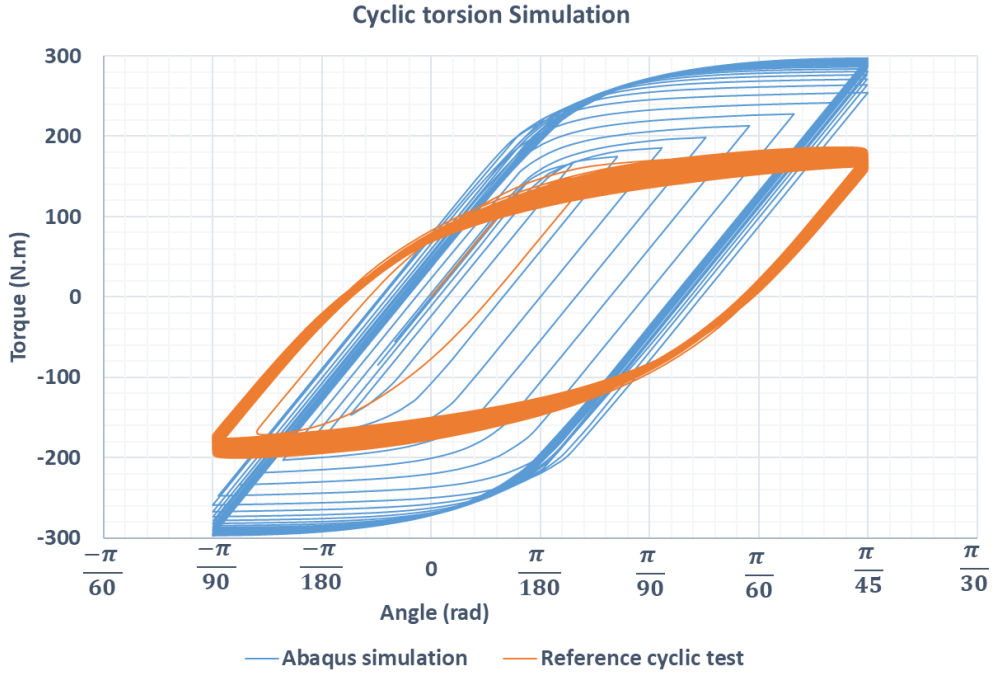

Figure 142 – Comparison between mechanical test result (orange curve) and Abaqus® simulation (blue curve) for cyclic torsion test with imposed progressive increasing amplitude of angle to $+\frac{\pi}{45}/-\frac{\pi}{90}$ radians

As expected for a torsion test simulation, Figure 143 shows that the plastic strain is non-homogeneously distributed and localised at the periphery of the cylinder.

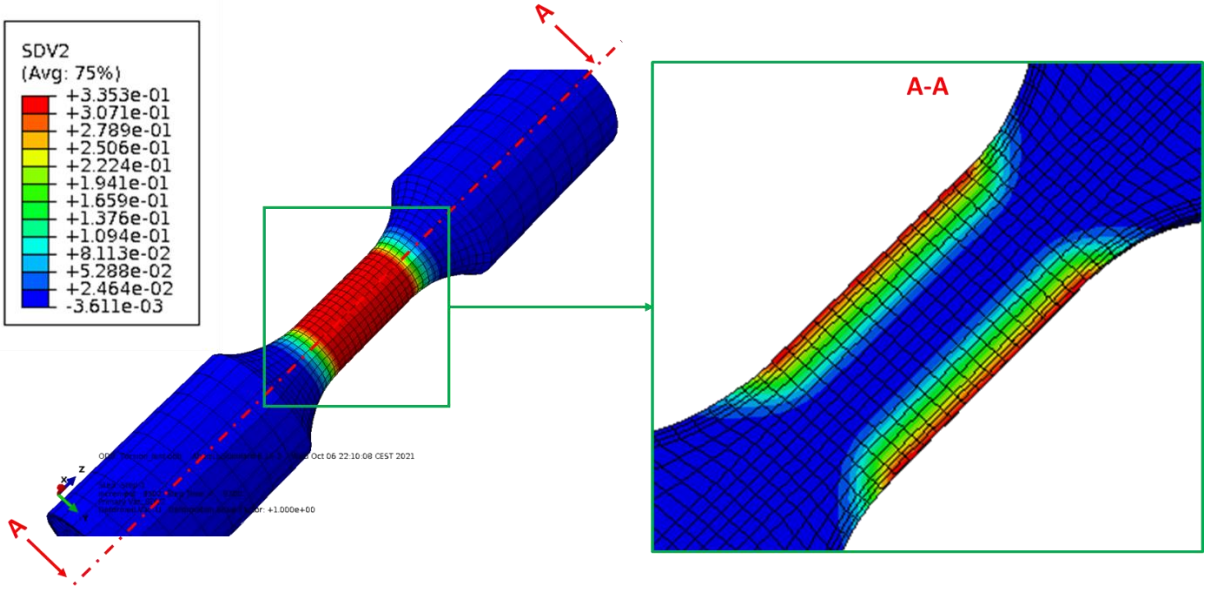

Figure 143 – Maximum principal strain map

It is difficult to simulate torsion with respecting the small strain hypothesis, in particular in our case where the material is very ductile. With the selected angle range, we should have run more cycles to observe a significant damage evolution. For this reason, it is difficult to interpret the observed damage map, in Figure 144.

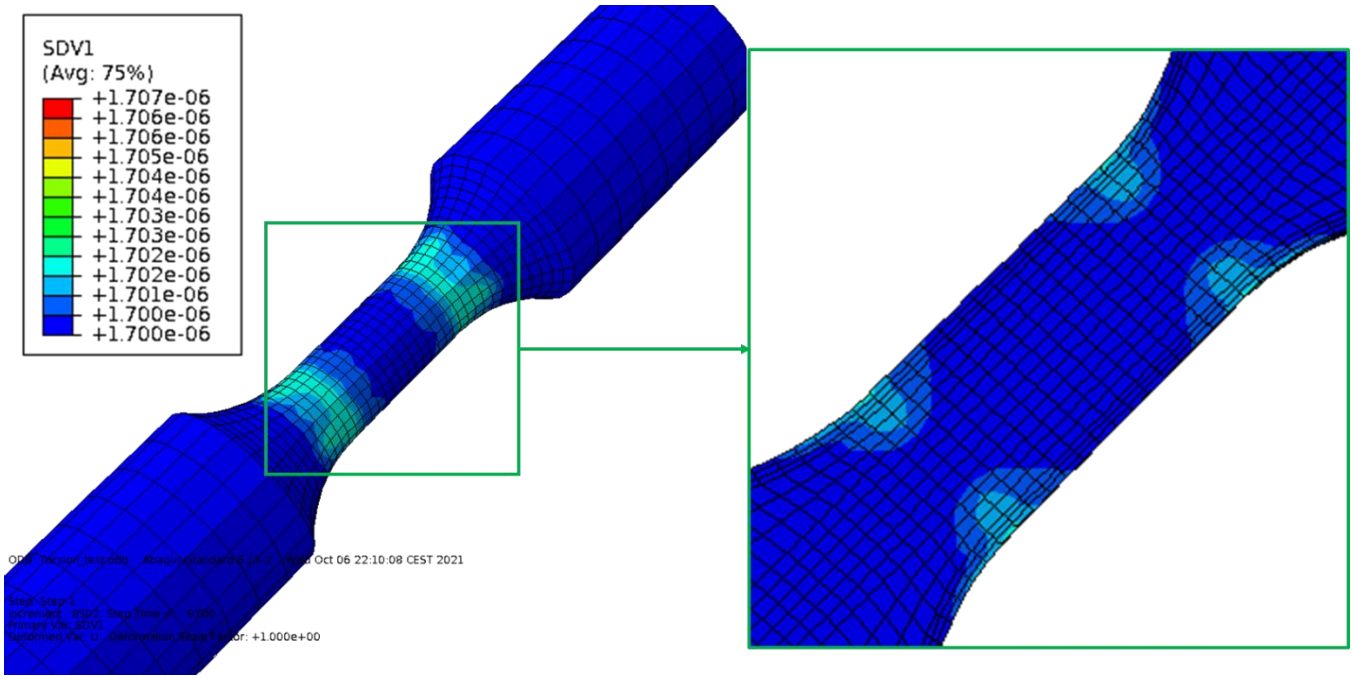

Figure 144 – Damage map

4.3.2.3. Thermomechanical simulation: Cyclic tensile test

For this last simulation, we have applied the same mechanical loading conditions than the one presented in §4.3.2.1 and for the thermal boundary conditions, we have applied, on the external surface of the cylinder, a heat transfer coefficient of 100W/m²K at 20°C, which is representative of the natural convection between the specimen and ambient air.

Although the strain map resulting from the thermomechanical simulation, see Figure 145, shows similar distribution than for the mechanical one, see Figure 137, we can observe in Figure 146 some discrepancies between the two corresponding stress/strain maps. For the thermomechanical curve (green), the loading and unloading occurs at a smaller strain value than the mechanical one (orange). This difference is explained by coupled simulation hypothesis where the stress tensor is function of the temperature as it is described in eq.(68). Effectively, Figure 147 shows temperature gradient in the specimen area where the plastic deformation appears: this is the effect of the work hardening described in eq.(96). The temperature evolution plotted in Figure 148 describes three phases: temperature decrease linked to the elastic behaviour, temperature increase due to the work hardening and damage, and temperature recovery induced by the applied heat transfer coefficient.

This observation highlight the effect of the thermomechanical coupling on the plastic flow.

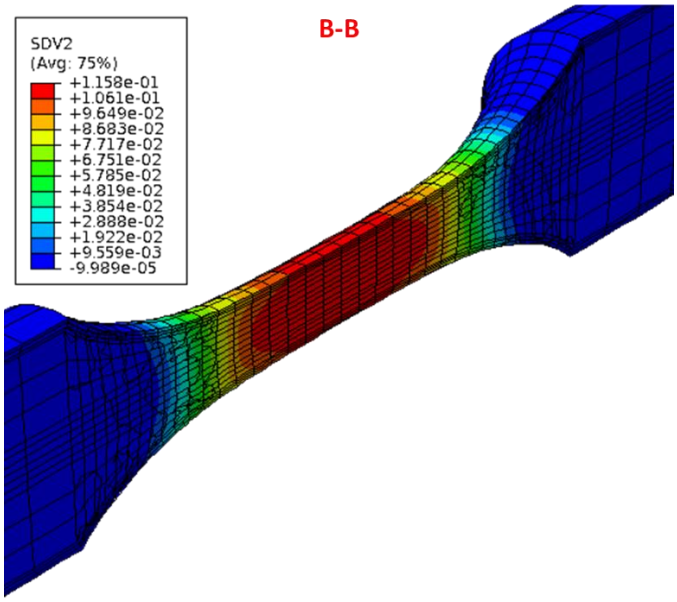

Figure 145 – Maximum principal strain map

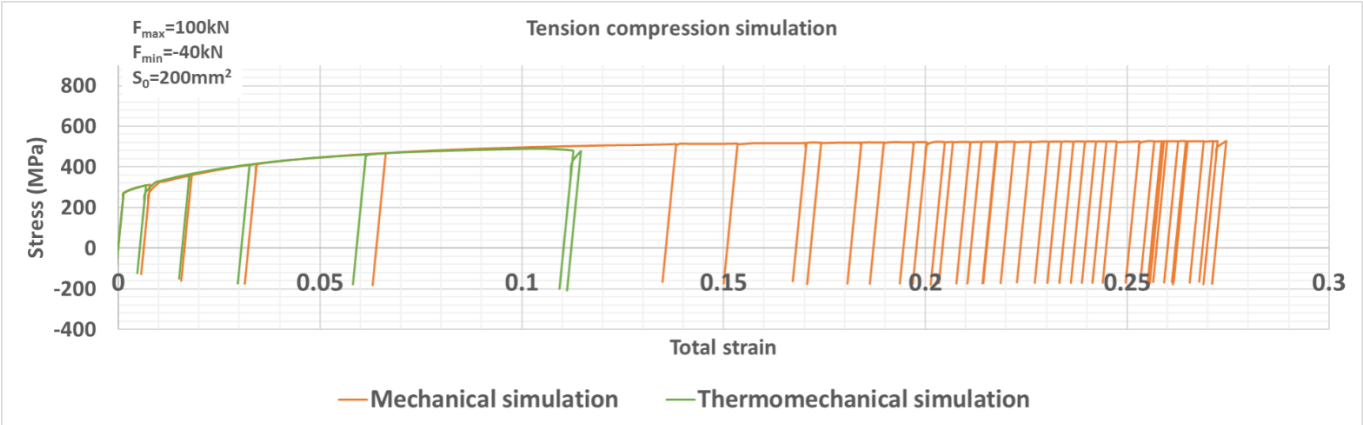

Figure 146 – Stress/strain curve comparison between mechanical simulation result (orange curve) and thermomechanical simulation (green curve) for cyclic tension compression test with imposed force loading 100kN/-40kN

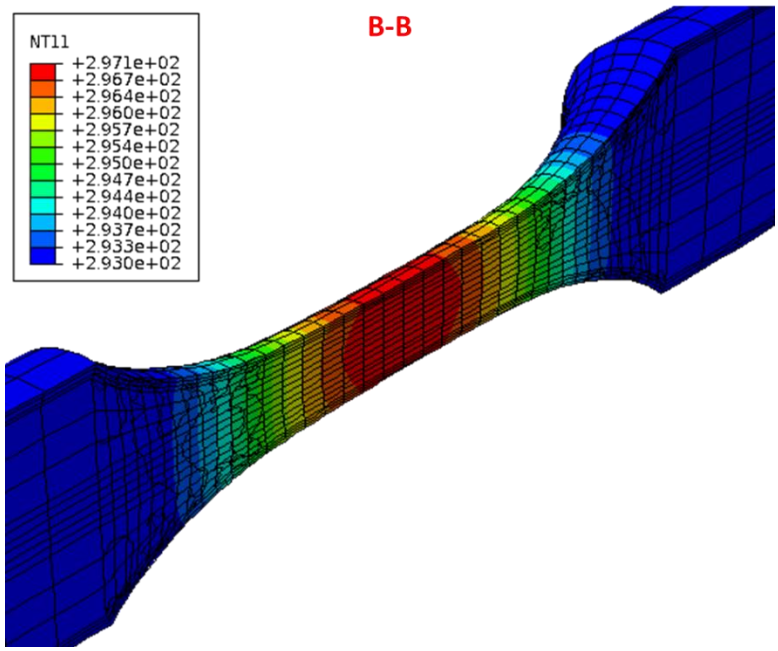

Figure 147 – Temperature map

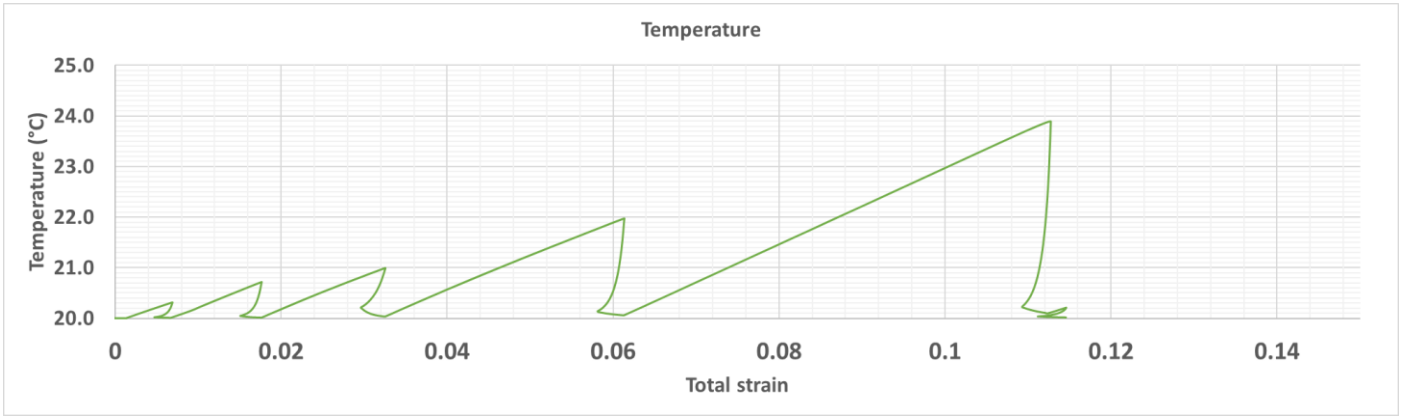

Figure 148 – Temperature evolution in the core of the cyclinder

Since the damage evolution is linked to the trace of the stress tensor, similar observation should be done on the damage evolution comparison between the mechanical and thermomechanical simulation, see Figure 150. However, the analysis have been stopped before reaching a significant damage value.

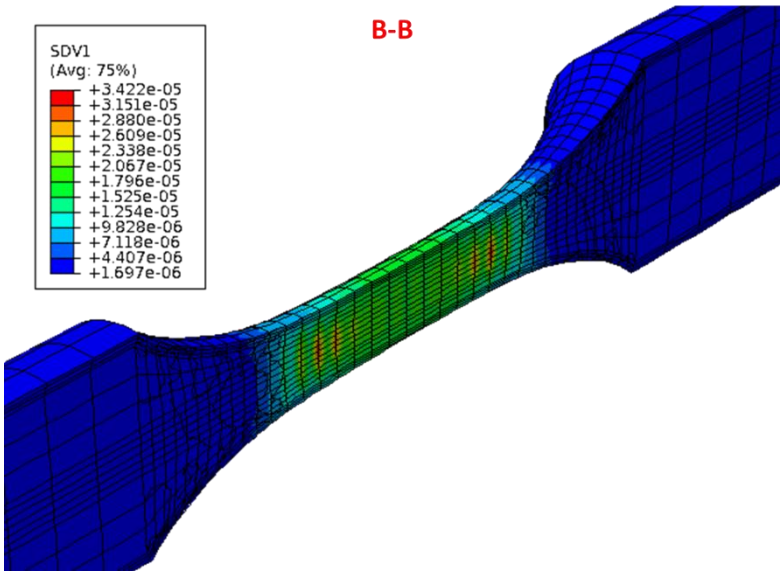

Figure 149 – damage map

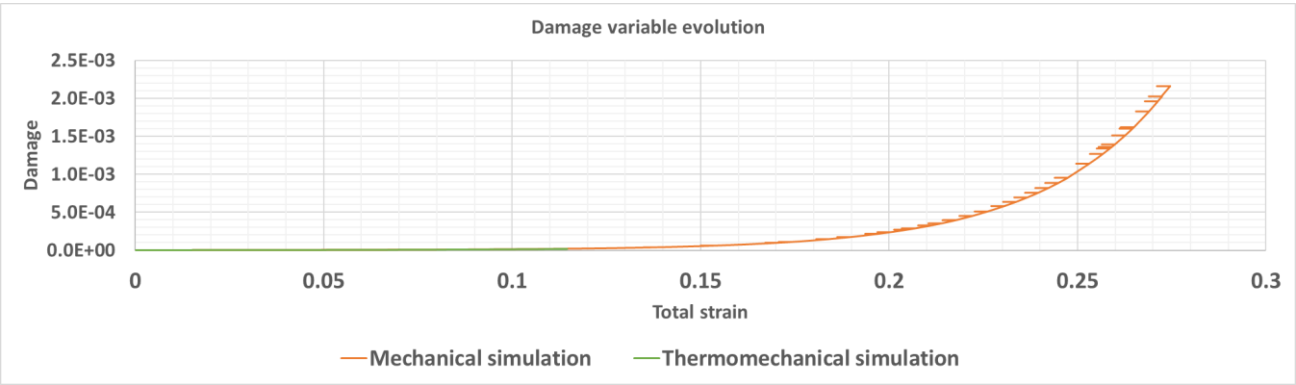

Figure 150 – Damage map Comparison between mechanical simulation result (orange curve) and thermomechanical simulation (green curve)

4.3.3. ITER Vacuum Vessel application

The ITER Vacuum Vessel interfaces with various systems of the machine through a bolted connection onto a supporting “rail” welded to the confinement barrier. Figure 151 shows the manifold rails of the blanket system in the ITER vacuum vessel. The design justification for these rails consists in evaluating the maximum stress and/or strain in the weld cross section for the worst load combination (Martinez, 2016), and comparing it with design criteria defined in the RCC-MR code.

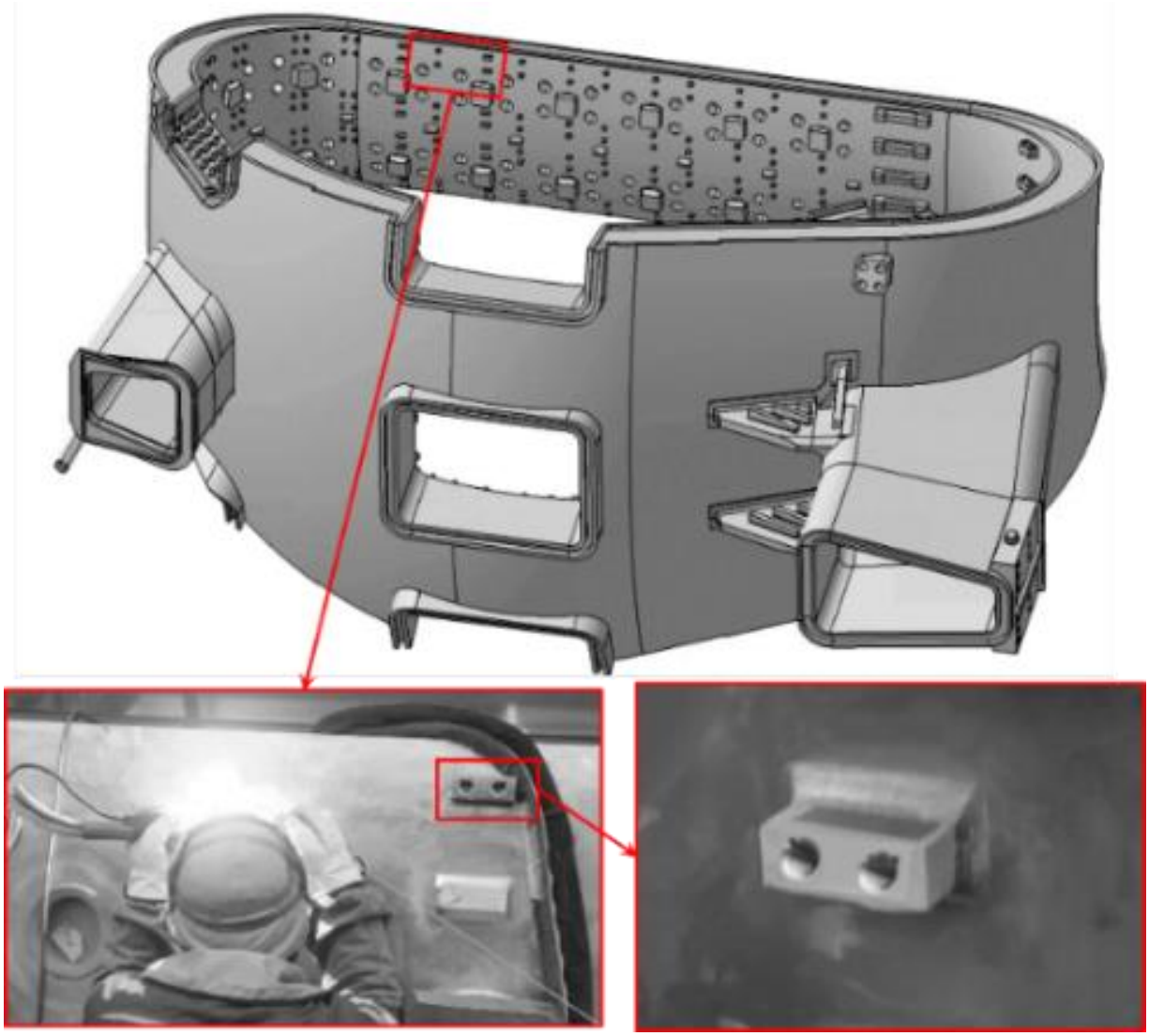

Figure 151 – ITER VV rails (ITERwebsite).

4.3.3.1. Thermomechanical test hypothesis

Because of the large amount of rails in the VV and all the different mechanical load types that could act on it, the method proposed here consists in redefining the loading vector applied at the centroid of the weld cross section A (in m^2) in two forces: one normal force $F_n(t)$ (in N) and one tangential force $F_t(t)$ (in N), see eq.(321)-(322)-(323).

$$F_n = F_z + \frac{e \cdot A}{2 \cdot I_y} \cdot M_y + \frac{h \cdot A}{2 \cdot I_x} \cdot M_x \tag{231}$$

$$F_t = \sqrt{\left(F_x^2 + F_y^2\right)} + F_{torque} \tag{232}$$

$$F_{torque} = \frac{3 \cdot M_z}{8 \cdot w \cdot e^2} \cdot A \cdot \left(1 + 0.6095 \cdot \frac{w}{e} + 0.8865 \cdot \left(\frac{w}{e}\right)^2 - 1.8023 \cdot \left(\frac{w}{e}\right)^3 + 0.9100 \cdot \left(\frac{w}{e}\right)^4\right) \tag{233}$$

where Fx, Fy, Fz are the forces, and Mx, My, Mz are the moments (in N.m) defined in a given orthonormal basis (**x**, **y**, **z**), and e corresponds to the rail thickness (in m), w the rail width (in m), I_x and I_y are the flexion moments of inertia (in m^4). The force induced by torsion in a rectangular section, F_{torque} (N), has been adapted from (Budynas, et al., 2002).

From a thermal point of view, the power deposition onto the rail is a combination of nuclear heating, conduction and radiation with the surrounding components. To simplify this combination of heat depositions, it is proposed to model it as an imposed temperature gradient in the rail, where the VV shell temperature is fixed at 393K and the maximum temperature, defined by g(t), is applied on top of the rails, see Figure 152.

The geometry has also been simplified by neglecting the radius of curvature of the VV and removing the weld fillet at the junction of the rail. We have therefore 2 rectangular blocks with a perfect interface. Symmetry conditions are applied on the largest rectangular block (dark blue in Figure 152) and vertical displacement are prescribed to be null on its top edges (light blue in Figure 152).

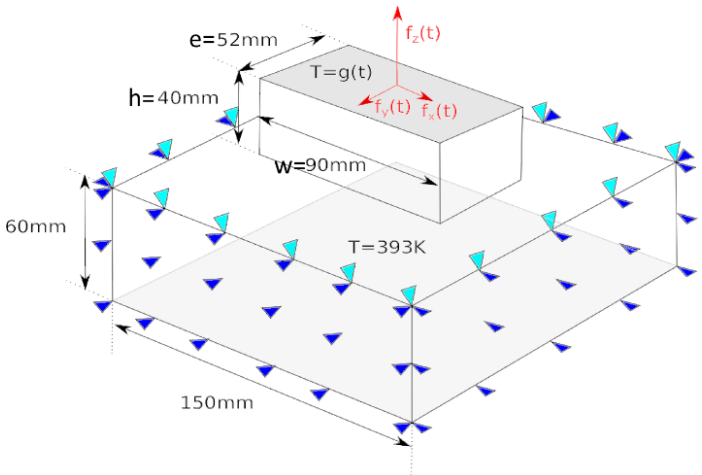

Figure 152 – Welded interface between VV and rail.

Finally, the same material parameters than the one proposed in §4.3 have been used.

4.3.3.2. Results for monotonic loading

In the first numerical simulation, a ramped thermal load (see Figure 153) is combined with a piecewise linear, mechanical load (see Figure 154). The values proposed here are not realistic. They aim at reaching the damage mode to test the proposed model.

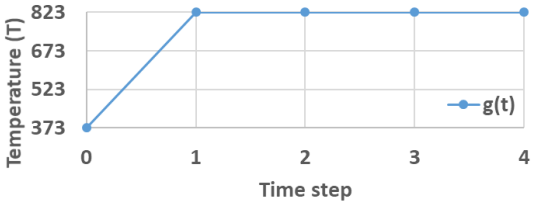

Figure 153 – Applied input temperature for monotonic simulation

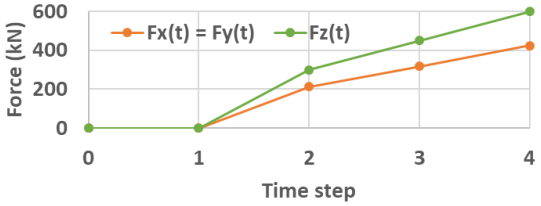

Figure 154 – Applied input forces for monotonic simulation

Figure 155 shows the maximum principal strain map distribution at the end of step-03. It can be observed that the rail bends under the combination of loads, which localizes the strain in the two opposite corners; one is subjected to compression and the second to tension.

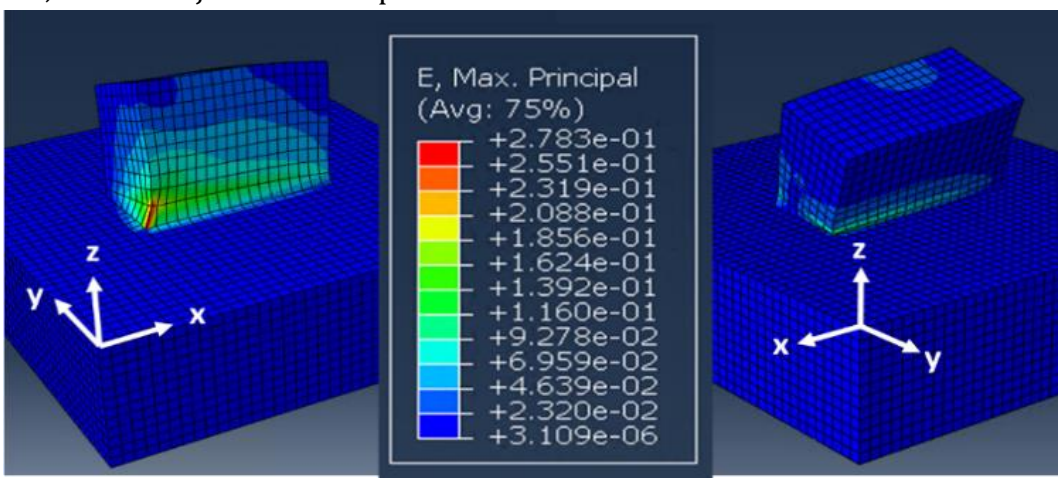

Figure 155 – Maximum principal strain map at the end of step-03 (monotonic simulation)

Figure 156 shows the damage map distribution at the end of step-03. Although the strain is localized in the two corners, the damage occurs only in the tension area. This material response corresponds to the damage evolution defined in eq.(91), which supposes that the microcrack propagation and the growth of cavities depends on the tensile loading only.

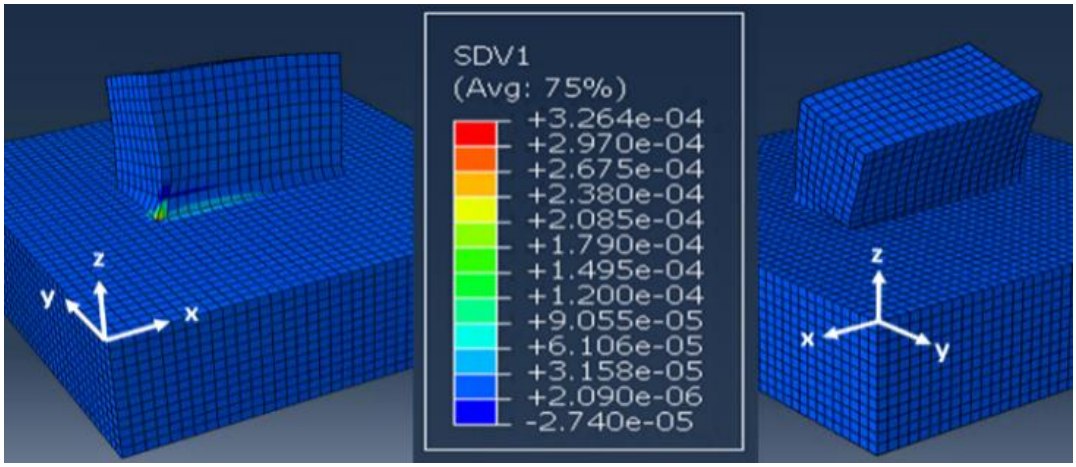

Figure 156 – Damage map at the end of step-03 (monotonic simulation)

Figure 157 shows the damage evolution in a Gauss point of the corner element where the strain is maximum. Similarly to what was observed for "0D"simulation, see §3.3, the damage variable starts increasing exponentially between step-02 and step-03, which corresponds to a total strain value between 10% and 20%, see the total strain evolution in the same Gauss point in Figure 158. We can notice that the rapid damage evolution leads to the divergence of the algorithm before reaching step-04.

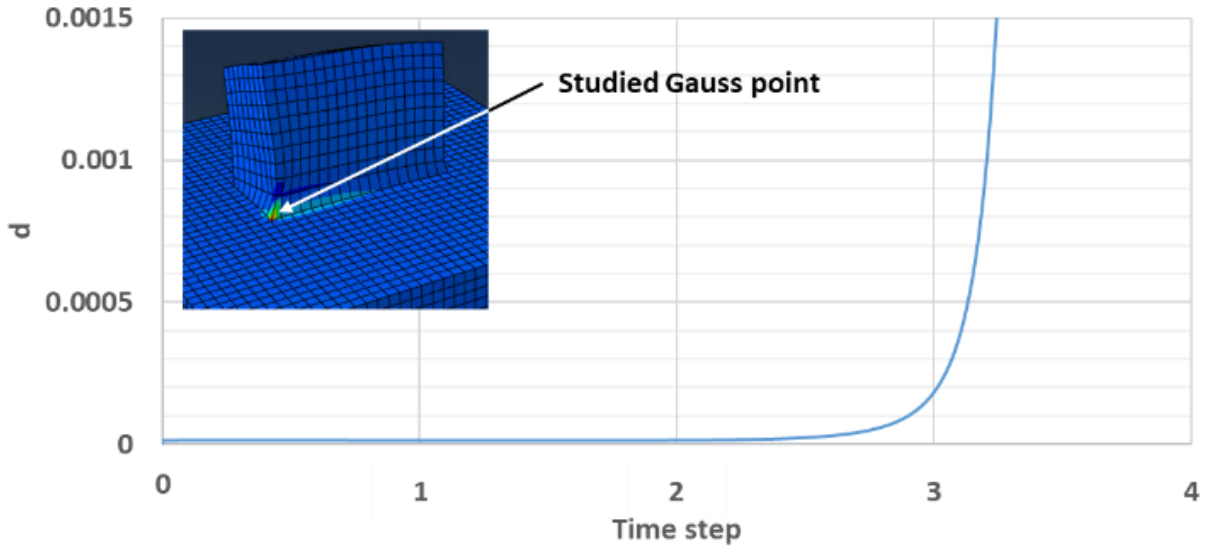

Figure 157 – Damage evolution for monotonic simulation

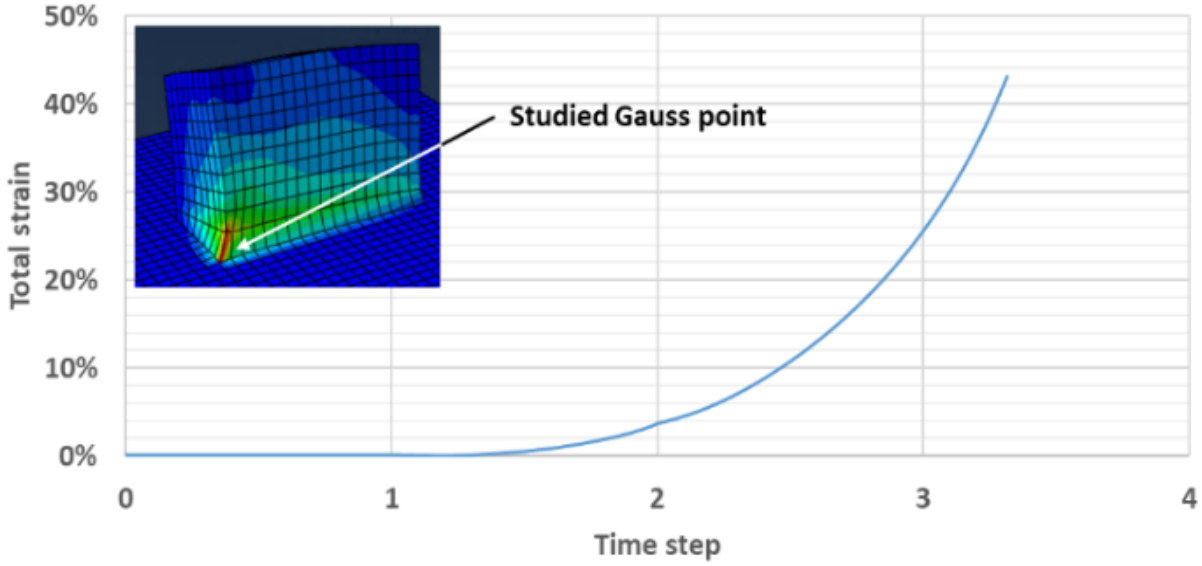

Figure 158 – Total strain evolution for monotonic simulation

4.3.3.3. Results for cyclic loading

For the second simulation, we propose to start from the end of step-03 of the monotonic simulation, where the damage variable start to growth. From this step, the mechanical load is kept at a constant value, and the thermal load is cycled 20 times, see Figure 159 and Figure 160.

For this scenario where the primary load is fixed and the secondary load is cycled, the goal is to check if the material response will lead to shakedown or ratcheting.

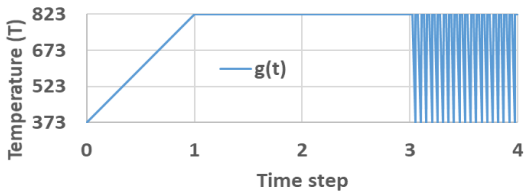

Figure 159 – Applied input temperature for cyclic simulation

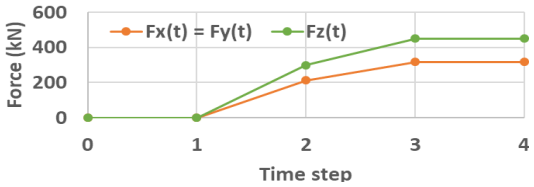

Figure 160 – Applied input forces for cyclic simulation

Figure 161shows the maximum principal strain map distribution at the end of step-04. A similar behavior as in the monotonic loading case is observed, where the strain mainly localizes in the two opposite corners.

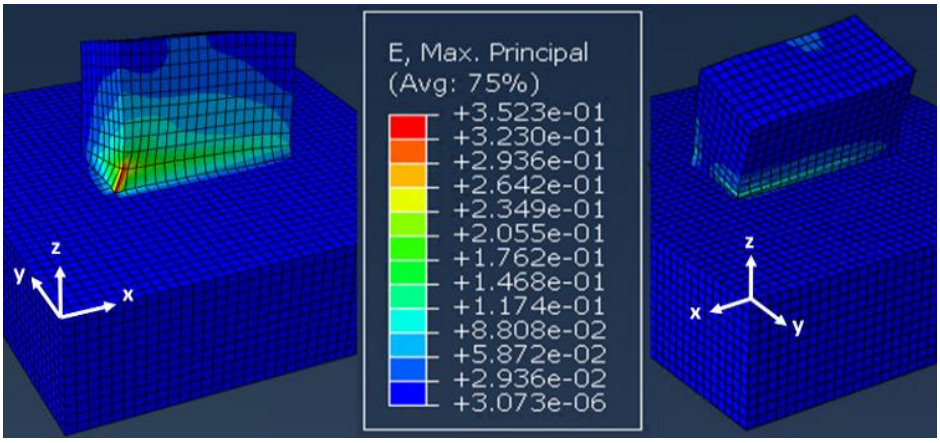

Figure 161 – Maximum principal strain map at the end of step-04 (cyclic simulation)

Figure 162 shows the damage map at the end of step-04. In comparison to the monotonic loading case, the damage still occurs in the same corner. Moreover, even if the damage variable increases on the loaded corner under cyclic thermal load, it remains close to its initial value in the opposite corner.

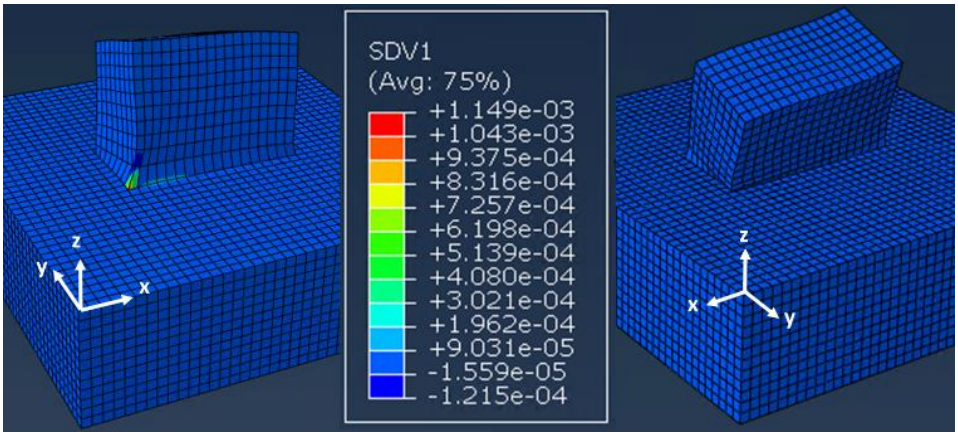

Figure 162 – Damage map at the end of step-04 (cyclic simulation)

Figure 163shows the damage evolution in a Gauss point of the corner element where the strain is maximum. At the end of step-03, when the primary load is fixed and the cyclic secondary load starts, we can observe a change in the damage evolution. Effectively, the exponential trend has changed to a logarithmic one, which corresponds to an accommodation of the material. It should be noted that this evolution is strongly localized and we have not studied the influence of the mesh size on it.

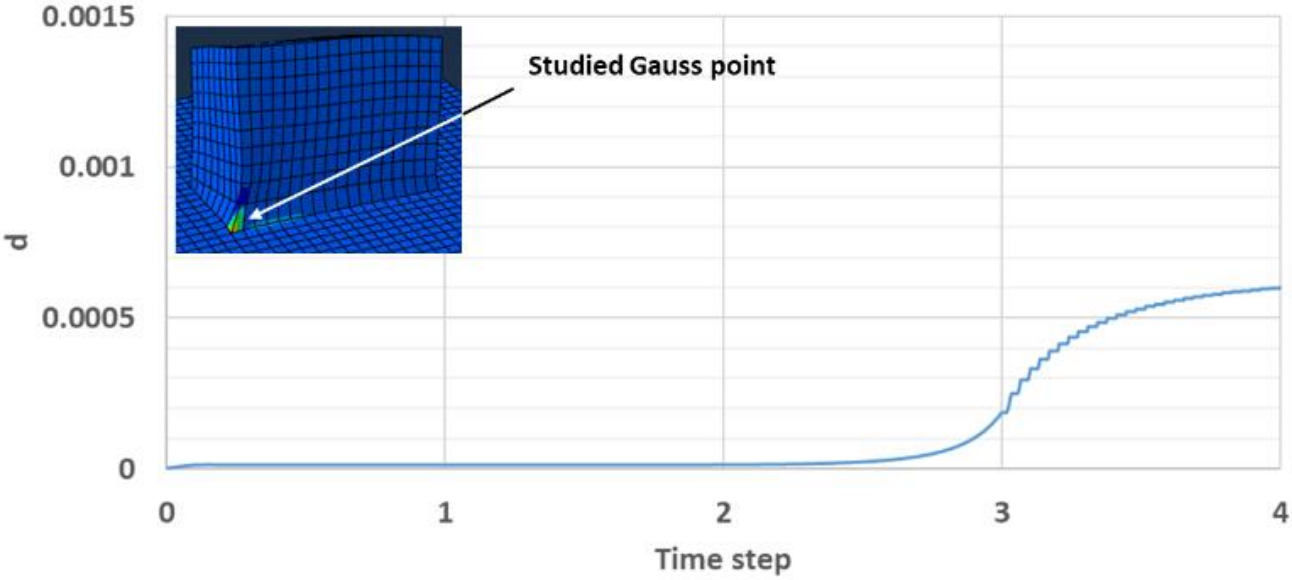

Figure 163 – Damage evolution for cyclic simulation

Finally, Figure 164, which shows the total strain evolution in a Gauss point of the corner element, confirms that a shakedown occurs under thermal cyclic loads.

This observation allows us to conclude that the failure mode could be due to high-cycle fatigue rather than to ratcheting.

However, the present model is limited to shakedown justification. Further analysis following the RCC-MR code methodology, which is more adapted for fatigue justification, would be required to confirm the observed behaviour.

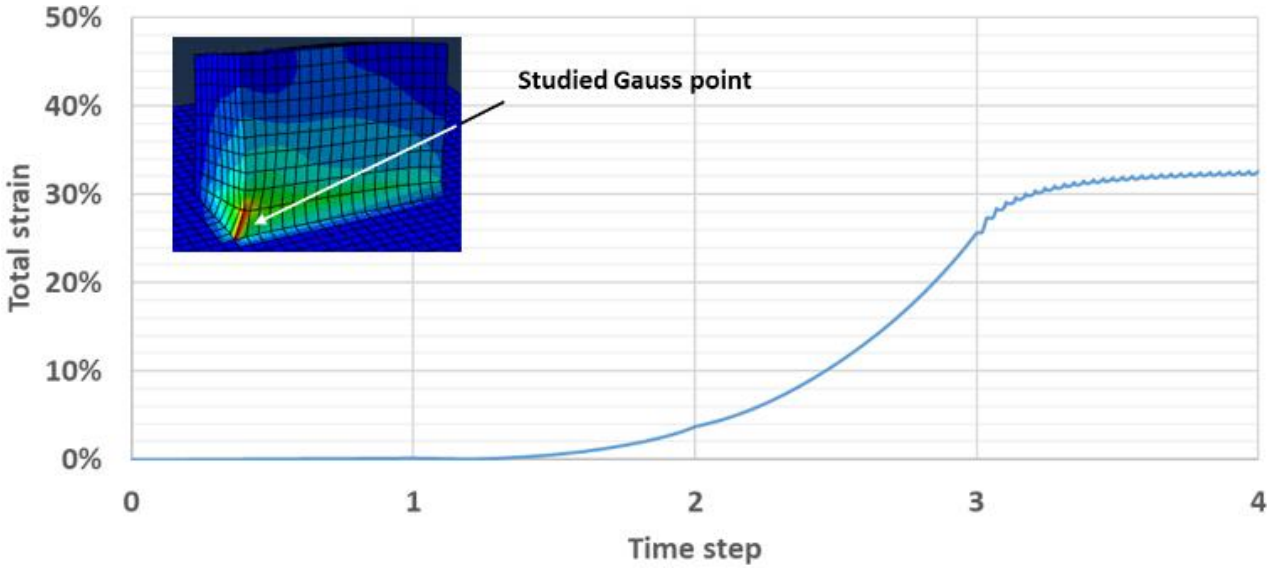

Figure 164 – Total strain evolution for cyclic simulation

4.4. Conclusion

We have implemented our model in the Abaqus® finite element code, which allows solving simultaneously the first law of motion and the heat equation. To do so, we had to adapt the return radial method for the local integration of the internal variables, which required a local Newton resolution. In a second stage, we have linearized the problem and defined the tangent operators required by the Abaqus® subroutines UMAT & UMATH.

We have first compared a Matlab® simulation with an Abaqus® one on a 0D analysis case: the superposition of the two curves allowed the validation of the model FE implementation.

To complete the model validation, we have simulated a cyclic tension-compression and a cyclic torsion test with input signal from Chapter-II. The results have shown discrepancies between the simulations and the mechanical test results. However, the model provides similar behaviours that the ones observed experimentally, where the material adopts first a softening response, then a constant strain evolution, to probably finish with a ratcheting response.

The cyclic tension-compression simulation performed with strong thermocoupling showed a temperature evolution in the plastified area, which demonstrates the effect of work hardening on the temperature. Some variations in the stress evolution linked to this temperature evolution have also been identified. However, it is proposed to run again this simulation with a model version that takes into account material parameters dependent of the temperature. In that case, the FE implementation needs to be updated.

The last simulation was performed on the ITER Vacuum Vessel rail, and its main objective was to demonstrate the use of the model on real structure application.

To do so, a constant force (primary load) combined with a cyclic thermal load (secondary load), which represents a typical load case in line with the nuclear code stress decomposition (and associated load), have been applied onto the VV rail.

The results showed that the damage variable, which drives the strain evolution, is sensitive to the loading scenario, and for this specific configuration, the structure has reached a shakedown response.

Conclusion

The essential contribution of this work lies in the extension of existing pure mechanical models for thermo-mechanical loadings, in which the coupling between mechanical and thermal phenomena plays a preponderant role. The approach followed is the one of irreversible thermodynamic processes, which guarantees the thermodynamic admissibility (i.e. the respect of the second principle) of the proposed models. They also take into account dissipation mechanisms such as plasticity and damage.Some experimental works have been performed for a better understanding of the SS316L(N)-IG response phenomena under cyclic loading, such as shakedown (elastic and/or Plastic) and ratcheting. A basic material parameters identification procedure has also been proposed, based on 0D simulation. Finally, the proposed model has been implemented in the Abaqus® finite element software, which allowed testing its relevance on simple structural cases.

Based on the works found in the bibliography, we have found that predicting the ratcheting failure mode remains a complex phenomenon to be modelled for the 316L austenistic stainless steel. Moreover, for damage prediction in nuclear power plants, many thermomechanical and/or mechanical tests performed at different temperatures have already been carried out, but very few (at least to our knowledge) take into account the strong thermo-mechanical coupling and damage phenomenon.

Thus, we have performed cyclic tension/compression tests conducted with an imposed stress (almost non-existent in the literature), and we have observed that the material undergoes elastic shakedown at low stress amplitudes and plastic shakedown up to ratcheting at higher stress amplitudes. Similar observations have been made on cyclic torsion tests conducted with an imposed moment.

For the modelisation of the 316L(N)-IG austenistic stainless steel, we have proposed to start from Chaboche's model available in the literature, and to enrich it to explicitly take into account the influence of the temperature on the mechanical behaviour and, reciprocally, the influence of the mechanical behaviour on the temperature (i.e. the thermomechanical coupling).

In addition, and based on the observations made on the cyclic tests, we have proposed to implement a damage variable in both kinematic and isotropic hardening behaviours. The objective was to make the two hardening modes working in opposition, meaning that in the low damage state the isotropic hardening is dominant whereas in a higher damage state, the kinematic hardening becomes dominant. Ratcheting occurs in the final stage only if the damage variable evolution progresses significantly up to a threshold value.

In a first step, the different phenomena highlighted above were demonstrated through "0D analysis" using Matlab® software. This simplistic approach made it possible to choose appropriate parameters, which generally requires complex methodologies.

In a second step, the model has been implemented in Abaqus® code, which proposes subroutines to facilitate material model developments. For the local integration of internal variables, we had to implement a return radial method. It can be noted that this implementation induces no major difficulties.

By comparing the reference curves of cyclic tension-compression and cyclic torsion test with the associate FE simulations, some differences have been observed, in particular for the torsion simulation. Although the simulation provides higher stress amplitudes than expected, a similar behaviour to the one reported during the tests has been observed.

Finally, a finite element geometry representative of the ITER Vacuum Vessel structure was tested under different load conditions, demonstrating the proper behaviour of the model under strong thermomechanical coupling in a 3D context.

To conclude, we have developed a behaviour model enabling us to model the ratcheting and/or shakedown response under thermomechanical loadings. Based on our findings, we recommend additional investigations into the experimental, numerical and/or theoretical fields. Among these, we can propose:

- **Additional tests for different temperature environments.**
  Since the test campaign carried out to identify the material parameters was done only at 20°C for uniaxial loading, additional tests for different temperature environments could be done.
- **Mechanical tests under vacuum condition.**
  To validate the temperature evolution (linked to the thermomechanical coupling), some tests could be done under vacuum conditions, with an infrared camera in order to precisely monitor the surface temperature field.
- **Parameter identification with adapted algorithms.**
  Although the "0D simulation" enables the identification of the material's parameters, a more complex methodology including algorithms could be developed for a better fitting to the experimental data.
- **Model formulation in large deformations.**
  The nuclear design rules aim to ensure that the structures do not undergo large deformation. However, the torsion test results have highlighted the ductility of the material that cannot be realistically simulated using the infinitesimal tensor.
- **Temperature dependency of the material parameters.**
  In this first thermomechanical development, for simplifying the equation setting, we did not take into account the temperature dependency of the different parameters. It is proposed to start with the first and second lamé coefficient.
- **Damage variable for neutron structure interactions.**
  Furthering the work would also consist in enriching the thermo-mechanical model by including a second damage variable. This new variable would be associated with the neutron flux that drives the displacement per atoms (dpa) and a part of the nuclear heating (r^v in eq.(56)), see (Maki, 1999) (Barabash, 2007) (Boutard, 2014) (Kalinin, 2001) and (Klueh, 2008).

Résumé en français

En guise de résumé en français du mémoire, nous proposons ici la traduction de l'article publié dans la revue « Fusion Engineering and Design » qui donne un bon aperçu du travail effectué pour la présente thèse.

F. Sabourin and al., « Development of a thermo-mechanical behaviour model adapted to the ITER Vacuum Vessel material », *Fusion Engineering and Design*, vol. 173, 2021.

Résumé

Le réacteur thermonucléaire ITER a été classifié Installation Nucléaire de Base (INB n°174) par l'autorité de sureté nucléaire française, ceci impliquant qu'ITER sera le premier Tokamak soumis à la réglementation française en vigueur des équipements nucléaires sous pression.

Les chargements mécaniques et électromagnétiques combinés aux chargements thermiques induits par la réaction de fusion nucléaires nécessitent d'avoir une approche multiphysique de l'endommagement, ce qui, à ce jour ne fait pas parti des codes & standards nucléaires.

La méthode de prévention de l'endommagement se justifie par la garantie de l'intégrité structurelle d'un composant. Les règles de conception suivent deux approches en particulier: la prévention d'un endommagement dû à un effort mécanique monotone et la prévention d'un endommagement résultant d'un chargement cyclique (thermique et/ou mécanique). Dans la majorité des cas, l'intégrité structurelle est justifiée au travers de méthodes analytiques et/ou éléments finis supposant un comportement élastique du matériau. Lorsque ces types de méthode ne suffisent plus à justifier une structure, d'autres méthodes basées sur des comportements non-linéaires du matériau peuvent être utilisées. Cependant, les modèles de comportement proposés dans les codes nucléaires, ne permettent pas de représenter avec précision des comportements observés expérimentalement, plus particulièrement, dans le cas de notre étude: le phénomène de rochet.

Les experts matériaux et calculs d'ITER s'accordent à dire que le développement d'un modèle de comportement thermomécanique adapté au matériau ITER, est nécessaire pour affiner la prédiction d'endommagement dans un environnement nucléaire et multiphysique tel que celui d'un tokamak.

Cet article décrit le développement d'un modèle de comportement non linéaire pour le matériau de l'enceinte à vide d'ITER (VV), incluant un couplage thermomécanique fort ainsi qu'une variable d'endommagement. Plus précisément, il s'agit d'un modèle type Chaboche (modèle elasto-(visco)-plastique) comprenant différent types d'écrouissages, qui a été amélioré afin de pouvoir prendre en compte l'effet de la température sur le comportement mécanique, et réciproquement, l'influence de la mécanique sur la température. Des essais mécaniques cycliques ont été réalisés sur des échantillons du matériau constitutif du VV, mettant en avant la déformation progressive, c.à.d., le phénomène de rochet. Le présent modèle a été testé sur un problème homogène, communément appelé analyse "0D", dont les résultats ont été comparés aux essais uniaxiaux. La dernière partie de ce document décrit l'implémentation numérique dans un code éléments finis, permettant de tester le modèle sur un support soudé de la VV.

Mots clés: ITER, chambre à vide, couplage thermomécanique, modèle de comportement, écrouissage non linéaire, endommagement, phénomène de rochet, SS316L(N)-IG.

Introduction

L'organisation ITER est un projet intergouvernemental visant à démontrer la faisabilité scientifique et technique de l'énergie de fusion à des fins industrielles.

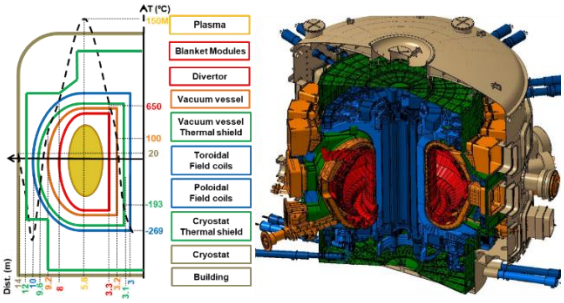

Fig. 165 – Composants du Tokamak ITER et températures associés en condition normal d'opération (Sabourin, 2018).

Le tokamak d'ITER est constitué de composants superposés (Fig. 165), dont la température varie de $150x10^6$K au cœur du plasma à 4K pour les supraconducteurs, sur une distance inférieure à 5m. Malgré ce gradient thermique entre les composants, la réaction de fusion nucléaire au cœur du réacteur génère le chargement thermique principal. Afin de maintenir les composants de la chambre à vide à des températures acceptables (généralement en dessous du seuil de fluage thermique), ces composants sont activement refroidis par des fluides sous pression (généralement de l'eau). La pression du système de refroidissement peut être suffisamment importante pour constituer un cas de chargement critique, dimensionnant ainsi la conception des structures (Martinez, 2014). Un réacteur à fusion nucléaire de type tokamak se singularise par des instabilités magnétohydrodynamique du plasma, qui se traduisent par des efforts électromagnétiques importants (force de Laplace) sur les structures environnantes. Ce type de chargement est l'un plus sévère que peut subir la machine et il peut induire le déplacement du VV (3600T) dans le sens vertical de plusieurs millimètres.

A partir de la quantité de tritium qui sera contenue dans le réacteur d'ITER, celui-ci a été classifié en tant qu'Installation Nucléaire de Base (INB n°174) par l'autorité de sûreté nucléaire française, ceci impliquant qu'ITER sera le premier réacteur à fusion soumis à la réglementation française en vigueur des équipements nucléaires sous pression.

Les experts matériaux et calculs d'ITER s'accordent à dire que la singularité d'ITER, en tant que centrale de fusion thermonucléaire soumis à la réglementation ESPN, requière le développement d'un modèle de comportement adapté au matériau ITER, afin de répondre aux exigences de l'autorité de sûreté nucléaire française (ASN).

La première barrière de confinement d'ITER

La chambre à vide (VV) est un tore composé de différentes ouvertures à trois niveaux, qui permettent l'accès des systèmes de chauffage du plasma, des instruments de mesures, ainsi que des outillages nécessaires à la manutention des composants face au plasma, voir Fig. 166. Cette structure est composée de deux parois d'acier liées par des raidisseurs. Elle est remplie d'eau pressurisée, permettant ainsi de maintenir une température homogène et constante, tout en extrayant la puissance thermique engendrée par les opérations plasma.

La pression maximale admissible du système de refroidissement est 25 bars relatif en opération normale de fonctionnement (11 bars en mode plasma et jusqu'à 24 bars en étuvage), classifiant le VV en tant qu'Equipement Sous Pression Nucléaire (ESPN), ce qui nécessite une évaluation de conformité, c.à.d., par un Organisme Notifié Agréé (ONA), qualifié par l'ASN afin de s'assurer de la bonne application des règles de conception et de fabrication décrites dans le code de l'environnement à l'article R557.12 et dans l'arrêté ministériel du 30/12/2015 modifié .

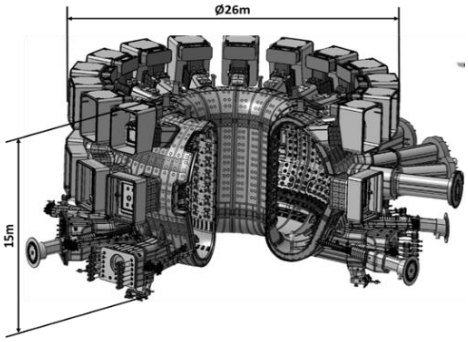

Fig. 166 – Chambre à vide (VV) d'ITER.

De plus, le VV en tant que première barrière de confinement du réacteur, est classifié en tant que "composant important pour la protection PIC/SIC-1" suivant la classification spécifique à

ITER. La conception, la fabrication et le contrôle de la VV sont effectués en suivant les dispositions du code RCC-MR (AFCEN, 2007), qui a été proposé comme code nucléaire de référence (Martinez, 2016). Ce code propose les règles de base pour la conception, la fabrication et le contrôles des équipements mécaniques pour des installations expérimentales ou de fusion nucléaire.

L'application de ces règles vise à assurer une sécurité suffisante pour garantir l'intégrité structurelle des composants tout au long du cycle de vie du réacteur. Les critères utilisés pour ces règles ont principalement deux origines:

- les dommages de type-P qui résultent de l'application à une structure d'un chargement croissant de façon monotone, ou d'un chargement constant:
  - modes d'endommagement ductiles; effondrement plastique immédiat, instabilité plastique immédiate,
  - modes d'endommagement non ductiles; localisation immédiate de la plasticité, rupture locale immédiate due à l'épuisement de la ductilité, rupture rapide.
- les dommages de type-S qui résultent de l'application répétée de chargements :
  - déformation progressive; la déformation plastique augmente après chaque cycle, induisant d'avantage de déformations jusqu'à la ruine de la structure (c.à.d., phénomène de rochet),
  - fatigue (par propagation de fissure); fatigue dépendante (fluage) et indépendante du temps.

Phénomène de rochet

De façon générale, l'intégrité structurelle des composants est justifiée avec des lois de comportement élastiques au travers de méthodes analytiques, et/ou éléments finis. Lorsque les analyses élastiques sont insuffisantes pour justifier l'intégrité structurelle des composants, des lois de comportement nonlinéaires sont utilisées, pour une justification plus élaborée de la conception (Martinez, 2015). L'évaluation des structures sous chargement cycliques ne peut être faite que si les critères de dommages de type-P ont été validés. En plus de l'endommagement par fatigue, l'un des critères de type-S les plus difficiles à satisfaire, reste le phénomène de rochet.

Deux types de phénomène de rochet se distinguent: le rochet matériaux, et le rochet structurel (Hübel, 1996).

Sous chargement cyclique de traction-compression, la plupart des expériences mettent en avant une évolution des propriétés d'écrouissage des métaux et des alliages, au cours des différents cycles. On observe un adoucissement ou un durcissement en fonction du matériau, de la température, et des conditions initiales. Dans le cas d'un chargement non symétrique, en contrainte imposée, l'éprouvette subit un écrouissage, qui dans le cas le plus critique, s'accroît au fil des cycles, jusqu'à la rupture: c'est le phénomène de rochet, voir Fig. 168. De la même façon, sous chargement non symétrique, en déplacement imposé, le phénomène de rochet se traduit par une diminution de la contrainte moyenne, voir Fig. 167 (Chaboche, et al., 1988).

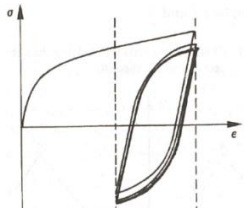

Fig. 167 – Phénomène de rochet: diminution de la contrainte moyenne sous chargement non symétrique en déplacement imposé (Chaboche, et al., 1988)

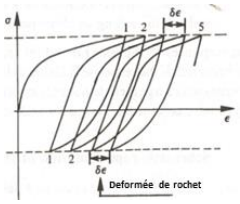

Fig. 168 – Phénomène de rochet: augmentation de la déformation moyenne après chaque cycle sous chargement non symétrique en contrainte imposée (Chaboche, et al., 1988)

Le phénomène de rochet structurel peut apparaître sans aucune influence du rochet matériau. Ce type de rochet est observé sous un état de contrainte non homogène de la structure, et peut être simulé par des modèles élasto-plastiques simples (Kobayashi, et al., 1996). Le cylindre de Bree est une bonne représentation d'un ESPN, tel que le VV, sous condition normale d'opération (Bree, 1967). L'essai du cylindre de Bree consiste à observer l'évolution structurelle d'un tube sous pression interne constante et sujet à des cycles thermiques. Cet essai permet de mettre en avant le phénomène de rochet structurel.

La représentation de ces deux précédents phénomènes par la méthode des éléments finis, est le cœur du sujet présenté dans cet article.

Essais mécaniques sur l'acier inoxydable 316L(N)-IG

Parmi les nombreux types d'acier inoxydable, différents par leur normes, grades et variations dans leurs spécifications, les experts matériaux d'ITER ont désigné un acier spécifique au projet ITER, pour lequel seules des modifications mineures ont été apportées pour faire face aux limites de sécurité radiologique et aux exigences de soudabilité (Barabash, 2007). Outre les exigences de bonne résistance mécanique, de résistance à la fatigue et de ductilité adéquate pour fonctionner dans les conditions de charge sévères décrites dans le précédant paragraphe, le matériau structurel ITER doit également satisfaire aux exigences de bonne soudabilité, de résistance à la corrosion et de compatibilité avec l'environnement sous vide. Le principal matériau utilisé dans l'enceinte à vide ITER, dont la plage de température de fonctionnement se situe entre 100°C et 200°C avec un endommagement neutronique inférieur à 0,5 dpa, est l'acier inoxydable austénitique recuit désigné sous le nom de 316L(N)-IG voir Table 8. Les deux lettres "IG" sont l'abréviation de "ITER Grade".

Table 8 – Pricipales propriétés de l'acier 316L(N)-IG (Kalinin, 1996)

Temp	Density	Young's Modulus	Poisson 's Ratio	Mean Thermal Expansion	Thermal Conductivity	Specific Heat
°C	kg/m³	GPa		10^{-6}, 1/K	W/m K	J/kg K
20	7930	200	0.3	15.3	14.28	472
100	7899	193	0.3	15.9	15.48	501
200	7858	185	0.3	16.6	16.98	522

Dans la littérature, de nombreux résultats d'essais mécaniques sont disponibles pour l'acier inoxydable de type 316. Néanmoins, pour assurer une identification plus précise des paramètres du matériau, des essais mécaniques ont été effectués sur un échantillon usiné à partir d'une plaque du matériau de base du VV de dimensions 400x400x40mm.

Tous les essais ont été réalisés sur une machine hydraulique de traction/compression MTS 322 100 kN équipée d'un extensomètre axial MTS, voir Fig. 169.

Fig. 169 – Machine d'essai de traction avec extensomètre.

Essais de traction monotone

Pour les essais de traction, trois éprouvettes ont été usinées dans le sens longitudinal de la plaque, et trois autres dans le sens transversal. Les dimensions sont rapportées en Fig. 170.

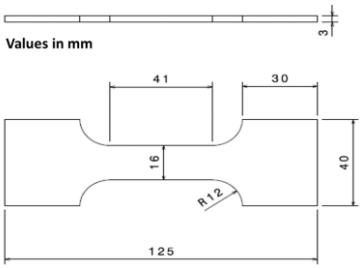

Fig. 170 – Dimension de l'éprouvette de traction.

Le premier objectif de ces essais était de démontrer que le matériau est initialement isotrope. De plus, des essais ont été effectués pour vérifier l'éventuelle évolution du module d'Young après différentes phases de déchargement et de rechargement. Aucune déviation notable n'a été trouvée dans les résultats, voir Fig. 171.

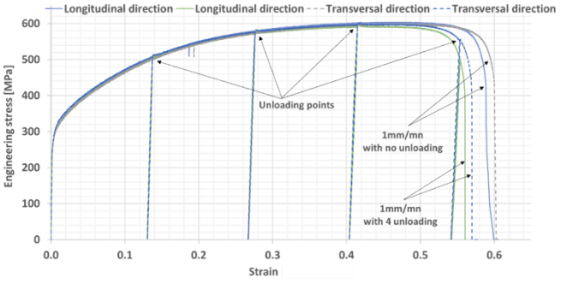

Fig. 171 – Comparaison entre les essais de traction avec déchargement (#4) et rechargement (#4) dans le sens transversal et longitudinal.

Enfin, la viscosité du matériau a été identifiée via des tests effectués à différentes vitesses. On constate qu'à faible vitesse (1 mm/min), la résistance ultime est 30 % plus élevée que celle mesurée dans les autres essais réalisés, voir Fig. 172.

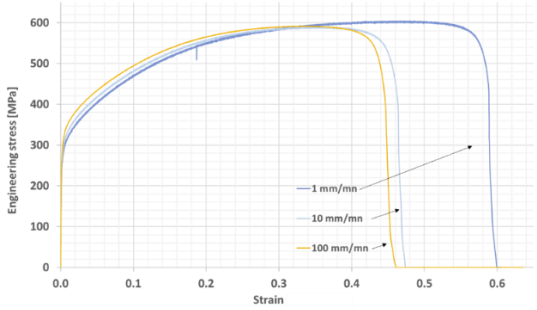

Fig. 172 – Comparaison entre des essais de traction à différentes vitesses de chargement.

Essais de traction/compression cyclique

Les essais de traction ayant démontré que le matériau est isotrope, dix éprouvettes axisymétriques supplémentaires adaptées aux chargements cycliques ont été préparées. Les dimensions sont décrites en Fig. 173.

La campagne d'essais mécaniques réalisée visait à mettre en évidence la réponse du matériau aux sollicitations oligocycliques. Afin de faciliter la compréhension et l'interprétation des résultats obtenus, seuls deux d'entre eux sont présentés dans cet article.

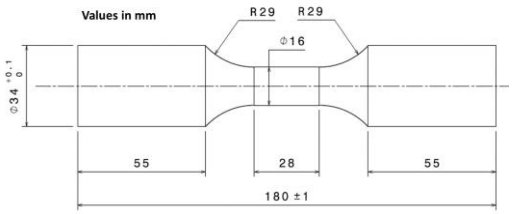

Fig. 173 – Dimension de l'éprouvette de traction/compression.

À partir de l'essai de traction/compression, deux types de résultats peuvent être rapportés, la courbe de contrainte-déformation nominale, basée sur la section initiale, et la courbe de contrainte-déformation vraie, basée sur la section mesurée. Pour nos expériences, l'extensomètre a été adapté pour mesurer l'évolution du diamètre de l'échantillon d'essai, comme indiqué dans la Fig. 174.

Cette configuration permet de mesurer la contrainte vraie lors d'un essai en force imposée et de piloter l'essai en contrainte imposée. L'essai en contrainte imposée vise à représenter le phénomène de rochet, tel qu'il est décrit dans le paragraphe 1.2.

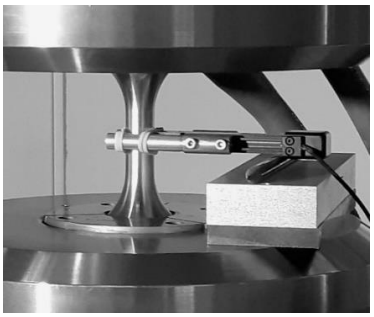

Fig. 174 – Configuration de l'extensomètre pour les essais cycliques.

Cet article présente deux essais cycliques de traction/compression, dont le premier a été réalisé en effort imposé, et le second en contrainte imposée.

Sur les Fig. 175 et Fig. 177, la courbe orange illustre la contrainte-déformation nominale et la courbe bleue la contrainte-déformation vraie. Il est important de noter que les 10 cycles initiaux, qui ressemblent à un phénomène d'accommodation, sont dus à la séquence initiale de la machine qui atteint progressivement le chargement nominal, voir point A Fig. 175 et Fig. 177.

La Fig. 175 présente les résultats d'essais réalisés en effort imposé avec les paramètres suivants : F_{max}=100kN and F_{min}=-40kN. La force a été appliquée suivant un signal sinusoïdal défini en éq.(234), avec une force moyenne F_{moy}= 30kN, une amplitude de force ΔF=140kN et une fréquence f=0.3s^{-1}.

$$F(t) = F_{moy} + \frac{\Delta F}{2} \sin(2\,\pi\,f\,t) \qquad (234)$$

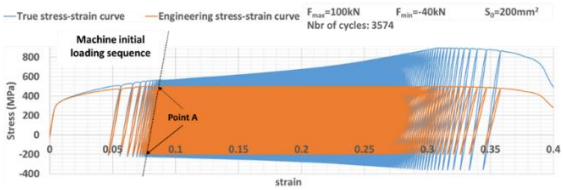

Fig. 175 – Résultat d'essais cycliques en effort imposé

Par définition, l'adaptation apparaît lorsque l'évolution de la déformation entre deux cycles est égale ou proche de zéro. Cependant, les résultats montrent que la contrainte augmente continuellement après chaque cycle. C'est pourquoi, pour dissocier l'accommodation plastique du phénomène de rochet, nous avons proposé de tracer l'évolution de la déformation le long des cycles cumulés, cf. Fig. 176.

La ligne noire en pointillés représente l'évolution de la déformation à partir d'une fonction affine, pour laquelle le coefficient de pente renseigne sur le taux de rochet. En effet, lorsque la pente est proche de l'infini, il se produit une accommodation plastique, sinon, un rochet se produit, voir Fig. 176.

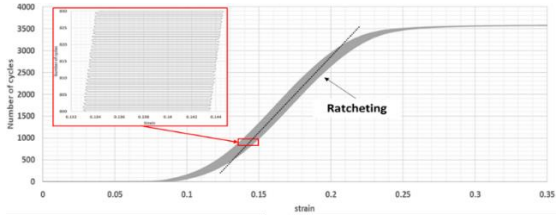

Fig. 176 – Nombre cumulé de cycles pour l'essai en force imposée

La Fig. 13 présente les résultats d'essais réalisés en contrainte imposée avec les paramètres suivants : σ_{max}=780MPa et σ_{min}=-300MPa. La contrainte a été appliquée suivant un signal sinusoïdal définit en éq.(235), avec une contrainte moyenne σ_{moy}= 240MPa, une amplitude de contrainte $\Delta\sigma$=1080MPa et une fréquence f=0.3s^{-1}.

$$\sigma(t) = \sigma_{moy} + \frac{\Delta\sigma}{2}\sin(2\,\pi\,f\,t) \qquad (235)$$

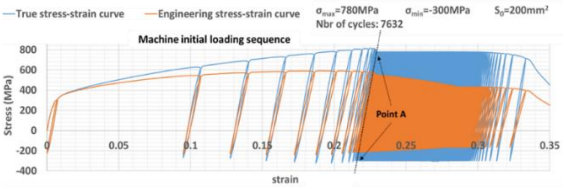

Fig. 177 – Résultats d'essai cyclique en contrainte imposée

Cette fois, cependant, nous avons tracé en Fig. 178 la déformée de rochet (δε), définie en Fig. 168, fonction de la déformation depuis le point A jusqu'à la fin de l'essai. Il montre une évolution exponentielle qui augmente rapidement au cours des 10 derniers cycles.

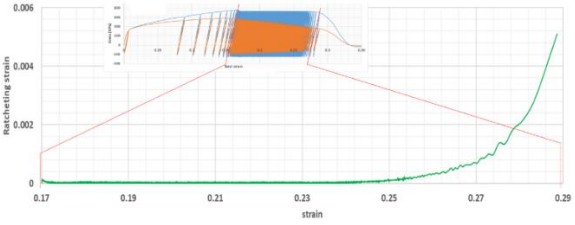

Fig. 178 – Déformée de rochet (δε) fonction de la déformation, pour un chargement cyclique en contrainte imposée

Les vues macroscopiques de l'échantillon d'essai cyclique présentées en Fig. 179 montrent une rupture ductile à la périphérie et une rupture fragile au centre, survenant après 3574 cycles pour le chargement en effort cyclique et après 7632 cycles pour le chargement en contrainte cyclique.

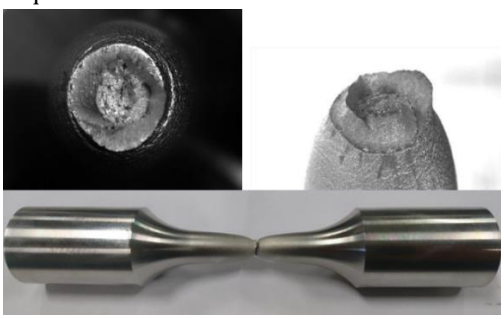

Fig. 179 – Vue macroscopique de l'éprouvette après rupture

A ce stade, l'enjeu est de représenter le comportement observé du matériau lors des essais par une approche phénoménologique.

Développement d'un modèle de comportement thermomécanique.

Dans le cas général, l'élaboration d'un modèle de comportement est basée sur la superposition de plusieurs fonctions d'écrouissage afin de représenter les phénomènes complexes qui peuvent être observés dans les différents essais (thermo)mécaniques (Chaboche, et al., 1988).

Dans un souci de représentation du comportement réel du matériau, avec l'objectif de définir un nombre raisonnable de variables d'état et de paramètre matériau, il est obligatoire d'identifier l'environnement dans lequel le modèle sera utilisé. Dans le cas présent, le modèle proposé devra représenter les comportements d'écrouissage suivants:

- effet Bauschinger,
- adoucissement ou durcissement cyclique,
- accommodation plastique et/ou adaptation élastique,
- phénomène de rochet,
- endommagement, c.à.d., formation et évolution de microcavités (micropores).

Bien que les niveaux de déformation enregistrés lors des essais expérimentaux dépassent 50 %, le tenseur des déformations infinitésimales sera retenu comme variable cinématique de base dans le modèle. En suivant les règles de conception nucléaire, il est en effet exclu que le matériau de structure VV puisse

subir des déformations importantes, qui ne sont néanmoins pas nécessaires pour que l'adaptation plastique et le phénomène de rochet se produisent. Les champs de contraintes et de déformations dans le VV en conditions normales de fonctionnement seront hétérogènes, et cette hétérogénéité peut suffire à déclencher ces phénomènes, même si les déformations restent, globalement et localement, bien inférieures à 50 %.

Variables et potentiel d'états

Les deux variables d'état qu'il faut nécessairement considérer lorsqu'on traite des problèmes thermomécaniques sont la température absolue $T \in R^+$ (en K) et, dans les cas où les déformations du matériau restent « faibles », le tenseur des petites déformations $\varepsilon \in R^3 \times R^3$ (sans unité). Cependant, dès que le comportement du matériau n'est plus thermoélastique, d'autres variables d'état, généralement appelées variables d'état « internes », (Coleman, et al., 1967), doivent être ajoutées à T et ε, pour prendre en compte différents mécanismes irréversibles, tels que la déformation permanente, l'écrouissage et l'endommagement. Dans la présente étude, ces variables supplémentaires sont :

- $\boldsymbol{\varepsilon^p} \in R^3 \times R^3$: tenseur des déformations plastiques,
- $\mathbf{X_i} \in R^3 \times R^3$: $i^{ème}$ tenseur d'écrouissage cinématique,
- $p \in R^+$: variable d'écrouissage isotrope,
- $d \in [0,1]$: variable d'endommagement.

On suppose aussi que l'écoulement plastique est incompressible, soit $Tr(\boldsymbol{\varepsilon^p})=0$ et $Tr(\mathbf{X_i})=0$.

La densité d'énergie libre de Helmholtz Ψ (en J/kg) est prise comme potentiel thermodynamique, correspondant à une fonction de toutes les variables d'état. Nous supposons l'expression suivante pour le développement du modèle constitutif :

$$\begin{aligned}\Psi(T, \boldsymbol{\varepsilon}, \boldsymbol{\varepsilon^p}, \boldsymbol{X_i}, \mathrm{p}, \mathrm{d}) = \\ +\frac{1}{2\rho_0}\lambda\left(Tr(\boldsymbol{\varepsilon}-\boldsymbol{\varepsilon^p})\right)^2 + \frac{1}{\rho_0}\mu(\boldsymbol{\varepsilon}-\boldsymbol{\varepsilon^p}):(\boldsymbol{\varepsilon}-\boldsymbol{\varepsilon^p}) \\ -\frac{1}{\rho_0}(3\lambda+2\mu)\gamma Tr(\boldsymbol{\varepsilon}-\boldsymbol{\varepsilon^p})(T-T_0) \\ -\frac{C_\varepsilon(T-T_0)^2}{2T_0} \\ +\frac{1}{\rho_0}k(1-d)\left(p+\frac{1}{m}e^{-mp}\right) \\ +\frac{1}{2\rho_0}\sum_{i=1}^{N_{kh}} M_i\, \boldsymbol{X_i}:\boldsymbol{X_i}\end{aligned} \tag{236}$$

où ρ_0 (en $kg.m^{-3}$) est la densité initiale, T_0 est la température initiale, et Tr(.) est l'opérateur trace. λ, μ, γ, C_ε, M_i, k et m sont des paramètres matériaux (dépendant de la température), qui doivent être identifiés à partir des résultats expérimentaux, tels que les résultats d'essais de tension-compression monotones et cycliques.

Le premier terme de l'énergie libre représente la partie mécanique de la déformation élastique linéaire qui dépend des paramètres matériau λ (en Pa) et μ (en Pa), premier et deuxième coefficient de Lamé.

$$\begin{aligned}\rho_0\bar{\Psi}^1_{\varepsilon^e}(\boldsymbol{\varepsilon}, \boldsymbol{\varepsilon^p}) = \\ \frac{\lambda}{2}\left(Tr(\boldsymbol{\varepsilon}-\boldsymbol{\varepsilon^p})\right)^2 + \mu Tr\left((\boldsymbol{\varepsilon}-\boldsymbol{\varepsilon^p}):(\boldsymbol{\varepsilon}-\boldsymbol{\varepsilon^p})\right)\end{aligned} \tag{237}$$

Evidemment, le tenseur de déformation plastique $\boldsymbol{\varepsilon^p}$, le tenseur de déformation élastique $\boldsymbol{\varepsilon^e} \in R^3 \times R^3$ et le tenseur des déformations totales $\boldsymbol{\varepsilon}$ sont liés par l'équation suivante:

$$\boldsymbol{\varepsilon} = \boldsymbol{\varepsilon^e} + \boldsymbol{\varepsilon^p} \Leftrightarrow \boldsymbol{\varepsilon^e} = \boldsymbol{\varepsilon} - \boldsymbol{\varepsilon^p} \tag{238}$$

Le deuxième terme de l'énergie libre représente la partie thermoélastique où γ (in K^{-1}) est le coefficient de dilatation thermique :

$$\begin{aligned}\rho_0\bar{\Psi}^2_{\varepsilon^e}(\boldsymbol{\varepsilon}, \boldsymbol{\varepsilon^p}, \mathrm{T}) = \\ -(3\lambda+2\mu)\gamma \mathrm{Tr}(\boldsymbol{\varepsilon}-\boldsymbol{\varepsilon^p})(\mathrm{T}-\mathrm{T}_0)\end{aligned} \tag{239}$$

Les effets purement thermiques sont bien évidemment pris en compte dans le modèle, via le troisième terme de l'énergie libre, où intervient la capacité calorifique C_ε (in J/kg.K):

$$\bar{\Psi}_T(T) = -\frac{C_\varepsilon(T-T_0)^2}{2T_0} \tag{240}$$

Cette forme permet d'obtenir une dépendance linéaire en température de la capacité calorifique, comme observé expérimentalement (Kalinin, 1996).

L'écrouissage cinématique représente la déformation plastique non homogène liée au

coefficient caractéristique du matériau M_i (en Pa). L'écrouissage cinématique est communément représenté en additionnant N_{kh} variables X_i (où N_{kh}=2 ou 3 dans la plupart des cas) visant à lisser le comportement plastique afin d'obtenir un meilleur accord avec les résultats d'essais. La superposition des variables cinématiques se fait en sommant les différents termes comme suit, pour représenter la partie écrouissage cinématique de l'énergie libre (Nouailhas, 1988):

$$\rho_0 \overline{\Psi}_X(\boldsymbol{X_i}) = \frac{1}{2}\sum_{i=1}^{N_{kh}} M_i \, \boldsymbol{X_i} : \boldsymbol{X_i} \qquad (241)$$

Il a été observé à partir des essais de traction-compression cycliques que le matériau présente un comportement de durcissement avec une tendance logarithmique. Pour en rendre compte, nous proposons une expression non linéaire de l'écrouissage isotrope (Nouailhas, 1988), où m (sans unité) et k (en Pa) sont deux coefficients caractéristiques du matériau. Pour un matériau non endommagé, l'expression de l'énergie libre représentant l'écrouissage isotrope peut être écrite :

$$\rho_0 \overline{\Psi}_p(p) = k\left(p + \frac{1}{m}e^{-mp}\right) \qquad (242)$$

La modélisation de la rupture ductile dans le cadre de la mécanique de l'endommagement continu est issue de la compétition entre écrouissage et endommagement. La variable d'endommagement est basée sur le concept selon lequel la rupture ductile résulte de la formation, de la croissance et de la coalescence de cavités, voir Fig. 180 (Rousselier, 1987). Malgré la complexité de ce mécanisme d'endommagement, l'hypothèse retenue ne suppose qu'un seul type de cavité à évolution isotrope.

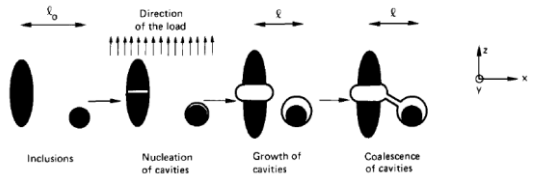

Fig. 180 – Modélisation de la rupture ductile (Rousselier, 1987).

Dans l'hypothèse où ce phénomène est isotrope, la densité surfacique de ces microfissures et microcavités peut être représentée par une variable scalaire d, où d=0 correspondant à l'état non endommagé et d=1 perte totale de cohésion de la matière (Rousselier, 1987). La Fig. 181 montre un exemple d'évolution de la variable d'endommagement (Lemaitre, 1985).

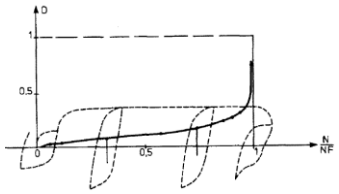

Fig. 181 – Exemple d'évolution de l'endommagement lors d'un essai de fatigue par fluage (Lemaitre, 1985)

Pour un matériau endommagé, une compétition est supposée exister entre la plasticité (tendance à l'écrouissage positif) et l'endommagement (tendance à l'écrouissage négatif). En conséquence, l'éq.(242) est modifiée de la manière suivante:

$$\rho_0 \overline{\Psi}_p(p,d) = (1-d)k\left(p + \frac{1}{m}e^{-mp}\right) \qquad (243)$$

Il est important de noter que tous les paramètres du matériau peuvent dépendre de la température. Néanmoins, pour simplifier les équations suivantes dans cet article, cette dépendance sera négligée sous l'hypothèse que la plage de température étudiée n'a pas d'effet significatif (<5%).

De plus, l'identification des paramètres, y compris la dépendance à la température, nécessite un ensemble vaste et complexe de résultats de campagnes d'essais, qui ne font pas partie de cet article.

Expression de la dissipation intrinsèque

La première loi de la thermodynamique postule d'abord qu'une énergie interne peut être définie pour tous les systèmes thermodynamiques et, d'autre part, que la variation de cette énergie interne est toujours égale à celle de l'énergie fournie au système sous forme de chaleur (partie thermique) et de travail (partie mécanique). En thermodynamique des milieux continus, on lit :

$$\rho_0 T\dot{s} + div(\boldsymbol{q}) - r^v = \boldsymbol{\sigma} : \dot{\boldsymbol{\varepsilon}} - \rho_0 \dot{\Psi} - \rho_0 s\dot{T} \qquad (244)$$

où s est l'entropie massique (J/kg.K), $\boldsymbol{q}$ est la puissance surfacique (W/m^2), et r^v est une source de chaleur externe (W/m^3).

La deuxième loi de la thermodynamique stipule d'abord qu'une entropie peut être définie pour tous les systèmes thermodynamiques et, deuxièmement, que la variation de l'entropie est toujours supérieure ou égale à celle de l'environnement du système. En thermodynamique des milieux continus, elle s'écrit :

$$\rho\dot{s} + div\left(\frac{\boldsymbol{q}}{T}\right) - \frac{r^v}{T} \geq 0 \qquad (245)$$

Cette évolution est la somme de la dissipation thermique (conduction thermique) et de la dissipation intrinsèque, toutes deux supposées positives ou nulles. L'expression de la dissipation intrinsèque $\emptyset_{int}$ (W/m^3) est fonction de l'expression de la dérivée de l'énergie libre, exprimée comme (voir (Coleman, et al., 1967)):

$$\begin{aligned}\emptyset_{\boldsymbol{int}} = \left(\boldsymbol{\sigma} - \rho_0 \frac{\partial \Psi}{\partial \boldsymbol{\varepsilon}}\right) : \dot{\boldsymbol{\varepsilon}} \\ - \rho_0 \left(s + \frac{\partial \Psi}{\partial T}\right)\dot{T} \\ - \rho_0 \frac{\partial \Psi}{\partial \boldsymbol{\alpha}} . \dot{\boldsymbol{\alpha}} \geq 0\end{aligned} \qquad (246)$$

où $\boldsymbol{\alpha}$ est une représentation synthétique de l'ensemble des variables internes (p, d, $\boldsymbol{\varepsilon^p}$ et $\mathbf{X}_i$, dans cette étude).

Du fait que l'entropie massique est une fonction d'état, une première condition pour la non négativité de la dissipation intrinsèque, voir éq.(246) est :

$$s = -\frac{\partial \Psi}{\partial T} \qquad (247)$$

De plus, afin d'être en accord avec tous les essais expérimentaux réalisés sur le matériau de structure VV (voir §2), les phénomènes viscoélastiques ne seront pas pris en compte dans la présente étude. Le tenseur des contraintes $\boldsymbol{\sigma}$ peut alors être considéré comme une fonction d'état, qui peut s'écrire comme suit :

$$\boldsymbol{\sigma} = \rho_0 \frac{\partial \Psi}{\partial \boldsymbol{\varepsilon}} \qquad (248)$$

Comme décrit à la fin du §3.1, pour simplifier les équations suivantes, la dépendance des paramètres du matériau à la température est omise.

En utilisant l'éq. (236), nous pouvons maintenant exprimer explicitement la contrainte et l'entropie massique pour notre modèle :

$$\begin{aligned}\boldsymbol{\sigma} = \rho_0 \frac{\partial \Psi}{\partial \boldsymbol{\varepsilon}} = \\ \lambda Tr(\boldsymbol{\varepsilon} - \boldsymbol{\varepsilon^p})\boldsymbol{G} + 2\mu(\boldsymbol{\varepsilon} - \boldsymbol{\varepsilon^p}) \\ -(3\lambda + 2\mu)\gamma(T - T_0)\boldsymbol{G}\end{aligned} \qquad (249)$$

où $\mathbf{G}$ est le tenseur métrique (dans toute base orthonormée, $G_{ij}=\delta_{ij}$ où δ_{ij} représente le symbole de Kronecker).

$$\begin{aligned}s = -\frac{\partial \Psi}{\partial T} = \\ \frac{C_\varepsilon (T - T_0)}{T_0} + \frac{(3\lambda + 2\mu)\gamma Tr(\varepsilon - \varepsilon^p)}{\rho_0}\end{aligned} \qquad (250)$$

La dérivée partielle de Ψ par rapport aux variables internes peut être développée comme suit:

$$\begin{aligned}\rho_0 \frac{\partial \Psi}{\partial \boldsymbol{\alpha}} . \dot{\boldsymbol{\alpha}} = \rho_0 \frac{\partial \Psi}{\partial p}\dot{p} + \rho_0 \frac{\partial \Psi}{\partial d}\dot{d} + \\ \rho_0 \frac{\partial \Psi}{\partial \boldsymbol{\varepsilon^p}} : \dot{\boldsymbol{\varepsilon}}^{\boldsymbol{p}} + \rho_0 \sum_{i=1}^{N_{kh}} \frac{\partial \Psi}{\partial \boldsymbol{X}_i} : \dot{\boldsymbol{X}}_i\end{aligned} \qquad (251)$$

Par conséquent, l'expression de la dissipation intrinsèque est :

$$\begin{aligned}\emptyset_{\boldsymbol{int}} = \rho_0 \frac{\partial \Psi}{\partial p}\dot{p} + \rho_0 \frac{\partial \Psi}{\partial d}\dot{d} + \rho_0 \frac{\partial \Psi}{\partial \boldsymbol{\varepsilon^p}} : \dot{\boldsymbol{\varepsilon}}^{\boldsymbol{p}} \\ + \rho_0 \sum_{i=1}^{N_{kh}} \frac{\partial \Psi}{\partial \boldsymbol{X}_i} : \dot{\boldsymbol{X}}_i \geq 0\end{aligned} \qquad (252)$$

L'expression de la dérivée partielle de Ψ par rapport au tenseur des déformations plastiques $\boldsymbol{\varepsilon^p}$ nous donne la force thermodynamique $\boldsymbol{A^{\varepsilon^p}}$ associée à la déformation plastique (le signe moins étant conventionnel):

$$\boldsymbol{A^{\varepsilon^p}} = -\rho_0 \frac{\partial \Psi}{\partial \boldsymbol{\varepsilon^p}} = \rho_0 \frac{\partial \Psi}{\partial \boldsymbol{\varepsilon}} = \boldsymbol{\sigma} \qquad (253)$$

L'expression de la dérivée partielle de Ψ par rapport au i^{ème} tenseur d'écrouissage cinématique X_i, nous donne la i^{ème} force thermodynamique $\boldsymbol{A^{X_i}}$ associé à l'écrouissage cinématique:

$$\boldsymbol{A^{X_i}} = -\rho_0 \frac{\partial \Psi}{\partial \boldsymbol{X_i}} = -M_i \boldsymbol{X_i} \qquad (254)$$

La fonction isotrope incluant la variable d'endommagement est définie par la dérivée partielle de Ψ par rapport à la variable isotrope p:

$$A^p = -\rho_0 \frac{\partial \Psi}{\partial p} = -k(1 - \mathrm{d})(1 - e^{-mp}) \qquad (255)$$

L'expression de la dérivée partielle de Ψ par rapport à la variable d'endommagement (d) est:

$$A^d = -\rho_0 \frac{\partial \Psi}{\partial d} = k\left(p + \frac{1}{m}e^{-mp}\right) \qquad (256)$$

Avec toutes ces expressions, il faut formuler des équations d'évolution qui assureront la positivité de la dissipation intrinsèque quel que soit l'état (T, $\boldsymbol{\varepsilon}$, $\boldsymbol{\varepsilon^p}$, $\boldsymbol{X_i}$, p, d) et quels que soient $\dot{T}$ et $\dot{\boldsymbol{\varepsilon}}$.

Equations d'évolution des variables internes

Les variables internes commencent à évoluer lorsque les déformations irréversibles se produisent. Le critère de Von Mises a été choisi pour exprimer le seuil de non élasticité tel qu'il est décrit dans (Chaboche, et al., 1988).

Prenant en compte l'expression de la fonction d'écrouissage isotrope éq. (255), l'expression de la fonction du seuil de non élasticité apparaît comme :

$$f(\boldsymbol{\sigma}, \boldsymbol{A^{X_i}}, A^p) = J\left(\boldsymbol{\sigma} + \sum_{i=1}^{N_{kh}} \boldsymbol{A^{X_i}}\right) - A^p - \sigma_0 \qquad (257)$$

Nous proposons d'implémenter la variable d'endommagement d également dans la partie écrouissage cinématique de la fonction seuil, de telle sorte que les écrouissages isotrope et cinématique fonctionnent en opposition. En gardant l'objectif d'un développement de modèle simple, le couplage de l'endommagement avec l'écrouissage cinématique est identique pour toutes les variables.

Par conséquent, en utilisant des variables internes au lieu des forces thermodynamiques et en incluant la variable d'endommagement, l'éq.(24) est modifiée de la manière suivante :

$$f(\boldsymbol{\sigma}, \boldsymbol{X_i}, \mathrm{p}, \mathrm{d}) = J\left(\boldsymbol{\sigma} - \mathrm{d}\sum_{i=1}^{N_{kh}} M_i \boldsymbol{X_i}\right) - k(1-\mathrm{d})(1-e^{-mp}) - \sigma_0 \qquad (258)$$

où σ_0 (en Pa) est la limite d'élasticité initiale, et la contrainte équivalente au sens de Von Mises est exprimée par:

$$J(\boldsymbol{\sigma}) = \sqrt{\frac{3}{2}\boldsymbol{Dev}(\boldsymbol{\sigma}) : \boldsymbol{Dev}(\boldsymbol{\sigma})} \qquad (259)$$

où **Dev(.)** est l'opérateur déviatorique décrit comme:

$$\boldsymbol{Dev}(\boldsymbol{\sigma}) = \boldsymbol{\sigma} - \frac{1}{3}\mathrm{Tr}(\boldsymbol{\sigma})\mathbf{G} \qquad (260)$$

Les équations d'évolution des variables internes doivent être telles que l'inégalité concernant la dissipation intrinsèque, voir éq.(252), est toujours satisfait. Le cadre des matériaux dits standards généralisés, e.g. (Germain, et al., 1983), permet la vérification systématique de cette contrainte. Elle repose sur deux hypothèses, à savoir qu'il existe:

iii) un multiplicateur plastique Λ, qui ne peut pas être négatif,
iv) au moins un potentiel d'écoulement plastique, dont la dérivée partielle fixe la direction d'évolution des variables internes.

En conséquence de i) et ii), l'équation d'évolution de l'ensemble des variables internes **α**, voir éq.(246), s'écrit :

$$\dot{\boldsymbol{\alpha}} = \Lambda \frac{\partial g}{\partial \boldsymbol{A^{\alpha}}} \qquad (261)$$

Dans le présent article, du fait que la plasticité et l'endommagement sont des phénomènes irréversibles qui peuvent évoluer de manières très différentes, deux potentiels d'écoulement sont clairement distingués, l'un pour la plasticité, g, et l'autre pour l'endommagement, g^d. La dissipation intrinsèque s'écrit alors :

$$\emptyset_{int} = -\rho_0 \Lambda \left(\frac{\partial \Psi}{\partial \boldsymbol{\varepsilon^p}} : \frac{\partial g}{\partial \boldsymbol{\sigma}} + \frac{\partial \Psi}{\partial p}\frac{\partial g}{\partial A^p} + \sum_{i=1}^{N_{kh}} \left(\frac{\partial \Psi}{\partial \boldsymbol{X}_{\mathrm{i}}} : \dot{\boldsymbol{X}}_{\mathrm{i}} \right) : \frac{\partial g}{\partial \boldsymbol{A^{X_i}}} + \frac{\partial \Psi}{\partial d}\frac{\partial g^d}{\partial A^d} \right) \qquad (262)$$

Pour représenter le phénomène de rochet, l'utilisation d'un modèle non associé est requis où le potentiel d'écoulement plastique g n'est pas seulement défini par l'expression de la fonction seuil de non élasticité éq.(257), mais aussi avec un terme supplémentaire initialement décrit par Armstrong & Frederick comme suit (Armstrong, et al., 1966):

$$g(\boldsymbol{\sigma}, \boldsymbol{A^{X_i}}, A^p, A^d) = f(\boldsymbol{\sigma}, \boldsymbol{A^{X_i}}, A^p, A^d) + \sum_{i=1}^{N_{kh}} \left(\frac{\Gamma_i}{2M_i} \left(\boldsymbol{Dev}(\boldsymbol{A^{X_i}}) : \boldsymbol{Dev}(\boldsymbol{A^{X_i}}) \right) \right) \qquad (263)$$

Où les Γ_i (sans unités) sont des paramètres matériaux.

Ce terme supplémentaire, qui est lié à la déformée de rochet, voir Fig. 168, est trop prononcée, et la plupart des études antérieures réalisées dans le but de minimiser cette réponse du matériau ont conduit à l'introduction de paramètres supplémentaires induisant une élaboration plus complexe du modèle de comportement du matériau voir (Chaboche, 1991), (Ohno, et al., 1993), (Ohno, et al., 1993), (Jiang, et al., 1996), (Jiang, et al., 1996), (Abdel-Karim, et al., 2000) and (Abdel-Karim, et al., 2000).

Nous avons observé lors de la campagne d'essais mécaniques qu'après chaque cycle, l'éprouvette évolue, et la seule différence entre la réponse stabilisée et le phénomène de rochet est la valeur de la déformée de rochet (δε) entre chaque cycle. De plus, pour des essais de traction-compression menés en contrainte imposée, nous avons observé que la déformée de rochet a une évolution exponentielle qui augmente rapidement au cours des 10 derniers cycles, comme cela est décrit sur la Fig. 178.

Comme le phénomène de rochet est induit par une rupture ductile, et comme l'évolution de la variable d'endommagement, proposée par Lemaitre (Lemaitre, 1985) et Rousselier (Rousselier, 1987) en mécanique de la rupture, adopte un comportement exponentiel similaire à celui observé expérimentalement sur la Fig. 181, nous proposons un couplage entre la variable d'endommagement et le potentiel d'écoulement plastique, soit:

$$\begin{gathered} g(\boldsymbol{\sigma}, \boldsymbol{A}^{\boldsymbol{X}_i}, A^p, A^d) = \\ f(\boldsymbol{\sigma}, \boldsymbol{A}^{\boldsymbol{X}_i}, A^p, A^d) \\ + \mathrm{d} \sum_{i=1}^{N_{kh}} \left(\frac{\Gamma_i}{2M_i} \left(\boldsymbol{Dev}(\boldsymbol{A}^{\boldsymbol{X}_i}) : \boldsymbol{Dev}(\boldsymbol{A}^{\boldsymbol{X}_i}) \right) \right) \end{gathered} \tag{264}$$

Ce couplage supplémentaire avec la variable d'endommagement garantit que l'évolution de la déformée de rochet est minimisée en mode de faible endommagement, c'est-à-dire lorsque d est proche de 0, alors que lorsque d est proche de 1, δε est suffisamment élevée pour générer une réponse de rochet.

Le second potentiel d'écoulement plastique g^d est dédié à l'évolution de la variable d'endommagement et est découplé du principal potentiel d'écoulement plastique g. En supposant que la propagation des microfissures soit isotrope et que la croissance des cavités ne dépende que du chargement en traction, cet écoulement plastique est fonction de la partie positive du tenseur des contraintes et de la variable d'endommagement. Ce potentiel d'écoulement est ajusté par un coefficient caractéristique du matériau, n (en Pa). Enfin, pour s'assurer que la variable d n'excédera pas 1, nous avons introduit le terme $\langle 1-d \rangle$ qui met à zéro l'évolution de la variable dès que d=1. Le potentiel d'écoulement plastique g^d peut être exprimé comme suit:

$$g^d = \frac{d}{n} \langle 1-d \rangle \langle Tr(\boldsymbol{\sigma}) \rangle A^p \tag{265}$$

Exprimons l'évolution de toutes les variables en fonction des dérivées partielles du potentiel d'écoulement plastique g, en commençant par la dérivée par rapport à la déformation plastique ($\boldsymbol{\varepsilon^p}$):

$$\begin{aligned} \dot{\boldsymbol{\varepsilon}}^{\boldsymbol{p}} &= \Lambda \left(\frac{3}{2J\left(\boldsymbol{\sigma} - \mathrm{d} \sum_{i=1}^{N_{kh}} M_i \boldsymbol{X_i}\right)} \right) \\ &\quad . \boldsymbol{Dev} \left(\boldsymbol{\sigma} - \mathrm{d} \sum_{i=1}^{N_{kh}} M_i \boldsymbol{X_i} \right) \end{aligned} \tag{266}$$

L'évolution de la variable tensorielle d'écrouissage cinématique ($\mathbf{X_i}$) s'écrit quant à elle:

$$\dot{\boldsymbol{X}}_i = \Lambda \frac{\partial g}{\partial \boldsymbol{A}^{\boldsymbol{X}_i}} = \mathrm{d} \dot{\boldsymbol{\varepsilon}}^{\boldsymbol{p}} - d\Lambda\Gamma_i \boldsymbol{X}_i \tag{267}$$

L'évolution de la variable isotrope (p) s'écrit:

$$\dot{\boldsymbol{p}} = \Lambda \frac{\partial g}{\partial A^p} = \Lambda \tag{268}$$

L'évolution de la variable d'endommagement (d), en revanche, est définie par l'équation suivante:

$$\dot{d} = \Lambda \frac{\partial g^d}{\partial A^d} = \Lambda \frac{d\langle 1-d \rangle}{n} \langle Tr(\boldsymbol{\sigma}) \rangle \tag{269}$$

En supposant que la propagation des microfissures est isotrope et que la croissance des cavités ne dépend que du chargement en traction, (Rousselier, 1987), l'éq.(269) implique des crochets de Mc Cauley définis comme suit:

$$\langle Tr(\boldsymbol{\sigma}) \rangle = \begin{cases} 0 & if\ Tr(\boldsymbol{\sigma}) < 0 \\ Tr(\boldsymbol{\sigma}) & if\ Tr(\boldsymbol{\sigma}) \geq 0 \end{cases} \tag{270}$$

Une valeur strictement positive est requise pour que la variable d'endommagement interne autorise l'évolution du dommage (voir éq.(269)) . Il est proposé de fixer le paramètre d_0 à une valeur comprise entre 10^{-4} et 10^{-5}, ce qui correspond à la fraction initiale de cavités. L'évolution des cavités sera principalement pilotée par le multiplicateur d'écoulement plastique et elle sera ajustée par un coefficient caractéristique du matériau, n (en Pa).

Avec l'hypothèse proposée ici, seul le comportement viscoplastique, qui est par définition fonction du temps, sera étudié. Ce type de modèles peut représenter le fluage et la relaxation, c'est pourquoi le modèle proposé par (Perzyna, 2005) pour représenter le comportement de viscoplasticité a été sélectionné.

Il faut proposer une expression pour $\Lambda \geq 0$ où η (en s) est le temps caractéristique de la viscosité du matériau:

$$\Lambda = \frac{1}{\eta}\left(\frac{\langle J\left(\boldsymbol{\sigma} - \mathrm{d}\sum_{i=1}^{N_{kh}} M_i \boldsymbol{X_i}\right) - A^p - \sigma_0\rangle}{\sigma_0}\right) \quad (271)$$

Tous les termes dans l'expression de la dissipation intrinsèque éq.(262) ont maintenant été développées, et la nouvelle expression apparaît comme:

$$\begin{aligned} \emptyset_{int} = \\ \Lambda\left(\begin{array}{c} J\left(\boldsymbol{\sigma} - \mathrm{d}\sum_{i=1}^{N_{kh}} M_i \boldsymbol{X_i}\right) + \mathrm{d}\sum_{i=1}^{N_{kh}} M_\mathrm{i}\Gamma_i \boldsymbol{X}_\mathrm{i}\colon \boldsymbol{X}_\mathrm{i} \\ +k(1-\mathrm{d})(1-e^{-mp}) \\ +\frac{d(1-d)}{n}\langle Tr(\boldsymbol{\sigma})\rangle\, k\left(p+\frac{1}{m}e^{-mp}\right) \end{array}\right) \end{aligned} \quad (272)$$

On peut montrer que $\emptyset_{int}$ est toujours positive ou nulle quel que soit l'état thermodynamique.

Expression de l'équation de la chaleur (premier principe de la thermodynamique)

L'évolution de l'entropie massique s peut être déduite en dérivant l'éq. (250) par rapport au temps, soit:

$$\dot{s} = \mathrm{C}_\varepsilon \frac{\dot{T}}{T_0} + \frac{(3\lambda + 2\mu)\gamma Tr(\dot{\boldsymbol{\varepsilon}})}{\rho_0} \quad (273)$$

La conduction thermique dans un volume homogène peut être exprimée avec la loi de Fourier, qui stipule que le flux interne de génération de chaleur est proportionnel au gradient de température. Selon la loi de Fourier isotrope, cette distribution de flux s'exprime comme suit:

$$div(\boldsymbol{q}) = -k\, div\big(grad(T)\big) = -k_T \Delta T \quad (274)$$

où k_T est le coefficient de conductivité thermique.

A partir du premier principe, éq.(244), et du second principe, éq.(246), de la thermodynamique, et compte tenu de l'expression de la dissipation intrinsèque, éq.(272), l'évolution de l'entropie massique, éq.(275), et la distribution de flux thermique, éq.(274), l'équation de la chaleur peut être écrite comme suit :

$$\begin{aligned} \frac{\rho_0 C_\varepsilon}{T_0} T\dot{T} - k_T \Delta T - r^v \\ = \\ -(3\lambda + 2\mu)\gamma Tr(\dot{\boldsymbol{\varepsilon}})T \\ +\Lambda J\left(\boldsymbol{\sigma} - \mathrm{d}\sum_{i=1}^{N_{kh}} M_i \boldsymbol{X_i}\right) \\ +\mathrm{d}\sum_{i=1}^{N_{kh}} M_\mathrm{i}\Lambda\Gamma_i \boldsymbol{X_i}\colon \boldsymbol{X_i} \\ +k\Lambda(1-\mathrm{d})(1-e^{-mp}) \\ +\left(k\left(p+\frac{1}{m}e^{-mp}\right)\right)\Lambda\frac{d(1-d)}{n}\langle Tr(\boldsymbol{\sigma})\rangle \end{aligned} \quad (275)$$

Le couplage thermomécanique fort nécessite que l'équation de la chaleur éq.(275) soit résolu simultanément avec le principe fondamental de la statique lequel s'ecrit:

$$\boldsymbol{Div}(\boldsymbol{\sigma}) + \boldsymbol{f^v} = \boldsymbol{0} \quad (276)$$

où $\boldsymbol{f^v}$ sont les forces volumiques. Ces équations d'équilibre doivent être complétées par des conditions initiales et aux limites appropriées.

Prédictions du modèle dans un cas de chargement simple (simulations "0D")

Afin d'illustrer la capacité du modèle proposé à représenter les caractéristiques spécifiques pour lesquelles il a été développé, il a été testé sur des problèmes homogènes. Nous avons considéré le cas d'un essai de traction uniaxiale homogène cyclique avec un couplage thermomécanique fort. Pour cela, toutes les variables impliquées dans les équations différentielles ordinaires (ODE) non linéaires ont été résolues à l'aide du logiciel Matlab®.

Hypothèse pour la simulation d'un essai de traction

Afin de simplifier la résolution des équations thermiques et mécaniques, les hypothèses suivantes ont été faites:

- forces volumiques nulles: $\mathbf{f}^v=0$,
- état de contrainte uniforme: $\mathbf{div}(\boldsymbol{\sigma})=0$,
- distribution de température homogène: grad(T)=0 d'où $k\Delta T=0$,
- puissance thermique volumique nulle: $r^v=0$,
- chargement uniaxial $\sigma_{22}= \sigma_{33}=0$ et $\varepsilon_{22}= \varepsilon_{33}$,

Le signal d'entrée est une contrainte imposée suivant la direction $\mathbf{e_1}$ où le tenseur des contraintes dans une base orthonormée donnée ($\mathbf{e}_1$, $\mathbf{e}_2$, $\mathbf{e}_3$) est:

$$[\sigma(t)] = \begin{bmatrix} \sigma_{11}(t) & 0 & 0 \\ 0 & 0 & 0 \\ 0 & 0 & 0 \end{bmatrix} \quad (277)$$

La partie déviatorique du tenseur des contraintes $\boldsymbol{\sigma}$ est donnée par:

$$[Dev\sigma(t)] = \begin{bmatrix} \frac{2}{3}\sigma_{11}(t) & 0 & 0 \\ 0 & -\frac{1}{3}\sigma_{11}(t) & 0 \\ 0 & 0 & -\frac{1}{3}\sigma_{11}(t) \end{bmatrix} \quad (278)$$

Dans la même base orthonormée ($\mathbf{e}_1$, $\mathbf{e}_2$, $\mathbf{e}_3$), le tenseur de déformation totale, le tenseur de déformation plastique et les tenseurs d'écrouissage cinématique sont définis comme:

$$[\varepsilon(t)] = \begin{bmatrix} \varepsilon_{11}(t) & 0 & 0 \\ 0 & \varepsilon_{22}(t) & 0 \\ 0 & 0 & \varepsilon_{22}(t) \end{bmatrix} \quad (279)$$

$$[\varepsilon^p(t)] = \begin{bmatrix} {\varepsilon^p}_{11}(t) & 0 & 0 \\ 0 & {\varepsilon^p}_{22}(t) & 0 \\ 0 & 0 & {\varepsilon^p}_{22}(t) \end{bmatrix} \quad (280)$$

$$[X_{(i)}(t)] = \begin{bmatrix} X_{(i)11}(t) & 0 & 0 \\ 0 & X_{(i)22}(t) & 0 \\ 0 & 0 & X_{(i)22}(t) \end{bmatrix} \quad (281)$$

Equations différentielles du problème

L'objectif est d'exprimer l'évolution du tenseur des déformations par rapport au tenseur des contraintes en fonction de l'évolution des autres variables. À partir de l'éq.(249), les composantes du tenseur des contraintes peuvent être exprimées sous la forme:

$$\begin{cases} \sigma_{11} = \lambda Tr(\boldsymbol{\varepsilon}) + 2\mu(\varepsilon_{11}) - 2\mu(\varepsilon^p_{11}) - Th_{11} \\ 0 = \lambda Tr(\boldsymbol{\varepsilon}) + 2\mu(\varepsilon_{22}) - 2\mu(\varepsilon^p_{22}) - Th_{22} \\ 0 = \lambda Tr(\boldsymbol{\varepsilon}) + 2\mu(\varepsilon_{22}) - 2\mu(\varepsilon^p_{22}) - Th_{33} \end{cases} \quad (282)$$

où la partie thermique du tenseur des contraintes est définie comme suit:

$$Th_{11} = Th_{22} = Th_{33} = (3\lambda + 2\mu)\gamma(T - T_0) \quad (283)$$

Partant de l'éq. (282), l'expression de la déformation totale suivant la direction $\mathbf{e_1}$ s'exprime par:

$$\varepsilon_{11} = \frac{1}{2\mu}\sigma_{11} - \frac{1}{2\mu}Tr(\boldsymbol{\varepsilon}) + \frac{1}{2\mu}Th_{11} + \varepsilon^p_{11} \quad (284)$$

De plus, l'expression de la trace du tenseur de déformation totale peut être déduite de l'éq. (282), soit:

$$Tr(\boldsymbol{\varepsilon}) = \frac{1}{3\lambda + 2\mu}\sigma_{11} + 3\gamma(T - T_0) \quad (285)$$

Après quelques calculs, l'expression de l'évolution de la déformation totale et de sa trace est obtenue, qui s'écrit:

$$Tr(\dot{\varepsilon}) = \frac{1}{3\lambda + 2\mu}\dot{\sigma}_{11} + 3\gamma\dot{T} \quad (286)$$

Les équations différentielles faisant intervenir l'évolution du tenseur de déformation plastique suivant $\mathbf{e}_1$, $\mathbf{e}_2$ & $\mathbf{e}_3$ sont respectivement:

$$\dot{\varepsilon^p}_{11} = \frac{3}{2J(\boldsymbol{\sigma} - d\sum_{i=1}^{2} M_i \boldsymbol{X}_i)} . \left((Dev\ \sigma)_{11} - d\sum_{i=1}^{2} M_i \left(DevX_{(i)}\right)_{11} \right) \dot{p} \quad (287)$$

$$\dot{\varepsilon^p}_{22} = \dot{\varepsilon^p}_{33} = \frac{3}{2J(\boldsymbol{\sigma} - d\sum_{i=1}^{2} M_i \boldsymbol{X}_i)} . \left((Dev\ \sigma)_{22} - d\sum_{i=1}^{2} M_i \left(DevX_{(i)}\right)_{22} \right) \dot{p} \quad (288)$$

Les équations différentielles faisant intervenir l'évolution de la variable tensorielle d'écrouissage cinématique le long des axes $\mathbf{e}_1$ et $\mathbf{e}_2$ sont respectivement:

$$\dot{X}_{(i)11} = d\dot{\varepsilon^p}_{11} - \dot{p}d\Gamma_i \left(DevX_{(i)}\right)_{11} \quad (289)$$

$$\dot{X}_{(i)22} = d\dot{\varepsilon^p}_{22} - \dot{p}d\Gamma_i \left(DevX_{(i)}\right)_{22} \quad (290)$$

L'équation différentielle faisant intervenir l'évolution de l'écrouissage isotrope est:

$$\dot{p} = \frac{1}{\eta}\left\langle \frac{\boldsymbol{J}(\boldsymbol{\sigma} - d\sum_{i=1}^{2} M_i \boldsymbol{X}_i)}{-k(1-\mathrm{d})(1-e^{-mp}) - \sigma_0} \right\rangle \qquad (291)$$

L'équation différentielle faisant intervenir l'évolution de l'endommagement est:

$$\dot{d} = \dot{p}\frac{d}{n}(1-d)\langle \sigma_{11}(t)\rangle \qquad (292)$$

L'équation différentielle impliquant l'évolution de la température est:

$$\begin{aligned}\dot{T} = &\left(\frac{T_0}{\rho_0 T C_\varepsilon}\right) r^v - \frac{(3\lambda+2\mu)\gamma Tr(\dot{\boldsymbol{\varepsilon}})T_0}{\rho C_\varepsilon} \\ &+\left(\frac{T_0}{\rho_0 T C_\varepsilon}\right)\dot{p}\begin{pmatrix} J\left(\boldsymbol{\sigma} - d\sum_{i=1}^{2} M_i \boldsymbol{X}_i\right) \\ -k(1-\mathrm{d})(1-e^{-mp}) \end{pmatrix} \\ &+\left(\frac{T_0}{\rho_0 T C_\varepsilon}\right)\dot{p}d\sum_{i=1}^{2}\Gamma_i M_i \boldsymbol{X}_\mathrm{i}:\boldsymbol{X}_\mathrm{i} \\ &+\left(\frac{T_0}{\rho_0 T C_\varepsilon}\right)\dot{p}\left(p+\frac{1}{m}e^{-mp}\right)\frac{d(1-d)}{n}\langle\sigma_{11}(t)\rangle\end{aligned} \qquad (293)$$

Toutes les équations d'évolution des variables définies par les éqs. (286) à (293) sont ensuite résolu à l'aide du solveur d'équations différentielles ordinaires non linéaires ODE23, avec des options prédéfinies, du logiciel Matlab®.

Paramètres matériaux

La plupart des propriétés matériaux de l'acier inoxydable austénitique 316L(N)-IG se trouvent facilement dans la littérature : densité (ρ), coefficients de lamé (λ et μ), coefficient de dilatation thermique moyen (γ), chaleur spécifique du matériau (C_ε), limite d'élasticité (σ_0) (Kalinin, 1996). Les paramètres matériaux suivants sont applicables à température ambiante:

- ρ_0=7930 kg/m^3,
- γ=15.3.10^{-6} K^{-1},
- C_ε=472 J/kg.K,
- λ=115 385 MPa et μ=76 923 MPa,
- σ_0=280 MPa.

Les paramètres matériau associés à l'écrouissage isotrope (k, m), l'écrouissage cinématique non linéaire (M_i, Γ_i), la viscosité (η), l'endommagement (n) ont été définis selon les résultats des essais mécaniques décrits précédemment.

Les paramètres matériau suivants sont applicables à température ambiante:

- k=220 MPa and m=30
- M_1=400 MPa and Γ_1=10^3,
- M_2=15 MPa and Γ_2=0,
- η=0.1 s^{-1},
- n=20 MPa.

Il faut noter que l'ensemble des paramètres matériaux proposés ici ne sont pas les seuls possibles. Ils ont été choisis par l'interprétation physique de l'essai mécanique présenté ci-dessus et est valable pour des conditions de chargement similaires.

Résultat des chargements monotones

La Fig. 182 représente la simulation en contrainte imposée avec une vitesse de chargement de 35MPa/min (trait bleu pointillé) et celle en déformation imposée avec une vitesse de chargement de 1 mm/min (trait rouge pointillé), conformément au test de référence (trait bleu continu) décrit au §2.

Passé le point A, voir Fig. 182, ce qui correspond au seuil de la zone dite d'endommagement, les deux courbes ne sont plus confondues. Ce phénomène peut s'expliquer par la relation entre la variable d'endommagement et la fonction isotrope décrite dans l'éq.(255), via laquelle la relation entre contraintes et déformations est conditionnée par des phénomènes antagonistes que sont l'écrouissage et l'endommagement. Dans la simulation en déplacement imposé, lorsque la zone d'endommagement est atteinte, la contrainte diminue jusqu'à zéro, alors que dans la simulation en contrainte imposée, l'algorithme diverge.

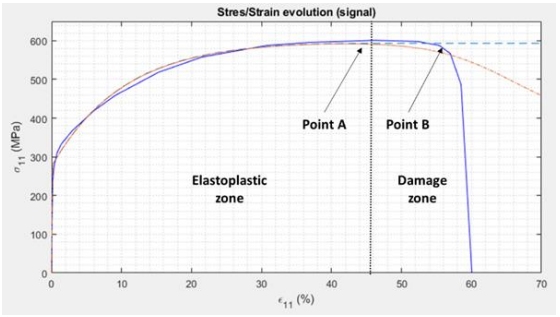

Fig. 182 – Courbe de contrainte déformation (chargement monotone)

La Fig. 183 montre l'évolution de la variable d'endommagement, définie dans l'éq. (269). En comparant cette évolution à l'évolution du tenseur des contraintes de la Fig. 182, on peut

observer que la variable d'endommagement reste proche de zéro jusqu'à 40% de déformation. Au-delà de cette valeur, la variable d'endommagement commence à augmenter, impactant l'évolution contrainte-déformation, voir point A sur les deux figures. La valeur de d=1 est atteinte à 100% de déformation, loin de la résistance ultime observée lors de l'essai expérimental, qui se produit autour de 58% de déformation, voir point B sur la Fig. 182.

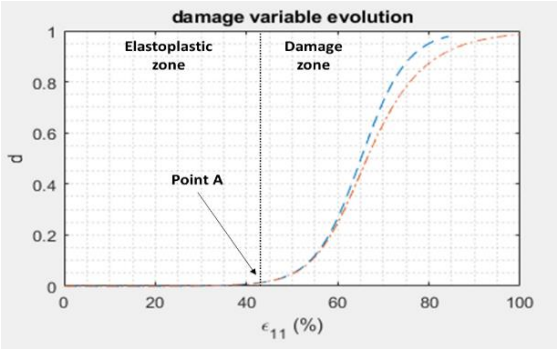

Fig. 183 – Évolution de la variable d'endommagement

Lorsque la variable d'endommagement est proche de 10^{-2}, voir le point A de la Fig. 183, signifiant que la rupture est imminente, l'évolution de la déformation totale ainsi que celle des variables internes divergent. Au-delà de ce point critique, les valeurs calculées des différentes variables sont physiquement dépourvues de sens.

Pour valider l'évolution de la température, les essais mécaniques présentés au §2 auraient dû être réalisés dans des conditions de vide, en considérant un échange thermique par rayonnement minimisé avec un contrôle de température approprié. En raison de ce manque de données expérimentales, la courbe d'évolution de la température présentée dans la Fig. 184 ne peut être superposé à aucune courbe de référence.

L'équation de la chaleur donnée en éq. (275), montre que l'évolution de la température est dépendante de l'évolution de la trace du tenseur de déformation. Dans le domaine élastique, où toutes les évolutions des variables internes sont égales à 0, une diminution de la température est observée, ce qui est en accord avec les résultats classiques en thermoélasticité, e.g. (Moreau, 2005) . Lorsque la limite d'élasticité est atteinte, l'évolution de la température dépend des mécanismes de dissipation (écrouissage et endommagement) qui l'emportent sur le mécanisme thermoélastique et, parce que la puissance volumique qui leur est associée est nécessairement positive, en gardant une augmentation de la température.

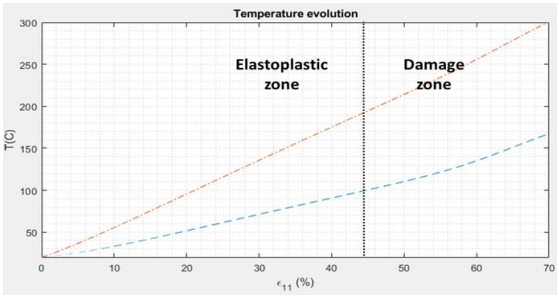

Fig. 184 – Évolution de la température

Rappelons que la différence de vitesses de déformation pour les deux simulations, qui est rapportée en Fig. 185, justifie la différence d'évolution de la température entre les deux conditions de chargement.

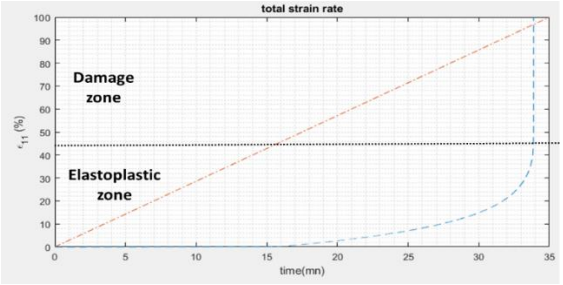

Fig. 185 – Évolution de la déformation totale

Résultats des chargements cycliques

Pour les simulations cycliques, le couplage thermomécanique a été supprimé, mais l'évolution de la température selon l'équation de la chaleur a été conservée.

La Fig. 186 montre la superposition de la courbe contrainte-déformation nominale de référence (ligne pointillée) obtenue dans le cas d'une force cyclique imposée, voir §2, Fig. 175, et la courbe d'évolution contrainte-déformation simulée en contrainte imposée (trait plein).

La courbe simulée a été obtenue suivant l'évolution sinusoïdale décrite dans l'éq.(235) où σ_{moy} représente la contrainte moyenne, $\Delta\sigma$ est l'amplitude de contrainte et f=0.3Hz la fréquence, avec σ_{max}=500MPa et σ_{min}=-200MPa.

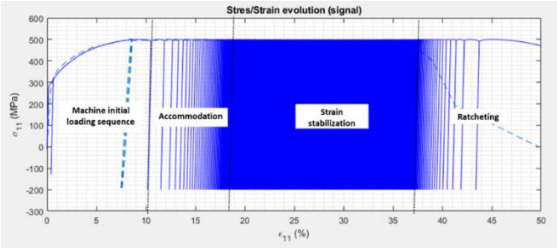

Fig. 186 – Courbe de contrainte déformation (chargement cyclique)

Comme dans l'étude expérimentale, les dix premiers cycles correspondent à la séquence initiale qui atteint progressivement la valeur de contrainte nominale, autour de 10 % de déformation. A partir de ce point jusqu'à 18% de déformation, une accommodation liée à l'écrouissage isotrope est observée. Ensuite, de 18 % jusqu'à 37 % de déformation, l'évolution de la déformation est quasi constante : dans cette zone, l'écrouissage isotrope a atteint sa valeur maximale. La dernière partie de la courbe montre le phénomène de rochet jusqu'à la divergence du modèle (d=1). Au-delà de ce point critique, les valeurs calculées des différentes variables sont physiquement dépourvues de sens.

La Fig. 187 donne le nombre de cycles cumulé par rapport à l'évolution totale de la déformation, où la courbe bleue en pointillés représente les 3574 cycles réalisés lors de l'essai de référence, et la bleu foncé celui simulé. Bien que les paramètres choisis permettent de récupérer le même nombre de cycles, la réponse simulée a un décalage de 10% en déformation.

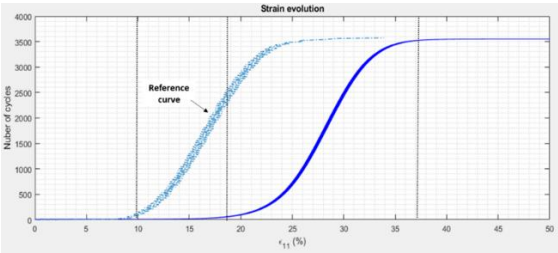

Fig. 187 – Déformation totale par rapport au nombre de cycles cumulés

Comme cela a déjà été observé pour la simulation monotone, lorsque l'évolution de l'endommagement devient rapide, le phénomène de rochet apparaît. En regardant la Fig. 187, on peut observer que le nombre total de cycles cesse de croître à 35% de la déformation totale, ce qui correspond au changement de pente pour la variable d'endommagement, voir Fig. 188. Contrairement à ce qui était attendu, l'algorithme diverge pour une valeur de « d » d'environ 0,02, loin de la valeur maximale admissible (d=1).

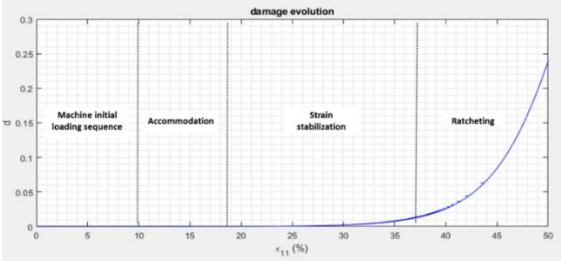

Fig. 188 – Évolution de la variable d'endommagement

La Fig. 189 montre l'évolution de la température liée au comportement mécanique via l'éq.(293). L'hypothèse adiabatique choisie pour cette simulation ne permet aucune dissipation thermique, ce qui entraîne une plage de température irréaliste.

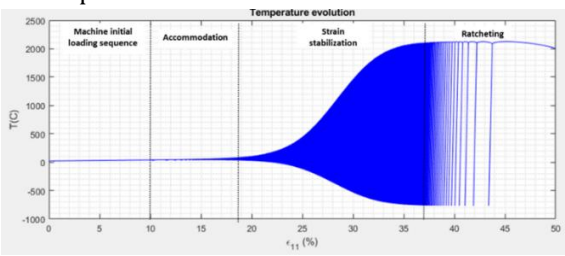

Fig. 189 – Évolution de la température

Enfin, le signal d'entrée a été modifié de ±60MPa. Les résultats sont rapportés sur les Fig. 190 et Fig. 191. Par rapport à la simulation de référence où Δσ=700MPa (courbe bleue), une diminution de l'amplitude du signal (courbe rose) augmente le nombre de cycles et réduit la déformation totale tandis qu'une augmentation de l'amplitude du signal (courbe rouge) mène au résultat inverse. A partir de ces trois simulations, on peut observer une accomodation élastique (signal à petite amplitude de contrainte), une évolution de la déformation jusqu'au phénomène de rochet (signal de référence) et une réponse de rochet pure (signal de forte amplitude de contrainte). Ainsi, le modèle démontre sa capacité à rendre compte de différents phénomènes, tels l'accommodation et le rochet, en fonction de l'intensité de la contrainte.

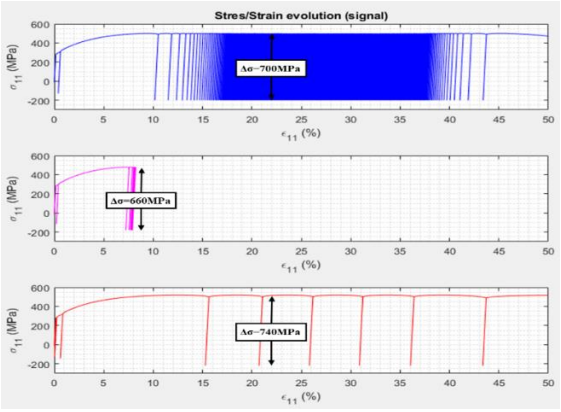

Fig. 190 – Prédictions du modèle : comparaison pour différents signaux d'entrée, courbes de contrainte déformation

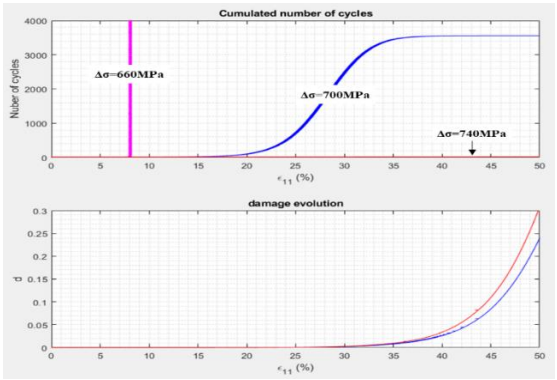

Fig. 191 – Prédictions du modèle : comparaison pour différents signaux d'entrée, nombre de cycles cumulé en fonction de la déformation(haut), évolution de la variable d'endommagement (bas)

Les résultats présentés dans ce paragraphe montrent que le modèle proposé est capable de reproduire tous les phénomènes mécaniques observés expérimentalement, voir §2. Les cas plus complexes (problèmes de structure) nécessitent l'implémentation du modèle de comportement dans un logiciel éléments finis.

Implémentation numérique

Dans ce qui suit, nous adoptons une formulation thermomécanique entièrement couplée du problème. L'implémentation du modèle a été réalisée dans Abaqus® à l'aide des sous-programmes UMAT et UMATHT.

Implémentation dans Abaqus® d'un couplage thermomécanique fort

Pour une meilleure compréhension, nous rappelons ici la formulation qui est mise en œuvre dans Abaqus® pour le cas des couplages thermomécaniques forts et transitoires. On considère un domaine, Ω, qui est sans contrainte dans la configuration initiale et à la température initiale, T_0. Les conditions aux limites mécaniques s'appliquent sur $\partial\Omega_u$ pour les déplacements et sur $\partial\Omega_\sigma$ pour les forces. Les conditions aux limites thermiques s'appliquent sur $\partial\Omega_T$ pour la température et $\partial\Omega_q$ pour le flux thermique. La formulation du problème thermomécanique, en petite déformations, est:

Trouver $(\boldsymbol{u}, T)$ tel que $\forall(\boldsymbol{\delta u}, \boldsymbol{\delta} T)$:

$$\begin{cases} \int_\Omega \boldsymbol{\sigma}:\left(\boldsymbol{grad}\,(\delta \boldsymbol{u})\right)_{sym} d\Omega - \int_{\partial\Omega\sigma} (\boldsymbol{\sigma}.\boldsymbol{n}).\delta\boldsymbol{u} ds \\ \qquad - \int_\Omega \boldsymbol{f}^v.\delta\boldsymbol{u}\, d\Omega = 0 \\ \int_\Omega \left(\frac{\rho_0 C_\varepsilon}{T_0} T\dot{T}\delta T - T\left(\frac{\partial \boldsymbol{\sigma}}{\partial T}:\dot{\boldsymbol{\varepsilon}}\right)\delta T - \emptyset_{int}\delta T - r^v \delta T \right. \\ \left. \quad -\boldsymbol{q}.\boldsymbol{grad}\,\delta T\right) d\Omega + \int_{\partial\Omega q} (\boldsymbol{q}^s.\boldsymbol{n})\delta T ds = 0 \end{cases} \tag{294}$$

où $\boldsymbol{q}^s$ est le flux prescrit à la surface $\partial\Omega$q.

Abaqus® utilise un schéma de différence en amont qui consiste en les approximations suivantes: $\dot{T} = (T(t_{n+1}) - T(t_n))/\Delta t$ et $\dot{\boldsymbol{u}} = (\boldsymbol{u}(t_{n+1}) - \boldsymbol{u}(t_n))/\Delta t$. Par souci de simplicité, nous notons toutes les quantités au temps t_{n+1} sans indexation et on note T_n la température au temps t_n (même notation pour **u**). Par conséquent, la discrétisation temporelle du système (294) est:

Sur l'intervalle de temps $[t_n, t_{n+1}]$, chercher $(\boldsymbol{u}, T)$ connaissant $(\boldsymbol{u}_n, T_n)$ tel que $\forall(\boldsymbol{\delta u}, \boldsymbol{\delta} T)$:

$$\begin{cases} \int_\Omega \boldsymbol{\sigma}:\left(\boldsymbol{grad}(\delta \boldsymbol{u})\right)_{sym} d\Omega - \int_{\partial\Omega\sigma} (\boldsymbol{\sigma}.\boldsymbol{n}).\delta\boldsymbol{u} ds \\ \qquad - \int_\Omega \boldsymbol{f}^v.\delta\boldsymbol{u}\, d\Omega = 0 \\ \int_\Omega \begin{pmatrix} \frac{\rho_0 C_\varepsilon}{T_0} T \frac{(T - T_n)}{\Delta t}\delta T \\ -T\left(\frac{\partial \boldsymbol{\sigma}}{\partial T}:\frac{(\boldsymbol{\varepsilon} - \boldsymbol{\varepsilon}_n)}{\Delta t}\right)\delta T \\ -r^v\delta T - \emptyset_{int}\delta T - \boldsymbol{q}.\boldsymbol{grad}\,\delta T \end{pmatrix} d\Omega \\ \qquad + \int_{\partial\Omega q} (\boldsymbol{q}^s.\boldsymbol{n})\delta T ds = 0 \end{cases} \tag{295}$$

Dans le sous-programme UMAT, nous devons implémenter le calcul de $\boldsymbol{\sigma}, \emptyset_{int}$ et $\boldsymbol{\partial\Delta\sigma}/\partial\Delta T$(dans Abaqus® une formulation incrémentale du système d'éq.(295) est utilisée). De plus, nous devons également définir la matrice jacobienne, $\boldsymbol{\partial\Delta\sigma}/\partial\Delta\boldsymbol{\varepsilon}$, et la variation de la dissipation par rapport à la température $\boldsymbol{\partial\emptyset}_{int}/\partial T$ qui vient de la linéarisation de la forme

incrémentale du système d'éq.(295). Dans le sous-programme UMATHT, nous devons implémenter la partie thermique de l'énergie interne, notée U dans la documentation Abaqus®, et sa dérivée en fonction de la température. En identifiant l'énergie thermique interne du système d'éq.(295), on peut trouver: $U = C_\varepsilon(T/T_0)T$ et $\boldsymbol{\partial} U/\partial T = 2C_\varepsilon(T/T_0)$. L'expansion thermique est définie indépendamment des sous-programmes UMAT et UMATHT. Dans ce cas la déformation passée en argument dans UMAT n'est que la déformation mécanique (la contribution à l'expansion thermique est préalablement supprimée).

Intégration locale des équations d'évolution des variables internes

La formulation éléments finis précédente nécessite d'évaluer les contraintes mécaniques au temps t_{n+1} au niveau des points de Gauss sur chaque élément. Par conséquent, nous devons intégrer l'évolution des variables internes au cours de l'intervalle de temps connaissant leurs valeurs à l'instant précédent et ayant une prédiction de la valeur de déformation actuelle $\boldsymbol{\varepsilon}_{n+1}$ et la température actuelle T_{n+1} localement à chaque point de Gauss. Dans ce travail, nous adoptons l'approche de retour radial proposé par Simo (Hughes, et al., 2000) et utilisé plus tard par plusieurs auteurs (voir (Adam, et al., 2005) et (Benaarbia, et al., 2018)). L'organigramme de cette approche est illustré par la Fig. 192.

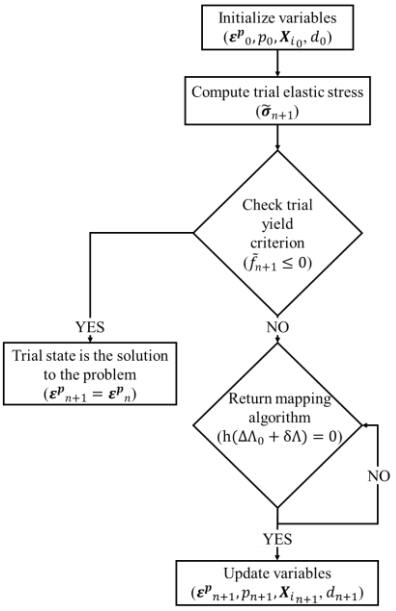

Fig. 192 – Organigramme de l'algorithme de retour radial (Hughes, et al., 2000)

L'algorithme de retour radial est basé sur la définition d'un état « prédicteur élastique », aussi appelé état « trial », pour lequel l'écoulement plastique est gelé.

On suppose donc que l'état trial au temps t_{n+1}, est égal à la dernière valeur convergée, de sorte que :

$$\begin{aligned}\tilde{\boldsymbol{\varepsilon}}^{\boldsymbol{p}}{}_{n+1} = \boldsymbol{\varepsilon^p}_n\,, \tilde{p}_{n+1} = p_n,\\ \tilde{d}_{n+1} = d_n, \tilde{\boldsymbol{X}}_{(i)n+1}\\ = \boldsymbol{X}_{(i)n}\ \forall i\end{aligned} \tag{296}$$

On peut donc définir un tenseur de contraintes trial $\tilde{\boldsymbol{\sigma}}_{\boldsymbol{n+1}}$, éq.(297) et une fonction seuil trial $\tilde{f}_{n+1}$, éq.(298) tels que:

$$\begin{aligned}\tilde{\boldsymbol{\sigma}}_{n+1} = \lambda Tr(\boldsymbol{\varepsilon}_{n+1} - \boldsymbol{\varepsilon^p}_n)\boldsymbol{G}\\ + 2\mu(\boldsymbol{\varepsilon}_{n+1} - \boldsymbol{\varepsilon^p}_n)\\ - (3\lambda + 2\mu)\gamma(T_{n+1}\\ - T_0)\boldsymbol{G}\end{aligned} \tag{297}$$

$$\begin{aligned}\tilde{f}_{n+1} = \sqrt{\frac{3}{2}}\left\|\boldsymbol{Dev}\left(\tilde{\boldsymbol{\sigma}}_{\boldsymbol{n+1}}\right.\right.\\ \left.\left. - d_{\boldsymbol{n}}\sum_{i=1}^{N_{kh}} M_i \boldsymbol{X}_{(i)n}\right)\right\|\\ - \sigma_0 - A^p{}_n\end{aligned} \tag{298}$$

Si le critère trial d'élasticité est satisfait ($\tilde{f}_{n+1} \leq 0$), cela signifie que l'état trial est admissible, induisant une déformation élastique. Dans ce cas, l'expression de $\boldsymbol{\sigma}_{n+1}$ peut être calculée explicitement et l'on a:

$$\boldsymbol{\varepsilon^p}_{n+1} = \boldsymbol{\varepsilon^p}_n \tag{299}$$
$$p_{n+1} = p_n \tag{300}$$
$$\boldsymbol{X}_{(i)n+1} = \boldsymbol{X}_{(i)n}\ \ \forall \boldsymbol{i} \tag{301}$$
$$d_{\boldsymbol{n+1}} = d_{\boldsymbol{n}} \tag{302}$$

Si le critère trial d'élasticité n'est pas satisfait ($\tilde{f}_{n+1} > 0$), nous devons intégrer l'évolution des variables internes sur l'intervalle de temps. Nous supposons d'abord une expression d'Euler de l'écoulement plastique dans l'éq. (266):

$$\boldsymbol{\varepsilon^p}_{n+1} - \boldsymbol{\varepsilon^p}_n = \sqrt{\frac{3}{2}}\mathbf{n}_{n+1}\Delta\Lambda \tag{303}$$

où la direction d'écoulement, $\mathbf{n}_{n+1}$, est définie par:

$$\mathbf{n}_{n+1} = \frac{\mathbf{S}_{n+1}}{\|\mathbf{S}_{n+1}\|} \tag{304}$$

avec $\mathbf{S}_{n+1}$, défini par:

$$\mathbf{S}_{n+1} = \boldsymbol{Dev}\left(\boldsymbol{\sigma}_{n+1} - d_{\boldsymbol{n+1}}\sum_{i=1}^{N_{kh}} M_i \boldsymbol{X}_{(i)n+1}\right) \quad (305)$$

et

$$\Delta\Lambda = \Lambda_{n+1}(t_{n+1} - t_n) = \Delta t \frac{1}{\eta\sigma_0}\langle f_{n+1}\rangle \quad (306)$$

Suivant la même méthode, l'expression de l'évolution des autres variables $\dot{\boldsymbol{X}}$, $\dot{p}$ et $\dot{d}$, voir éq.(267), éq.(268) et éq.(269), donne:

$$\boldsymbol{X}_{(i)n+1} - \boldsymbol{X}_{(i)n} = \Delta\Lambda\left(d_{\boldsymbol{n+1}}\sqrt{\frac{3}{2}}\mathbf{n}_{n+1} - d_{n+1}\Gamma_i \boldsymbol{X}_{(i)n+1}\right) \quad (307)$$

$$p_{n+1} - p_n = \Delta\Lambda \quad (308)$$

$$d_{n+1} - d_n = \Delta\Lambda\frac{d_{n+1}(1-d_{n+1})}{n}\langle Tr(\boldsymbol{\sigma}_{n+1})\rangle \quad (309)$$

Partant de l'éq. (297) et en introduisant l'éq. (303), on peut obtenir:

$$\boldsymbol{Dev}(\boldsymbol{\sigma}_{n+1}) = \boldsymbol{Dev}(\tilde{\boldsymbol{\sigma}}_{\boldsymbol{n+1}}) - 2\mu\boldsymbol{Dev}(\boldsymbol{\varepsilon^p}_{n+1} - \boldsymbol{\varepsilon^p}_n) \quad (310)$$

en réécrivant l'éq. (307), sous la forme:

$$\boldsymbol{X}_{(i)n+1} = \left(d_{n+1}\sqrt{\frac{3}{2}}\mathbf{n}_{n+1}\Delta\Lambda + \boldsymbol{X}_{(i)n}\right)\delta_{(i)n+1} \quad (311)$$

avec:

$$\delta_{(i)n+1} = \frac{1}{(1 + d_{n+1}\Gamma_i\Delta\Lambda)} \quad (312)$$

Utilisant les éqs.(305), (310) et (311), on obtient:

$$\boldsymbol{Dev}\left(\boldsymbol{\sigma}_{n+1} - d_{n+1}\sum_{i=1}^{N_{kh}} M_i \boldsymbol{X}_{(i)n+1}\right)\left(1 + \frac{\xi_{(i)n+1}}{\left\|\boldsymbol{Dev}\left(\boldsymbol{\sigma}_{n+1} - d_{n+1}\sum_{i=1}^{N_{kh}} M_i \boldsymbol{X}_{(i)n+1}\right)\right\|}\right) = \boldsymbol{Dev}\left(\tilde{\boldsymbol{\sigma}}_{\boldsymbol{n+1}} - d_{n+1}\sum_{i=1}^{N_{kh}} M_i \delta_{(i)n+1}\boldsymbol{X}_{(i)n}\right) \quad (313)$$

où :

$$\xi_{(i)n+1} = \left(2\mu + d_{n+1}\sum_{i=1}^{N_{kh}} M_i\delta_{(i)n+1}\right)\sqrt{\frac{3}{2}}\Delta\Lambda \quad (314)$$

En prenant la norme du terme donné par l'éq. (313) et en utilisant le fait que $\xi_{(i)n+1}$ est strictement positif, on peut obtenir la relation suivante:

$$\left\|\boldsymbol{Dev}\left(\boldsymbol{\sigma}_{n+1} - d_{n+1}\sum_{i=1}^{N_{kh}} M_i \boldsymbol{X}_{(i)n+1}\right)\right\| = \left\|\boldsymbol{Dev}\left(\tilde{\boldsymbol{\sigma}}_{\boldsymbol{n+1}} - d_{n+1}\sum_{i=1}^{N_{kh}} M_i \delta_{(i)n+1}\boldsymbol{X}_{(i)n}\right)\right\| - \xi_{(i)n+1} \quad (315)$$

Partant des éqs. (313) et (315) on peut alors en déduire:

$$\mathbf{n}_{n+1} = \frac{\boldsymbol{Dev}\left(\tilde{\boldsymbol{\sigma}}_{\boldsymbol{n+1}} - d_{n+1}\sum_{i=1}^{N_{kh}} M_i\delta_{(i)n+1}\boldsymbol{X}_{(i)n}\right)}{\left\|\boldsymbol{Dev}\left(\tilde{\boldsymbol{\sigma}}_{\boldsymbol{n+1}} - d_{n+1}\sum_{i=1}^{N_{kh}} M_i\delta_{(i)n+1}\boldsymbol{X}_{(i)n}\right)\right\|} \quad (316)$$

Pour calculer la direction de l'écoulement plastique, $\mathbf{n}_{n+1}$, nous devons déterminer l'incrément du multiplicateur plastique et la valeur actuelle de l'endommagement. Partant de l'éq. (271) et de l'éq. (309) on obtient le système d'équations non linéaire suivant :

$$\begin{cases} \sqrt{\frac{3}{2}}\left(\left\|\boldsymbol{Dev}\left(\tilde{\boldsymbol{\sigma}}_{\boldsymbol{n+1}} - d_{n+1}\sum_{i=1}^{N_{kh}} M_i\delta_{(i)n+1}\boldsymbol{X}_{(i)n}\right)\right\| - \xi_{(i)n+1}\right) & (317) \\ -A^p{}_{n+1} - \sigma_0 - \eta\left(\frac{\Delta\Lambda}{\Delta t}\sigma_0\right)^{\frac{1}{\alpha}} = 0 & (318) \\ \mathrm{d}_{n+1} - \mathrm{d}_n - \Delta\Lambda\frac{\mathrm{d}_{n+1}(1-\mathrm{d}_{n+1})}{n}\langle Tr(\tilde{\boldsymbol{\sigma}}_{\boldsymbol{n+1}})\rangle = 0 & \end{cases}$$

avec :

$$Tr(\boldsymbol{\sigma}_{\boldsymbol{n+1}}) = (3\lambda + 2\mu)Tr(\varepsilon_{n+1}) + 3(3\lambda + 2\mu)\gamma(T_{n+1} - T_0) \quad (319)$$

$$A^p{}_{n+1} = k(\mathrm{d}_{n+1} - 1)\left(1 - e^{-m(\Delta\Lambda + p_n)}\right) \quad (320)$$

Le système d'éq.(317)-(318) dépend seulement de $\Delta\Lambda, d_{n+1}$ sachant que $\varepsilon_{n+1}, T_{n+1}$ sont données à partir du schéma global de Newton-Raphson (valeurs prédictives) et que toute autre quantité est connue à partir du dernier incrément convergé. Le système non linéaire précédent peut être linéarisé et résolu avec un schéma de Newton local (au niveau du point de Gauss). Cet algorithme et le schéma de Newton local sont implémentés dans le sous-programme UMAT.

Dès que $\Delta\Lambda$ et d_{n+1} sont connus, nous pouvons évaluer la direction d'écoulement plastique, $\mathbf{n}_{n+1}$ à partir de l'éq. (316) et de l'évolution du tenseur cinématique $\boldsymbol{X}_{(i)n+1}$ et du tenseur de déformation plastique à partir des éqs. (307) and (303).

Application sur un rail d'interface du VV

Le VV est en interface avec certains systèmes de la machine par une connexion boulonnée sur un « rail » soudé à la barrière de pression. La Fig.

193 montre la géométrie du rail en interface avec la tuyauterie du système de refroidissement des composants face au plasma. La justification structurelle de ces rails consiste à évaluer la contrainte et/ou la déformation maximale dans la section de soudure pour la combinaison de chargement la plus critique (Martinez, 2016). Cette valeur de contrainte et/ou de déformation est comparée aux critères de conception définis dans le code RCC-MR.

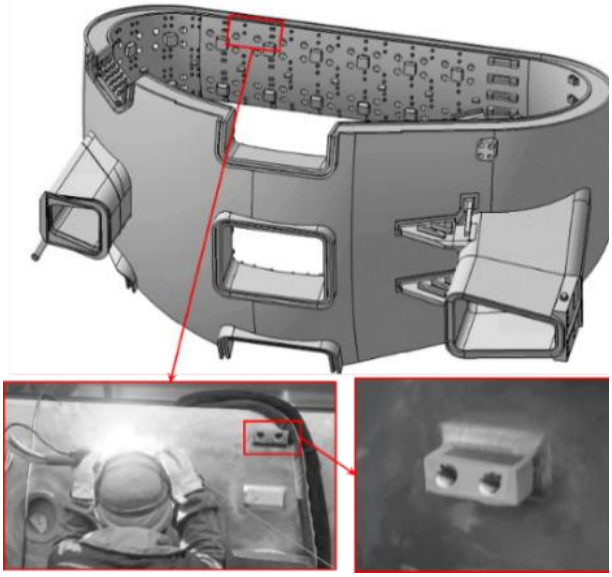

Fig. 193 – Exemple de rail soudé au VV d'ITER (ITERwebsite).

Hypothèses thermomécaniques de la simulation

En raison du nombre important de rails dans la VV et de tous les différents types de charges mécaniques qui pourraient agir sur celui-ci, la méthode proposée ici consiste à redéfinir le tenseur d'efforts appliqué au centre d'inertie de la section de soudure A (en m^2) en deux forces : une force normale $F_n(t)$ (en N) et une force tangente $F_t(t)$ (en N), voir les éqs.(321)-(322)-(323).

$$F_n = F_z + \frac{e \cdot A}{2 \cdot I_y} \cdot M_y + \frac{h \cdot A}{2 \cdot I_x} \cdot M_x \qquad (321)$$

$$F_t = \sqrt{\left(F_x^2 + F_y^2\right)} + F_{torque} \qquad (322)$$

$$F_{torque} = \frac{3 \cdot M_z}{8 \cdot w \cdot e^2} \cdot A \cdot \left(1 + 0.6095 \cdot \frac{w}{e} + 0.8865 \cdot \left(\frac{w}{e}\right)^2 - 1.8023 \cdot \left(\frac{w}{e}\right)^3 + 0.9100 \cdot \left(\frac{w}{e}\right)^4\right) \qquad (323)$$

où Fx, Fy, Fz sont les forces, et Mx, My, Mz sont les moments (en N.m) définis dans la base orthonormée (**x**, **y**, **z**), et e correspond à l'épaisseur du rail (en m), w la longueur du rail (en m), I_x et I_y sont les moment quadratiques (en m^4). La force induite par la torsion dans une section rectangulaire, F_{torque} (N), a été adaptée de (Budynas, et al., 2002).

D'un point de vue thermique, le dépôt de puissance sur le rail est une combinaison de chauffage nucléaire, de conduction et de rayonnement avec les composants environnants. Pour simplifier cette combinaison de dépôts de puissance thermique, il est proposé de la modéliser comme un gradient de température imposé dans le rail, où la température du VV est fixée à 393K et la température maximale, noté g(t), est appliquée sur le dessus du rail, voir Fig. 194.

La géométrie a également été simplifiée en négligeant le rayon de courbure du VV et en supprimant le congé de soudure à la jonction du rail. Nous avons donc 2 blocs rectangulaires avec une interface parfaite. Les conditions de symétrie sont appliquées sur le plus grand bloc rectangulaire (bleu foncé sur la Fig. 194) et le déplacement vertical est interdit sur les bords supérieurs (bleu clair sur la Fig. 194).

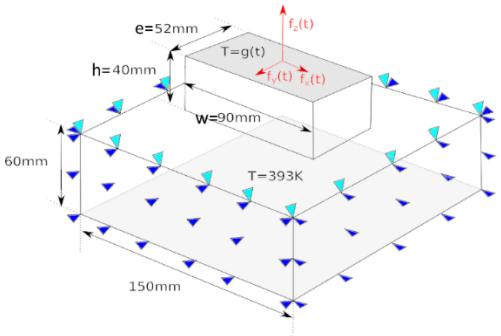

Fig. 194 – Interface soudée entre VV et rail

Enfin, les mêmes paramètres matériau que ceux proposés dans §4.3 ont été utilisés

Résultats pour un chargement monotone

Dans la première simulation numérique, une charge thermique en rampe (voir Fig. 195) est combinée avec une charge mécanique linéaire par morceaux (voir Fig. 196). Les valeurs proposées ici ne sont pas réalistes. Elles visent à atteindre la zone d'endommagement pour tester le modèle proposé.

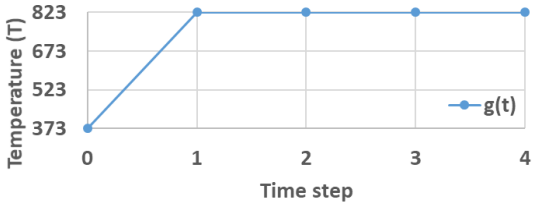

Fig. 195 – Température appliquée pour la simulation monotone

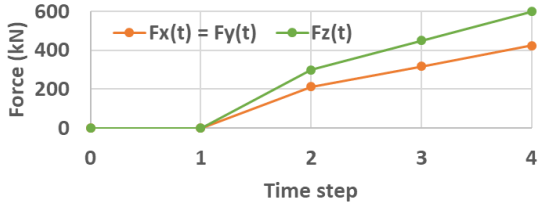

Fig. 196 – Forces appliquées pour la simulation monotone

La Fig. 197 montre la distribution de déformation principale maximale à la fin du pas de temps-03. On constate que le rail fléchit sous la combinaison des chargements, qui localise la déformation dans les deux coins opposés ; l'un est soumis à la compression et le second à la traction.

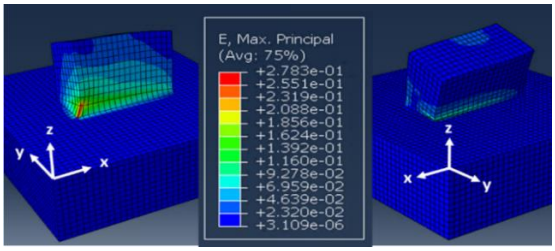

Fig. 197 – Carte de déformation principale maximale à la fin du pas de temps-03 (simulation monotone)

La Fig. 198 montre la répartition des dommages à la fin du pas de temps-03. Bien que la déformation soit localisée dans les deux coins, l'endommagement ne se produit que dans la zone de tension. Cette réponse du matériau correspond à l'évolution de l'endommagement définie dans l'éq.(269), qui suppose que la propagation des microfissures et la croissance des cavités dépendent uniquement du chargement en traction.

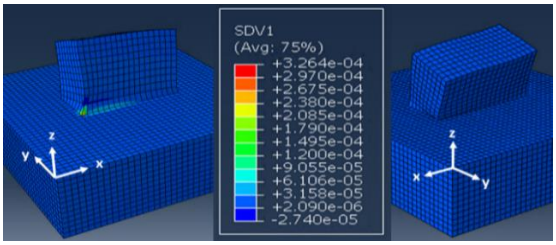

Fig. 198 Carte d'endommagement à la fin du pas de temps-03 (simulation monotone)

La Fig. 199 montre l'évolution de l'endommagement en un point de Gauss de l'élément de coin où la déformation est maximale. De manière similaire à ce qui a été observé pour la simulation "0D", voir §4.4, la variable d'endommagement commence à augmenter de façon exponentielle entre le pas de temps-02 et le pas de temps-03, ce qui correspond à une valeur de déformation totale comprise entre 10% et 20% (voir l'évolution de la déformation totale dans le même point de Gauss à la Fig. 200). On peut remarquer que l'évolution rapide de la variable d'endommagement conduit à la divergence de l'algorithme avant d'atteindre le pas de temps-04.

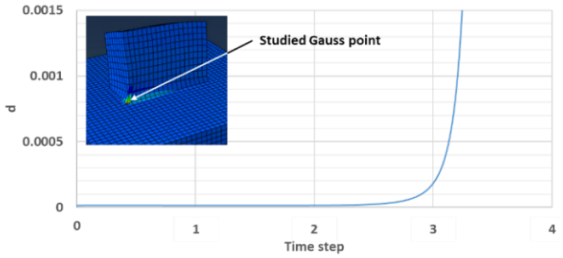

Fig. 199 – Évolution de la variable d'endommagement dans le cas du chargement monotone

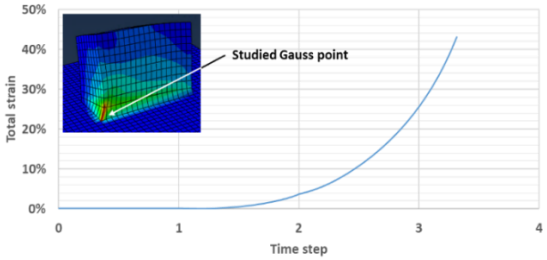

Fig. 200 – Évolution de déformation totale dans le cas du chargement monotone

Résultats pour un chargement cyclique

Pour la seconde simulation, nous proposons de partir de la fin du pas de temps-03 de la simulation monotone, où la variable d'endommagement commence à croître. A partir de cette étape, la charge mécanique est

maintenue à une valeur constante et la charge thermique est cyclée 20 fois, voir les Fig. 195 et Fig. 196.

Pour ce scénario où la charge primaire est fixe et la charge secondaire est cyclée, l'objectif est de vérifier si la réponse du matériau conduira à une accommodation plastique ou à un phénomène de rochet.

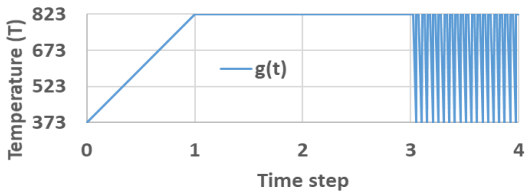

Fig. 201 – Température appliquée pour la simulation cyclique

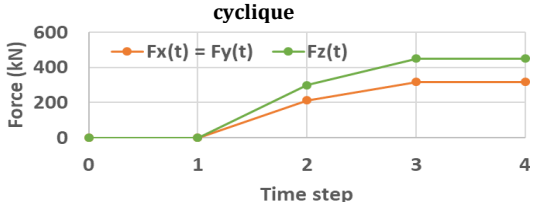

Fig. 202 – Forces appliquées pour la simulation cyclique

La Fig. 203 montre la distribution de contrainte principale maximale à la fin du pas de temps-04. Un comportement similaire à celui du cas de chargement monotone est observé, où la déformation se localise principalement dans les deux coins opposés.

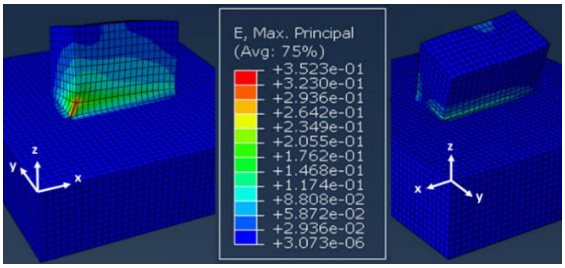

Fig. 203 – Carte de déformation principale maximale à la fin du pas de temps-04 (simulation cyclique)

La Fig. 204 montre la carte d'endommagement à la fin du pas de temps-04. De la même façon que pour le cas du chargement monotone, l'endommagement se produit dans le même coin. De plus, même si la variable d'endommagement augmente sur le coin chargé en chargement thermique cyclique, elle reste proche de zéro dans le coin opposé.

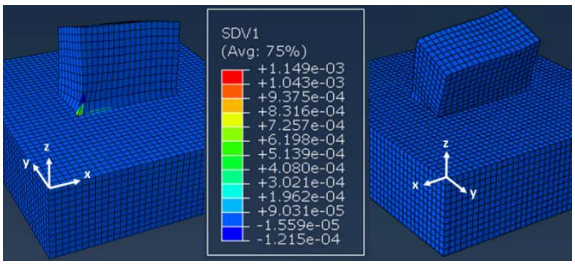

Fig. 204 – Carte d'endommagement à la fin du pas de temps-04 (simulation cyclique)

La Fig. 205 montre l'évolution de l'endommagement en un point de Gauss de l'élément du coin où la déformation est maximale. A la fin du pas de temps-03, lorsque la charge primaire est fixée et que la charge secondaire cyclique démarre, on peut observer un changement dans l'évolution de la variable d'endommagement. En effet, la tendance exponentielle est passée à une tendance logarithmique, ce qui correspond à une accommodation du matériau. Il est à noter que cette évolution est fortement localisée. Nous n'avons toutefois pas étudié l'influence de la taille du maillage sur celle-ci.

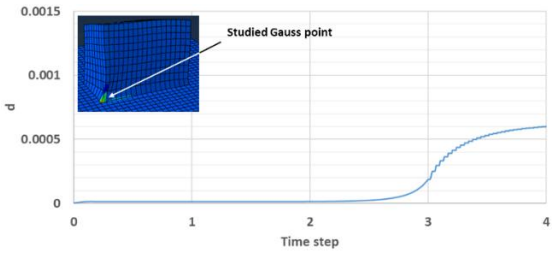

Fig. 205 – Évolution de la variable d'endommagement dans le cas du chargement cyclique

Finalement, la Fig. 206, qui montre l'évolution de la déformation totale en un point de Gauss de l'élément, confirme qu'une accommodation se produit sous des chargement cycliques thermiques.

Cette observation nous permet de conclure que le mode de défaillance pourrait être dû à la fatigue à grand nombre de cycles plutôt qu'à un phénomène de rochet.

Cependant, le modèle actuel est limité à la justification de l'adaptation et/ou accommodation. Une analyse plus poussée suivant la méthodologie du code RCC-MR, plus adaptée à la justification de la fatigue, serait nécessaire pour confirmer le comportement observé.

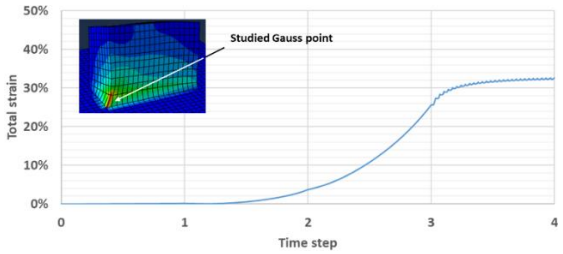

Fig. 206 – Évolution de déformation totale dans le cas du chargement cyclique

Conclusions

Le présent article a tout d'abord montré les principales caractéristiques du comportement de l'acier inoxydable austénitique 316L(N)-IG utilisé pour la première barrière de confinement du réacteur thermonucléaire à fusion ITER. L'un des phénomènes les plus complexes dans des conditions de chargement cyclique reste le rochet, qui se produit lors de la fatigue oligocyclique.

Basée sur une approche phénoménologique, l'étude a ensuite consisté à enrichir un modèle élasto-viscoplastique incluant à la fois des variables d'écrouissage isotrope et cinématique ainsi qu'un couplage thermomécanique fort et une variable d'endommagement.

Les résultats d'essais de traction/compression cycliques menés en contrainte imposée montrent que le matériau subit une adaptation élastique à faible amplitude de contrainte et un accommodation plastique jusqu'à un phénomène de rochet à amplitude de contrainte plus élevée. C'est pourquoi dans le modèle proposé, nous avons intégré une variable d'endommagement aux fonctions décrivant l'écrouissage isotrope et l'écrouissage cinématique. L'objectif était de faire fonctionner les deux modes d'écrouissage en opposition, c'est-à-dire qu'à l'état d'endommagement faible l'écrouissage isotrope est dominant alors qu'à l'état d'endommagement plus élevé, l'écrouissage cinématique devient dominant. Le phénomène de rochet se produit dans la phase finale, uniquement si l'évolution de la variable d'endommagement progresse de manière significative jusqu'à une valeur seuil préalablement définie.

Les différents phénomènes mis en évidence ci-dessus ont d'abord été simulés numériquement par une « analyse 0D » à l'aide du logiciel Matlab®. Cette approche simpliste a aussi permis de choisir des paramètres appropriés.

Enfin, ce modèle a été implémenté dans Abaqus® spécialement conçu pour faciliter les développements de formulations multi-domaines et multi-physiques. Une géométrie d'éléments finis représentative de la structure de l'enceinte à vide ITER a été testée dans différentes conditions de chargement démontrant le bon comportement du modèle sous un couplage thermomécanique fort dans un environnement 3D.

Il est important de noter que cet article n'est que l'amorce d'un travail qu'il convient de consolider avec davantage de données expérimentales, puisque la campagne d'essais utilisée pour identifier les paramètres du matériau n'a été réalisée qu'à 20°C et pour un chargement uniaxial. Il peut être complété par la réalisation de tests de chargement combinés (comme la torsion/compression) pour différents environnements de température. Pour valider l'évolution de la température, certains tests devront aussi être effectués dans des conditions de vide, en considérant un échange thermique par rayonnement minimisé.

Perspectives

Les composants face au plasma et la chambre à vide d'ITER seront exposés à des flux de neutrons hautement énergétiques de l'ordre de 14 MeV, générés lors de la réaction de fusion Deutérium-Tritium. Ces interactions entre les neutrons et les structures produiront divers types de réactions secondaires, à partir desquelles des rayons gamma et/ou des particules chargées seront créés. Les neutrons et photons, qui sont par définition électriquement neutres, traversent le confinement magnétique et pénètrent profondément dans les pièces de structure, convertissant leur énergie cinétique en énergie thermique (Maki, 1999).

Le logiciel d'analyse utilisé dans ITER pour l'évaluation de l'échauffement volumique prend en compte deux contributeurs que sont les sources de chauffage neutronique et photonique. La Fig. 207 montre un exemple de ce que pourrait être une répartition du chauffage nucléaire sur l'enceinte à vide d'ITER.

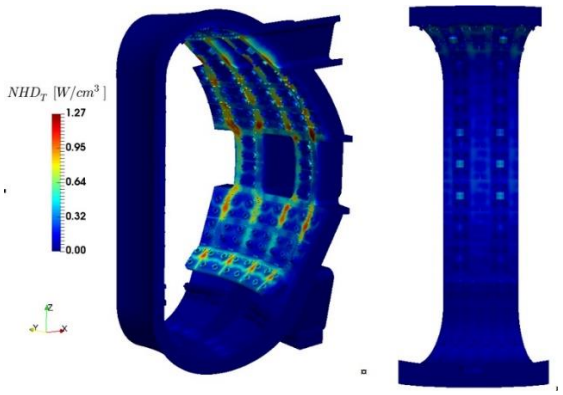

Fig. 207 – Répartition du chauffage nucléaire sur le VV d'ITER (Fabbri, 2018).

En plus de l'échange de puissance thermique, l'énergie cinétique des neutrons est si élevée qu'elle permet aux atomes de se déplacer de leur site. Il en résulte des déplacements locaux en chaine, limités dans le temps et dans l'espace, qui modifient la structure cristalline du matériau. La Fig. 208 montre une représentation schématique d'une cascade de déplacements induite après un premier atome frappé (PKA en anglais: Primary Knocked-on Atom). Ce phénomène est quantifié en déplacement par atomes (dpa). Cela signifie que pour un matériau recevant une dose de 100 dpa, chaque atome a été déplacé en moyenne 100 fois (Boutard, 2014).

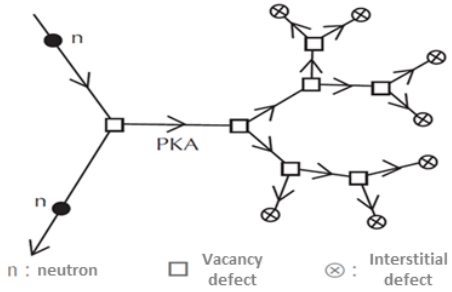

Fig. 208 – Représentation schématique d'une cascade de déplacement (Boutard, 2014)

Lors de la collision initiale entre le neutron et l'atome (PKA), des réactions de transmutation nucléaire se produisent. Dans les réacteurs de fusion nucléaire, ces réactions génèrent des atomes d'hélium et d'hydrogène. Cette génération d'atomes se fait à l'intérieur de la structure métallique avec un taux de ~12 appmHe/dpa (12 10^{-6} atomes d'hélium par atomes déplacés), et ~45 appmH/dpa pour l'hydrogène.

Pour les composants de première paroi d'ITER, qui fonctionnent à des conditions de température fixées à un maximum de 450 °C (en dessous du fluage thermique pour l'acier), le flux neutronique attendue est d'environ 0,3 MWa/m^2 correspondant à un pic de dommage dans l'acier d'environ 2 dpa avec une génération d'hélium maximale de 55appm (Kalinin, 2001).

L'irradiation affecte les propriétés physiques à travers des générations de dpa et de transmutation nucléaire qui peuvent être divisées en deux cas. Le premier couvre divers coefficients mécaniques comme la limite d'élasticité, la résistivité électrique et la perméabilité magnétique, et le second couvre la densité et le module d'Young.

Pour l'acier inoxydable austénitique, cet endommagement se traduit par une augmentation de la limite d'élasticité et une réduction de la zone d'écoulement plastique. La Fig. 210 montre les courbes calculées pour la limite d'élasticité minimale de l'acier inoxydable 316L (N)-IG en fonction de l'endommagement des neutrons (dpa) dans une plage de température de 100 à 300 °C ainsi que de l'allongement uniforme minimal pour différentes doses (Barabash, 2007).

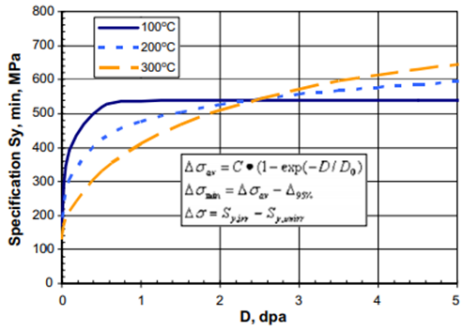

Fig. 209 – Effet de l'irradiation neutronique sur la limite d'élasticité (σ0) de l'acier inoxydable 316L(N)-IG (Barabash, 2007).

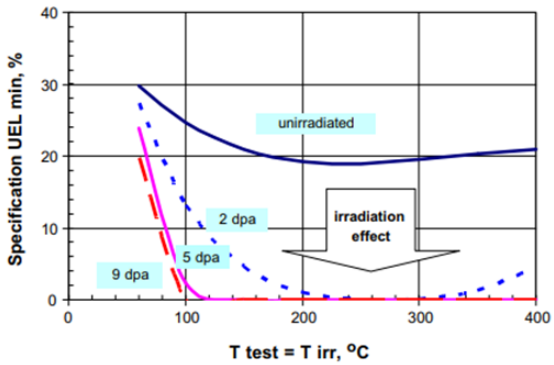

Fig. 210 – Effet de l'irradiation neutronique sur la ductilité du materiau (UE) de l'acier inoxydable (Barabash, 2007).

Le gonflement correspond à une augmentation de volume due à l'accumulation de cavités et de lacunes induites par les dommages neutroniques. La Fig. 211 montre l'évolution du volume entre le coupon initial d'acier CW 316 et le même coupon après irradiation jusqu'à 15 dpa à 533ºC (Klueh, 2008). Il est important de noter que ce phénomène est amplifié à certaines plages de température, généralement proches de la température de fluage thermique, voir Fig. 212. Ce phénomène de gonflement peut avoir un effet sur le module d'Young lorsque de grandes quantités d'hélium sont formées en raison de la réduction de section efficace du matériau.

Fig. 211 – Gonflement (effet du regroupement des lacunes) de l'acier CW 316 (Klueh, 2008).

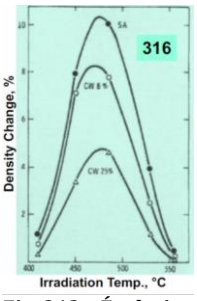

Fig. 212 – Évolution de la densité de l'acier CW 316 en fonction de la température d'environnement (Klueh, 2008).

Une suite possible des travaux présentés dans cet article serait d'enrichir le modèle thermomécanique en incluant une deuxième variable d'endommagement. Cette nouvelle variable serait associée au flux neutronique qui piloterait les dpa et une partie du chauffage nucléaire (r^v en éq.(275)).

Ce modèle actualisé renforcerait l'intérêt d'utiliser une approche tenant compte d'un couplage thermomécanique fort.

References

Abdel-Karim M. and Ohno N. Uniaxial Ratchetting of 316FR Steel at Room Temperature Part I: Experiments [Journal] // Journal of Engineering Materials and Technology. - 2000.

Abdel-Karim M. and Ohno N. Uniaxial Ratchetting of 316FR Steel at Room Temperature Part II: Constitutive Modeling and Simulation [Journal] // Journal of Engineering Materials and Technolog. - 2000.

Adam L. and Ponthot J.P. Thermomechanical modeling of metals at finite strains: First and mixed order finite elements [Journal] // International Journal of Solids and Structures. - 2005. - 21 : Vol. 42. - pp. 5615-5655.

AFCEN RCC-MR -Regles de Conception et de Construction des materiels mecaniques des installations nucleaires- [Book]. - 2007.

Armstrong P-J and Frederick C-O A mathematical representation of the multiaxial Bauschinger effect [Report]. - [s.l.] : Central Electricity Generating Board & Berkeley Nuclear Laboratories, 1966.

ASME American Society of Mechanical Engineers [Book]. - [s.l.] : AFNOR.

Barabash V. Materials challenges for ITER - Curent status and future activities - [Journal] // Journal of Nuclear Materials. - 2007. - Vols. 367-370. - pp. 21-32.

Benaarbia A., Rae Y. and Sun W. Unified viscoplasticity modelling and its application to fatigue-creep behaviour of gas turbine rotor [Journal] // International Journal of Mechanical Sciences. - 2018. - Vol. 136. - pp. 36-49.

Boutard J-L Endommagement des alliages métalliques par les neutrons rapides [Journal] // Reflets physique. - 2014. - Vol. Numéro 38. - pp. 17 - 21.

Bree J. Elastic-plastic behaviour of thin tubes subjected to internal pressure and intermittent high-heat fluxes with application to fast-nuclear-reactor fuel elements [Journal] // The Journal of Strain Analysis for Engineering Design. - 1967. - 3 : Vol. 2.

Budynas R.G and Young W.C. Roark's Formulas for Stress and Strain [Book]. - [s.l.] : McGraw-Hill, 2002.

Cailletaud G. and Pilvin P. Utilisation de modèles polycristallins pour le calcul par éléments finis [Journal] // Revue Européenne des Éléments Finis. - [s.l.] : International Journal of Mechanical Sciences, 1994. - 4 : Vol. 3. - pp. 515-541.

Cailletaud G. Une approche micromécanique du comportement des polycristaux [Journal] // Revue Physique Appliquée. - 1988. - Vol. 23. - pp. 353-365.

CEAwebsite [Online]. - http://www-fusion-magnetique.cea.fr.

Chaboche J-L. and Lemaitre J. Mechanics of solid materials [Book]. - France : Dunod, 1988. - second.

Chaboche J-L. and Nouailhas D. Constitutive Modeling of Ratchetting Effects—Part I: Experimental Facts and Properties of the Classical Models [Journal] // Journal of Engineering Materials and Technology . - 1989. - Vol. 4. - p. 1111.

Chaboche J-L. and Nouailhas D. Constitutive Modeling of Ratchetting Effects—Part II: Possibilities of Some Additional Kinematic Rules [Journal] // Journal of Engineering Materials and Technology . - 1989. - Vol. 4. - p. 111.

Chaboche J-L. Constitutive equations for cyclic plasticity and cyclic viscoplasticity [Journal] // International journal of plasticity. - 1989. - Vol. 5. - pp. 247-302.

Chaboche J-L. Modelization of the strain memory effect on the cyclic hardening of 316 stainless steel [Journal] // Structural mechanics in reactor technology. - 1979. - Vol. L.

Chaboche J-L. On some modifications of kinematic hardening to improve the description of ratchetting effects [Journal] // International Journal of Plasticity. - 1991. - 7 : Vol. 7. - pp. 661-678.

Chaboche J-L. Time independent constitutive theories for cyclic plasticity [Journal] // International Journal of Plasticity. - 1989. - 2 : Vol. 2. - pp. 149-188.

Chen X. Thermo-viscoplastic modeling incorporating dynamic strain aging effect on the uniaxial behavior of Z2CND18.12N stainless steel [Journal] // International Journal of Plasticity. - 2012. - Vol. 37. - pp. 119-139.

Coleman B.D. and Gurtin M.E. Thermodynamics with Internal State Variables [Journal] // The Journal of Chemical Physics. - 1967. - Vol. 47.2. - pp. 597-613.

Colomer C. Progress status of the ITER Vacuum Vessel sectors manufacturing design thermal hydraulic performance [Journal] // Fusion Engineering and Design. - 2017. - Vol. 124. - pp. 578-581.

Delobelle P., Robinet P. and Bocher L. Experimental study and phenomenological modelization of ratchet under uniaxial and biaxial loading on an austenitic stainless steel [Journal] // International Journal of plasticity . - 1995. - Vol. 11. - pp. 295-330.

EUROFUSIONwebsite [Online]. - https://www.euro-fusion.org.

F4Ewebsite [Online]. - http://fusionforenergy.europa.eu.

Fabbri M. Nuclear heat analysis for the ITER Vacuum Vessel regular sector [Journal] // Fusion Engineering and Design. - 2018. - Vol. 137. - pp. 435-439.

Germain P., Suquet P. and Nguyen Q.S. Continuum Thermodynamics [Journal] // Journal of Applied Mechanics, American Society of Mechanical Engineers (ASME). - 1983. - Vol. 50. - pp. 1010-1020.

Hassan T. and Bari S. An advancement in cyclic plasticity modeling for multiaxial ratcheting simulation [Journal] // International Journal of Plasticity. - 2002. - Vol. 18. - pp. 873–894.

Hassan T. Ratcheting in cyclic plasticity, part i: uniaxial behavior and part ii:multiaxial behavior [Journal] // International journal of plasticity. - 1992. - Vol. 8. - pp. 91-116 and 117-146.

Hassan T. Ratcheting of cyclically hardening and softening materials: i.uniaxial behavior, [Journal] // International journal of plasticity. - 1994. - 2 : Vol. 10. - pp. 149-184.

Haupt A. and Schinke B. Experiments on the ratchetting behavior of AISI316L(N) Austenitic Steel at Room Temperature [Journal] // Journal of engineering and materials. - 1996. - Vol. 118.

Hazard C., Lelong F. and Quinzain B. Mémotech: Structures Métaliques [Book]. - [s.l.] : Castella, 1997.

Hübel H. Basic conditions for material and structural ratcheting [Journal] // Nuclear Engineering and Design. - 1996. - 1 : Vol. 162. - pp. 55-65.

Hughes T.J.R and Simo J.C. Computational Inelasticity [Book]. - [s.l.] : Springer, 2000.

Hugues Thomas j.r. Linear Static and Dynamic - Finite Element Analysis [Book Section] // The Finite Element Method. - 1987.

Hyde C.J., Sun W. and Leen S.B. Cyclic thermo-mechanical modelling and testing of the 316 stainless steel [Book]. - [s.l.] : International journal of Pressure Vessels and piping, 2010.

Ikeda K. ITER on the road to fusion energy [Journal] // IAEA Nuclear Fusion. - 2009. - Vol. 50. - p. 014002.

IO web site [Online]. - https://www.iter.org.

ITER Structural Design Criteria for ITER In-vessel Components [Book]. - [s.l.] : ITER Document, 2012.

Jiang Y. and Sehitoglu H. Modeling of Cyclic Ratchetting Plasticity, Part I: Development of Constitutive Relations [Journal] // Journal of Applied Mechanics. - 1996. - Vol. 63. - pp. 720-725.

Jiang Y. and Sehitoglu H. Modeling of Cyclic Ratchetting Plasticity, Part II: Comparison of Model Simulations With Experiments [Journal] // Journal of Applied Mechanics. - 1996. - Vol. 63. - pp. 726-733.

Jiang Y. and Zhang J. Benchmark experiments and characteristic cyclic plasticity deformation [Journal] // International Journal of Plasticity . - 2008. - Vol. 24. - pp. 1481-1515.

Kalinin G. Assessment and selection of metrials for ITER in-vessel components [Journal] // Journal of Nuclear MATERIALS. - 2000. - pp. 10-19.

Kalinin G. ITER R&D: Vacuum Vessel and In-Vessel components: material deveolopment and test [Journal] // Fusion Engineering and Design. - 2001. - Vol. 55. - pp. 231-246.

Kalinin G. Structural materials for ITER in-vessel component design [Journal] // Journal of Nuclear Materials. - 1996. - Vols. 233-237. - pp. 9-16.

Kang G. Ratchetting: recent progresses in phenomenon observation [Journal] // International journal of fatigue. - 2008. - Vol. 30. - pp. 1448-1472.

Klueh R. Cladding and Duct Materials for Advanced Nuclear Recycle Reactors [Journal] // JOM: the journal of the Minerals, Metals & Materials Society. - 2008. - Vol. 60. - pp. 15-23.

Kobayashi M. and Ohno N. Thermal ratchetting of a cylinder subjected to a moving temperature front: Effects of kinematic hardening rules on the analysis [Journal] // International Journal of Plasticity. - 1996. - 2 : Vol. 12. - pp. 255-271.

Kullig E. and Wippler S. Numerical integration and FEM-implementation of a viscoplastic Chaboche-model with static recovery [Journal]. - [s.l.] : Computational Mechanics, 2006. - Vol. 38.

Lee H-L. Thermal ratchetting deformation of a 316L stainless steel cylindrical structure under an axial moving temperature distribution [Journal] // International journal of pressure vessels and piping. - 2003. - Vol. 80. - pp. 41-48.

Lemaitre J. Coupled elasto-viscoplasticity and damge constituve equations [Journal] // Computer methods in applied mechanics and engineering. - 1985. - Vol. 51. - pp. 31-49.

Lo_Frano R. Fluid dynamics analysis of loss of vacuum accident of ITER cryostat [Journal] // Fusion Engineering and Design. - 2016. - Vols. 109-111. - pp. 1302-1307.

Maki K. Nuclear heating in fusion reactor [Conference] // JAERI-Conf-99-002. - Japan : [s.n.], 1999.

Martinez J-M Structural analysis of the ITER Vacuum Vessel regarding 2012 ITER Project-Level Loads [Journal] // Fusion Engineering and Design. - 2014. - Vol. 89. - pp. 1836-1842.

Martinez J-M. ITER vacuum vessel structural analysis completion during manufacturing phase [Journal] // Fusion Engineering and Design. - 2016. - Vols. 109-111. - pp. 688-692.

Martinez J-M. Structural damages prevention of the ITER vacuum vessel and ports by elasto-plastic analysis with regards to RCC-MR [Journal] // Fusion Engineering and Design. - 2015. - Vols. 98-99. - pp. 1552-1555.

Mitteau R. Heat loads and shape design of the ITER first wall [Journal] // Fusion Engineering and Design. - 2010. - Vol. 85. - pp. 2049-2053.

Moreau S. Analysis of thermoelastic effects accompanying the deformation of PMMA and PC polymers [Journal] // Comptes Rendus Mécaniques. - [s.l.] : Comptes Rendus Mécaniques, 2005. - 8 : Vol. 333. - pp. 648-653.

Nouailhas D Modélisation de l'écrouissage et de la restauration en viscoplasticité cyclique [Journal] // Revue de physique appliquée. - 1988. - Vol. 23. - pp. 339-349.

Ohno N. and Wang J.-D. Kinematic hardening rules with critical state of dynamic recovery, part I: formulation and basic features for ratchetting behavior [Journal] // International Journal of Plasticity. - 1993. - Vol. 9. - pp. 375-390.

Ohno N. and Wang J.-D. Kinematic hardening rules with critical state of dynamic recovery, part II: application to experiments of [Journal] // International Journal of Plasticity. - 1993. - Vol. 9. - pp. 391-40.

Perez G. Optimized mass flow rate distribution analysis for cooling the ITER blanket system [Journal] // Fusion Engineering and Design. - 2014. - Vol. 89. - pp. 1324-1329.

Perzyna P The thermodynamical theory of elasto-viscoplasticity [Journal] // Engineering Transactions. - 2005. - Vol. 53. - pp. 235-316.

Rothe Steffen Monolithic and partitioned coupling schemes for thermo-viscoplasticity [Journal]. - [s.l.] : Computer Methods in Applied Mechanics and Engineering, 2015. - Vol. 293.

Rousselier G. Ductile fracture models and their potential [Journal] // Nuclear Engineering and Design. - 1987. - Vol. 105. - pp. 97-11.

Sabourin F. Application of 3D View Factor method for heat fluxes deposition on ITER Cryostat Thermal Shield [Journal] // Fusion Engineering and design. - 2018.

Salavy J-F. Ferritic–Martensitic steel Test Blanket Modules: Status and future needs for design criteria requirements and fabrication validation [Journal] // Journal of Nuclear Materials. - 2009. - Vols. 386-388. - pp. 922-926.

Sannazzaro G. Development of design Criteria for ITER In-vessel Components [Journal] // Fusion Engineering and Design. - 2013. - Vol. 88. - pp. 2138-2141.

Tavassoli A.A. Assesment of austenistic stainless steels [Journal] // Fusion Engineering and Design. - [s.l.] : Fusion Engineering and Design, 1995. - Vol. 29. - pp. 371-390.

Vincent Ludovic Une amélioration de la description du phénomène de déformation progressive dans les métaux par la prise en compte de la distorsion du domaine d'élasticité [Report]. - [s.l.] : Thèse soutenue le 18 Octobre 2002, 2003.

Lists of illustrations

List of figures

List of tables